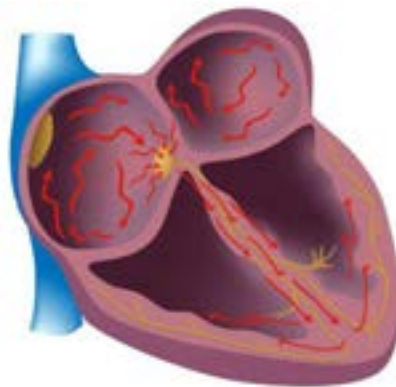


PhD Thesis

Multiscale Analysis of Atrial Fibrillation Mechanisms



Carlos Sánchez Tapia

Supervisors:

Esther Pueyo Paules

Blanca Rodríguez López

Zaragoza, April 2014



PhD Thesis

Multiscale Analysis of Atrial Fibrillation Mechanisms

Carlos Sánchez Tapia

Supervisors:

Esther Pueyo Paules

Blanca Rodríguez López

Zaragoza, April 2014

Acknowledgements

There are many people that have been very important to me during the course of this thesis and I would like to express my gratitude to all of them.

First of all, I would like to thank the two persons without whom this thesis would have never been done: Esther Pueyo and Blanca Rodríguez. I have learnt a lot from both of them and it has been a real pleasure for me to be their PhD student all these past few years. I have found their guidance, hard work, dedication and, primarily, their passion for scientific investigation really encouraging and helpful.

To Pablo Laguna, for his fantastic ability to manage our research group and being a good support to all of us in both personal and academic stuff.

To Alfonso Bueno, for his invaluable help in so many occasions, becoming a very good colleague but a better friend.

To Alberto Corrias, for being such a good flatmate and friend, and introducing me not only into Chaste but into the Oxonian life.

To José Félix Rodríguez, the main Elvira-software developer, for his high efficacy and speed solving all the simulation problems I have had.

To all the people and institutions I have collaborated with: AstraZeneca, Karlsruhe Institute of Technology, Technische Universität Dresden and Universidad Politécnica de Valencia, for all the useful data, software and comments provided that helped me to improve the work performed in this thesis.

To all my colleagues of the signal processing group in Zaragoza, Juan, Fer, Julia, Álex, Pepo, Ana... and everyone who has ever been part of this unique and special group in the last 6 years, for being like a second family to me. They have made me feel comfortable since the first day and all the time we have passed together has been full of unforgettable moments: the scientific discussions at the seminars or in the laboratory, the "coffee-dudes" time, the support they gave me when I had a bad day, the good and original sense of humour that is always present in the laboratory, the "doodle-lies", the frequent celebrations, the moments of shared passion for doing science... Thanks for everything.

To my friends Álex, Carlos, Javi, Gema, José Ignacio, Montse, Cristina, Daniel, Juampa, José Luis... because relaxing moments and leisure time have been very important to keep my mind clear.

To my family, Carlos, Rosa Blanca, David and María José, for their unconditional support and love. Their encouragement and wise advice have been essential for me to face all the issues I have encountered on the way to finish this thesis.

Finally, to Lorena, my love, my honey, for being so comprehensive and patient specially during my residencies in Oxford because it was really tough to be far away. Her company, affection and care for me are something I am, and always will, thankful to her for.

Abstract

Atrial fibrillation (AF) is the most commonly diagnosed cardiac arrhythmia, particularly in developed countries. AF is mainly initiated and sustained by reentrant circuits (rotors) and ectopic foci in different parts of the atria, which entail a chaotic electrical activation pattern in the muscular tissue. However, the ionic mechanisms underlying the generation and maintenance of AF are not fully understood, thus leading to a limited efficacy of current pharmacological AF therapies, which often require concomitant surgical ablation of atrial tissue. In this thesis we provide mechanistic descriptions of the physiological and pathophysiological behavior of atrial cells and tissues by means of modeling and simulation of human atrial electrical activity.

During the course of this thesis, a number of models have been used to simulate the electrical activity of human atrial cardiomyocytes and investigate properties related with arrhythmic risk. The models used in this thesis provide a full description of all the ionic currents and intracellular dynamics of sodium, potassium and calcium ions that underlie differences between the potentials in the intracellular and the extracellular spaces during each cardiac cycle. The time course of this transmembrane potential when an external stimulus is applied to the cell is known as action potential (AP).

The first part of this thesis consisted of the analysis of the adaptation of the AP duration (APD), in both individual cells and unidimensional fibers, to changes in heart rate. Simulations showed that APD adaptation occurred in two phases, fast and slow, with different underlying ionic mechanisms. The maximal conductance of I_{CaL} and the activity of the $NaCa$ exchanger were the main drivers of the fast adaptation phase, while the activity of the NaK pump was the major determinant of the slow phase.

In the second part of the present thesis, the investigations were extended to study additional cell and tissue electrophysiological properties related to the risk of suffering atrial arrhythmias, including APD and resting membrane potential at steady-state after periodic stimulation, APD restitution curves with SIS2 and dynamic restitution protocols, conduction velocity in unidimensional fibers, and effective refractory period, dominant frequency and phase singularities in bidimensional tissue. The ionic mechanisms modulating these electrophysiological properties were investigated in sinus rhythm

(SR) and AF conditions. The results from the conducted simulations allowed to conclude that the activity of the *NaK* pump and the I_{K1} current are the most important ionic mechanisms modulating properties at cell level, both in SR and AF conditions, whereas the role of I_{Na} was proved to be key in the modulation of tissue properties, particularly in AF. Interestingly, simulations showed that temporal adaptation of atrial electrophysiological properties to alterations in ionic currents was monotonic, except for alterations in the *NaK* pump where adaptation was biphasic (initial increase followed by progressive decrease, or viceversa).

The third part of this thesis dealt with the study of the large variability that exists between cells from different patients and different regions of the atria. Particularly, the ionic mechanisms involved in the variability in atrial cell repolarization and AP morphology were investigated. Populations of models were built to mimic the variability of experimental data from patients diagnosed with SR and with chronic AF by generating combinations of the most important ionic mechanisms in AP modulation. Only AP models within experimentally determined physiological ranges were selected. Using the developed populations of models, the ionic mechanisms underlying variability in the APD measured at different stages of repolarization were ascertained. I_{K1} and the *NaK* pump were identified as the most relevant mechanisms determining variability in APD_{90} , whereas I_{CaL} , I_{to} and I_{Kur} were key in modulating inter-subject differences in APD_{20} and APD_{50} , both in SR and AF conditions. The unraveled ionic mechanisms underlying variability in AP morphology were I_{K1} , I_{NaK} and I_{NaCa} . Results obtained with different AP models were consistent with each other, except for some differences such as the relevance of I_{CaL} in modulating variability in APD_{90} , the importance of I_{K1} and the *NaK* pump in modulating variability in APD_{20} and the likelihood of presenting AP alternans within the population at fast pacing rates.

In the fourth part of this thesis, AF dynamics at whole atria level were investigated using a three-dimensional (3D) virtual human atrial model developed at the Karlsruhe Institute of Technology. From the analysis of 49 pseudo-electrogram signals mapping the atria, we observed the dominant frequency of the signals was strongly reduced when either inhibition I_{Na} or, to a lesser extent, I_{K1} and the *NaK* pump. The temporal regularity of the arrhythmia was increased by both I_{Na} and I_{K1} inhibition in left atrium, but the effects were reduced in the right atrium, whereas *NaK* pump inhibition acted to reduce the regularity in both atria. The effects on AF dynamics of introducing variability in APD_{90} , APD_{50} and APD_{20} were studied by calculating sub-populations of models (extracting them from the total population of models previously described) and assigning each cell in the 3D model with a model of the sub-population. The results of the simulations showed that human atria presenting long APDs could be associated with slow but very

regular fibrillatory patterns, whereas those with short APDs may have high frequency reentrant rotors and high organization.

To summarize, the results presented in this thesis have improved the understanding of the ionic mechanisms underlying electrophysiological properties related to arrhythmic risk in human atria through the use of cardiac computational modeling techniques.

Resumen y conclusiones

La fibrilación auricular (AF) es la arritmia cardíaca más comúnmente diagnosticada, especialmente en países desarrollados. AF se inicia y mantiene principalmente por circuitos reentrantes (rotores) y focos ectópicos, los cuales producen un patrón de activación caótico en el tejido cardíaco auricular. Sin embargo, los mecanismos iónicos subyacentes no son totalmente conocidos, lo que conlleva una efectividad limitada de las actuales terapias farmacológicas para tratar AF y, por tanto, la necesidad de utilizar ablación quirúrgica. En esta tesis describimos el comportamiento fisiológico y pato-fisiológico de células y tejidos auriculares mediante modelado y simulación de la actividad eléctrica auricular.

Durante el desarrollo de esta tesis se han utilizado varios modelos para simular la actividad eléctrica de cardiomiocitos de aurícula humana e investigar propiedades relacionadas con el riesgo arritmico. Los modelos utilizados en esta tesis poseen una descripción detallada de todas las corrientes iónicas y dinámicas intracelulares de los iones de sodio, potasio y calcio que subyacen a las diferencias de potencial entre el interior y el exterior de la célula durante cada ciclo cardíaco. La evolución de este potencial transmembrana tras aplicar un estímulo externo se conoce como potencial de acción (AP).

La primera parte de esta tesis consistió en el análisis de la adaptación de la duración del AP (APD) en células individuales y fibras unidimensionales ante cambios en el ritmo cardíaco. Las simulaciones mostraron que la adaptación del APD ocurría en dos fases, rápida y lenta, cada una con diferentes mecanismos iónicos subyacentes. La máxima conductancia de I_{CaL} y la actividad del intercambiador $NaCa$ eran los más relevantes en la fase rápida, mientras que la actividad de la bomba NaK era el principal modulador de la fase lenta.

En la segunda parte de la presente tesis, las investigaciones se extendieron al estudio de un mayor número de propiedades electrofisiológicas, en célula y tejido, relacionadas con el riesgo arritmico auricular, incluyendo el APD, el potencial de reposo, las curvas de restitución de APD, la velocidad de conducción, el período refractario efectivo, la frecuencia dominante y las singularidades de fase. Los mecanismos iónicos que modulan estas propiedades electrofisiológicas se investigaron en condiciones de ritmo sinusal (SR) y

de AF. Los resultados de las simulaciones mostraron que la actividad de la bomba NaK y la corriente I_{K1} eran los mecanismos iónicos más importantes en la modulación de las propiedades a nivel celular, mientras que I_{Na} era esencial en las propiedades tisulares, especialmente en AF. En las simulaciones se observó que la adaptación temporal de las propiedades estudiadas ante cambios en las corrientes iónicas se producía de forma monotónica, excepto para las alteraciones de la bomba NaK cuya adaptación era bifásica (aumento inicial seguido de una reducción progresiva, o viceversa).

La tercera parte de esta tesis trató del estudio de los mecanismos iónicos involucrados en las diferentes fases de la repolarización celular teniendo en cuenta la gran variabilidad que existe entre células de distintos pacientes o incluso de diferentes partes de las aurículas. Para imitar la variabilidad medida en pacientes en SR y AF, se construyeron poblaciones de modelos con combinaciones de los mecanismos iónicos con mayor relevancia en la modulación del AP, seleccionando finalmente aquéllos dentro de un rango fisiológico determinado experimentalmente. Utilizando las poblaciones de modelos generadas, se identificaron los mecanismos iónicos más relevantes en la variabilidad de cada fase de la repolarización. I_{K1} y la bomba NaK se identificaron como los más relevantes modulando la variabilidad en APD_{90} ; mientras que I_{CaL} , I_{to} e I_{Kur} eran esenciales en la variabilidad de APD_{50} y APD_{20} . Los mecanismos iónicos subyacentes a la variabilidad en la morfología del AP fueron I_{K1} , I_{NaK} e I_{NaCa} . Los resultados fueron consistentes entre los modelos de AP utilizados, excepto por algunas diferencias en el papel de I_{CaL} en la modulación de la variabilidad en APD_{90} , la importancia de I_{K1} como de la bomba NaK en la variabilidad de APD_{20} y la probabilidad de presentar AP alternantes dentro de la población ante ritmos rápidos de marcapaseado.

En la cuarta parte de esta tesis se investigó la dinámica de AF a nivel de aurícula completa utilizando un modelo tridimensional (3D) desarrollado en el Karlsruhe Institute of Technology. Del análisis de 49 pseudo-electrogramas mapeando las aurículas, se observó que la frecuencia dominante de las señales se redujo considerablemente bloqueando I_{Na} o, en menor medida, I_{K1} y la bomba NaK . La regularidad temporal de la arritmia se incrementó en la aurícula izquierda bloqueando tanto I_{Na} como I_{K1} , pero con apenas cambios en la aurícula derecha, mientras que el bloqueo de la bomba NaK redujo la regularidad en ambas aurículas. Para estudiar los efectos de la variabilidad en APD_{90} , APD_{50} y APD_{20} se extrajeron sub-poblaciones de modelos respecto a las calculadas previamente y se asignó a cada célula del modelo 3D un modelo de la sub-población. Los resultados mostraron que aurículas humanas con APDs largos se asociaban con patrones fibrilatorios lentos pero regulares, mientras que los APDs mostraban rotores reentrantes de alta frecuencia con alta organización.

En resumen, los resultados presentados en esta tesis han mejorado el

conocimiento de los mecanismos iónicos subyacentes a propiedades electrofisiológicas relacionadas con riesgo arrítmico en aurícula human mediante el uso de técnicas de modelado cardiaco computacional.

Contents

Acknowledgements	v
Abstract	vii
Resumen y conclusiones	xi
Contents	xiv
List of Figures	xvi
List of Tables	xviii
1 Introduction	1
1.1 Cardiac Arrhythmias	1
1.2 Electrical Activity of the Heart	1
1.2.1 Body Surface Electrocardiogram	2
1.2.2 Myocardial Wall Electrograms	3
1.2.3 Cellular Electrical Activity	4
1.2.4 Ionic Currents	11
1.2.5 Ionic Concentrations	21
1.3 Atrial Fibrillation: Incidence and Pathophysiology	24
1.3.1 Types of Atrial Fibrillation	24
1.3.2 Triggering and Maintenance of Atrial Fibrillation	25
1.3.3 Therapies for Arrhythmia Treatment	26
1.4 Thesis Objectives	29
1.5 Thesis Outline	30
2 General Materials and Methods	35
2.1 Materials	35
2.1.1 Cardiac Computational Models	35
2.2 Methods	40
2.2.1 Numerical Methods	40

2.2.2	Computing Resources	41
3	Quantification of APD Rate Adaptation in Human Atria and its Relationship with Arrhythmogenesis	43
3.1	Introduction	43
3.1.1	Objetives	44
3.2	Methods	44
3.2.1	Stimulation Protocols	44
3.2.2	Characterization of APD Rate Adaptation and Underlying Mechanisms	47
3.2.3	Preclinical Markers of Arrhythmic Risk	48
3.3	Results	49
3.3.1	APD Rate Adaptation in Human Atrial Myocytes	49
3.3.2	APD Rate Adaptation in 1D Atrial Fibers	52
3.3.3	Ionic Mechanisms of APD Rate Adaptation	55
3.3.4	Relation between APD Rate Adaptation and Arrhythmogenesis	60
3.3.5	APD Rate Adaptation in Atrial versus Ventricular Myocytes	60
3.4	Discussion	62
3.4.1	Limitations of the Study	64
4	Ionic Modulation of Electrophysiological Properties and Rotor Dynamics in Human Atria	67
4.1	Introduction	67
4.1.1	Objectives	68
4.2	Methods	68
4.2.1	Membrane Kinetics	68
4.2.2	Cell Simulations	69
4.2.3	Tissue Simulations	70
4.2.4	Sensitivity Analysis	71
4.3	Results	72
4.3.1	Electrophysiological Markers Related to Arrhythmic Risk in SR versus AF	72
4.3.2	Role of Ionic Currents in Modulating Human Atrial Electrophysiological Markers	73
4.3.3	Temporal Adaptation of Human Atrial Electrophysiological Markers to Changes in Ionic Currents	82
4.3.4	Reentrant Activity in Human Atrial Tissue and Role of Ionic Currents in its Modulation	84
4.4	Discussion	91
4.4.1	Limitations of the Study	94

5	Intercellular Variability in Human Atrial Action Potential in SR versus AF Patients	97
5.1	Introduction	97
5.1.1	Objectives	98
5.2	Methods	98
5.2.1	Experimental Dataset	98
5.2.2	Populations of Models of Human Atrial Electrophysiology	100
5.2.3	Statistical Analysis	102
5.3	Results	103
5.3.1	Ionic Determinants of Inter-subject Variability in APD	103
5.3.2	Ionic Determinants of Inter-subject Variability in AP Morphology	106
5.3.3	Ionic Determinants of Inter-subject Variability in AP Rate Dependence	109
5.4	Discussion	110
5.4.1	Limitations of the Study	113
6	Ionic Modulation of Atrial Fibrillation Dynamics in a Human Atrial 3D Model	115
6.1	Introduction	115
6.1.1	Objectives	116
6.2	Methods	116
6.2.1	Cell and 3D Models of Human Atria	116
6.2.2	Simulated Ionic Current Alterations	117
6.2.3	Repolarization Variability within the 3D Model	117
6.2.4	EGM Processing and Arrhythmia-related Indices	119
6.2.5	Ann-Arbor Database	121
6.3	Results	121
6.3.1	Parasympathetic Influence on Fibrillatory Dynamics	121
6.3.2	Ionic Modulation of Reentrant Behavior in Human Atria	121
6.3.3	Impact of Inter-subject Variability in Cell Repolarization on AF Dynamics	124
6.3.4	Validation of Simulation Results with EGMs from AF Patients	131
6.4	Discussion	132
6.4.1	Limitations of the Study	133
7	Conclusions and Future Extensions	135
7.1	Conclusions	135
7.1.1	Ionic Mechanisms Underlying Human Atrial Electrophysiology Markers in SR	135

7.1.2	Ionic Mechanisms Underlying Human Atrial Electrophysiology Markers in AF Conditions	137
7.1.3	Ionic Mechanisms Underlying Inter-subject Variability in Human Atrial AP	137
7.1.4	Ionic Mechanisms Underlying AF Dynamics in 3D Virtual Human Atria	138
7.2	Future Extensions	139
	Glossary	141
	Publications Derived from the Thesis	147
	Bibliography	149

List of Figures

1.1	Electrode positions in the standard 12-lead ECG (modified from [2]) and characteristic waves of the ECG signal.	2
1.2	Example of an ECG signal and the corresponding EGM measured at the high right atrium (HRA).	3
1.3	A: Capture of a rainbow trout cardiomyocyte with a micropipette (modified from [6]). B: Schematic view of the Patch Clamp technique.	4
1.4	A: Ionic current of a single potassium channel measured with the Voltage Clamp technique in a cardiomyocyte (modified from [8]). B: V_m measured with the Current Clamp technique in a murine neuron (modified from [9]).	5
1.5	Electrical circuit representing the cell membrane. Resistors of sodium (R_{Na}) and potassium (R_K) are variable, dependent on both time and V_m and inverse to the associated conductances. Resistor associated to the rest of ions (R_l) is considered constant [11].	7
1.6	Simulated V_m and the most relevant ionic currents determining the phases of the AP of a human atrial cardiomyocyte. . .	8
1.7	Action potentials from different types of cardiomyocytes and their contribution to the ECG signal (modified from [12]). . .	9
1.8	Schematic representation of the membrane of the human atrial cell (modified from [13]).	10
1.9	Experimental human atrial AP (modified from [14]) and ion fluxes of sodium (green), calcium (red) and potassium (blue). . .	10
1.10	Simulated human atrial AP (top panel) and corresponding I_{Na} (bottom panel) measured during the last cardiac cycle following a train of periodic stimuli every 1 second for 20 minutes. <i>Note: the activation interval of I_{Na} is zoomed in due to its very short duration.</i>	12
1.11	Simulated human atrial calcium currents measured during the last cardiac cycle following a train of periodic stimuli every 1 second for 20 minutes: I_{CaL} , I_{up} , $I_{up,leak}$, I_{tr} and I_{rel}	13

1.12	Schematic representation of ionic currents and SRret compartments in human atrial cardiomyocytes according to the Courtemanche <i>et al.</i> model (A , modified from [15]) and the Nygren <i>et al.</i> model (B , modified from [13])	15
1.13	Simulated human atrial potassium currents measured during the last cardiac cycle following a train of periodic stimuli every 1 second for 20 minutes: I_{to} , I_{Kur} , I_{Kr} , I_{Ks} and I_{K1}	16
1.14	A: I_{KACH} intensity-voltage relations (data points are mean \pm standard deviation) in both experiments with different [ACh] levels (color symbols) and with the equation 1.9 (red lines). B and C: Comparison of canine atrial experiments (left) and canine atrial model (right) AP duration (top) and morphology (bottom) (modified from [28]).	19
1.15	Simulated human atrial sodium/potassium pump current (I_{NaK} , top panel) and sodium/calcium exchanger current (I_{NaCa} , bottom panel) measured during the last cardiac cycle following a train of periodic stimuli every 1 second for 20 minutes.	20
1.16	Schematic view of a human atrial cardiomyocyte and the most important ionic concentration gradients: K^+ (blue), Ca^{2+} (red) and Na^+ (black).	22
1.17	ECG signals corresponding to normal SR (top) and AF (bottom).	24
1.18	Schematic view of the hypotheses for AF generation and maintenance (modified from [47]). A: Multiple reentrant wavelets; B: Focal hypothesis; C: Rotor hypothesis.	26
1.19	Effects of class I antiarrhythmic drugs: ventricular AP in control conditions (solid black line), and after administration of class IA (solid red line), class IB (solid blue line) and class IC (dashed green line) drugs (modified from [55]).	28
1.20	Magnetic resonance imaging (MRI) scan of the left atrium (viewed from the patient's back). Chaotic electrical activation pattern associated with AF (left panel) and ablation lesions produced around pulmonary veins by a catheter in order to electrically isolate them (right panel) (modified from [58]).	29
2.1	Simulated APs obtained after pacing for 50 s with a cycle length (CL) of 1 s with the five atrial cell models (modified from [60]).	36
2.2	Tissue model commonly used in propagation models consisting of cells (boxes) connected to each other with resistances in both intracellular (white cylinders) and extracellular (grey cylinders) space (modified from [61]).	38

2.3	Anatomical 3D model of the human atria. A: RA in a frontal view. B: LA in a dorsal view. C: View through tricuspid and mitral valve. SAN, CT and PMs are visible in the RA. (modified from [65]).	40
3.1	Experimental devices in a confocal microscopy laboratory. . .	45
3.2	Example of a stimulation protocol with a series of 300-ms conditioning potentials between -70 and +10 mV used to inactivate I_{CaL} in a zebrafish ventricular myocyte followed by a 300-ms test pulse to measure I_{CaL} after the conditioning pulse (left panel). The family of I_{CaL} current traces obtained (right panel) for the potentials shown on the right side is shown (modified from [83]).	46
3.3	APDR curves (APD vs. DI) with the S1S2 restitution protocol (blue) and dynamic restitution protocol (red).	47
3.4	CL time course with the default pacing protocol: $CL_1=1000$ ms and $CL_2=600$ ms (left). APD time course corresponding to the pacing protocol (right).	50
3.5	Comparison between APD adaptation to changes in HR in atrial cell simulations with the Courtemanche model (left) versus results obtained experimentally in canine atrial tissue (right; modified from [81]).	51
3.6	APD time courses with different combinations of CL changes using the pacing protocol: the default case (1000-600-1000 ms, black solid line), two cases with different initial CL but the same magnitude of CL change (2000-1600-2000 ms, green solid line; and 1600-1200-1600 ms, blue dash-dotted line), and two cases with different magnitude of change in CL but the same initial CL (1000-800-1000 ms, pink dashed line; and 1000-400-1000 ms, red dotted line).	53
3.7	APs generated after the third stimulus with the Courtemanche model in a periodic protocol with $CL = 1000$ ms. APs corresponding to cell 1 (blue), cell 50 (pink), cell 100 (red), cell 150 (black) and cell 200 (green) in a 1D fiber consisting of 200 cells. Stimuli applied only to cell 1.	54
3.8	APD time course of three cells in a one-dimensional fiber of 200 cells when applying the pacing protocol 1000-600-1000 ms with the Nygren model. Alternating behavior of the APD shown in the zoomed in box.	55

3.9	Values of the markers τ_{fast} , τ_{slow} , ρ , δ , S_{s1s2} and S_{dyn} when the three ionic mechanisms modulating cardiac memory in human atrial cells (G_{NaCa} , G_{CaL} and G_{NaK}) were modified by -30%, -15%, 0, +15% and +30% with respect to the default values in the Courtemanche model.	56
3.10	APD time course under control, G_{CaL} inhibition (left top panel), G_{NaCa} inhibition (right top panel), $[Na^+]_i$ clamping (left bottom panel) and G_{NaK} inhibition (right bottom panel) in cells simulated with the Courtemanche model.	57
3.11	Time course of the stimulation CL (top panel) and the amplitude of I_{CaL} peaks in some experimental recordings of human atrial cells in the simulations with the Courtemanche and Nygren models (bottom panel).	58
3.12	APD time course with the pacing protocol 1000-600-1000 ms using the Nygren (blue dash-dotted line) and Courtemanche (black solid line) models.	59
3.13	Comparison of simulation results of APD adaptation to sudden changes in HR in cells from the ventricular epicardium [80] and atrial cells, both in human, showing the values of t_{90} for HR acceleration and HR deceleration.	61
4.1	Steady-state AP and ionic currents under SR conditions (solid line) and permanent AF conditions (dashed line) at CL=1000 ms using the Maleckar (left) and the Courtemanche (right) human atrial AP models.	73
4.2	APDR curves obtained using the S1S2 (top) and dynamic (bottom) protocols, in SR (left) and permanent AF conditions (right) with the Maleckar and the Courtemanche models for default values and following $\pm 30\%$ alterations in G_{NaK} and G_{K1}	74
4.3	Steady-state human atrial AP in SR (top) and AF (bottom) for default ($\pm 0\%$) and following alterations in G_{K1} (panels A, A'), G_{NaK} (panels B, B'), G_{Kur} (panels C, C'), G_{CaL} (panels D, D'), G_{NaCa} (panels E, E') and G_{to} (panels F, F'), using the Maleckar model.	77
4.4	Percent changes in steady-state APD ₉₀ (ΔAPD_{90} , A-B), RMP (ΔRMP , C-D), S_{s1s2} (ΔS_{s1s2} , E-F) and S_{dyn} (ΔS_{dyn} , G-H) with respect to default conditions produced by $\pm 30\%$ alterations in ionic conductances for SR (left) and AF (right) using the Maleckar model.	78

- 4.5 Percent changes in steady-state APD₉₀ (Δ APD₉₀, A-B), RMP (Δ RMP, C-D), S_{s1s2} (Δ S_{s1s2}, E-F) and S_{dyn} (Δ S_{dyn}, G-H) with respect to default conditions produced by $\pm 30\%$ alterations in ionic conductances for SR (left) and AF (right) using the Courtemanche model. 79
- 4.6 Temporal adaptation of percent changes in APD₉₀ (Δ APD₉₀, A-B) and RMP (Δ RMP, C-D), for single cell simulations, RP (Δ RP, E-F), for 2D tissue simulations, and CV (Δ CV, G-H), for 1D fiber simulations, with respect to default conditions during $\pm 30\%$ alterations in G_{NaK} , G_{K1} and G_{Na} in SR (left) and AF (right) using the Maleckar model. **Note: Following 5 min of G_{K1} 30% block repolarization fails.* 83
- 4.7 Time course of AP (A), $[Na^+]_i$ (B), $[Ca^{2+}]_i$ (C), I_{NaCa} (D), I_{CaL} (E), I_{up} (F) and I_{rel} (G) for default conditions (left), and following 15 s and 30 s after 30% G_{NaK} block using the Maleckar model. APD₉₀ values are shown in bold for each AP. 85
- 4.8 Reentrant activity in 2D 5x5 cm² atrial tissue. A: Snapshots showing V_m distribution for different timings during the application of a S1S2 cross-stimulation protocol in SR. B: pEGM and power spectral density corresponding to the simulation shown in A. C: Snapshots showing V_m distribution for different timings during the application of an S1S2 cross-stimulation protocol in AF. D: pEGM and power spectral density corresponding to the simulation shown in C. 86
- 4.9 Percent changes in DF (Δ DF) with respect to default conditions produced by $\pm 30\%$ alterations in G_{NaK} , G_{K1} and G_{Na} in SR (A) and AF (B) using the Maleckar model. DF values are shown for reentry initiated at 10 s (blue bars) and 5 min (red bars) following changes in ionic parameters. Snapshots of reentry 10 s after the change in ionic parameters under default conditions and 30% block of G_{NaK} , G_{K1} and G_{Na} in SR (C) and AF (D). Black lines on snapshots represent the corresponding PS trajectories. 87
- 4.10 Changes in the characteristics of simulated reentry caused by changes in ionic current conductances for SR (black bars) and AF (grey bars). 30% increase/decrease of each ionic conductance is shown in the last row. Panels A, B and C show VW upper and lower limits, W_{vw} and DF, respectively, for each simulation. Specific cases **a**, **b**, **c** and **d** are referred in the text. 89

- 4.11 Changes in the characteristics of simulated reentry caused by simultaneous changes in G_{K1} , G_{NaK} and G_{Na} for SR (black bars) and AF (grey bars). 30% increase/decrease in G_{K1} , G_{NaK} and G_{Na} for each case is shown in the last row. Panels A, B and C show VW upper and lower limits, W_{vw} and DF, respectively, for each simulation. Specific cases **a** (same as in Figure 4.10), **e** and **f** are referred in the text. 90
- 5.1 APs recorded in atrial preparations from SR (left) and AF (right) patients. 99
- 5.2 Variability of ionic conductances G_{K1} , G_{NaK} , G_{CaL} , G_{to} , G_{Kur} and G_{NaCa} in experimentally-calibrated populations of human atrial AP models, sampled within a $\pm 100\%$ range of their original values in the Maleckar (A), Courtemanche (B) and Grandi (C) human atrial AP models in SR (black) and AF (gray). Estimated median physiological values are shown as central horizontal lines within each boxplot. (Mann-Whitney U test: * $p < 0.05$; ** $p < 0.01$; *** $p < 0.001$). 102
- 5.3 Experimentally-calibrated human AP model populations for SR (left) and AF (right) patients. Initial unrestricted $\pm 100\%$ sampled population (A), experimentally calibrated $\pm 30\%$ sampled populations (B) and histograms corresponding to APD_{90} , APD_{50} and APD_{20} distributions in both the calibrated model populations (C) and the experimental measurements (D) are shown based on the Courtemanche model. Histogram bar widths are 10 ms for both APD_{90} and APD_{50} , and 4 ms for APD_{20} 104
- 5.4 Transmembrane potential and ionic current traces in SR (left) and AF (right) with the Maleckar model corresponding to maximum APD_{90} (red dash-dotted lines), minimum APD_{90} (black dash-dotted lines), maximum APD_{50} (red thin solid lines), minimum APD_{50} (black thin solid lines), maximum APD_{20} (red dashed lines) and minimum APD_{20} (black dashed lines). Note: I_{to} panels are zoomed in. 105

- 5.5 Ionic conductances determining inter-subject variability in the different stages of human atrial repolarization under SR conditions at 1 Hz pacing. Regression surfaces for APD_{90} , APD_{50} and APD_{20} are presented with respect to the two most significant ionic factors determining their variability, using populations of the Maleckar (A-C), Courtemanche (D-F), and Grandi (G-I) models of human atrial electrophysiology. Regression surfaces are color coded according to APD magnitudes, whereas each big dot denotes one simulated subject in the calibrated populations of sampled models. 107
- 5.6 Ionic conductances determining inter-subject variability in the different stages of human atrial repolarization under AF conditions at 1 Hz pacing. Regression surfaces for APD_{90} , APD_{50} and APD_{20} are presented with respect to the two most significant ionic factors determining their variability, using populations of the Maleckar (A-C), Courtemanche (D-F), and Grandi (G-I) models of human atrial electrophysiology. Regression surfaces are color coded according to APD magnitudes, whereas each big dot denotes one simulated subject in the calibrated populations of sampled models. 108
- 5.7 Main ionic determinants of inter-subject variability in human atrial APD_{90} (blue), APD_{50} (green) and APD_{20} (pink) in SR (panel A) and permanent AF (panel B) with the Maleckar, Courtemanche and Grandi model populations. 109
- 5.8 Inter-subject variability in human atrial AP triangulation. The most and least triangular APs in each population are shown (solid and dotted lines, respectively), obtained with the Maleckar (A), Courtemanche (B) and Grandi (C) models in SR. Corresponding time course of ionic mechanisms of AP triangulation are shown: I_{K1} and I_{NaK} (D and F), I_{K1} and I_{NaCa} (E). 110
- 5.9 A: AP traces with the Grandi model population for CL = 400 ms in SR of the same accepted models as for CL = 1000 ms (blue), the models showing AP alternans ($|APD_{90,odd} - APD_{90,even}| > 30$ ms; magenta) and the models showing strong AP alternans ($|APD_{90,odd} - APD_{90,even}| > 100$ ms black). B: Variability of ionic conductances G_{K1} , G_{NaK} , G_{CaL} , G_{to} , G_{Kur} and G_{NaCa} for the models in panel A. (Mann-Whitney U test alternans vs. accepted range: $*p < 0.05$; $**p < 0.01$; $***p < 0.001$). 111

- 6.1 Population of simulated AF cell models (panel A). First (blue) and fourth (red) quartile sub-populations according to APD_{90} , APD_{50} and APD_{20} , respectively (panels B-D). Note zoomed in time axis in panel D. 118
- 6.2 Position of the 49 virtual electrodes (red dots) in LA (left panel) and RA (right panel). 119
- 6.3 Pseudo-EGM signal measured at one of the 49 electrodes during a simulation of 10 s duration (left). Example of LAW obtained from the pEGM signal (right). 120
- 6.4 Dorsal view of the atria. V_m map after 10 seconds of simulation for AF when $[ACh]=1$ nM (top panel) and 5 nM (bottom panel). 122
- 6.5 Dorsal view of the atria. Interpolated maps of DF (A), OI (B), RI (C) and CP (D) for $[ACh]=1$ nM (left) and $[ACh]=5$ nM (right). 123
- 6.6 Dorsal view of the atria. V_m map after 10 seconds of simulation for AF, and following 30% I_{K1} inhibition, 15% I_{Na} inhibition and 30% I_{NaK} inhibition in AF, respectively. . . . 124
- 6.7 Dorsal view of the atria. Interpolated OI (left) and RI (right) map for default conditions (permanent AF), 30% I_{K1} inhibition, 15% I_{Na} inhibition and 30% I_{NaK} inhibition, respectively. 125
- 6.8 Coupling between pEGM in adjacent electrodes for LA (left) and RA (right) for default conditions (permanent AF), 30% I_{K1} inhibition, 15% I_{Na} inhibition and 30% I_{NaK} inhibition, respectively. Thick white lines represent $CP \geq 0.9$, thin solid lines represent $0.75 \leq CP < 0.9$ and soft gray lines represent $0.6 \leq CP < 0.75$. $CP < 0.6$ is represented by absence of lines. . . 125
- 6.9 Dorsal view of the atria. Interpolated DF (top-left), OI (top-right), RI (middle-left), CP (middle-right; thick white lines represent $CP \geq 0.9$, thin solid lines represent $0.75 \leq CP < 0.9$ and soft gray lines represent $0.6 \leq CP < 0.75$. $CP < 0.6$ is represented by absence of lines), CaT (bottom-left) and CaT_{max} (bottom-right) for AF conditions with no variability. 127
- 6.10 Dorsal view of the atria. Interpolated maps of DF, OI and RI for short and long APD_{90} , APD_{50} and APD_{20} sub-populations of models, respectively. 128
- 6.11 Dorsal view of the atria. CP between pEGM in adjacent electrodes for LA (left) and RA (right) for short and long APD_{90} , APD_{50} and APD_{20} sub-populations of models, respectively. Thick white lines represent $CP \geq 0.9$, thin solid lines represent $0.75 \leq CP < 0.9$ and soft gray lines represent $0.6 \leq CP < 0.75$. $CP < 0.6$ is represented by absence of lines. . . 129

6.12 Dorsal view of the atria. Interpolated CaT and CaT _{max} for short and long APD ₉₀ , APD ₅₀ and APD ₂₀ sub-populations of models, respectively.	130
6.13 Scatter plot of DF, OI and RI calculated from the 20 EGM at the HRA in AF patients (A) and the corresponding histograms showing the number of EGMs for different intervals of DF, OI and RI (B).	131

List of Tables

3.1	Time constants for fast and slow phases following HR deceleration and acceleration.	52
3.2	Time for 90% of APD adaptation, t_{90} , and time constant for the slow APD adaptation phase following HR deceleration and acceleration with $D = 0.001$ (top) and $0.01 \text{ cm}^2/\text{ms}$ (bottom) in cells 1, 100 and 200 with the Nygren model.	54
4.1	Absolute and relative sensitivities in SR conditions obtained from cell and tissue simulations. The highest absolute sensitivities of each marker (listed in the first column) to changes in ionic conductances (listed in the first row) are shown as a % of change. Negative values are represented as "-". Relative sensitivities, $R_{m,p}$, are calculated for each marker and shown in a grey scale.	80
4.2	Absolute and relative sensitivities in AF conditions obtained from cell and tissue simulations. The highest absolute sensitivities of each marker (listed in the first column) to changes in ionic conductances (listed in the first row) are shown as a % of change. Negative values are represented as "-". Relative sensitivities, $R_{m,p}$, are calculated for each marker and shown in a grey scale.	81
4.3	Ionic currents investigated in this study, drugs targeting them and modulation of atrial electrophysiological properties.	94
5.1	Range of human atrial AP features in SR and AF patients	100
5.2	Number and percentages of accepted sampled models in the experimentally-calibrated Maleckar, Courtemanche and Grandi populations in SR and permanent AF out of a total of 2275 sampled models.	103
6.1	Human atrial tissue anisotropy and heterogeneities.	117

Chapter 1

Introduction

1.1 Cardiac Arrhythmias

Over 30% of the total number of deaths in Spain and over 35% in the European Union are caused by circulatory system-related diseases, overcoming the number of casualties caused by tumours and diseases on the respiratory, nervous and digestive systems [1]. The origin of the diseases on the circulatory system is often connected to cardiac dysfunctions leading to abnormal beating, known as cardiac arrhythmias, other than the normal sinus rhythm. Despite big efforts in the clinical and pharmaceutical fields, the efficacy of antiarrhythmic therapies is far from being optimum in both prevention and post-treatment, thus highlighting the necessity of improving our understanding of cardiac electrophysiology and the mechanisms involved in the generation and maintenance of arrhythmias in the search for improved therapies. In this thesis, we investigate the ionic mechanisms underlying electrophysiological properties of the human atria for both sinus rhythm (SR) and the most common cardiac arrhythmia, i.e. atrial fibrillation (AF), with the main aim of aiding in the screening, design and development of new antiarrhythmic therapies.

1.2 Electrical Activity of the Heart

The human heart is a fist-sized organ whose main function is to pump blood to the rest of the organs in the human body. The heart consists of four chambers, two atria and two ventricles, composed of thousands of aligned muscle cells, known as cardiomyocytes, forming muscular fibers contracting and relaxing synchronously. From the electrical point of view, cardiomyocytes are polarized during their resting state, i.e. the transmembrane potential between the intracellular and the extracellular space (V_m) is about -80 mV, depolarize when they receive a stimulation current, i.e. V_m increases to positive voltages, and repolarize when depolarization finishes, i.e. V_m decreases

back to its resting value (known as resting membrane potential (RMP)). The cardiac cycle starts with an impulse generated at the sinoatrial node that propagates through the atria and depolarizes them, reaches the atrioventricular node and then propagates to the ventricles, depolarizing them, through a set of nervous fibers known as the Purkinje system. Each cardiac cycle is divided into two parts: electrical depolarization or systole, which triggers contraction, and electrical repolarization or diastole, which is followed by mechanical relaxation.

1.2.1 Body Surface Electrocardiogram

At the body surface level, it is possible to measure the electrical waves generated in the heart by using a set of electrodes positioned at specific locations, thus obtaining the electrocardiographic signal (ECG). The ECG describes the different electrical phases of a cardiac cycle and represents a summation in time and space of the V_m gradients generated in the cardiac tissue. According to the position of the electrodes and the relationships between them, a standard 12-lead ECG consists of the following recording channels: 6 precordial leads (V1-V6), 3 bipolar limb leads (I, II and III) and 3 augmented limb leads (aVR, aVL and aVF) (see Figure 1.1).

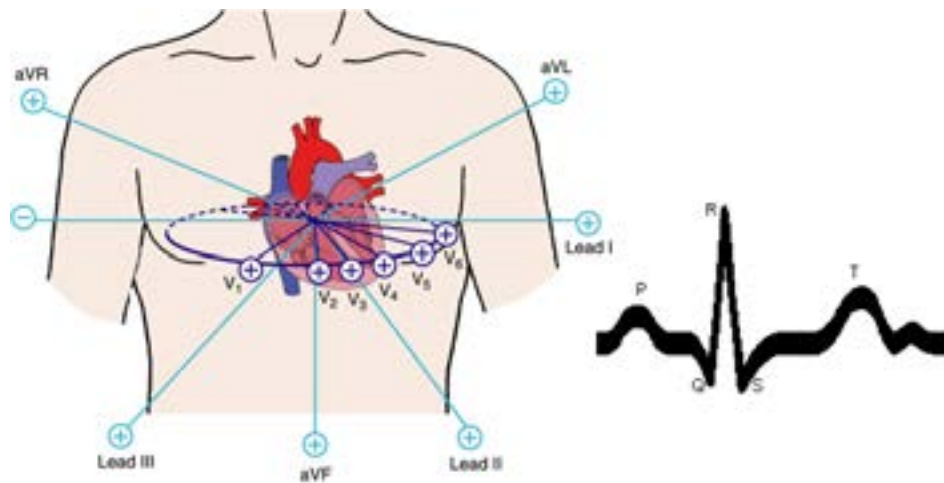


Figure 1.1: Electrode positions in the standard 12-lead ECG (modified from [2]) and characteristic waves of the ECG signal.

The different phases of each cardiac cycle in the ECG signal and the corresponding waves are shown in Figure 1.1:

- The P-wave corresponds to atrial depolarization.
- The QRS-complex corresponds to ventricular depolarization, masking atrial repolarization.

- The T-wave corresponds to ventricular repolarization.

The ECG is easy to obtain and provides simultaneous information of cardiac electrical events in time and space (as a function of the recording lead) thus making it a powerful tool for diagnosis of cardiovascular-related diseases.

1.2.2 Myocardial Wall Electrograms

The electrical activity of the heart can also be measured by placing electrodes on the surface of the cardiac wall (see Figure 1.2). These electrodes can be invasively used during cardiac surgery via catheters to record electric field, known as electrograms (EGM), and their use is very common in the clinics to investigate the mechanisms underlying certain arrhythmias. This recording technique is useful to analyze activation patterns, locate areas with impaired electrical propagation and guide antiarrhythmic therapies such as surgical ablation procedures.

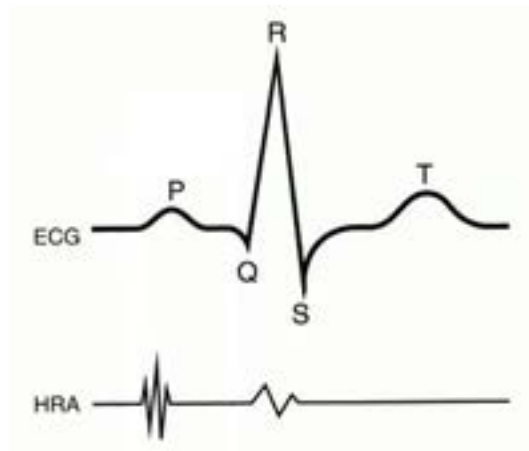


Figure 1.2: Example of an ECG signal and the corresponding EGM measured at the high right atrium (HRA).

As an example, the study of complex fractionated atrial electrograms, i.e. EGMs composed by two or more consecutive deflections and/or with very short time between consecutive depolarizations as compared to the rest of atrial tissue, in patients diagnosed with AF is useful to locate areas that sustain the arrhythmia [3].

1.2.3 Cellular Electrical Activity

1.2.3.1 Patch Clamp Recording Techniques

The technique normally used for recording the electrical activity at cellular and sub-cellular (ion channels) levels of myocytes and neurons is generally called Patch Clamp. This laboratory technique can be divided into three steps: tissue preparation, cell stimulation and recording of the desired data.

First of all, for the investigation of cardiac electrophysiology, small samples of cardiac tissue are extracted from patients undergoing cardiac surgery and stored at low temperature in order to prolong their lives until the experimentation is performed. Then, tissue samples are rinsed and subjected to a complex disaggregation process so that individual myocytes can be analyzed. Only the longest and less granulated cells are chosen for posterior analysis in order to reduce the likelihood of cellular death during experiments [4–7].

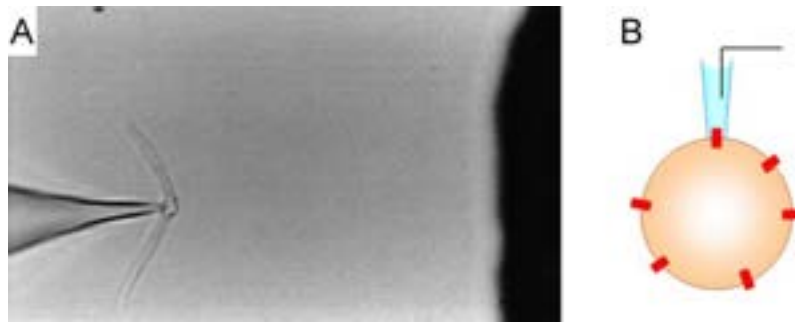


Figure 1.3: **A:** Capture of a rainbow trout cardiomyocyte with a micropipette (modified from [6]). **B:** Schematic view of the Patch Clamp technique.

Once an adequate cell is located, a micropipette is used to capture it (see Figure 1.3A). This micropipette is built just before the experiment with a tiny opening. The electrical resistance associated to this opening has to be between 1.5 y 4 M Ω in order to minimize leakage current and increase signal to noise ratio, otherwise the micropipette would not be suitable to perform Patch Clamp and a new micropipette would have to be built. The interior of the micropipette is filled with a solution matching the ionic composition of the cell substrate.

Then the tip of the micropipette is carefully approached to the cell so as not to damage it. A 'gigaseal' between the tip and the cellular membrane is then formed by applying slight suction in the micropipette. The membrane area enclosed inside the tip often contains one or a few ion channels that can be externally stimulated with electrodes (see Figure 1.3B).

There are two particular variants of the Patch Clamp technique, depend-

ing on the magnitude, current or voltage, that is measured:

- Voltage Clamp: electrodes are used to maintain V_m at a preset value and then ionic currents are measured, as shown in Figure 1.4A.
- Current Clamp: total membrane current is held at a certain value and then V_m is measured, as shown in Figure 1.4B.

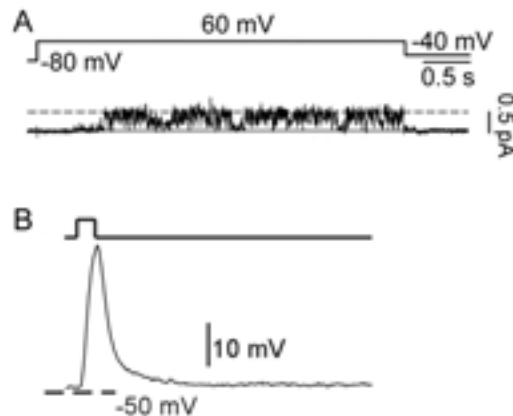


Figure 1.4: **A:** Ionic current of a single potassium channel measured with the Voltage Clamp technique in a cardiomyocyte (modified from [8]). **B:** V_m measured with the Current Clamp technique in a murine neuron (modified from [9]).

1.2.3.2 Limitations of Experiments

Patch Clamp techniques in atrial tissue preparations have important limitations that cannot be neglected, such as the following [10]:

- The apparent seal resistance, determined by changing the potential in a patch electrode, may be a poor estimate of true seal resistance, since it includes the parallel combination of seal- and patch-resistance.
- Patch resistance may be influenced by the electrode filling solution, and is often much lower than is usually assumed.
- Measurements of single-channel conductance using a cell-attached patch electrode may be inaccurate because cell membrane potential does not remain constant as electrode potential is varied, since input resistance of the clamped cell is usually in the gigaohm range.

- Stabilization of an adequate RMP by externally injecting a holding current is challenging but key to obtain reliable measurements. Since the ionic conductance associated to voltage values close to the RMP in human atrial myocytes is very low in comparison with ventricular myocytes, small changes in the holding current may lead to significant changes in the transmembrane voltage [7].

Furthermore, the number of intracardiac experiments on human beings, i.e. experiments aiming at obtaining data and/or tissue samples from the heart invasively through surgical procedures, is limited due to associated ethical constraints, thus making it difficult to draw accurate conclusions in general. In addition, it is important to note that many patients undergoing cardiac surgery have cardiovascular related diseases, such as myocardial infarction, heart failure or cardiac arrhythmias, thus entailing a limited amount of data on healthy hearts.

Due to all these ethical and intrinsic limitations of experiments, alternative methods for the investigation of cardiac behavior at different levels should be exploited. During the last decades a new approach has been widely extended for giving solution to many questions about electrophysiology: computational modelling.

1.2.3.3 Computational Modeling

Computational modeling represents a useful tool for understanding the functioning of different parts or organs of animal species and humans at different levels (molecular, ionic, cellular, tissue, whole-organ, system) and shedding light on the mechanisms of specific physiopathological alterations that remain unclear nowadays. Furthermore, the most important advantage of using computational models is the possibility of testing multiple hypothesis with no risk for either patients or animals, with high spatio-temporal resolution, thus allowing dissecting multiscale mechanisms from subcellular to whole organ level.

The origins of computational modeling date back to 1952, when the physicists Alan Lloyd Hodgkin and Andrew Fielding Huxley performed a study on squid nerve cells (chosen due to their large size) and theoretically described the ionic currents crossing the cell membrane [11]. In that study, they included details of activation and inactivation ionic gates corresponding to different types of ionic currents, equilibrium potentials (i.e. the potential at which there is no net flow of a particular ion from one side of the membrane to the other) and time-varying ionic conductances (determining the number of channels open and thus the overall amplitude of the ionic current). The electrical circuit equivalent to the cell membrane was a mesh consisting of some parallel branches representing both the different types of ion channels between the intracellular space and the extracellular space,

with series circuits of voltage sources (equilibrium potentials) and the corresponding variable conductances, and a capacitor modeling the capacitive behavior of the membrane (Figure 1.5). Hodgkin and Huxley performed the study on neurons, but they laid the foundations to study and model every cell type in the body, no matter their nature.

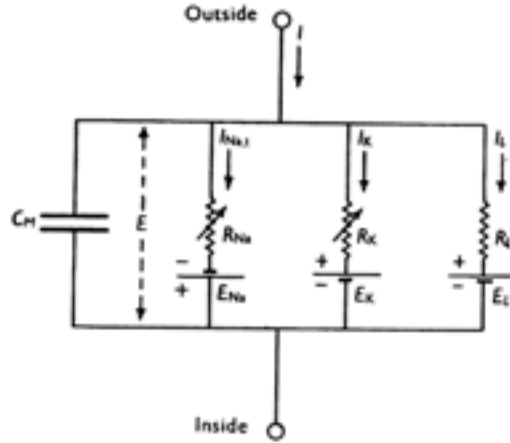


Figure 1.5: Electrical circuit representing the cell membrane. Resistors of sodium (R_{Na}) and potassium (R_K) are variable, dependent on both time and V_m and inverse to the associated conductances. Resistor associated to the rest of ions (R_l) is considered constant [11].

The mathematical equation characterizing this circuit model can be written as follows:

$$C_m \frac{dV_m}{dt} + I_{Na,t} + I_K + I_l + I_{st} = 0, \quad (1.1)$$

where V_m is the difference in potential between the inside and the outside of the cell; $I_{Na,t}$, I_K and I_l are the different ionic currents, corresponding to the total sodium current, the total potassium current and the total current of the rest of ions, respectively; I_{st} is the stimulation current; and C_m is the capacitive value of the membrane.

1.2.3.4 Action Potentials

Cardiac contraction is possible due to electrical propagation through excitable cardiomyocytes. Cardiomyocytes become excitable when they are stimulated by an electric current of enough magnitude from neighbour cardiomyocytes, generating a rapid increase in the cellular V_m (depolarization) followed by a progressive decrease (repolarization). The time course determined by both depolarization and repolarization phases at cellular level is

denoted as action potential (AP) (see Figure 1.6). The minimum value of stimulation current needed to generate an AP when the cell is at resting state is called diastolic threshold.

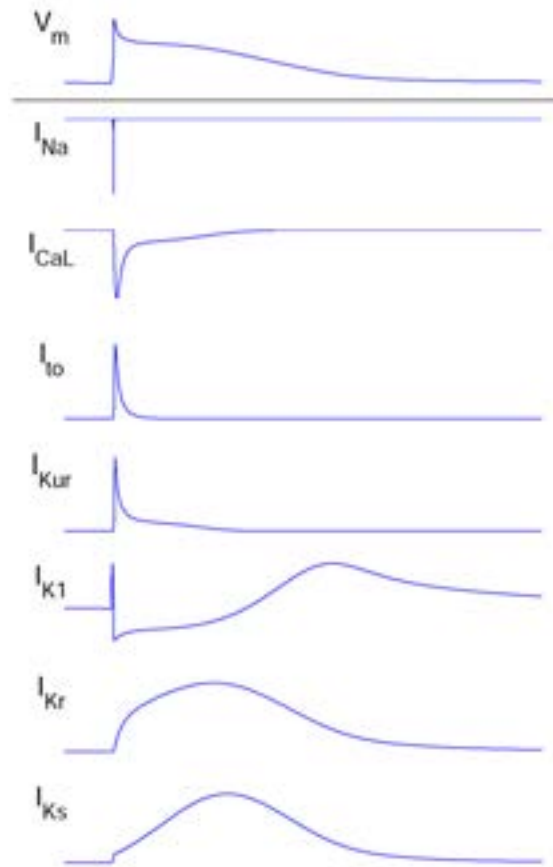


Figure 1.6: Simulated V_m and the most relevant ionic currents determining the phases of the AP of a human atrial cardiomyocyte.

The AP is determined by ionic interchanges between the intracellular and the extracellular spaces through ion channels generating inward and outward ionic currents. In general, there are three different types of ion channels in human cardiomyocytes depending on the ions they let pass through: sodium channels (Na^+), potassium channels (K^+) and calcium channels (Ca^{2+}). The time course of the AP is divided into five phases:

- Phase 0: The initial upstroke is generated by the inward flux of sodium ions due to the quick opening of the corresponding ion channels when an external stimulus is applied. These sodium channels immediately close, thus generating the fast sodium current, I_{Na} .

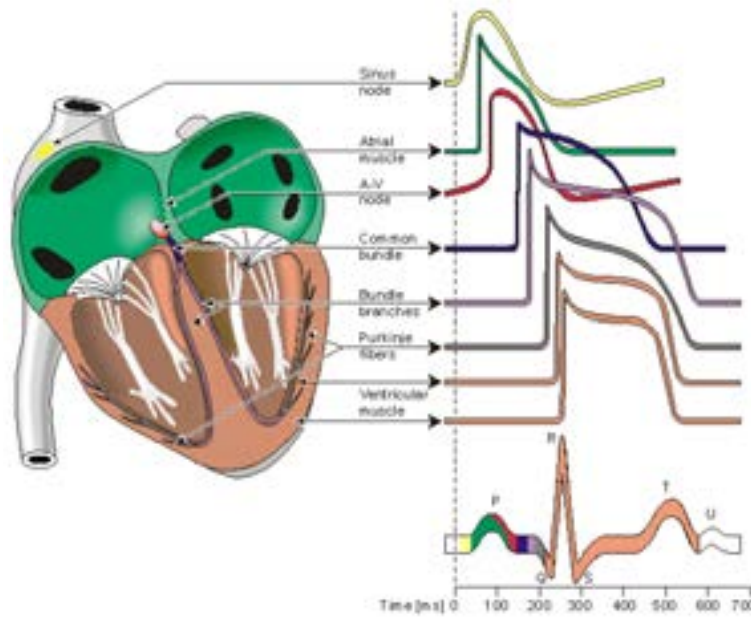


Figure 1.7: Action potentials from different types of cardiomyocytes and their contribution to the ECG signal (modified from [12]).

- Phase 1: The subsequent decrease in the transmembrane potential is caused by both the closing of sodium channels and the activation of transient outward potassium currents that try to return the cell to its resting state.
- Phase 2: Inward calcium ion flux creates slow calcium currents, I_{Ca} , that compensate the outward potassium currents and therefore slow down the decrease in the potential. This phase is also known as "plateau phase".
- Phase 3: Calcium channels begin closing while slow potassium currents, such as the rapid delayed rectifier current (I_{Kr}) and the slow delayed rectifier current (I_{Ks}), start acting until the cell recovers its initial resting state.
- Phase 4: During this phase, the cell remains at its resting state when there is no external stimulation (RMP is normally between -70 and -85 mV in cardiac cells of the human atria).

Both the morphology and the activation time of the AP are strongly dependent on the location of the cardiomyocytes within the heart. The combined effect of all the cellular APs in the heart leads to the surface ECG signal, as shown in Figure 1.7.

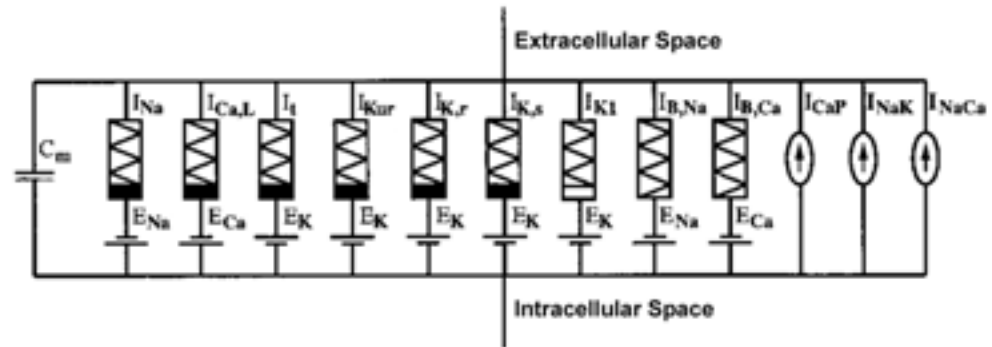


Figure 1.8: Schematic representation of the membrane of the human atrial cell (modified from [13]).

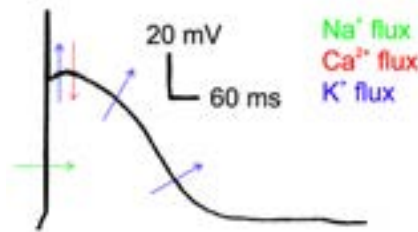


Figure 1.9: Experimental human atrial AP (modified from [14]) and ion fluxes of sodium (green), calcium (red) and potassium (blue).

1.2.3.5 Electrophysiology of Human Atrial Cells

In this thesis we focused on the electrophysiology of human atrial cells and tissue. Atrial tissue is highly heterogeneous and anisotropic. The atrial wall is substantially thinner than the ventricular wall. Despite the electrophysiological heterogeneities, electrical activity in human atrial myocytes can be generally described by specific ion interchanges between intracellular and extracellular spaces resulting in the corresponding AP. These transmembrane interchanges in atrial cells are summarized in Figure 1.8 as in the Hodgkin and Huxley formalism.

Figure 1.9 shows a typical human atrial AP waveform and ion fluxes between the intracellular and extracellular spaces during the different AP phases [14].

1.2.4 Ionic Currents

In this section, ionic current formulations corresponding to the Courtemanche *et al.* model are described for illustration purposes [15]. These formulations include constants and variables (usually dependent on other variables such as 'time' or ' V_m ') whose values and equations are adjusted to fit specific experimental observations. Other human atrial cell models, which will be detailed in section 2.1.1.1, use different formulations for some ionic currents as they aim at reproducing other sets of experimental data [13, 15–18].

1.2.4.1 Sodium Currents

Once the cell receives external stimulation of an amplitude above its diastolic threshold, a chain of events begins, starting with fast opening and subsequent fast closing of the sodium channels, that generate the I_{Na} current [19].

Fast Sodium Current

I_{Na} is an extremely fast inward current of several nanoamperes of amplitude and less than 2-ms duration that depolarizes the transmembrane potential from about -80 mV to +20 mV (see Figure 1.10). In this and the following five figures, the temporal axis represents time and is denoted by 't'.

Following the formulation proposed by Hodgkin and Huxley, but including slight modifications according to experimental studies [20], fast sodium channel dynamics can be characterized by both activation gating variables (m) and inactivation gating variables (h and j), leading to the following equation:

$$I_{Na} = g_{Na} m^3 h j (V_m - E_{Na}), \quad (1.2)$$

where g_{Na} is the constant conductance associated to I_{Na} ; m , h and j are independent, first order (i.e. its calculation involves only its first derivative), dimensionless variables; V_m is the transmembrane potential; and E_{Na} is the sodium equilibrium potential. Note that m is raised to the third power, meaning that activation kinetics are modeled through three gating variables of the same type.

In healthy conditions, the fast sodium current is the sodium current playing the major role in the atrial AP time course. Nevertheless, it has been recently shown that certain atrial arrhythmias, such as AF, lead to protracted inactivation of specific sodium channels, thus enhancing the sodium current, known as late sodium current (I_{NaL}) [21].

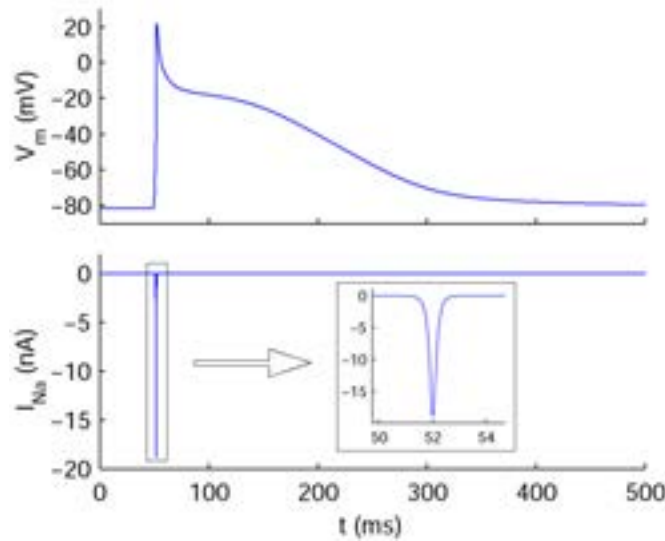


Figure 1.10: Simulated human atrial AP (top panel) and corresponding I_{Na} (bottom panel) measured during the last cardiac cycle following a train of periodic stimuli every 1 second for 20 minutes. *Note: the activation interval of I_{Na} is zoomed in due to its very short duration.*

1.2.4.2 Calcium Currents

Inward calcium ion flux begins after the depolarization of the transmembrane potential due to the initial upstroke. Human cardiomyocyte membrane mainly presents one type of calcium channels known as L-type calcium channels [22], with their associated ionic current being the L-type calcium current (I_{CaL}). Other areas of the human heart, such as the sinoatrial node (SAN), present another type of calcium channels in the cell membrane, known as T-type calcium channels, that contribute to pacemaker cell depolarization [23]. The corresponding ionic current is known as T-type calcium current (I_{CaT}).

Importantly, intracellular calcium in atrial cells is also regulated thanks to ionic interchanges between the intracellular space and the two main compartments of the sarcoplasmic reticulum (an organelle in animal cells that surrounds its nucleus, denoted by SRet in this thesis): the network sarcoplasmic reticulum (NSR) and the junctional sarcoplasmic reticulum (JSR), which generate different ionic currents as well. The combined effects of I_{CaL} and the SRet currents on the intracellular calcium concentration ($[Ca^{2+}]_i$) lead to so called intracellular calcium dynamics.

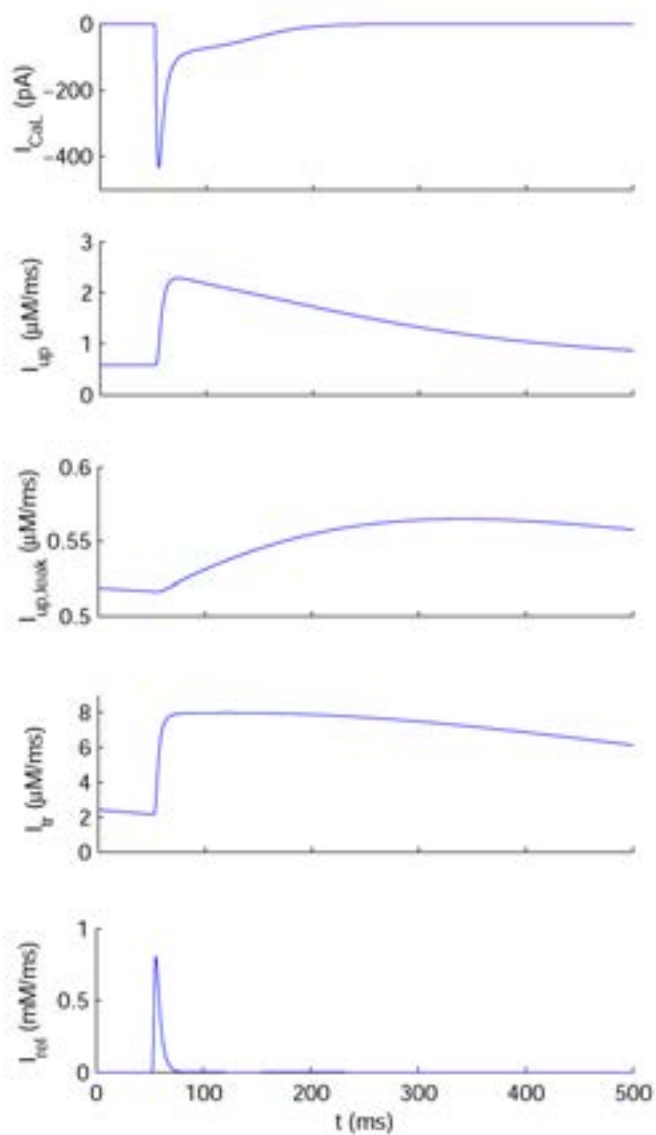


Figure 1.11: Simulated human atrial calcium currents measured during the last cardiac cycle following a train of periodic stimuli every 1 second for 20 minutes: I_{CaL} , I_{up} , $I_{up,leak}$, I_{tr} and I_{rel} .

L-Type Calcium Current

I_{CaL} is an inward ionic current with slower activation time and lower amplitude than I_{Na} , but with much longer duration, as shown in Figure 1.11. It is characterized by two voltage-dependent gating variables, an activation gating variable (d) and an inactivation gating variable (f), and a $[Ca^{2+}]_i$ -dependent inactivation gating variable (f_{Ca}). This transmembrane ionic current is essential in the "plateau" phase (phase 2) of the AP time-course, as described in section 1.2.3.

Similar formulation to that of I_{Na} can be used to describe I_{CaL} as a function of its associated gating variables:

$$I_{CaL} = g_{CaL} d f f_{Ca} (V_m - E_{Ca}), \quad (1.3)$$

where g_{CaL} is the constant conductance associated to I_{CaL} ; d , f and f_{Ca} are independent, first order, dimensionless variables; and E_{Ca} is the calcium equilibrium potential.

Due to the role of I_{CaL} in increasing $[Ca^{2+}]_i$, it plays a key role in the excitation-contraction coupling, as an increase in intracellular calcium activates calcium-sensitive contractile proteins that then use ATP to cause cell contraction [22, 24].

Sarcoplasmic Reticulum Currents

Different calcium ion fluxes occur between the SRet and the intracellular space. These ionic currents regulate $[Ca^{2+}]_i$ and importantly contribute to cell contraction.

Figure 1.12 shows two different schemes, corresponding to two different human atrial cell models, of the SRet compartments, NSR and JSR, both taking as a reference the model of the SRet developed by Luo and Rudy for guinea pig ventricular cells [20]. Also shown in Figure 1.12 are the ionic currents involved in the intracellular calcium dynamics, whose time course during a cardiac cycle is illustrated in Figure 1.11: calcium uptake current by NSR (I_{up}), calcium leak current by NSR ($I_{up,leak}$), transfer calcium current from NSR to JSR (I_{tr}) and calcium release current from JSR (I_{rel}). These ionic currents are both a regulating factor and a consequence of the dynamics of $[Ca^{2+}]_i$, the release calcium concentration ($[Ca^{2+}]_{rel}$) and the uptake calcium concentration ($[Ca^{2+}]_{up}$).

1.2.4.3 Potassium Currents

Potassium currents are usually triggered when the cell depolarizes and they mainly act by bringing the transmembrane potential back to its resting state by extruding potassium ions out of the cell.

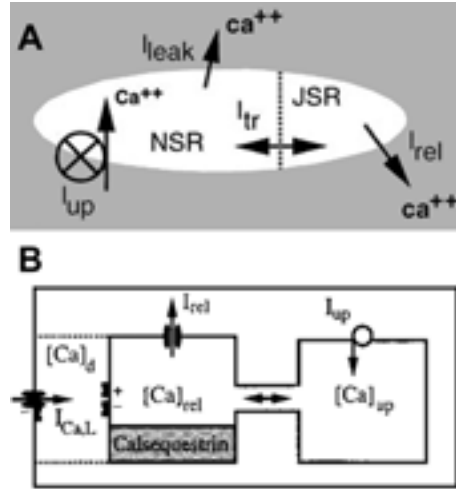


Figure 1.12: Schematic representation of ionic currents and SR compartments in human atrial cardiomyocytes according to the Courtemanche *et al.* model (A, modified from [15]) and the Nygren *et al.* model (B, modified from [13])

Human atrial cells present different types of potassium channels in terms of structure and kinetics, thus evoking different ionic potassium currents [19, 25, 26]: transient outward potassium current (I_{to}), ultrarapid delayed rectifier potassium current (I_{Kur} , also known as sustained outward potassium current), I_{Kr} , I_{Ks} and inward rectifier potassium current (I_{K1}).

Furthermore, certain ion channels react to changes in the concentration of specific neurotransmitters from the parasympathetic system such as acetylcholine (ACh) [27]. The effects of an increase in the ACh concentration ($[ACh]$), which alter the AP duration (APD) and morphology, can be modeled through an acetylcholine-activated potassium current (I_{KACh}) [28].

Transient Outward Potassium Current

I_{to} is a large amplitude outward potassium current characterized by a very short duration as a result of very fast kinetics of both activation and inactivation (Figure 1.13). I_{to} activates when the transmembrane potential reaches positive values and acts to decrease V_m it at the same time that I_{CaL} acts to increase it. The interaction of these two currents and I_{Kur} may lead to the spike-and-dome morphology that some human atrial APs present [14].

The formulation of I_{to} includes one activation gating variable (o_a) and one inactivation gating variable (o_i):

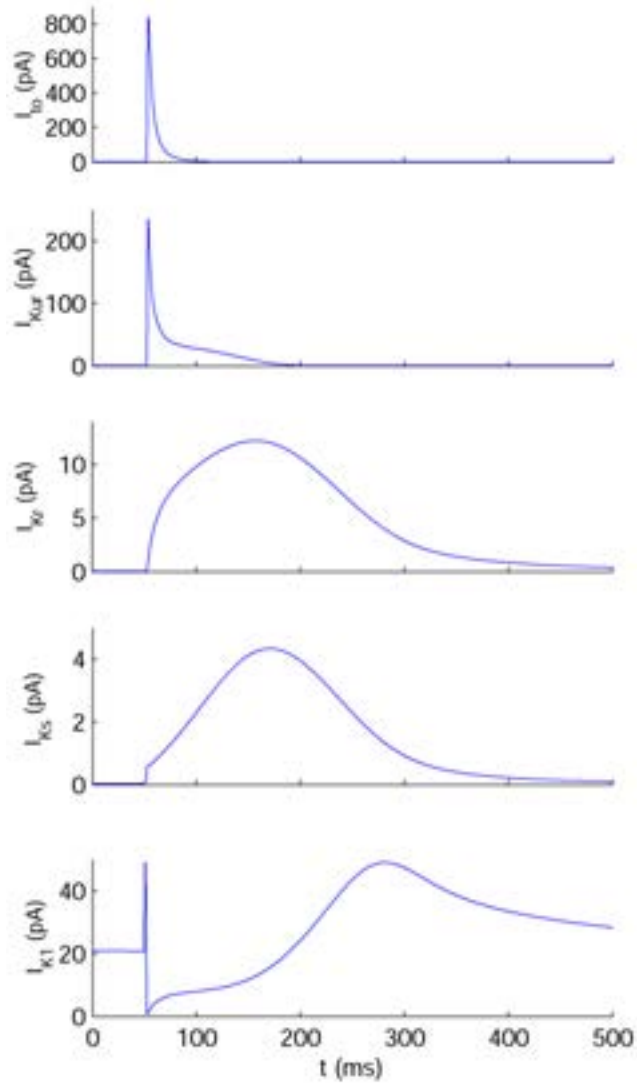


Figure 1.13: Simulated human atrial potassium currents measured during the last cardiac cycle following a train of periodic stimuli every 1 second for 20 minutes: I_{to} , I_{Kur} , I_{Kr} , I_{Ks} and I_{K1} .

$$I_{to} = g_{to} o_a^3 o_i (V_m - E_K), \quad (1.4)$$

where g_{to} is the constant conductance associated to I_{to} ; o_a and o_i are independent, first order, dimensionless variables; and E_K is the potassium equilibrium potential. Note that o_a is raised to the third power, meaning that activation kinetics are modeled through three gating variables of the same type.

Ultrarapid Delayed Rectifier Potassium Current

I_{Kur} , also known as sustained outward potassium current, is an outward potassium current with activation kinetics similar to those of I_{to} but significantly slower inactivation gating variables, thus prolonging its duration (Figure 1.13). I_{Kur} is an atrial-specific current, with its expression in ventricular cardiomyocytes being almost negligible [29].

The I_{Kur} formulation is similar to that of I_{to} :

$$I_{Kur} = g_{Kur} u_a^3 u_i (V_m - E_K), \quad (1.5)$$

where g_{Kur} is the constant conductance associated to I_{Kur} ; and u_a and u_i are independent, first order, dimensionless variables. Note that u_a is raised to the third power, meaning that activation kinetics are modeled through three gating variables of the same type.

Rapid and Slow Delayed Rectifier Potassium Currents

Human atrial cardiomyocytes present two types of delayed rectifier potassium currents according to their activation kinetics: I_{Kr} , the rapid delayed rectifier potassium current, and I_{Ks} , the slow delayed rectifier potassium current [26]. I_{Kr} -associated channels, also known as hERG channels, start opening at more negative V_m than those associated with I_{Ks} (Figure 1.13). Both ionic currents have activation gating variables, x_r for I_{Kr} and x_s for I_{Ks} , and can be modeled as follows:

$$I_{Kr} = \frac{g_{Kr} x_r (V_m - E_K)}{1 + e^{\frac{V+15}{22.4}}}, \quad (1.6)$$

$$I_{Ks} = g_{Ks} x_s^2 (V_m - E_K), \quad (1.7)$$

where g_{Kr} and g_{Ks} are the constant conductances associated to I_{Kr} and I_{Ks} , respectively; and x_r and x_s are independent, first order, dimensionless variables (notice I_{Ks} dependence on x_s is quadratic, meaning that activation

kinetics are modeled through two gating variables of the same type, while I_{K_r} dependence on x_r is linear).

Inward Rectifier Potassium Current

I_{K1} is a time-independent potassium current that remains active during the whole time-course of the AP including during the resting state [25], as shown in Figure 1.13. The magnitude of I_{K1} only reaches values close to 0 when V_m takes positive values. I_{K1} can be modeled as follows:

$$I_{K1} = \frac{g_{K1}(V_m - E_K)}{1 + e^{0.07(V+80)}}, \quad (1.8)$$

where g_{K1} is the constant conductance associated to I_{K1} . Notice there are no time-dependent gating variables in equation 1.8, in contrast with the previously described potassium currents.

Acetylcholine-Activated Potassium Current

I_{KAC_h} is an outward potassium current that accounts for the effects of parasympathetic stimulation of the human atria. Its magnitude is directly dependent on the [ACh] level [27].

A formulation of I_{KAC_h} was presented by Kneller *et al.* [28] based on experiments in canine atria using carbamylcholine (CBC), whose effects on the AP are very similar to those caused by ACh:

$$I_{KAC_h} = \left(\frac{10}{1 + \frac{9.13652}{[ACh]^{0.477811}}} \right) \left(0.0517 + \frac{0.4516}{1 + e^{\frac{V_m + 59.53}{17.18}}} \right). \quad (1.9)$$

Figure 1.14 shows both the relations between the magnitude of I_{KAC_h} and V_m for different levels of [ACh] in experiments and simulations, and the correspondence between AP morphology and APD in experiments with CBC and simulations with ACh: [CBC] of 0.1 and 1 $\mu\text{mol/l}$ correspond to the effects of 0.003 and 0.03 $\mu\text{mol/l}$ of [ACh] in the model [28].

1.2.4.4 Electrogenic Pumps

Specific types of transport proteins located in the cellular membrane act to maintain differences in ion concentrations between the extracellular and the intracellular spaces, thus counteracting the effects produced by the rest of ionic currents. These ionic mechanisms are known as electrogenic pumps since they generate electricity by producing a net movement of positive charge out of a cell. In contrast with the rest of ionic currents, electrogenic pumps need energy to work, usually obtained via the hydrolysis of ATP molecules.

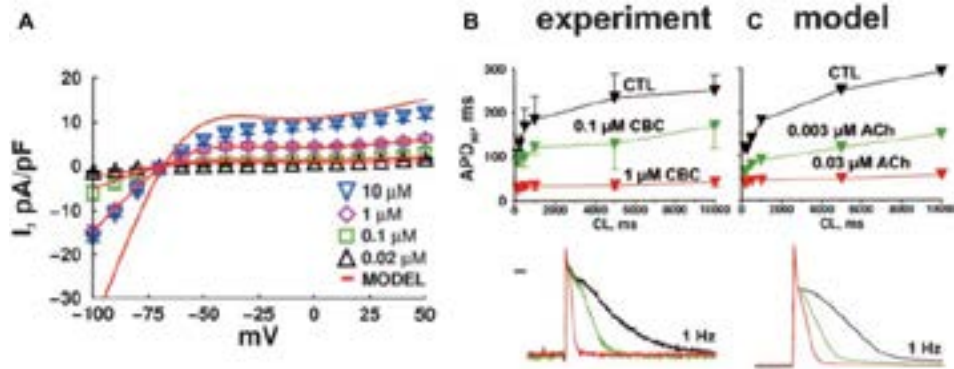


Figure 1.14: **A**: I_{KACh} intensity-voltage relations (data points are mean \pm standard deviation) in both experiments with different [ACh] levels (color symbols) and with the equation 1.9 (red lines). **B and C**: Comparison of canine atrial experiments (left) and canine atrial model (right) AP duration (top) and morphology (bottom) (modified from [28]).

Human atrial cardiomyocytes present two main electrogenic pumps: the sodium/potassium pump (NaK pump) and the calcium pump (Ca pump).

Sodium/Potassium Pump

The NaK pump is key in diverse physiological functions of excitable cells such as maintaining osmolarity between extracellular and intracellular spaces to control cell volume, maintaining the gradients of sodium and potassium ion concentrations and regulating RMP [30, 31].

Regarding the ion transport mechanism, the protein transports 2 potassium ions into the cell while pumps out 3 sodium ions, thus generating an outward positive ion flux which generates an ionic current, I_{NaK} , which is shown in Figure 1.15 (top panel). I_{NaK} is modeled by the following general equation firstly used by Luo and Rudy in a guinea pig ventricular myocyte model [20]:

$$I_{NaK} = p_{NaK} \left(\frac{[Na^+]_i}{[Na^+]_i + K_{m,Na}} \right)^{\gamma_{Na}} \left(\frac{[K^+]_i}{[K^+]_i + K_{m,K}} \right)^{\gamma_K} f_v, \quad (1.10)$$

where p_{NaK} represents the maximum NaK pump permeability; $K_{m,Na}$ and $K_{m,K}$ are the half affinity constants of sodium and potassium, respectively; $[Na^+]_i$ and $[K^+]_i$ are the intracellular sodium and potassium concentrations, respectively; γ_{Na} and γ_K are the Hill coefficients for each ion; and f_v is a particular V_m -dependent function.

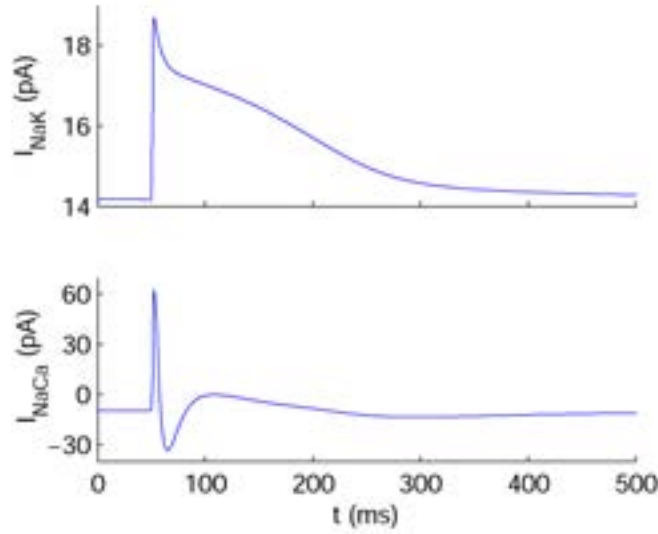


Figure 1.15: Simulated human atrial sodium/potassium pump current (I_{NaK} , top panel) and sodium/calcium exchanger current (I_{NaCa} , bottom panel) measured during the last cardiac cycle following a train of periodic stimuli every 1 second for 20 minutes.

Calcium Pump

The most important function of the Ca pump is to maintain $[Ca^{2+}]_i$ at physiological levels. The pump current formulation is given by:

$$I_{pCa} = I_{pCa,max} \frac{[Ca^{2+}]_i}{0.0005 + [Ca^{2+}]_i}, \quad (1.11)$$

where $I_{pCa,max}$ is a constant.

1.2.4.5 Ion Exchangers

Another type of active transport protein present in human cardiomyocytes is the sodium/calcium exchanger ($NaCa$ exchanger or NCX).

Sodium-Calcium Exchanger

This protein uses secondary active transport to extrude calcium out of the cell, meaning it does not use energy from ATP but from the electrochemical gradient between the extracellular and the intracellular sodium concentrations ($[Na^+]_o \gg [Na^+]_i$) [32, 33]. The sodium/calcium exchanger mainly acts to regulate calcium ion homeostasis in the myocardium [33]. In its

forward mode, extrusion of one calcium ion is coupled with the entry of three sodium ions, thus generating a net inward current, whereas in its reverse mode it generates an outward current to counteract the increase in $[Na^+]_i$ produced when the cell depolarizes (see Figure 1.15). Equation 1.12 represents this behavior:

$$I_{NaCa} = K_{NaCa} \frac{(e^{\gamma \frac{V_m F}{RT}} [Na^+]_i^3 [Ca^{2+}]_o - e^{(\gamma-1) \frac{V_m F}{RT}} [Na^+]_o^3 [Ca^{2+}]_i)}{(K_{m,Na}^3 + [Na^+]_o^3)(K_{m,Ca} + [Ca^{2+}]_o)(1 + k_{sat} e^{(\gamma-1) \frac{V_m F}{RT}})}, \quad (1.12)$$

where K_{NaCa} is a constant that modulates the maximum amplitude of I_{NaCa} ; γ , F , R , T and k_{sat} are constants; $K_{m,Ca}$ is the half affinity constant of calcium; $[Ca^{2+}]_o$ is the extracellular calcium concentration, respectively.

1.2.4.6 Background Currents

The main purpose of both background sodium leak current and background calcium leak current is to maintain stable $[Na^+]_i$ and $[Ca^{2+}]_i$, respectively, at rest. These ionic currents are modeled as follows:

$$I_{b,Na} = g_{bNa}(V_m - E_{Na}), \quad (1.13)$$

$$I_{b,Ca} = g_{bCa}(V_m - E_{Ca}), \quad (1.14)$$

where g_{bNa} and g_{bCa} are the constant conductances associated to I_{bNa} and I_{bCa} .

1.2.5 Ionic Concentrations

Both intracellular and extracellular spaces present notable differences in their chemical composition, mainly in the ionic concentrations of sodium (Na^+), potassium (K^+) and calcium (Ca^{2+}) (Figure 1.16). These ionic concentration gradients are essential for ion transport between the intracellular and the extracellular spaces, thus generating the different currents described in previous sections.

The time course of all the ionic concentrations is determined by the net flux of ions of each type as a result of the ionic currents flowing between the extracellular and intracellular spaces.

1.2.5.1 Sodium Concentrations

$[Na^+]_o$ in human atrial cardiomyocytes is usually modeled as a constant value of about 140 mM. Regarding $[Na^+]_i$, its reference value is about 13 mM whereas its variations over time depend on the inward sodium currents

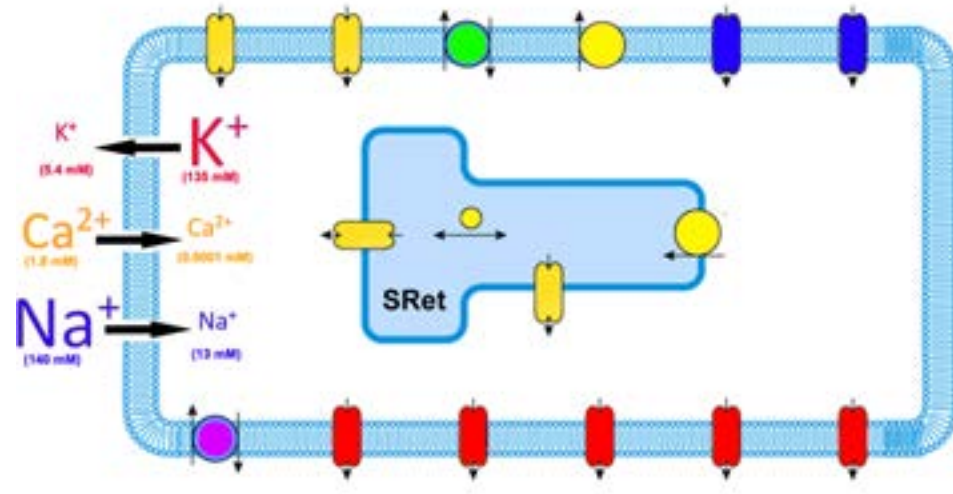


Figure 1.16: Schematic view of a human atrial cardiomyocyte and the most important ionic concentration gradients: K^+ (blue), Ca^{2+} (red) and Na^+ (black).

as well as the NaK pump ionic current and the $NaCa$ exchanger ionic current:

$$\frac{d[Na^+]_i}{dt} = \frac{-I_{Na} - I_{b,Na} - 3I_{NaK} - 3I_{NaCa}}{FV_i}, \quad (1.15)$$

where V_i is a constant accounting for the volume of a single cell. Note that both I_{NaK} and I_{NaCa} are multiplied by 3 since their respective ion interchanges involve 3 sodium ions in exchange for 2 potassium ions or one calcium ion, respectively.

1.2.5.2 Potassium Concentrations

Similarly to sodium concentrations, $[K^+]_o$ in human atrial cardiomyocytes is also modeled as a constant value of about 5 mM. Regarding $[K^+]_i$, its reference value is about 135 mM whereas its variations over time depend on the outward potassium currents as well as the NaK pump ionic current:

$$\frac{d[K^+]_i}{dt} = \frac{-I_{to} - I_{Kur} - I_{K1} - I_{Kr} - I_{Ks} + 2I_{NaK}}{FV_i}, \quad (1.16)$$

where, as stated in the previous section, I_{NaK} is multiplied by 2 due to the number of potassium ions that flow from the extracellular space to the intracellular space in exchange for 3 sodium ions.

Importantly, some human atrial cell models include the external stimulation current in the calculation of potassium concentration, such as the Maleckar *et al.* model [18], since previous studies showed this prevented other electrophysiological properties from reaching values out of physiological range [34].

1.2.5.3 Calcium Concentrations

$[Ca^{2+}]_o$ in human atrial cardiomyocyte models is about 1.8 mM. As regards $[Ca^{2+}]_i$, its values are significantly lower than those of sodium and potassium (about 0.1 μ M), but its variations over a cardiac cycle are significant. The time course of $[Ca^{2+}]_i$ is known as calcium transient (CaT) and is closely related to muscular cell contraction. The dynamics involved in $[Ca^{2+}]_i$ regulation are much more complex than those in $[Na^+]_i$ and $[K^+]_i$ because, apart from calcium transmembrane current flows, the leakage and storage of calcium ions in the SRet play a very important role.

Following the formulation proposed by Courtemanche *et al.* [15], variations in $[Ca^{2+}]_i$ can be obtained by:

$$\frac{d[Ca^{2+}]_i}{dt} = \frac{-I_{CaL} - I_{pCa} - I_{b,Ca} + 2I_{NaCa}}{2FV_i} + \frac{V_{up}(I_{up,leak} - I_{up}) + I_{rel}V_{rel}}{V_i}, \quad (1.17)$$

$$1 + \frac{[Trpn]_{max}K_{m,Trpn}}{([Ca^{2+}]_i + K_{m,Trpn})^2} + \frac{[Cmdu]_{max}K_{m,Cmdu}}{([Ca^{2+}]_i + K_{m,Cmdu})^2},$$

where V_{rel} and V_{up} are the volumes of the SRet release and uptake compartments, respectively; and $[Trpn]_{max}$, $K_{m,Trpn}$, $[Cmdu]_{max}$ and $K_{m,Cmdu}$ are constants standing for troponin and calmodulin calcium buffering in the cytoplasm, as in previous models [20, 35].

Furthermore, an increase in the calcium concentration of the calcium uptake compartment in the SRet, $[Ca^{2+}]_{up}$, through the net flux of calcium ions entering NSR ($I_{up} - I_{up,leak}$), acts to decrease $[Ca^{2+}]_i$, while the gradient between the calcium concentration of the calcium release compartment, $[Ca^{2+}]_{rel}$, and $[Ca^{2+}]_i$ generates a calcium release current from the SRet, I_{rel} , that acts to increase $[Ca^{2+}]_i$. Therefore, calcium concentrations in the SRet compartments have strong influence in intracellular calcium dynamics playing an important role in cardiac cell contraction.

1.2.5.4 Other Ionic Concentrations

Extracellular and intracellular concentrations of other ions different from sodium, potassium and calcium are almost negligible in healthy human cardiac cells. Only atrial chlorine-activated currents are notable under certain conditions [36]. However, cardiac cells in other animal species, such as rabbit and dog, present chlorine ions both inside and outside the cytoplasm and also transmembrane ionic currents transporting them [37, 38].

1.3 Atrial Fibrillation: Incidence and Pathophysiology

As previously stated, experiments have provided useful insight into the mechanisms underlying cardiovascular diseases during the last decades. However, mechanisms involved in the triggering and sustaining of certain diseases remain under investigation, as occurs with AF. AF is the most commonly diagnosed cardiac arrhythmia, particularly in developed countries, with a 0.4-1% incidence in the overall population and over 8% incidence in patients over 80 years old [39]. AF patients have severe prognosis of high incidence of stroke and mortality, and the efficacy of current treatments for AF, usually surgical ablation combined with antiarrhythmic drugs, is far from being optimum [39].

Chaotic electrical activation in the atria associated with AF, described in more detail in chapter 1.3.2, manifests in the ECG as undistinguishable P-waves (as a consequence of asynchronous depolarization of atrial tissue) and irregular ventricular rate (as a consequence of abnormal electrical conduction from the atria to the ventricles through the atrioventricular node), as shown in Figure 1.17.



Figure 1.17: ECG signals corresponding to normal SR (top) and AF (bottom).

1.3.1 Types of Atrial Fibrillation

According to their duration, success of cardioversion techniques and capacity of restarting, four different types of AF can be distinguished [40, 41]:

- Recently diagnosed (or acute-onset): this type of AF occurs when the arrhythmia is detected for the first time in a patient or whose appearance has been recent or unknown. Once it is diagnosed, the arrhythmia will be associated with one of the following three types of AF.

- **Paroxysmal:** it is characterized by spontaneous recovery of SR generally in less than 24 hours and by definition in less than 7 days. If the patient suffers two or more paroxysmal AF episodes, the patient could be diagnosed with persistent AF.
- **Persistent:** this type of AF lasts for longer than 7 days until pharmacological or electrical cardioversion is performed. Persistent AF can either be the first sign of AF or occur after some episodes of paroxysmal AF. As occurs in paroxysmal AF, arrhythmic episodes in patients diagnosed with persistent AF are likely to be recurrent.
- **Chronic (or permanent):** in this case, cardioversion fails or the arrhythmia restarts in the first 48 hours following cardioversion. Long duration AF where no cardioversion is applied is also classified within this group.

This classification of AF categories is internationally accepted [42], but it is not unique. Different authors have reported slight differences in the classifying method [43] or included other patient characteristics to distinguish new types of AF, such as lone AF (absence of other cardiovascular-related diseases), nonvalvular AF (absence of valvular-related diseases) and secondary AF (consequence of a primary condition, such as myocardial infarction, cardiac surgery...) [40].

1.3.2 Triggering and Maintenance of Atrial Fibrillation

AF is considered to be a reentrant arrhythmia sustained by mechanisms including rapid ectopic activity (usually generated in pulmonary veins), reentrant circuits and structural and/or focal changes [44, 45]. Initiation of the arrhythmia is still a matter of debate. It is well established that pulmonary veins play a crucial role since it is the most frequent area of AF generation [46]. However, there are three main hypotheses regarding the generation and maintenance of permanent AF [47]:

- **Multiple reentrant wavelets:** AF is generated by various wavefronts that spread throughout the excitable atrial tissue (Figure 1.18A).
- **Focal hypothesis:** AF is maintained by continuous discharge of a very high frequency focal source in or around the pulmonary veins. Fibrillatory conduction is generated when the wavefronts arising from the focus become fractionated and disorganized in the heterogeneous atrial tissue (Figure 1.18B).
- **Rotor hypothesis:** AF is triggered by a burst of ectopic beats originating in the pulmonary veins whose wavefronts fragment in the surrounding tissue generating rotating vortices. One of the vortices becomes

stable giving rise to the formation of a functional reentry or rotor that acts as the main driver of the fibrillatory behavior [45, 48] (Figure 1.18C).

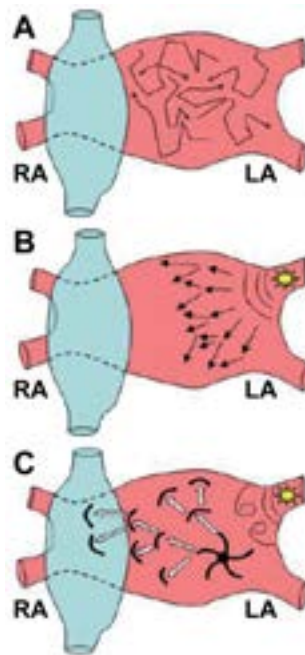


Figure 1.18: Schematic view of the hypotheses for AF generation and maintenance (modified from [47]). **A:** Multiple reentrant wavelets; **B:** Focal hypothesis; **C:** Rotor hypothesis.

A combination of the multiple reentrant wavelet hypothesis and the focal hypothesis has also been suggested as a new hypothesis in a recent study that reported permanent AF to be started and maintained by multiple foci in the atria [49].

Independently of the hypothesis, fibrillatory behavior is favored by short refractory periods and slow conduction [50] and enhanced by both electrical remodeling of atrial cell electrophysiology caused by permanent AF [51] and significant dilation of atrial cavities leading to fibrosis [52].

1.3.3 Therapies for Arrhythmia Treatment

In clinical practice, two types of treatments are used to manage patients diagnosed with cardiac arrhythmias, including AF: pharmacological and non-pharmacological. Most arrhythmia treatments frequently combine both types.

1.3.3.1 Antiarrhythmic Drugs

A wide range of pharmacological drugs and medicines are available in the market aimed at preventing arrhythmia from happening, maintaining SR, controlling cardiac frequency, anticoagulating blood or performing a chemical cardioversion.

Properties of antiarrhythmic drugs primarily depend on the receptor they affect and, based on their prevailing effects, can be separated into different categories according to the Vaughan-Williams classification [53, 54]. Therefore, five principal classes of antiarrhythmic drugs can be distinguished and the choice depends on the specific type of arrhythmia:

- Class I: antiarrhythmic drugs that block voltage-dependent sodium channels. They inhibit I_{Na} and thus reduce conduction velocity and cardiac excitability. They are also known as membrane stabilizing agents. This antiarrhythmic drugs are divided into three subclasses depending on their kinetics of association/dissociation (see Figure 1.19):
 - Class IA: class I drugs with intermediate association/dissociation. They prolong APD, reduce cardiac conductivity and increase effective refractory period (RP). They are useful for treating ventricular and supraventricular tachycardia, premature ventricular beats and ventricular fibrillation. Examples: quinidine and disopyramide.
 - Class IB: class I drugs with fast association/dissociation. They shorten APD and decrease refractoriness. They are frequently used for preventing ventricular fibrillation and treating both ventricular tachycardia and premature ventricular beats. Examples: lidocaine and ranolazine.
 - Class IC: class I drugs with slow association/dissociation. They reduce cardiac contractility but their effects on APD are negligible. Their degree of sodium blocking is the most significant of the three subclasses. They are used for treating ventricular tachycardia, ventricular fibrillation and atrial fibrillation. Examples: flecainide and propafenone.
- Class II: also known as β -blockers, drugs classified within this class act to block sympathetic activity on the heart. They are useful for treating supraventricular tachycardia since they reduce electrical conduction through the atrioventricular node. Examples: propranolol and pronethalol.
- Class III: antiarrhythmic drugs that block potassium channels and therefore prolong APD and RP. Furthermore, their effects on conduction velocity (CV) are nonexistent, making them effective to prevent

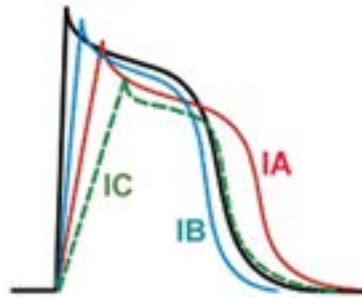


Figure 1.19: Effects of class I antiarrhythmic drugs: ventricular AP in control conditions (solid black line), and after administration of class IA (solid red line), class IB (solid blue line) and class IC (dashed green line) drugs (modified from [55]).

reentrant arrhythmias. Examples: sotalol, amiodarone and dronedarone.

- Class IV: antiarrhythmic drugs that affect calcium channels. They also decrease electrical conduction through the atrioventricular node, shorten the "plateau" phase of the AP and, as a consequence, reduce cardiac contractility. Examples: verapamil and diltiazem.
- Class V: antiarrhythmic drugs that work by other mechanisms different from the rest of the classes. Examples: adenosine and digoxin.

One important limitation of this Vaughan-Williams classification is the dependence on the primary mechanism of the drugs not accounting for the multi-channel effects that many antiarrhythmic drugs have. As an example, amiodarone has effects consistent with all of the first four classes.

Regarding AF treatment with antiarrhythmic drugs, previous studies have described the indications and contra-indications of using certain drugs [50]. For instance, β -blockers or verapamil can be useful to stop AF indirectly caused by myocardial infarction or respiratory diseases, but the negative inotropic side effects that can be derived from their use cannot be neglected. In general, class IC and, to a lesser extent, class IA drugs are effective to recover SR in AF patients [50], but their effects on potassium channels must be taken into account [56]. Amiodarone is effective even at relatively low doses, and with fewer side-effects than other drugs, making it a frequent choice for AF treatment [50]. If it is not possible to recover SR, an alternative approach is to optimize ventricular rhythm by using class V antiarrhythmic drugs, such as digoxin (affecting the NaK pump), β -blockers, verapamil or diltiazem [50].

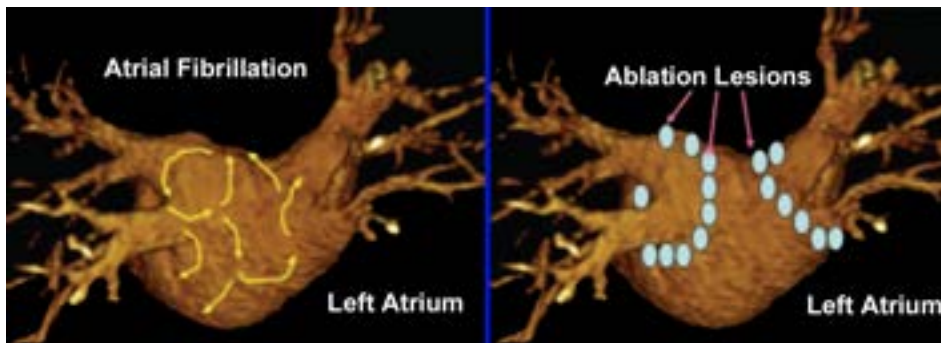


Figure 1.20: Magnetic resonance imaging (MRI) scan of the left atrium (viewed from the patient's back). Chaotic electrical activation pattern associated with AF (left panel) and ablation lesions produced around pulmonary veins by a catheter in order to electrically isolate them (right panel) (modified from [58]).

1.3.3.2 Non-Pharmacological Therapies

Antiarrhythmic drug action is usually insufficient by itself and it often requires application of other non-pharmacological therapies in order to revert the arrhythmia. Furthermore, when an arrhythmia is serious, urgent treatment to restore SR, such as applying an electrical shock therapy (also known as defibrillation or cardioversion) or implanting a short-term heart pacemaker, may be needed [57].

Other treatments to prevent or treat abnormal heart rhythms include: cardiac tissue ablation used to destroy or electrically isolate areas in the heart that may be causing the heart rhythm problems, as shown in Figure 1.20 [58], implantation of a cardiac defibrillator in patients who are at high risk of sudden cardiac death, and implantation of a pacemaker that senses when the heart is beating irregularly (too slowly or too fast) and then sends a signal that makes the heart beat at the correct pace [57].

In contrast with pharmacological therapies, most of these treatments require delicate cardiovascular surgical interventions, thus entailing high risk for the patients.

1.4 Thesis Objectives

The main objective of this thesis is to elucidate the ionic mechanisms underlying electrophysiological properties related to arrhythmic risk in human atria, ranging from the cellular level to the whole-cavity level, including one-dimensional (1D) cardiac fibers and two-dimensional (2D) atrial tissues. Different human atrial models are used and validated using experimental data

from both SR patients and patients diagnosed with permanent AF.

Specific objectives of the different parts of this thesis are:

- Elucidate the ionic mechanisms underlying APD adaptation to sudden changes in heart rate in human atria. Impairment of APD rate adaptation has been reported to be proarrhythmic, but the sources underlying the relation to arrhythmic risk remain unclear. In this thesis, APD rate adaptation will be characterized in both individual cells and 1D fibers and the relationship with arrhythmic risk will be evaluated.
- Unravel the ionic mechanisms underlying other electrophysiological properties related to arrhythmic risk. These properties are: APD, RMP and APD restitution (APDR) in single cells; CV in 1D fibers; and RP, wavelength (WL) dominant frequency (DF), phase singularities (PS) and vulnerability window (VW) in 2D tissues. The effects of AF-related remodeling on these properties will be investigated and differences in the unraveled ionic mechanisms between SR and permanent AF patients will be established.
- Investigate inter-subject variability in APD and AP morphology of human atrial cells from SR and AF patients and elucidate its underlying ionic sources. The elucidated sources of inter-subject variability will serve to postulate reasons for the different response of different patients to anti-AF treatments.
- Analyze arrhythmia-related electrophysiological properties in realistic anatomical human atrial three-dimensional (3D) models of AF patients. Such analysis will aim at providing a full multi-scale characterization of the effects of the previously elucidated ionic mechanisms and at investigating the implications on AF dynamics of inter-subject variability.

1.5 Thesis Outline

The thesis is organised as follows:

- In Chapter 2, the materials and methods used in the thesis are thoroughly described. In particular, details are provided about human atrial electrophysiological cell models, propagation in cardiac tissue, 3D human atrial models and computing facilities used to perform and run the simulations of this thesis.
- Chapter 3 describes the analysis of cardiac memory and its relation to risk in human atria, including the use of different stimulation protocols and arrhythmia-related markers. Two different human atrial

cell models are used for the investigations. Differences between cardiac memory, and underlying mechanisms, in atrial and ventricular myocytes are analyzed. To extend cell results, cardiac memory in 1D fibers is additionally investigated. The results of this chapter were presented at an international conference:

- C. Sánchez, E. Pueyo, P. Laguna and B. Rodríguez. Cardiac Memory in Human Atria and Relation to Arrhythmogenesis. *Computers in Cardiology*, Park City (Utah, USA), September 2009, vol. 36, pp. 81-84.
- Chapter 4 presents the analysis of human atrial electrophysiological properties in single cells, 1D fibers and 2D tissues. The role of ionic currents in the modulation of each property is evaluated by performing a sensitivity analysis, with particular focus on the temporal adaptation of the investigated properties. Furthermore, the combined effects of alterations in ionic currents on vulnerability to arrhythmias are shown. These results were published in two scientific journals and three conference proceedings:
 - C. Sánchez, A. Corrias, A. Bueno-Orovio, P. Laguna, M. Davies, J. Swinton, I. Jacobson, E. Pueyo and B. Rodríguez. The Na⁺/K⁺ Pump is an Important Modulator of Atrial Refractoriness and Rotor Dynamics in Human Atria. *Am J Physiol Heart Circ Physiol*, vol. 302, pp. H1146-H1159, 2012.
 - A. Bueno-Orovio, C. Sánchez, E. Pueyo and B. Rodríguez. Na/K Pump Regulation of Cardiac Repolarization: Insights from a Systems Biology Approach. *Pflügers Arch Eur J Physiol*, vol. 466, pp. 183-193, 2014.
 - C. Sánchez, A. Corrias, P. Laguna, M. Davies, J. Swinton, I. Jacobson, E. Pueyo and B. Rodríguez. Sensitivity of Atrial Fibrillation Related Biomarkers to Changes in Ionic Current Properties. *Heart Rhythm Society Scientific Sessions*, Denver (Colorado, USA), May 2010, vol. 7, n° 5, pp. S227.
 - C. Sánchez, A. Corrias, P. Laguna, M. Davies, J. Swinton, I. Jacobson, E. Pueyo and B. Rodríguez. Potential Pharmacological Therapies for Atrial Fibrillation. A Computational Study. *Computing in Cardiology*, Belfast (Northern Ireland, United Kingdom), September 2010, vol. 37, pp. 413-416.
 - C. Sánchez, B. Rodríguez and E. Pueyo. Ionic Modulators of Electrophysiology and Re-entry Properties in Human Atria. *Computing in Cardiology*, Hangzhou (China), September 2011, vol. 38, pp. 77-80.

- In Chapter 5, inter-subject variability in APD and AP morphology and its underlying ionic mechanisms are described. Populations of atrial cell models are constructed to simulate AP variability and are calibrated with experimental measurements. Multi-parametric regression techniques are used to investigate combined effects of ionic currents. The results of this chapter were published in a scientific journal and were presented at two conferences:
 - C. Sánchez, A. Bueno-Orovio, E. Wettwer, S. Loose, J. Simon, U. Ravens, E. Pueyo and B. Rodríguez. Inter-subject Variability in Human Atrial Action Potential in Sinus Rhythm versus chronic Atrial Fibrillation. *PLoS ONE*, 2014, (submitted).
 - C. Sánchez, A. Bueno-Orovio, E. Pueyo and B. Rodríguez. Analysis of Populations of Human Atrial Models Reveals the Relative Importance of Ionic Conductances in the Different Stages of Repolarization. *36th meeting of the European Working Group of Cardiac Cellular Electrophysiology*, Nantes (France), September 2012.
 - C. Sánchez, A. Bueno-Orovio, E. Pueyo and B. Rodríguez. Analysis of Populations of Human Atrial Models Reveals the Relative Importance of Ionic Conductances in the Different Stages of Repolarization. *Gordon Research Conference: Cardiac Arrhythmia Mechanisms*, Ventura (California, USA), February 2013.
- Chapter 6 shows the influence of ionic mechanisms on atrial fibrillation dynamics simulated in human atrial 3D models. This influence is investigated by calculating arrhythmic markers from pEGM signals recorded on the atrial surface. Inter-subject variability is included by generating 3D models with different cell repolarization dynamics. Simulation results are compared with measurements and obtained from the analysis of EGM recordings of permanent AF patients. This work is prepared to be published in a scientific journal and was presented at two international conferences:
 - C. Sánchez, A. Bueno-Orovio, M. W. Krueger, G. Seemann, O. Dössel, E. Pueyo and B. Rodríguez. Ionic Modulation of Atrial Fibrillation Dynamics in Heterogeneous Human 3D Virtual Atria with Repolarization Variability. (in preparation).
 - C. Sánchez, M. W. Krueger, G. Seemann, O. Dössel, E. Pueyo and B. Rodríguez. Ionic Modulation of Atrial Fibrillation Dynamics in a Human 3D Atrial Model. *Computing in Cardiology*, Krakow (Poland), September 2012, vol. 39, pp. 137-140.

-
- C. Sánchez, A. Bueno-Orovio, E. Pueyo and B. Rodríguez. Cell Repolarization Variability Modulates Atrial Fibrillation Dynamics in 3D Virtual Human Atria. *Computing in Cardiology, Zaragoza* (Spain), September 2013, vol. 40, pp. 911-914.
 - Finally, Chapter 7 presents the most important conclusions drawn in the thesis and reproduces the principal characteristics of Ca²⁺ dynamics possible future research lines.

Chapter 2

General Materials and Methods

In this chapter, general materials and methods used in the following chapters are described. In particular, the materials explained here include the human atrial cell computational models and the 3D human atrial model, whereas the methods include the propagation model, the numerical techniques and the computing resources. Specific simulations, signal processing methods and experimental data will be described in detail in each chapter.

2.1 Materials

2.1.1 Cardiac Computational Models

In this thesis, different cardiac computational models have been used to simulate electrical behavior in human atria. They can be separated into three categories: cell, 1D and 2D tissue and 3D whole-atrial models.

2.1.1.1 Human Atrial Electrophysiological Cell Models

To date, there are five main human atrial electrophysiological cell models in the literature, four of which have been used during the course of this thesis: the Courtemanche *et al.* [15], the Nygren *et al.* [13], the Maleckar *et al.* [18] and the Grandi *et al.* [16] models. The Köivumaki *et al.* model [17] is the most recently developed model and the main novelty of this model with respect to the others is its high accuracy to reproduce the principal characteristics of calcium dynamics, useful to investigate the excitation-contraction coupling in human atrial myocytes. This has not been studied in this thesis and therefore this model has not been used. For simplicity, the models will be referred to in the text by their first author's names.

All of these models provide detailed descriptions of human atrial cellular

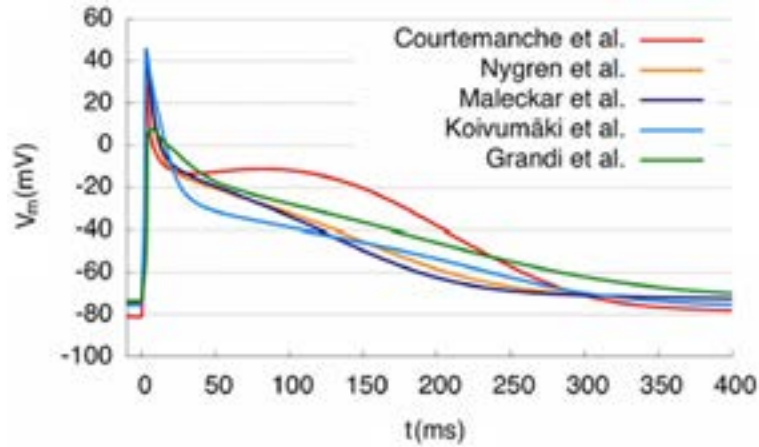


Figure 2.1: Simulated APs obtained after pacing for 50 s with a cycle length (CL) of 1 s with the five atrial cell models (modified from [60]).

electrophysiology including main transmembrane ionic currents, intracellular calcium handling and ionic homeostasis determining the time course of the human atrial AP, as shown in Figure 2.1. It is important to remark that both the Maleckar and the Köivumäki models are primarily based on the formulation given by the Nygren model, whereas the Grandi model inherits ionic current formulations from a previous human ventricular model developed by the same authors [59].

All these atrial cell models have many similarities, but important differences in the formulation of ionic currents and ion concentration dynamics, leading to significant differences in both electrophysiological behavior (see Figure 2.1) and electrical propagation behavior, as reported in [60]. These differences are reflective of the large variety of experimental data currently available, showing a wide range of electrical behavior due to the inter- and intra-subject variability in atrial tissue properties. Model differences can be summarized as follows:

- The Grandi model presents much lower AP amplitude (APA) than the other four models (81.4 mV, APA with the Grandi model, vs. 116.5 ± 5 mV, representing mean \pm standard deviation of APA values obtained with the other four models) and less steep initial upstroke (92.5 mV/ms, upstroke slope with the Grandi model, vs. 166.4 ± 15.5 mV/ms, representing mean \pm standard deviation of upstroke slope values obtained with the other four models).
- The RMP with the Courtemanche model is significantly more hyperpolarized with respect to the other four models (-81 mV, RMP with the Courtemanche model, vs. -74.4 ± 1.2 mV, representing mean \pm

standard deviation of RMP values obtained with the other four models).

- The duration of the "plateau" phase is notable in the Courtemanche model, but almost nonexistent in the rest of the models, thus leading to significant differences in the APD measured at 50% of repolarization.
- The APD measured at 90% of repolarization ranges from 197 ms with the Maleckar model to 330 ms with the Grandi model.
- The intracellular diastolic calcium concentration, i.e. $[Ca^{2+}]_i$ at resting state, is lower with both the Nygren and Maleckar models as compared with that of the other three models ($0.065 \mu\text{M}$, diastolic $[Ca^{2+}]_i$ with the Nygren and Maleckar models, vs. $0.153 \pm 0.05 \mu\text{M}$, representing mean \pm standard deviation of diastolic $[Ca^{2+}]_i$ with the other three models), whereas the CaT amplitude, i.e. difference between $[Ca^{2+}]_i$ and the maximum value of $[Ca^{2+}]_i$ in one cardiac cycle, in these two models is larger ($1.23 \mu\text{M}$, CaT amplitude with the Nygren and Maleckar models, vs. $0.47 \pm 0.2 \mu\text{M}$, representing mean \pm standard deviation of CaT amplitude with the other three models).
- Alternating behavior at fast pacing rates, i.e. significant differences in AP and/or CaT morphology and duration between consecutive activations, is only observed with the Courtemanche and Grandi models. Alternans are observed for CL values shorter than around 250 ms with the Courtemanche model and 500 ms with the Grandi model. The other three models do not present alternans for any value of CL.
- Restitution properties are also highly dependent on the model, with the Grandi model presenting the most significant differences: significantly shallower slopes of APD and RP restitution curves and steeper slopes of CV and WL restitution curves, with respect to other four models.
- Reentrant circuits in 2D tissue are not stable with the Courtemanche and Grandi models in SR conditions, meaning that a reentry cannot be sustained in 2D tissue for longer than a few seconds with these two models. The other three models lead to stable reentries in SR conditions, which could last indefinitely, and have associated DF values of about 4 Hz. Under electrical remodeling representing AF conditions, the five human atrial models lead to stable reentrant behavior. DF values in AF conditions are significantly higher with the Courtemanche and the Grandi models (about 8.5 Hz) than with the other three models (about 6.8 Hz).

2.1.1.2 Human Atrial Models of 1D Fibers and 2D Tissues

The electrical activity in the human heart is dependent on both cellular electrophysiology and electrical propagation between cells. In this thesis, 1D models representing cardiac fibers and 2D models representing cardiac tissues of human atria have been used. Both 1D and 2D models consist of a set of aligned cells in 1 and 2 directions, respectively, whose electrophysiology is defined by one of the models described in section 2.1.1.1. Two different sizes have been used for 1D models (1 and 5 cm) and other two sizes for 2D models (1x1 and 5x5 cm²) in order to investigate specific atrial properties related with arrhythmic risk.

The excitation of each cell in both types of models is generated by electrical propagation from neighbouring cells (except for the set of cells where the external stimulation is applied) through intercellular junctions.

Propagation Models of Electrical Activity

From a mathematical point of view, the electrical activity of cardiac tissue is often modeled by a coupled system of partial differential equations (PDEs), to simulate electrical wavefront propagation, and ordinary differential equations (ODEs), to simulate single-cell electrophysiological activity. A complete tissue model is obtained as in Figure 2.2.

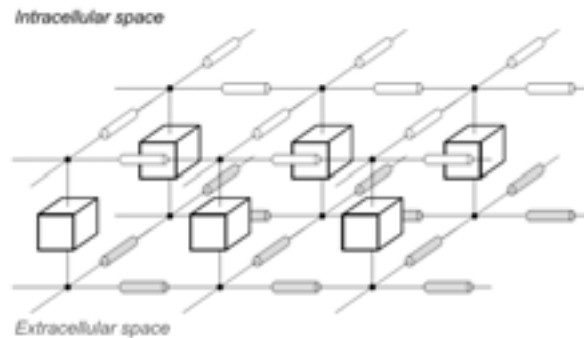


Figure 2.2: Tissue model commonly used in propagation models consisting of cells (boxes) connected to each other with resistances in both intracellular (white cylinders) and extracellular (grey cylinders) space (modified from [61]).

Two approaches have been widely used to solve this highly complex system: the bidomain equations and the monodomain equation. Both approaches model in detail the manner in which electrical activity spreads through the heart as a wave [62].

The bidomain equations consist of a parabolic PDE, an elliptic PDE

and a nonlinear system of ODEs, while the monodomain equation consists of a parabolic PDE coupled to a system of ODEs [63, 64]. The bidomain equations are:

$$\chi(C_m \frac{\partial V_m}{\partial t} + I_{ion}) - \nabla \cdot (\sigma_i \nabla (V_m + \phi_e)) = I_{s_i}, \quad (2.1)$$

$$\nabla \cdot ((\sigma_i + \sigma_e) \nabla \phi_e + \sigma_i \nabla V_m) = I_{s_e}, \quad (2.2)$$

where χ is the surface to volume ratio; I_{ion} is the total transmembrane current, ϕ_e is the extracellular potential; σ_i and σ_e are the intracellular and extracellular conductivity tensors; I_{s_i} and I_{s_e} are the external stimuli applied to the intracellular and extracellular spaces, respectively; and ∇ is the Nabla operator used to calculate gradient and divergence in vector calculus.

These two equations (2.1 and 2.2) can be simplified under the consideration of proportionality between the conductivity tensor matrices σ_i and σ_e , i.e. $\sigma_i = \alpha \sigma_e$, among others, as follows:

$$\chi(C_m \frac{\partial V_m}{\partial t} + I_{ion}) = \nabla \cdot (\sigma \nabla V_m), \quad (2.3)$$

where σ is a conductivity tensor given by $\sigma = \sigma_i(\sigma_i + \sigma_e)^{-1}$ [63, 64]. In this thesis, the monodomain equation approach was used to simulate electrical activity in human atrial tissue since the accuracy with respect to the bidomain model is similar, but its computational cost is considerably less expensive. Those cases when the use of the bidomain approach is essential have not been dealt with in this thesis (for instance when the effects of stimuli, bath, or extracellular conductivities need to be considered). Note that the first part of equation 2.3 corresponds to cellular electrophysiology dynamics, as explained in section 1.2.3.3, whereas the second part accounts for propagation of the transmembrane potential between neighbouring cells.

2.1.1.3 Human Atrial 3D Models

Combinations of realistic models of cardiac structures, muscle fibers, intercellular junctions and cellular electrophysiology can be very useful to investigate abnormal cardiac behavior. In this thesis, realistic human atrial 3D models have been used to investigate arrhythmia-related properties in AF conditions to extend the results in 1D fibers and 2D tissues.

A few biological models of the whole human atria with similar characteristics can be found in the literature [65–67]. In particular, the human atrial 3D model developed at the Karlsruhe Institute of Technology (KIT) has been used in this thesis [65].

Figure 2.3 shows the KIT 3D model with the corresponding human atrial structures from different viewpoints: left atrium (LA), right atrium (RA),

SAN, cresta terminalis (CT), pectinate muscles (PM), fossa ovalis (FO), Bachmann’s bundle (BB), cavotricuspid isthmus (CTI), left atrial appendage (LAPG), right atrial appendage (RAPG), atrioventricular ring (AVR), interatrial bridges (IAB) and ostia of pulmonary veins (PVs) and superior vena cava (SVC). Particular details of the simulations performed using this 3D model and the electrophysiological properties of each of the atrial structures will be explained in further detail in chapter 6. Electrical activity was simulated following the equation 2.3 described in section 2.1.1.2.

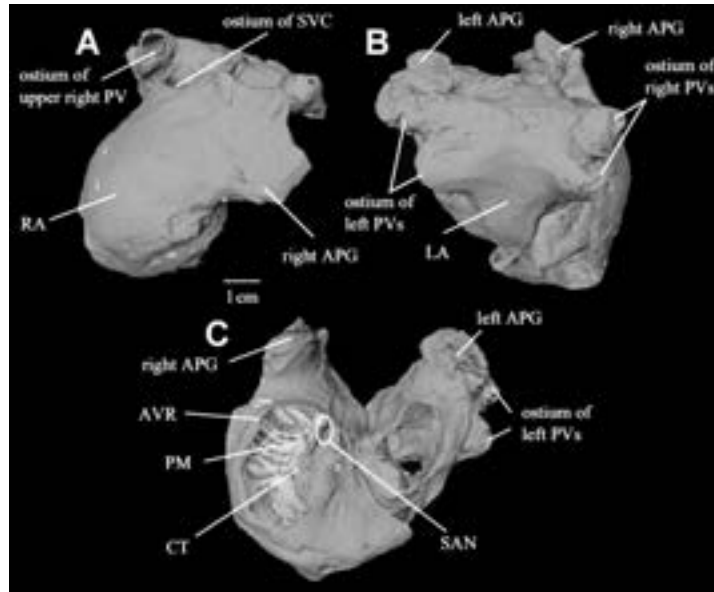


Figure 2.3: Anatomical 3D model of the human atria. **A:** RA in a frontal view. **B:** LA in a dorsal view. **C:** View through tricuspid and mitral valve. SAN, CT and PMs are visible in the RA. (modified from [65]).

2.2 Methods

2.2.1 Numerical Methods

The solution of the non-linear system of ODEs corresponding to the dynamics of cellular electrophysiology requires a very fine time step in order to achieve convergent solutions. In this thesis, the forward Euler method with a fixed time step of 0.02 ms was initially used for cell simulations. However, adaptive time step calculation was performed to save computing time without losing precision in Chapter 5: very short when very fast changes occur, such as during the initial AP upstroke, and very long when changes are slow, such as during the cellular resting state.

Similarly, the solution of the PDEs associated to propagation of electrical wavefronts in 1D fibers and 2D tissue requires fine resolution in both time and space, and thus fixed time and spatial steps of 0.02 ms and 250 μm , respectively, were used. Convergence of the numerical methods were proven by running simulations with different time steps ranging from 0.005 ms to 0.05 ms, and spatial steps ranging from 100 μm to 1000 μm . These simulations resulted in insignificant variations in the results for steps equal or shorter than 0.04 ms and 400 μm , respectively.

Regarding 3D simulations, the spatial resolution was given by the KIT 3D model itself through the separation between neighbouring cells, whereas the time step used to run the simulations was set to 0.04 ms, a bit coarser than that of 1D and 2D simulations in order to reduce the very expensive computational cost while keeping the reliability of the results.

2.2.2 Computing Resources

The cellular simulations were run using either C++ or MATLAB. C++ was used in the first parts of this thesis (Chapters 3 and 4) with a fixed time step to solve the ODEs of the models, whereas a particular ODE solver, *ode15s*, was used in MATLAB to solve the stiff equation system with an adaptive time step (Chapter 5). The main advantage of using C++ was that the models could be easily implemented and several simulations could be run simultaneously. However, we decided to change from C++ to MATLAB in the last parts of the thesis for two main reasons: 1) MATLAB is slightly cheaper in terms of computational cost; 2) most of the postprocessing analysis and figures of this thesis are obtained using MATLAB, therefore simulations and post-processing could be managed more efficiently if MATLAB was used for both.

For single cell simulations, an open-source software called COR [68], specialized in running computational models through the use of a particular programming language called cellml [69], was also used. The main advantage of using COR is that many electrophysiological models are already implemented in cellml. Furthermore, its very intuitive interface allows simultaneous simulation and visualization of the results during the course of the simulations.

The open source software Chaste [62, 70, 71], developed at the Department of Computer Science of the University of Oxford, was used in Chapter 4 to run both 1D-fiber and 2D-tissue simulations. Chaste is a software specialized in tissue simulations that allows the user to choose the electrophysiological model, the characteristics of the tissue mesh and the stimulation protocol to apply. All Chaste simulations were run on grid computing facilities through use of the middleware platform Nimrod/G, accessible via web interface [72], allowing the simultaneous launch of a large number of simulations with different stimulation protocols and model parameters.

3D-atria simulations were run using the Elvira software, specialized in multi-cell simulations and developed at the Department of Applied Mechanics and Bioengineering of the University of Zaragoza. This simulation software uses the finite element method described in [73]. The main advantage of using Elvira vs. Chaste is its cheaper computational cost for long simulations, entailing shorter times to perform simulations. In order to save computation time, parallel computing techniques based on Condor have been used to run Elvira [74]. Visualization of the 3D simulation results was performed using the software ENSIGHT [75].

Chapter 3

Quantification of APD Rate Adaptation in Human Atria and its Relationship with Arrhythmogenesis

3.1 Introduction

Cardiac memory refers to the time cardiomyocytes take to completely adapt to changes in heart rate (HR). It is well known that changes in HR entail alterations in the electrophysiology of atrial cells, thus leading to observable changes in AP. Two types of cardiac memory can be distinguished: short-term cardiac memory, i.e. the changes produced during the minutes following the change in HR, and long-term cardiac memory, i.e. the process of cell recovery lasting for several days after the change in HR occurs. At the body surface level, the non-instantaneous adaptation of the QT interval to changes in the RR interval (inversely dependent on HR) [76] or the variations in both magnitude and duration of the T-wave following ventricular pacing [77] are examples of cardiac memory.

In this chapter, we study short-term cardiac memory in cells and 1D fibers by analyzing the APD adaptation to changes in HR, an impairment of which has been previously related to an increased likelihood for the development of arrhythmias [76, 78]. It is well known that APD values strongly depend on the stimulation CL (equivalent to $1/\text{HR}$), as reported in previous studies in human ventricular myocytes [79, 80] and canine atrial myocytes [81, 82]; however, cardiac memory in human atria has been less well investigated and is the research focus of this thesis chapter.

3.1.1 Objectives

The main objectives of this part of the thesis can be summarized as follows:

1. Characterize and quantify APD rate adaptation in simulated human atrial cardiomyocytes.
2. Validate, qualitatively and quantitatively, the results of simulated APD rate adaptation with experiments in human atrial myocytes, from both the literature and the collaboration study with Hospital de la Santa Creu i Sant Pau in Barcelona.
3. Elucidate the cellular ionic mechanisms underlying APD adaptation in human atrial myocytes through the analysis of the contribution of the different ionic currents (both their conductances and their activation/inactivation kinetics) and the concentrations of Na^+ , K^+ and Ca^{2+} to the different phases of adaptation.
4. Assess model independence of the elucidated ionic mechanisms involved in human atrial APD rate adaptation by comparing the results obtained with two atrial cell models.
5. Compare the results and the conclusions obtained for cardiac memory in human atrial cells with those corresponding to cardiac memory in human ventricular cells.
6. Characterize and quantify APD rate adaptation in human atrial 1D fibers and compare the results with those obtained in single cells.
7. Evaluate the relationship between atrial APD adaptation and proarrhythmic risk by the use of preclinical markers.

3.2 Methods

3.2.1 Stimulation Protocols

Experimental and simulated stimulation protocols are described in the following sections.

3.2.1.1 Experiments

The experiments used for validation of the simulation results in this part of the thesis were performed in collaboration with the Cellular Electrophysiology Research Group at Hospital de la Santa Creu i Sant Pau in Barcelona. This group has recognized expertise in the experimental study of cardiac cells, having developed advanced tools to visualize and extract information of AP and ionic currents, particularly I_{CaL} [4–7].



Figure 3.1: Experimental devices in a confocal microscopy laboratory.

To perform the experiments of this thesis, confocal microscopy was used (Figure 3.1). First of all, a single cell is selected using a microscope. Then, Patch Clamp is applied, as described in section 1.2.3.1, with a set of particular parameters (CL, amplitude of the stimuli, duration of the stimuli...) controlled by a Patch Clamp amplifier (EPC 10-HEKA).

With the aid of a computer connected to the Patch Clamp amplifier, the correct generation and stability of the ‘gigaseal’ could be assessed by measuring the resistance in the micropipette opening. In this study the Voltage Clamp technique was applied to measure I_{CaL} by defining stimulation protocols where the amplitude of V_m was modified for shorts periods of time (known as conditioning potential), as shown in the example of Figure 3.2, and inhibiting the rest of ionic currents with specific substances in the internal and external solutions to eliminate sodium and potassium currents. The internal medium contained (in mM) 100 CsCl, 3.1 Na₂ATP, 4 MgCl₂, 5 sodium phosphocreatine, 0.42 Na₂GTP, 0.025 EGTA, 10 HEPES, and 20 tetraethylammonium; pH was adjusted to 7.2 with CsOH. The external medium contained (in mM) 107 NaCl, 20 CsCl, 1.8 MgCl₂, 4 NaHCO₃, 0.8 NaH₂PO₄, 1.8 CaCl₂, 10 HEPES, 5 glucose, and 5 pyruvate; pH was adjusted to 7.4 with NaOH [6].

Regarding the specific experimental protocol, a dynamic stimulation protocol with different values of CL and a certain number of stimuli for each CL was used to register I_{CaL} :

- 12 stimulation pulses with CL = 5 s.
- 30 stimulation pulses with CL = 2 s.
- 30 stimulation pulses with CL = 1.5 s.
- 30 stimulation pulses with CL = 1 s.
- 30 stimulation pulses with CL = 0.75 s.
- 30 stimulation pulses with CL = 0.5 s.

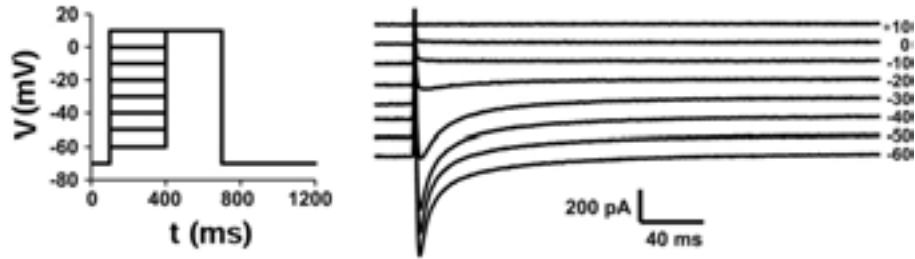


Figure 3.2: Example of a stimulation protocol with a series of 300-ms conditioning potentials between -70 and +10 mV used to inactivate I_{CaL} in a zebrafish ventricular myocyte followed by a 300-ms test pulse to measure I_{CaL} after the conditioning pulse (left panel). The family of I_{CaL} current traces obtained (right panel) for the potentials shown on the right side is shown (modified from [83]).

- 12 stimulation pulses with $CL = 5$ s.

3.2.1.2 Simulations

In this part of the thesis, the Courtemanche and the Nygren atrial cell models were used. A periodic stimulation protocol consisting of 30 minutes of periodic stimuli applied at a certain CL was used to obtain the steady-state values of all the variables in the models in order to initialize the simulations with the protocols described below. In order to characterize APD rate adaptation in human atrial cell simulations the following protocol was used:

- Pacing protocol: 10 minutes of stimuli applied at a CL_1 , 10 minutes of stimuli applied at a CL_2 , and 10 minutes of stimuli applied at a CL_1 , in order to observe the adaptation to sudden changes in HR. Different combinations of CL_1 and CL_2 , with $CL_1 > CL_2$, were used.

To relate ionic mechanisms underlying cardiac memory to arrhythmic risk, two different restitution protocols were used:

- S1S2 restitution protocol: this stimulation protocol is commonly used to study APDR, which refers to the degree of recovery of the APD following a new early heartbeat. The slope of the associated APDR curve has been strongly related to generation and stability of arrhythmias [84–86]. This protocol consisted of 10 heartbeats applied at a certain CL (S1 stimuli every 1000 ms) followed by an extra-stimulus S2 applied at a certain diastolic interval (DI) after the last AP generated by the S1 stimuli. This procedure was repeated for decreasing DIs in order to obtain an APDR curve which represented the APD

corresponding to the S2 stimulus versus the preceding DI (blue line in Figure 3.3). The DI values considered in this study were: 2000, 1600, 1500, 1400, 1300, 1200, 1100, 1000, 900, 800, 750, 700, 650, 600, 550, 500, 450, 400, 350, 300, 250, 225, 200, 175, 150, 125, 100, 75, 50, 25, 15, 10, 5, 4, 3 and 2 ms.

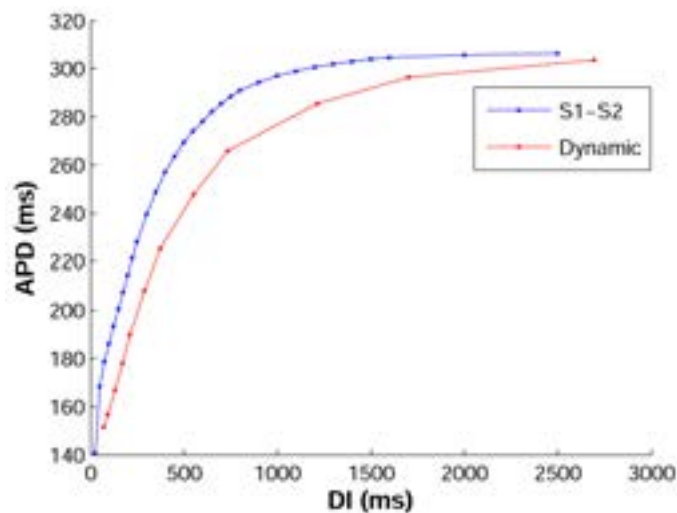


Figure 3.3: APDR curves (APD vs. DI) with the S1S2 restitution protocol (blue) and dynamic restitution protocol (red).

- Dynamic restitution protocol: this restitution protocol was also used to characterize APDR curves. The slope of the dynamic APDR curve has been related to arrhythmic risk [84–86]. This protocol consisted of pacing at an initial CL of 3000 ms for 100 heartbeats, then decreasing the CL and pacing again for 100 heartbeats. This procedure was repeated until reaching a CL of 225 ms with the following intermediate CL values: 3000, 2000, 1500, 1000, 800, 600, 500, 400, 350, 300, 250 and 225 ms. The APDR curve was obtained by plotting the last APD value for each CL versus the previous DI [87] (red line in Figure 3.3).

3.2.2 Characterization of APD Rate Adaptation and Underlying Mechanisms

In order to estimate the degree of cardiac memory, the time t_{90} required for the APD to complete 90% of its adaptation following a sudden and sustained change in HR was measured. The APD was measured at 90% of cell repolarization, unless otherwise stated. Furthermore, as two different phases were observed in the APD rate adaptation process: a fast phase, occurring during the first seconds after the change in HR and usually en-

tailing an abrupt alteration of APD, and a slow phase, lasting for some minutes and during which the APD gradually accommodates until reaching its new steady-state value corresponding to the new CL, each of these two phases were separately characterized. Specifically, in each of the two stages of the pacing protocol (corresponding to HR acceleration, i.e. $CL_1 \rightarrow CL_2$, and HR deceleration, i.e. $CL_2 \rightarrow CL_1$), exponential functions were fitted in the least squares sense to the fast and slow adaptation phases to characterize each phase of the adaptation by a time constant, τ_{fast} or τ_{slow} . These four-parameter exponential functions were of the form:

$$f(t) = a + be^{-\frac{t-c}{\tau}}. \quad (3.1)$$

where the values of a , b , c and τ were extracted from the best fitting function. In those cases where the fast phase has very few points, the number of extracted parameters is reduced by presetting a and c while extracting b and τ .

In order to unravel the ionic mechanisms underlying cardiac memory, a sensitivity analysis of APD rate adaptation was performed by simulating specific variations in physiological properties with respect to default SR conditions. The variations studied in the simulations were both inhibition and overexpression of the maximal conductances associated with the ionic currents and the time constants associated with the activation and inactivation gating variables. The maximum range of variation was $\pm 30\%$ with respect to the default values in the original model.

3.2.3 Preclinical Markers of Arrhythmic Risk

Since one of the main objectives of this part of the thesis was to relate ionic mechanisms involved in APD adaptation to arrhythmic risk, the following preclinical markers were used to evaluate proarrhythmic risk:

1. *Slopes of the APDR curves*: there is controversy in the literature regarding the relationship between the slope of the restitution curves and arrhythmic risk. Some studies relate steep restitution slopes (>1) with higher likelihood of arrhythmia generation [85, 86], whereas other studies report that shallow restitution slopes favor the stability of arrhythmias [84]. In this thesis the APDR curves obtained with both the S1S2 protocol and the dynamic protocol were adjusted with exponential functions of the form:

$$APD = a(1 - e^{-bDI}) + c, \quad (3.2)$$

within the range of DIs between 0 and 400 ms. The purpose of this fitting was to obtain a continuous function relating APD and DI, thus allowing to calculate the slopes of the APDR curves at any DI. Once

the fitting was performed, the slopes of the restitution curves were evaluated for DI=100 ms in order to avoid the effects of AP alternans, i.e. the phenomenon that occurs in some cases for rapid pacing when sequences of consecutive long-short APs are generated. The derivative of equation 3.2 was used to calculate the slope for DI=100 ms:

$$S_{DI} = abe^{-bDI}, \quad (3.3)$$

2. *Calcium current reactivation*: the magnitude of I_{CaL} recovery following inactivation has been proposed as an arrhythmic risk marker [88]. Values of this marker close to 1 have been related to higher likelihood of calcium current reactivation and, therefore, of generation of early afterdepolarizations (EADs) that could result in arrhythmia generation [88]. In order to obtain this marker, represented by ρ , the inactivation gating variables of I_{CaL} were measured at 90% of AP repolarization following periodic stimulation. Since values of inactivation gating variables represent probability of being open, ρ is calculated by multiplying them with the Courtemanche model ($f_{Ca} \cdot f$). The calculation of ρ is more complex with the Nygren model since it includes three inactivation gating variables. It is obtained by adding two multiplications: a function of the calcium dependent gating variable in open state ($f_{Ca} \cdot f_{L1}$) and a function of the calcium dependent gating variable in closed state ($(1 - f_{Ca}) \cdot f_{L2}$).
3. *AP triangulation*: Hondeghem *et al.* showed a strong relationship between AP triangulation and arrhythmic risk [89]. This marker can be obtained as the quotient of APD₉₀ and APD₅₀ (APD measured at 90% and 50% of repolarization, respectively) and is represented in this thesis by δ . Values close to 1 entail "square-shaped" APs, while larger values correspond to triangular AP morphologies.

3.3 Results

3.3.1 APD Rate Adaptation in Human Atrial Myocytes

3.3.1.1 Characterization and Quantification of APD Rate Adaptation

Figure 3.4 shows the default pacing protocol used to study APD adaptation (left panel, $CL_1 = 1000$ ms and $CL_2 = 600$ ms), as described in section 3.2.1.2, and the corresponding APD time course when this protocol was applied to cells simulated with the Courtemanche model (right panel). This figure shows that HR acceleration (equivalent to CL decrease) entailed an

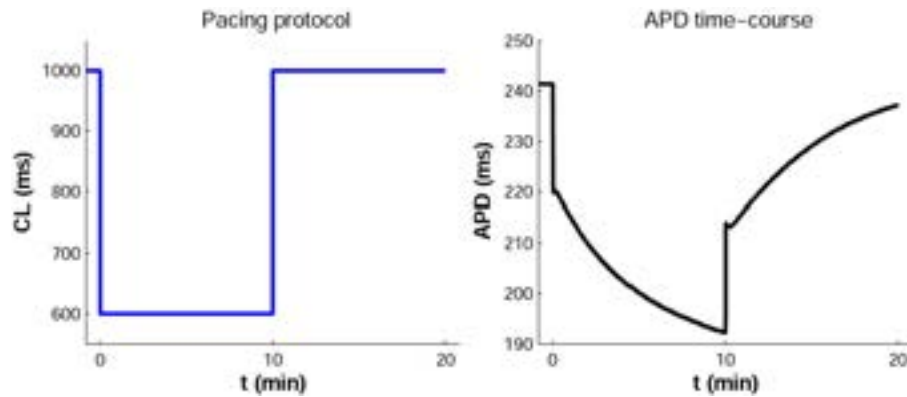


Figure 3.4: CL time course with the default pacing protocol: $CL_1=1000$ ms and $CL_2=600$ ms (left). APD time course corresponding to the pacing protocol (right).

initial abrupt decrease in APD (fast adaptation phase) followed by a progressive and slower decrease in APD until the new steady-state was reached (slow adaptation phase). In the same way, HR deceleration (equivalent to CL increase) entailed an increase in APD, being initially abrupt and subsequently more gradual.

In this thesis the time of cellular adaptation was quantified by measuring the time APD takes to reach 90% of the absolute difference between the initial and final values, corresponding to the steady-state values at each pacing stage. This value is represented by t_{90} , as described in section 3.2.2. As shown in Figure 3.4, the steady-state was not reached within the 10 minutes of stimulation at each CL, therefore t_{90} was measured in a new simulation where each stage was prolonged for 5 minutes, enough for APD to reach a stable value. The value of t_{90} measured following HR acceleration was 487 s (from $CL_1=1000$ ms to $CL_2=600$ ms), whereas following HR deceleration t_{90} was 564 s (from $CL_2=600$ ms to $CL_1=1000$ ms).

Besides the measurement of t_{90} , in order to estimate the speed of APD adaptation, the method described in section 3.2.2 of fitting exponential functions to each adaptation phase was used. Once these exponential functions were obtained, the associated time constants τ_{fast} and τ_{slow} , which measure the time required for APD to reach 63.2% of the absolute difference between the initial and the final values in both the fast phase and the slow phase of adaptation, respectively, were calculated. In the default case shown in Figure 3.4, the time constants that characterize each adaptation phase were: following HR acceleration, $\tau_{fast} = 6.4$ s and $\tau_{slow} = 297.2$ s; following HR deceleration, $\tau_{fast} = 7.3$ s and $\tau_{slow} = 404.3$ s.

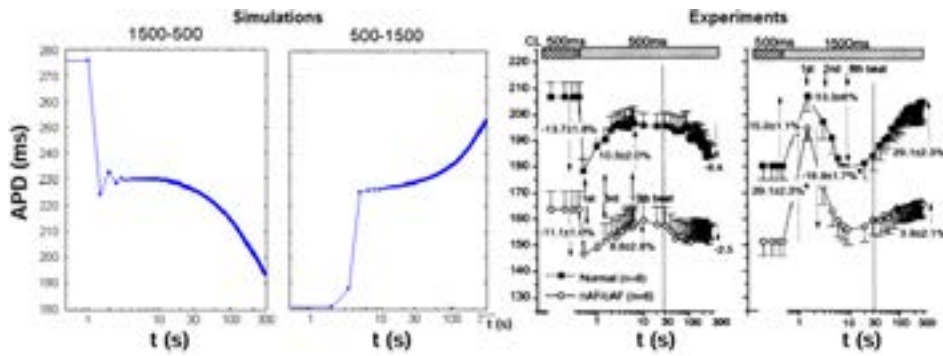


Figure 3.5: Comparison between APD adaptation to changes in HR in atrial cell simulations with the Courtemanche model (left) versus results obtained experimentally in canine atrial tissue (right; modified from [81]).

3.3.1.2 Experimental Validation

In order to validate the simulation results, a comparison between them and experimental studies for APD rate adaptation from the literature was performed. The results of APD adaptation following HR deceleration and acceleration obtained in our simulations (left panels in Figure 3.5) and in canine atrial tissue (right panels in Figure 3.5) [81] were compared. We could not find any experiments in the literature analysing cardiac memory in human atrial cells. The same stimulation protocol was used so that simulations and experiments could be properly compared: from $CL_1=1500$ ms to $CL_2=500$ ms (HR acceleration) and from $CL_1=500$ ms to $CL_2=1500$ ms (HR deceleration). Simulation and experimental results were qualitatively similar, since a sustained change in HR induced a large fast initial variation in APD followed by a slower accommodation. A quantitative comparison of the results revealed some differences between them. APD_{90} was significantly longer with $CL=1500$ ms in the simulations than in the experiments in canine atrial cells. The amplitude of the change in APD_{90} following HR acceleration/deceleration was larger in the simulations, as shown in Figure 3.5. The main cause of these differences was that the simulations corresponded to human atrial single cells whereas the experiments were performed with multicellular canine atrial tissue.

3.3.1.3 Sensitivity of APD Adaptation to the Stimulation Protocol

In this part of the thesis, a sensitivity analysis was performed to evaluate the dependence of APD adaptation on both the initial CL and the magnitude of change in CL. As shown in Table 3.1 and Figure 3.6, both factors had

notable influence on the two phases of adaptation. From the analysis of the results, it can be concluded that:

Table 3.1: Time constants for fast and slow phases following HR deceleration and acceleration.

Pacing Protocol	HR acceleration		HR deceleration	
	$\tau_{fast}(s)$	$\tau_{slow}(s)$	$\tau_{fast}(s)$	$\tau_{slow}(s)$
1000-600-1000 ms	6.4	297.2	7.3	404.3
1600-1200-1600 ms	58.8	239.8	33.4	274.1
2000-1600-2000 ms	176.2	231.0	99.4	240.3
1000-800-1000 ms	23.2	190.6	12.0	449.6
1000-400-1000 ms	1.6	245.2	4.4	593.2

- The initial CL significantly modulates τ_{fast} and τ_{slow} . As shown in Table 3.1, τ_{fast} gradually increased from values lower than 8 s when the initial CL was 1000 ms to values higher than 100 s when the initial CL was 2000 ms. On the other hand, τ_{slow} decreased when the initial CL increased, being longer than 300 s for initial CL=1000 ms and about 240 s when the initial CL was 2000 ms.
- The magnitude of CL change has clear influence on τ_{fast} , but not so clear on τ_{slow} . Table 3.1 shows τ_{fast} was longer if the magnitude of change in CL became smaller and viceversa. The values of τ_{slow} decreased following HR acceleration with both magnitudes of change in CL (1000-800-1000 ms and 1000-400-1000 ms) and increased following HR deceleration with both magnitudes of change in CL (1000-800-1000 ms and 1000-400-1000 ms), with respect to the default case (1000-600-1000 ms).

3.3.2 APD Rate Adaptation in 1D Atrial Fibers

In order to investigate the effects of electrical propagation on APD rate adaptation, simulations of 1D fibers consisting of a number of aligned cells were performed. Figure 3.7 shows the APs obtained with the Courtemanche model after the third stimulus in a periodic protocol with CL = 1000 ms was applied to the first cell of a 1D fiber consisting of 200 cells. Considering the length of a single cell equal to 250 μm (thus making the length of the fiber equal to 5 cm) and the diffusion coefficient (D) equal to 0.001 cm^2/ms , the propagation delay from one end to the other was approximately 93 ms, thus entailing a CV of 53.5 cm/s, only slightly faster than that obtained in some experiments with human atrial fibers (41-44 cm/s) [90].

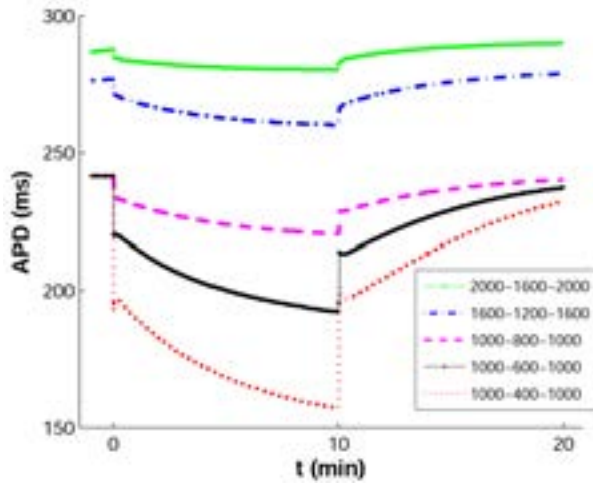


Figure 3.6: APD time courses with different combinations of CL changes using the pacing protocol: the default case (1000-600-1000 ms, black solid line), two cases with different initial CL but the same magnitude of CL change (2000-1600-2000 ms, green solid line; and 1600-1200-1600 ms, blue dash-dotted line), and two cases with different magnitude of change in CL but the same initial CL (1000-800-1000 ms, pink dashed line; and 1000-400-1000 ms, red dotted line).

In order to compare APD rate adaptation between single cells and 1D fibers, the values of t_{90} and τ_{slow} for three different cells located at the two ends and in the middle of the fiber (number 1, number 100 and number 200) and two different diffusion coefficients ($D=0.001$ y 0.01 cm^2/ms , corresponding to the default value and to a tenfold higher value) were calculated (see Table 3.2). Values of τ_{fast} are not shown in Table 3.2 due to the DADs that were generated immediately after the change in HR, particularly following HR deceleration (see Figure 3.8), thus making their calculation impossible. As shown in Table 3.2, values of t_{90} increased as the stimulus was propagated through the fiber with $D=0.001$ cm^2/ms , whereas it decreased through the fiber with $D=0.01$ cm^2/ms . On the other hand, the values of τ_{slow} were very similar between the different cells within the 1D fiber following both HR acceleration and deceleration. Furthermore, the values of τ_{slow} were also similar to those obtained in single cells (e.g. with the Nygren model τ_{slow} in single cells was 145 s and 131.1 s following HR acceleration and deceleration, respectively). APD rate adaptation computed in 1D fibers was significantly different with the two models used. Following a few minutes of pacing, diffusion of V_m between neighboring cells led to AP prolongation in 1 out of 2 stimuli, i.e. AP alternans, with the Courtemanche model, whereas APD rate adaptation led to very slight AP alternans with the Nygren model (Figure

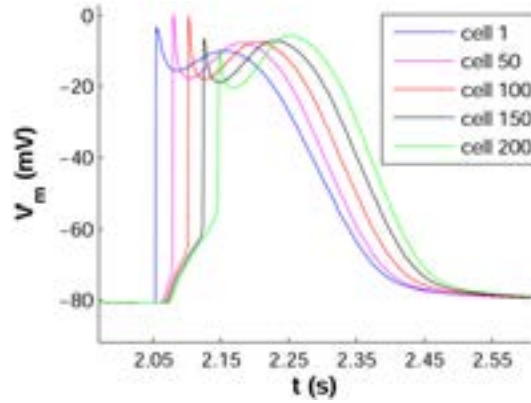


Figure 3.7: APs generated after the third stimulus with the Courtemanche model in a periodic protocol with $CL = 1000$ ms. APs corresponding to cell 1 (blue), cell 50 (pink), cell 100 (red), cell 150 (black) and cell 200 (green) in a 1D fiber consisting of 200 cells. Stimuli applied only to cell 1.

Table 3.2: Time for 90% of APD adaptation, t_{90} , and time constant for the slow APD adaptation phase following HR deceleration and acceleration with $D = 0.001$ (top) and 0.01 cm^2/ms (bottom) in cells 1, 100 and 200 with the Nygren model.

($D=0.001$ cm^2/ms)	cell 1	cell 100	cell 200
t_{90} (s) (acc/dec)	174.2/190.4	249.5/296.6	283.7/304.3
τ_{slow} (s) (acc/dec)	112.5/177.4	129.3/181.3	136.4/178.6
($D=0.01$ cm^2/ms)	cell 1	cell 100	cell 200
t_{90} (s) (acc/dec)	288.3/342	263.1/324.5	159.6/232.6
τ_{slow} (s) (acc/dec)	113.8/175.8	117.2/179.2	120.9/175.8

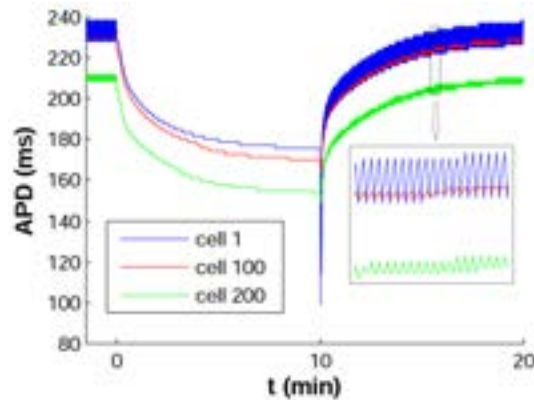


Figure 3.8: APD time course of three cells in a one-dimensional fiber of 200 cells when applying the pacing protocol 1000-600-1000 ms with the Nygren model. Alternating behavior of the APD shown in the zoomed in box.

3.8).

This proves that the dynamics of APD rate adaptation conform a process mainly originated at cellular level since they remain almost unchanged throughout the fiber, whereas the total adaptation time is modulated by characteristics related to electrical propagation in tissue.

3.3.3 Ionic Mechanisms of APD Rate Adaptation

Though all the ionic currents and concentrations described in the cardiac computational models of human atrial cells have importance in the determination of the AP, not all of them have significant effects on the process of APD adaptation to changes in HR. In order to unravel these ionic mechanisms, the values of the time constants, τ_{fast} and τ_{slow} , which characterize the APD adaptation process, were calculated and compared for electrophysiological conditions involving different contributions of ionic currents. As previously described in section 3.2.2, the maximal conductances and the time constants of the gating variables of all the ionic currents in the models were varied by +30%, +15%, 0, -15% and -30% with respect to their default values. The ionic mechanisms whose variation led to the most significant changes in τ_{fast} and τ_{slow} were identified as the main modulators of each adaptation phase and further simulations were performed to corroborate their role on cardiac memory in human atrial cells.

Fast phase

Regarding the fast phase of APD rate adaptation, τ_{fast} was only significantly altered when the maximal conductances of two ionic currents were

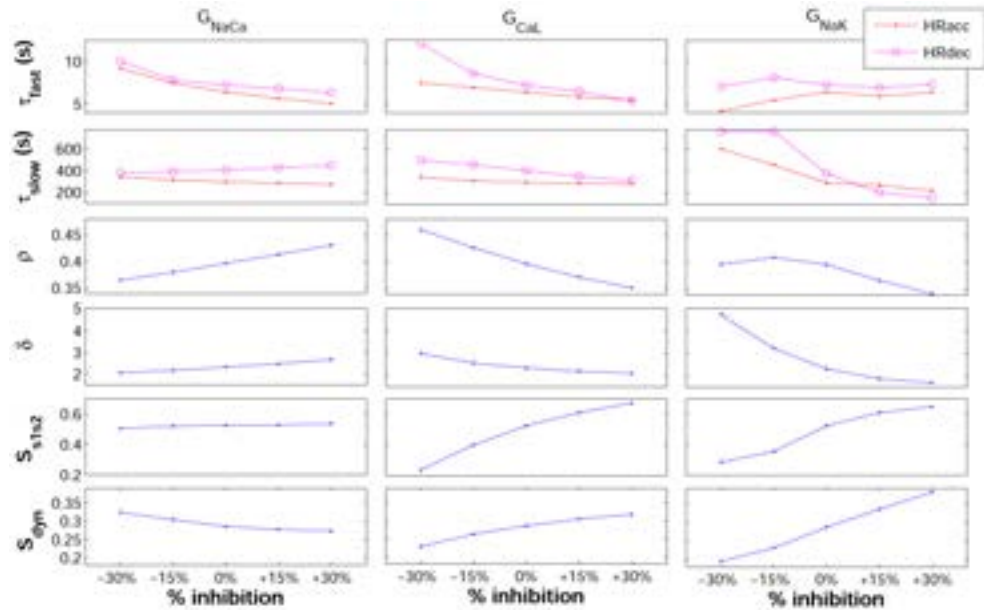


Figure 3.9: Values of the markers τ_{fast} , τ_{slow} , ρ , δ , S_{s1s2} and S_{dyn} when the three ionic mechanisms modulating cardiac memory in human atrial cells (G_{NaCa} , G_{CaL} and G_{NaK}) were modified by -30%, -15%, 0, +15% and +30% with respect to the default values in the Courtemanche model.

modified: I_{CaL} and $NaCa$ exchanger currents. The specific values of τ_{fast} for each percentage of variation are represented in the first row of Figure 3.9. This Figure shows that changes by 30% led to notable alterations in τ_{fast} . Following HR acceleration, $\tau_{fast} = 7.5$ s and 9.2 s when G_{CaL} and G_{NaCa} were blocked by 30%, respectively, whereas the value in control conditions was $\tau_{fast} = 6.4$ s. Following HR deceleration, $\tau_{fast} = 12.1$ s (30% block of G_{CaL}), 10.1 s (30% block of G_{NaCa}) and 7.3 s (control). In order to confirm the involvements of these currents in the adaptation process, large blocks (up to 90%) of their ionic conductances, G_{CaL} and G_{NaCa} , were simulated (top panels in Figure 3.10). As shown in Figure 3.10, the fast phase of adaptation is almost non-existent when either G_{CaL} or G_{NaCa} are strongly inhibited.

Validation of the simulation results showing I_{CaL} as key in the modulation of the fast phase of adaptation was performed by comparing them with those experimentally obtained in the Hospital de la Santa Creu i Sant Pau. The maximum peak of I_{CaL} in each cardiac cycle, $I_{CaL,peak}$, in simulations was compared with those obtained from experiments with human atrial myocytes (as described in chapter 1.2.3.1), as shown in Figure 3.11 (note that $I_{CaL,peak}$ values are negative since I_{CaL} is an inward ionic current). Due

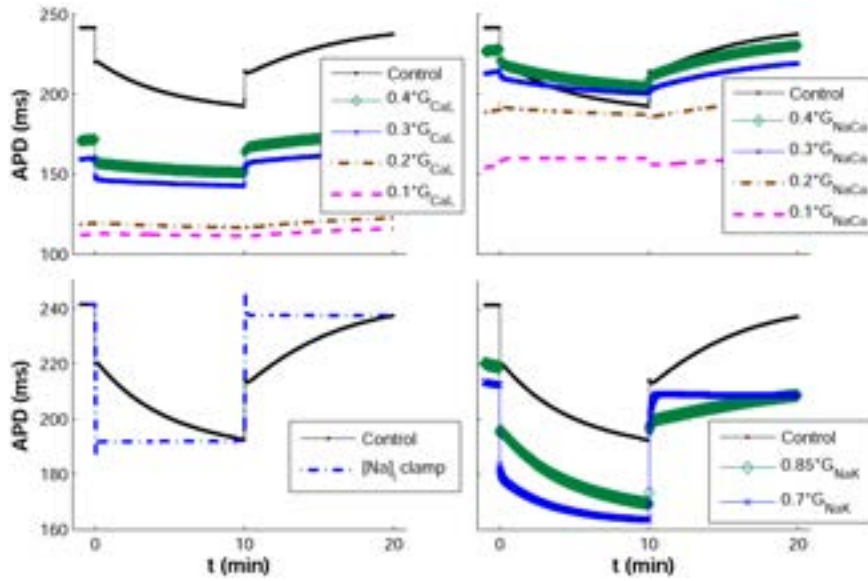


Figure 3.10: APD time course under control, G_{CaL} inhibition (left top panel), G_{NaCa} inhibition (right top panel), $[Na^+]_i$ clamping (left bottom panel) and G_{NaK} inhibition (right bottom panel) in cells simulated with the Courtemanche model.

to the ethical limitations associated with these types of experiments, only five recordings could be used for comparison with simulations. The same stimulation protocol applied to the experiments, shown in section 3.2.1.1, was simulated with the Courtemanche and the Nygren models.

Very similar tendencies were observed in the total response of I_{CaL} to changes in CL, with decreasing I_{CaL} amplitude when CL decreases, in most of them. In the first stages of pacing, with long CL ($CL > 1000$ ms), the amplitude of I_{CaL} remained very stable with no clear increments/decrements; whereas in the stages with short CL ($CL \leq 750$ ms), a notable reduction in the absolute value of the I_{CaL} was produced in both experimental recordings and simulations. However, variability between the amplitudes of I_{CaL} in different recordings was also observed (-2.1 ± 0.7 pA/pF).

In most of the experimental recordings, the peak of I_{CaL} was, in absolute value, lower than that obtained with the simulations due to the negative feedback of intracellular calcium that occurs with the perforated Patch Clamp technique used in the experiments, which has notable influence on the recorded inward calcium current.

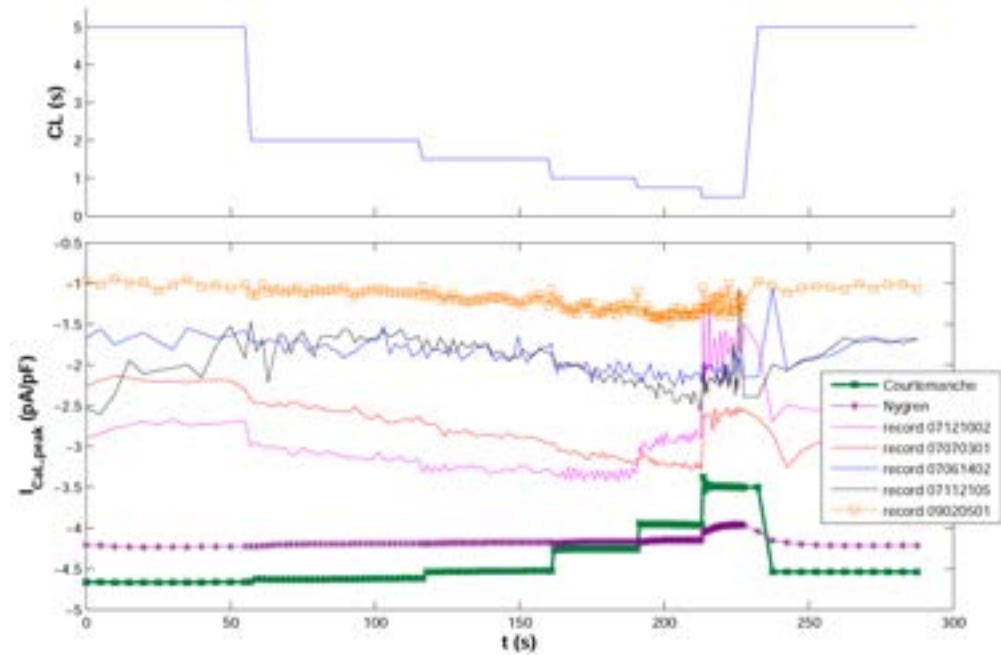


Figure 3.11: Time course of the stimulation CL (top panel) and the amplitude of I_{CaL} peaks in some experimental recordings of human atrial cells in the simulations with the Courtemanche and Nygren models (bottom panel).

Slow phase

From the analysis of the slow phase, we deduced that it is mainly modulated by the intracellular sodium dynamics ($[Na^+]_i$). The inhibition of the NaK pump activity has notable effects on $[Na^+]_i$ dynamics and, consequently, on the slow phase of APD adaptation (right bottom panel of Figure 3.10) and thus on τ_{slow} , as shown in the second row of Figure 3.9. Following HR acceleration, $\tau_{slow} = 601.9$ s and 453.6 s for I_{NaK} inhibition by 30% and 15%, respectively, whereas the value in control was 297.2 s. Following HR deceleration, $\tau_{slow} = 780.1$, 734.5 and 404.3 s, respectively. A new simulation where the value of $[Na^+]_i$ was clamped in each stage of the pacing protocol to the values it would take in the control case at the end of each stage (14.9 mM during pacing at CL = 600 ms, and 14.0 mM during pacing at CL = 1000 ms) was performed. This $[Na^+]_i$ clamping resulted in the abolishment of the slow phase of adaptation, as shown in the left bottom panel of Figure 3.10.

With the aim of confirming that the observations of this study were model independent, the same simulations described above were performed using the Nygren model. The ionic mechanisms involved in the fast and

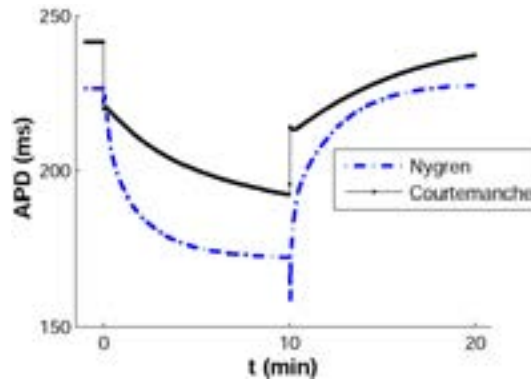


Figure 3.12: APD time course with the pacing protocol 1000-600-1000 ms using the Nygren (blue dash-dotted line) and Courtemanche (black solid line) models.

slow phase of APD rate adaptation were found to be the same using either of the two models. Figure 3.12 shows some differences between the time course of the APD obtained using the same pacing protocol with the two human atrial cell models. The causes of these differences will be discussed in further detail in section 3.4.

From the analysis of Figure 3.12, it can be observed that, during the fast phase of adaptation, APD initially increased following HR acceleration and decreased following HR deceleration with the Nygren model, in contrast with the results corresponding to the Courtemanche model. Due to this non-monotonic changes, fitting the fast phase with an exponential function was not adequate. Thus, the same simulations performed with the Courtemanche model to obtain the results shown in the top panels of Figure 3.10 were performed in order to unravel the underlying ionic mechanisms with the Nygren model. As occurred with the Courtemanche model, the fast phase of APD rate adaptation almost disappeared when either G_{NaCa} or G_{CaL} were strongly inhibited.

Regarding the slow phase of APD adaptation, the main difference lay in the shorter time needed to reach the steady-state with the Nygren model, thus entailing shorter values of t_{90} (288.7 and 329.6 s, following HR acceleration and deceleration, respectively). Despite these differences, the ionic mechanisms underlying the slow phase of APD adaptation to changes in HR were the same using either of the two models. G_{NaK} reduction by 30% entailed an increase in τ_{slow} from 145 s to 261.2 s following HR acceleration and from 131.1 s to 316.4 s following HR deceleration. These results highlight the key role of the activity of the NaK pump in the cardiac memory of human atrial myocytes.

3.3.4 Relation between APD Rate Adaptation and Arrhythmogenesis

A relationship between protracted cardiac memory, i.e. slow APD adaptation entailing long values of τ_{fast} or τ_{slow} , and arrhythmic risk was investigated. In order to do this, the preclinical markers described in section 3.2.3, ρ , δ , S_{s1s2} and S_{dyn} were quantified in simulations in which the ionic mechanisms elucidated as underlying APD adaptation dynamics were varied by $\pm 30\%$

Regarding the fast phase of adaptation, Figure 3.9 shows that the increase in τ_{fast} caused by G_{NaCa} inhibition is not directly related to an increase in the arrhythmic risk, as can be seen in the quantification of any of the markers studied. However, an increase in τ_{fast} prompted by G_{CaL} inhibition was associated with higher likelihood of generation of afterdepolarizations, produced by higher likelihood of calcium current reactivation (ρ took a value of 0.46 when G_{CaL} was blocked by 30%, whereas the value of ρ in control was 0.39), and more acute triangulation of the AP ($\delta = 2.99$ when G_{CaL} was blocked by 30%, and 2.33 in control conditions). As regards the slopes of APDR curves, S_{s1s2} and S_{dyn} , were shallower when G_{CaL} was blocked by 30% than in control conditions ($S_{s1s2} = 0.24$ versus 0.52; $S_{dyn} = 0.23$ versus 0.29). A decrease in the restitution slopes has been related in the literature to a higher stability of reentrant arrhythmias [84].

Furthermore, Figure 3.9 shows that NaK pump inhibition contributed to notably delay the slow phase of APD adaptation. This is related to higher arrhythmic risk, as manifested by higher probability of calcium current reactivation ($\rho = 0.40$), larger AP triangulation ($\delta = 4.73$) and shallower slopes of APDR curves ($S_{s1s2} = 0.29$; $S_{dyn} = 0.20$) when G_{NaK} was blocked by 30%.

3.3.5 APD Rate Adaptation in Atrial versus Ventricular Myocytes

The analogies and differences between cardiac memory in human atrial cells and human ventricular cells were studied by comparing the results of this study with those obtained with a human ventricular cell model, developed by ten Tusscher and Panfilov [91], in a previous study [80]. Despite the substantial differences between AP shape and duration in atrial and ventricular cells (more triangular and significantly shorter in duration in atrial cells as compared to ventricular cells) the APD adaptation to abrupt changes in HR follows a very similar pattern in both types of cells and occurs in two phases: fast and slow. However, while the time needed for human ventricular cells to adapt is about 3-4 minutes, the adaptation time in human atrial cells is longer than 8 minutes (Figure 3.13).

The ionic mechanisms underlying the fast phase of APD adaptation are

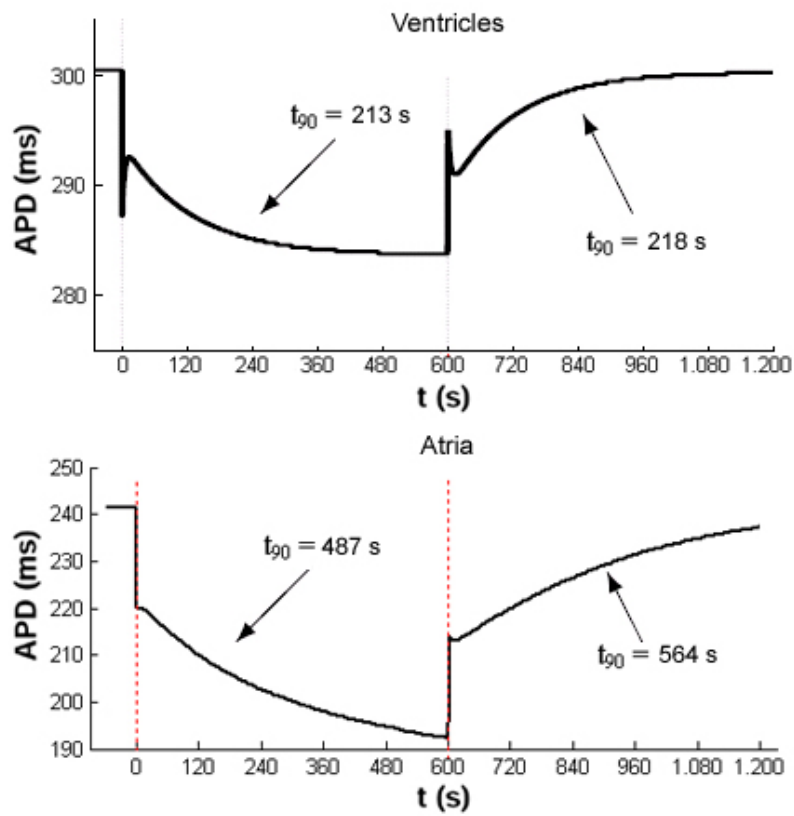


Figure 3.13: Comparison of simulation results of APD adaptation to sudden changes in HR in cells from the ventricular epicardium [80] and atrial cells, both in human, showing the values of t_{90} for HR acceleration and HR deceleration.

somewhat different in atrium and ventricle, being the inactivation kinetics of I_{CaL} and the activation kinetics of I_{Ks} the major determinants in ventricular cells [80], whereas in atrial cells the maximal conductances of I_{CaL} and I_{NaCa} are the main mechanisms, as shown in the present thesis. On the other hand, the ionic mechanisms modulating the slow phase of APD adaptation to changes in HR are common to atrial and ventricular cells, being the intracellular sodium dynamics, $[Na^+]_i$, the major determinant in both cases.

Another important difference between the activity of myocytes in both cavities of the human heart is the generation of EADs in ventricular cells under conditions associated with protracted rate adaptation. EADs are presented as increments in the transmembrane potential during phases 2 or 3 of the AP, frequently caused by an early recovery of the activation calcium channels. EADs do not occur when using human atrial cell models, no matter the simulated conditions. However, delayed afterdepolarizations (DADs) could be generated under certain conditions with the Nygren model. DADs are characterized by the depolarization of V_m when the cell is at its resting state and no external stimulation has been applied. The main cause for DADs generation is the opening of enough inward calcium channels to depolarize the cell. An increased likelihood of generation of afterdepolarizations has been associated in this thesis with delayed rate adaptation, as shown by the AP triangulation and calcium current reactivation markers studied.

3.4 Discussion

The present chapter focused on investigating the response of the APD in atrial cells to sudden and sustained changes in HR. To the best of our knowledge, there is very little investigation on this dependence in the atria, particularly in humans, and with only a few studies targeting cardiac memory in dogs [81, 82]. Despite differences between species, this study shows that dynamics of APD rate adaptation are similar in dog and human. In particular, our simulations in human atrial cells showed that the complete process of APD adaptation to changes in HR lasts for several minutes and consists of two phases, fast and slow, as occurs in canine experiments [81, 82].

A very limited number of experimental studies analyzing the role of the $NaCa$ exchanger and I_{CaL} in human atria can be found in the literature. Regarding the $NaCa$ exchanger, it is a protein that interchanges three sodium ions from the extracellular space with two calcium ions from the intracellular space in order to compensate for the large amount of inward calcium via I_{CaL} , as explained in section 1.2.4.5 [92]. Watano *et al.* related the effects of the drug KB-R7943, a $NaCa$ exchanger blocker, with arrhythmic protection in guinea-pig hearts, concluding the drug acted more notably on the $NaCa$ exchanger in its reverse mode (extruding sodium from the cell and importing calcium) and suppressed the arrhythmia previously generated

with other drugs [93], in good agreement with results shown in this chapter where an inhibition of the *NaCa* exchanger protracting the fast phase of adaptation was associated with lower arrhythmic risk through a lower likelihood of calcium current reactivation and AP triangulation. However, an experimental study in dogs showed that the effect of inhibiting the *NaCa* exchanger in its reverse mode was not useful to prevent arrhythmias generated through ischemia or reperfusion [94], so the role of these mechanisms could be controversial and dependent on the species. On the other hand, the investigation performed by Pott *et al.* showed that the effect of suppressing the *NaCa* exchanger in murine cardiomyocytes, which entailed a reduction in I_{CaL} , had very slight effects in the repolarization and duration of the AP [95].

Regarding I_{CaL} , Klein *et al.* studied the relationship between L-type calcium channels and AF in human beings, concluding that the likelihood of these channels to be open is higher in AF conditions, thus entailing a higher activity of each individual channel, but with a reduction in the total transmembrane current [96]. Other experimental studies in AF, like those performed by Bosch *et al.* in human [97] and by Laszlo *et al.* in rabbit [98], concluded that I_{CaL} was significantly reduced ($> 35\%$) in fibrillation conditions, thus entailing a notable shortening of the APDs and a decreased dependence of atrial repolarization on HR. Yue *et al.* investigated the effects of pacing for a long time in canine atria and concluded that I_{CaL} played a key role in the modulation of the "plateau" phase of the AP that was strongly attenuated under AF conditions [99]. In other studies that attempted to identify the contribution of I_{CaL} in human atrial cells to the value of APD, it was concluded that this ionic current had an important role in the autonomous control of the APD and its dependence on HR [100], in good agreement with the results obtained in this thesis showing I_{CaL} as a key mechanism modulating fast adaptation to HR.

The last of the ionic mechanisms involved in APD adaptation, as shown in this chapter, is the *NaK* pump, which has been the focus of a large number of investigations. This electrogenic pump interchanges three sodium ions from the intracellular space with two potassium ions from the extracellular space using the energy provided by ATP molecules (see section 1.2.4.4). Carmeliet described its relevance on atrial cardiac memory, mainly regulated by the intracellular sodium concentration ($[Na^+]_i$) [92, 101]. This dependence explains the fact that the pumping rate is very sensitive to the stimulation rate (an increase in the stimulation rate entails an increase in $[Na^+]_i$, resulting in a larger outward ionic current). According to the studies performed by Wang *et al.* [102] and Bers *et al.* [103], the *NaK* pump had lower activity in atrial cells than in ventricular cells (about 50% lower) due to the lower levels of certain subunits forming the proteins that make the function of electrogenic pump (*NaK*-ATPase). Furthermore, Bers *et al.* de-

scribed the numerous mechanisms of transport affecting intracellular sodium in cardiac cells and explained that the inhibition of the *NaK* pump had direct influence on the calcium transient, increasing its maximum peak due to the lower necessity of interchanging external sodium with internal calcium via the *NaCa* exchanger [103]. As regards cardiac memory, the importance of the *NaK* pump to APD adaptation at different HR was previously investigated in experiments with ventricular cardiomyocytes in dogs by Boyett *et al.*, who observed that the slow phase of adaptation practically disappeared after blocking the *NaK* pump with strophanthidin and ouabain [104]. Drake *et al.* described the relevance of the *NaK* pump on the APD shortening in canine ventricular cells when the HR was increased, stating that a higher activity of the *NaK* pump generated a higher density of outward current from the cell, thus leading to shorter APD values [105].

In addition to elucidating the ionic mechanisms underlying cardiac memory, an important point of this chapter focused on investigating how different cardiac memory was in cells from the atria and the ventricles. Cardiac memory is more pronounced in the atria, with both the fast and the slow phases of APD adaptation showing significantly longer time constants in comparison with ventricular cells [80]. The ionic mechanisms underlying cardiac memory are similar in both cavities in the slow phase of adaptation (intracellular sodium dynamics and *NaK* pump), but not in the fast phase (conductances of I_{CaL} and *NaCa* exchanger in the atria versus kinetics of I_{CaL} and I_{Ks} in the ventricles).

Another important objective of this study was to relate cardiac memory in human atria and arrhythmic risk. Simulation results show that protracted APD rate adaptation is associated with a higher risk of generation and maintenance of arrhythmias due to the increased likelihood of developing afterdepolarizations and the facilitation of reentrant arrhythmia stabilization. Our results are in good agreement with previous studies in canine atria where APD rate adaptation was evaluated in both normal and AF-induced conditions showing that protracted adaptation was strongly related to an increase in the probability of arrhythmia reactivation [81]. Furthermore, the slopes of APDR curves in conditions associated with prolonged cardiac memory are much shallower, which could favor the stability of reentries, as described in previous studies where CL oscillations effects on APD were analyzed [87].

3.4.1 Limitations of the Study

In this part of the thesis, the computational simulations were performed using two different models of human atrial cells: the Courtemanche model and the Nygren model. Each model has specific formulations for each ionic current and ionic concentration, thus entailing differences in the simulation results. Since both models were developed almost simultaneously, these differences come from the different nature and techniques of the experiments

they are based on. As a consequence, this has a significant influence on the relative importance of each ionic current with respect to the rest of them in each model, thus affecting the values of the transmembrane potential and, consequently, the AP, which is more triangular, shorter and with a less hyperpolarized resting potential. Nygren *et al.* thoroughly analysed the causes of the differences between the two models and observed that almost identical results can be obtained with both models if some ionic current conductances are weighted adequately [106]. Cherry *et al.* also studied both models and compared their results when applying the same stimulation protocols, concluding that both notably differ in some properties, [107, 108]. This is in good agreement with the results presented here showing quantitative differences in the analysis of cardiac memory with the Courtemanche model and the Nygren model, although both shared the same underlying ionic mechanisms.

On the other hand, in this chapter cardiac memory was studied in single cardiomyocytes and 1D fibers. However, muscle fibers in real patients are part of 2D tissues that are also part of the whole heart, therefore the effects on arrhythmia development or reentry maintenance may vary depending on the dimensionality of the study [109]. The extremely high computational cost associated to combine 3D simulations and the pacing protocol needed to assess cardiac memory made it practically unaffordable (one simulation could take a few weeks, depending on the simulation parameters and computing facilities). Nevertheless, APD rate adaptation in 1D fibers presents similar dynamics to single cells and therefore we would not expect large differences if the study was extended to 2D or 3D models.

Despite the mentioned limitations, the simulations performed in this study provide new insights into the ionic mechanisms involved in the adaptation of the APD to changes in HR in human atrial cells and 1D fibers that lay the foundations of the detailed analysis performed in the next episode where more electrophysiological properties and their mechanisms are investigated.

Chapter 4

Ionic Modulation of Electrophysiological Properties and Rotor Dynamics in Human Atria

4.1 Introduction

Despite the large number of studies focused on the investigation of AF mechanisms, these remain largely unknown. As described in Chapter 1, AF is considered to be a reentrant arrhythmia sustained by mechanisms including rapid ectopic activity (asynchronous excitation of cells usually around pulmonary veins), reentrant circuits (wavefronts of electrical propagation encountering excitable tissue due to different repolarization velocities between cardiac regions) and structural changes [44, 45]. Establishment and stability of reentrant circuits are favored by short refractory periods and slow conduction, enhanced by AF-induced electrical remodeling (AFER) caused by persistent AF [51]. Recent studies have stated that there are 4 general types of disturbances that promote ectopic firing and reentrant mechanisms, and include the following: (1) ion channel dysfunction, (2) calcium-handling abnormalities, (3) structural remodeling, and (4) autonomic neural dysregulation [110]. Monogenic causes of AF typically promote the arrhythmia via ion channel dysfunction, but the mechanisms of the more common polygenic risk factors are still poorly understood and under intense investigation [110].

Pharmacological management is still the main option for AF treatment [111], targeting modulation of excitability and refractoriness for rate or rhythm control [112]. Anti-arrhythmic Class I and Class III drugs are used to decrease excitability (by inhibiting the sodium current), and prolong the refractory period (by blocking potassium currents), respectively. Multichan-

nel action compounds such as amiodarone and dronedarone are commonly used but they exhibit limited efficacy and numerous adverse side effects [113]. Therefore, major breakthroughs are urgently needed for a more effective control of AF [113–117], which would benefit from a systems approach to drug development [118]. A large number of studies have provided insights into the ionic basis of atrial electrophysiology [107, 108, 117, 119–122]. Research has focused primarily on the role of either sodium or potassium channel block in modulating atrial electrophysiology [123, 124], and has often been performed in different animal species, usually either before or after AFER [51, 99]. Importantly, new agents such as vernakalant and dronedarone, and the commonly used amiodarone, all exhibit multichannel effects on a variety of sodium, potassium and calcium currents [125], and even NaK pump activity [126, 127]. However, very little is known about the relative importance of drug action on each current in modulating AF-related electrophysiology in human.

4.1.1 Objectives

The main objectives of this part of the thesis are the following:

1. Provide a systematic characterization of the relative importance of transmembrane ionic currents in modulating key electrophysiological properties and reentrant activity in human atrial tissue.
2. Assess the consequences of AF on the ionic modulators of human atrial electrophysiology.
3. Investigate the modulation of rotor inducibility and dynamics by alteration of key ionic current properties in SR and cAF conditions.
4. Aid in the identification of novel avenues for a more effective management of patients with AF and in the interpretation of existing findings.
5. Provide insight into differences in the response of atrial tissue to pharmacological interventions in short-term versus long-term AF.

4.2 Methods

4.2.1 Membrane Kinetics

Human atrial electrophysiology was simulated using the human atrial AP model proposed by Maleckar *et al.* [18] based on the original Nygren model [13]. The Courtemanche model [15] was also used to confirm model-independence

of the main results obtained in this chapter. Both models include formulations for the main transmembrane ionic currents in human atrial electrophysiology and detailed intracellular calcium dynamics, as well as homeostasis of the main ionic species involved in the course of the human atrial AP.

4.2.1.1 SR vs. AF-remodeled Cells

Default values and parameters in the models correspond to SR conditions. Specific model modifications were applied to simulate fibrillatory behavior and the corresponding electrical remodeling that accompanies permanent AF. Permanent AF was simulated by altering the following ionic properties [119, 121, 122, 128]: 70% reduction in L-type calcium current conductance (G_{CaL}); 50% reduction in transient outward current conductance (G_{to}); 50% reduction in ultrarapid delayed potassium current conductance (G_{Kur}); and 100% increment in inward rectifier potassium current conductance (G_{K1}).

4.2.2 Cell Simulations

Simulations were conducted for 20 min of periodic stimulation at a CL of 1000 ms [99], for default SR and permanent AF conditions. Furthermore, simulations following variations in conductances and gate time constants of ionic currents in a range between -100% and +300% were performed. The varied conductances included maximal value of the NaK pump current G_{NaK} , G_{K1} , G_{Kur} , G_{CaL} , maximal value of the NaCa exchanger current G_{NaCa} , G_{to} , fast inward sodium current conductance (G_{Na}), rapid delayed rectifier potassium conductance (G_{Kr}), and slow delayed rectifier potassium current (G_{Ks}). Ionic current kinetics of I_{Na} , I_{CaL} , I_{to} , I_{Kur} , I_{Kr} and I_{Ks} were also varied in the simulations, with varied parameters including activation and inactivation time constants of all gating variables. APD, measured at 90% repolarization (APD₉₀), and RMP were calculated.

The pacing protocol described in section 3.2.1.2 was applied to characterize APD rate adaptation through the calculation of τ_{fast} and τ_{slow} . The two APDR protocols described in section 3.2.1.2 were used to determine the S1S2 and the dynamic restitution curves, respectively. The maximal values of the slopes of the S1S2 and dynamic APD₉₀ restitution curves (S_{s1s2} and S_{dyn}) were computed, as they have been previously proposed as arrhythmic risk biomarkers related to rotor stability [86, 99]. In all single cell simulations, stimuli were of 2-ms duration and twice diastolic threshold amplitude (threshold is 750 pA for the Maleckar model, and 1000 pA for the Courtemanche model, for SR conditions).

4.2.3 Tissue Simulations

Tissue simulations were conducted to characterize the main determinants of RP, CV and rotor dynamics in human atrial tissue in SR and permanent AF conditions. Electrical propagation through atrial tissue was simulated using the monodomain equation with isotropic diffusion coefficient of $0.0013 \text{ cm}^2/\text{ms}$ in a homogeneous tissue, similar to those used in previous studies [107, 129]. Stimuli were of 2-ms duration and twice diastolic threshold amplitude (threshold is $0.025 \text{ pA}/\mu\text{m}^3$, for SR conditions with both the Maleckar and the Courtemanche models). RP and CV obtained from tissue simulations were evaluated in both SR and permanent AF for default conditions (i.e. original model parameters) and at different timings following the alteration of ionic currents properties (i.e. 1 s, 1, 3 and 5 min). In this study, a S1S2 protocol was chosen to determine the RP as in previous studies [51, 130]. Thus, RP was determined by applying a train of S1 stimuli (CL=1000 ms) at the center of a $1 \times 1 \text{ cm}^2$ tissue followed by an extra-stimulus (S2) at the same location for varying coupling intervals (CIs) (step of 1 ms). RP was defined as the shortest CI that ensured propagation following S2 [51, 56, 130]. The tissue size in the simulations was large enough to avoid boundary effects on RP measurements, as these were only noticeable in a strip of 0.25 cm close to the domain boundaries [131].

Additional simulations were conducted to determine ionic modulators of CV. As in [107, 131, 132], CV was measured in 1D simulations following a train of S1 stimuli (CL=1000 ms) at one end of a 1-cm long fiber. CV was calculated as the ratio between the distance separating two distant nodes (separated 0.1 cm) located at the center of the fiber, and the time taken by the wavefront to propagate between the two nodes following the last applied stimulus [51, 107, 131, 132]. This approach avoids measuring CV at locations that are too close to the domain boundaries, as well as to avoid further difficulties derived from front curvature [133]. No significant differences in CV were observed using longer fibers stimulated at CL=1000 ms.

Reentrant activity was initiated in $2\text{D } 5 \times 5 \text{ cm}^2$ atrial tissue by applying a cross-field stimulation protocol [134, 135]. As in previous studies [120, 136, 137], the choice of the 2D tissue geometry avoids confounding interpretation of the ionic mechanisms with added complexities such as structural and electrophysiological heterogeneities. A planar wavefront was initiated by a stimulus applied at the lower tissue edge, followed by another stimulus applied on a square area in the tissue bottom-left corner at a CI within the vulnerable window (VW). The limits of the VW for reentry were calculated as the shortest and the longest CI that resulted in sustained reentry (with a precision of 1 ms), whereas the width of the VW (W_{vw}) was obtained as the difference between both VW limits.

In this thesis, simulations were conducted using the Maleckar model to assess changes in reentrant activity occurring immediately (10 s) and 5 min

after each ionic alteration in SR and AF. Similar simulations were not conducted using the Courtemanche model due to the instability of the rotors in SR conditions, as stated in previous studies [107]. Tissue simulations were initialized using the steady-state values obtained in single cell simulations for default SR and AF conditions, and following 5 min of application of the corresponding ionic current alteration. Once established, rotors remained stable for all conditions simulated using the Maleckar model.

Corresponding pseudo-EGM (pEGM), measured with a virtual electrode located at the centre of the tissue, was calculated as in [138–140]. For the calculation of the DF, the pEGM signal was preprocessed with a fourth-order Butterworth band-pass-filter ($f_{c1}=40$ Hz; $f_{c2}=250$ Hz), followed by a signal-rectifier and finally a fourth-order Butterworth high-pass-filter ($f_c=20$ Hz) in order to minimize spectral components different from those of the main activation wavefront [141]. DF was obtained as the location of the maximum peak of the power spectral density of the preprocessed pEGM with a precision of 0.1 Hz. The trajectory of PS, defined as wavetips where all AP phases intersect, was calculated using the zero-normal-velocity condition [132].

4.2.4 Sensitivity Analysis

In order to ascertain the role played by ionic properties on human atrial electrophysiological markers, a sensitivity analysis was performed. Absolute and relative sensitivities for each of the markers to changes in each of the ionic properties (ionic current conductances and time constants of the gating variables) were calculated as in the study of Romero *et al.* [142]. In brief, the absolute sensitivity $S_{m,p}$ of each marker m to $\pm 30\%$ changes in an ionic property p was calculated as:

$$S_{m,p} = \frac{C_{m,p,+30\%} - C_{m,p,-30\%}}{0.6 C_{m,p,\pm 0\%}} 100, \quad (4.1)$$

where $C_{m,p,+30\%}$ and $C_{m,p,-30\%}$ are the values for the marker m after 30% increase and decrease in the value of a certain ionic property p , respectively; $C_{m,p,\pm 0\%}$ is the value for the marker m when no ionic properties are varied. Therefore, $S_{m,p}$ reflects the extent to which the marker m changes when the ionic property p is altered from -30% to +30% (i.e. by 60%). For each marker m , the maximum sensitivity amongst all property variations was defined as $\max_p\{S_{m,p}\}$. Relative sensitivities, $R_{m,p}$, for each marker m to changes in each ionic property p were calculated as:

$$R_{m,p} = \left| \frac{S_{m,p}}{\max_p\{S_{m,p}\}} \right|, \quad (4.2)$$

Therefore, $R_{m,p}$ gives an indication of the relative importance of each ionic property p in modulating marker m .

In this thesis, the sensitivity analysis was performed to assess similarities and differences in the ionic mechanisms underlying cell and tissue markers between SR and permanent AF conditions.

4.3 Results

4.3.1 Electrophysiological Markers Related to Arrhythmic Risk in SR versus AF

Figure 4.1 shows the time course of the steady-state AP and the main underlying ionic currents in SR and AF atrial cardiomyocytes, using the Maleckar model (left) and the Courtemanche model (right). In both models, AF results in shortening of APD₉₀ and slight RMP hyperpolarization, consistent with previous experimental and theoretical human atrial studies [108, 120, 143]. Steady-state APD₉₀ shortens from 200 ms in SR to 115.8 ms in AF in simulations using the Maleckar model and from 252 ms to 115.5 ms using the Courtemanche model.

Differences in APD₉₀ restitution properties between SR and permanent AF were also characterized using both AP models (Figure 4.2). Permanent AF results in flattening of the maximum slope in both S1S2 and dynamic restitution curves with the Maleckar model (S_{s1s2} is 0.63 in SR and 0.31 in AF, whereas S_{dyn} is 0.37 in SR and 0.23 in AF). With the Courtemanche model, the maximum slope of the dynamic restitution slope also flattens due to AF, but the S1S2 restitution curve is steeper in AF than in SR (S_{s1s2} is 0.44 in SR and 1.3 in AF, whereas S_{dyn} is 0.28 in SR and 0.16 in AF). AF-induced flattening of the restitution curves is consistent with previous studies showing that patients with persistent AF exhibit shallower restitution slopes than those with paroxysmal AF [86].

Tissue simulations also showed that AF results in alterations in RP and CV, with qualitatively similar results in both models. AF-induced changes in APD₉₀ and RMP result in a decrease of RP: RP decreases from 217 ms in SR to 147 ms in AF with the Maleckar model, and from 270 ms in SR to 124 ms in AF with the Courtemanche model, in agreement with clinical studies on chronic AF patients [144, 145]. In contrast, AF-induced changes in ionic currents lead to only a slight decrease in steady-state CV from 47.97 cm/s in SR to 46.17 cm/s in AF, using the Maleckar model, and from 58.14 cm/s in SR to 56.38 cm/s using the Courtemanche model. This decrease in steady-state CV in AF is in agreement with results in clinical studies [128, 146] and quantitatively consistent with those reported in previous theoretical AF studies [107].

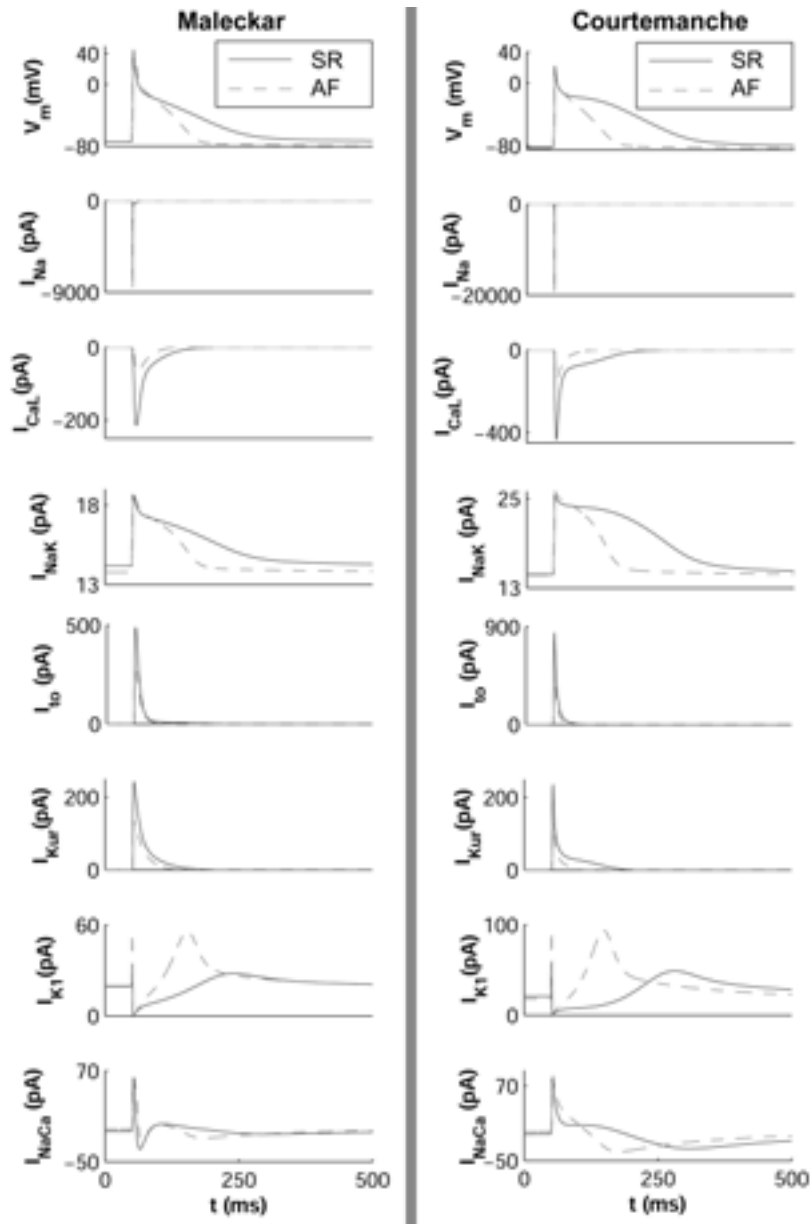


Figure 4.1: Steady-state AP and ionic currents under SR conditions (solid line) and permanent AF conditions (dashed line) at CL=1000 ms using the Maleckar (left) and the Courtemanche (right) human atrial AP models.

4.3.2 Role of Ionic Currents in Modulating Human Atrial Electrophysiological Markers

4.3.2.1 Role of Ionic Currents in Modulating Steady-state AP

Computer simulations were conducted as described in section 4.2 to investigate the relative importance of ionic current conductances and kinetics in

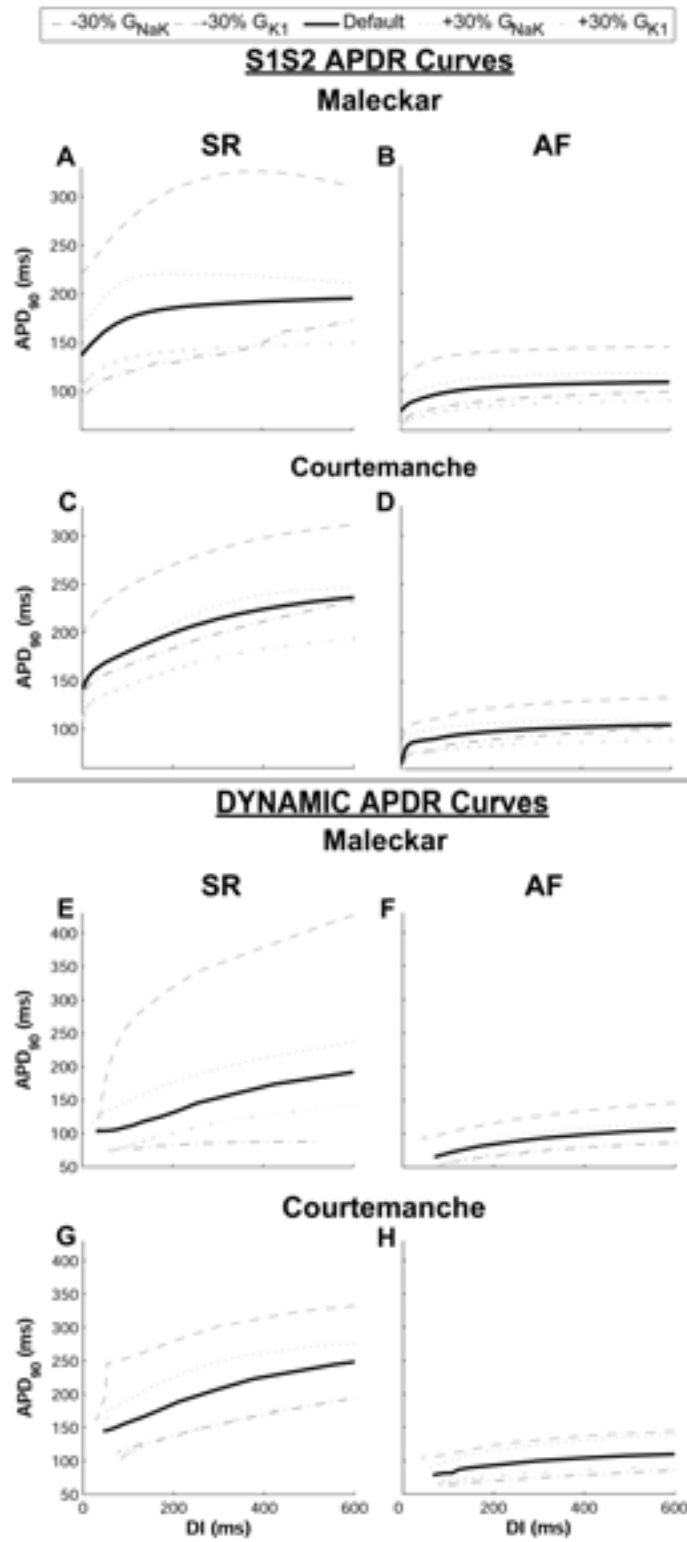


Figure 4.2: APDR curves obtained using the S1S2 (top) and dynamic (bottom) protocols, in SR (left) and permanent AF conditions (right) with the Maleckar and the Courtemanche models for default values and following $\pm 30\%$ alterations in G_{NaK} and G_{K1} .

modulating human atrial electrophysiology in SR and permanent AF. Figure 4.3 shows changes in steady-state AP induced by alterations in ionic conductances for SR (top) and AF (bottom) using the Maleckar model. Alterations in time constants, i.e. activation and inactivation kinetics of ionic currents, were also evaluated but results showed only small effects, i.e. $<10\%$, in the investigated human atrial electrophysiological properties (APD_{90} , RMP, S_{s1s2} , S_{dyn} , RP, CV) both in SR and AF.

In SR and AF, alterations in G_{K1} and G_{NaK} resulted in the largest AP changes (Figures 4.3 and 4.4 for the Maleckar model and Figure 4.5 for the Courtemanche model). G_{K1} inhibition resulted in significant APD_{90} prolongation and RMP depolarization (Figure 4.3A and 4.3A' and Figure 4.4A-D for the Maleckar model; Figure 4.5A-D for the Courtemanche model). This is caused by a decrease in the total outward current and is in agreement with previous studies [147, 148]. Interestingly, G_{NaK} inhibition results in APD_{90} shortening and RMP elevation (Figure 4.3B and 4.3B' and Figure 4.4A-D for the Maleckar model; Figure 4.5A-D for the Courtemanche model), in agreement with experiments conducted in atrial tissue from patients treated with digoxin [149]. The causes underlying this counterintuitive effect will be further described in section 4.3.3. As shown in Figure 4.4A-D for the Maleckar model and 4.5A-D for the Courtemanche model, the relative relevance of other conductances, such as G_{Na} , G_{Kur} , G_{CaL} and G_{to} , on steady-state APD_{90} is considerably lower than that of G_{K1} and G_{NaK} , both in SR and AF (with the exception of the effect of G_{CaL} in AF using the Courtemanche model, which is possibly explained by the larger magnitude of I_{CaL} in this model (Figure 4.1)). Simulations were repeated at a shorter CL value (CL=500 ms) with the two models, confirming that G_{NaK} and G_{K1} are the properties exerting the maximum influence in modulating APD_{90} and RMP in human atrial cells for both stimulation rates.

Whereas, in most cases, ionic alterations resulted in similar effects in SR and AF, some differences were identified. Firstly, changes caused by ionic alterations were overall smaller in AF than in SR (Figures 4.4 and 4.5, using the Maleckar and the Courtemanche model, respectively). Secondly, the effect of a 30% inhibition of G_{NaK} implied opposite changes in RMP in SR (slight hyperpolarization) and AF (depolarization) (panels C and D in Figures 4.4 and 4.5). Larger degrees of G_{NaK} inhibition ($>50\%$) however led to RMP depolarization both in control and AF (Figure 4.3B and 4.3B'). G_{NaK} upregulation resulted in insignificant changes in RMP in SR, but in larger RMP depolarization in AF.

4.3.2.2 Role of Ionic Currents in Modulating APD Restitution

Simulations using the two human atrial AP models were also conducted to investigate the ionic mechanisms modulating S1S2 and dynamic APD restitution properties (Figure 4.2, Figure 4.4E-H for the Maleckar model and

Figure 4.5E-H for the Courtemanche model). Simulations using the two models highlight G_{K1} and G_{NaK} as the main modulators of APD restitution properties (S_{s1s2} and S_{dyn}), in SR and AF. Results obtained with the two models were qualitatively similar but differences in the sensitivity of restitution properties to changes in ionic currents were observed. Firstly, the sensitivity of S_{dyn} to changes in G_{NaK} and, most notably, G_{K1} (ΔS_{dyn}) was high in both models, but larger in the Maleckar than in the Courtemanche model (Figure 4.4G and 4.5G). Furthermore, S_{s1s2} sensitivity to changes in ionic currents (ΔS_{s1s2}) in AF was significantly larger in simulations using the Courtemanche than the Maleckar model (Figure 4.4F and 4.5F). Finally, G_{CaL} inhibition resulted in a large increase in S_{s1s2} with the Courtemanche model, possibly explained by the larger magnitude of I_{CaL} in this model, as mentioned above (Figure 4.1).

4.3.2.3 Quantification of Sensitivity of Atrial Electrophysiology Markers to Changes in Ionic Currents

In order to investigate the relative importance of each ionic current in the modulation of atrial electrophysiology in SR and AF, the effect of changes in ionic current conductances and kinetics on electrophysiological markers was evaluated by calculating absolute and relative sensitivities as described in section 4.2.4. Results are depicted in Tables 4.1 and 4.2 for SR and permanent AF, respectively, with the Maleckar model. Relative sensitivities for each combination of marker (first column) and ionic property (first row) are shown in a grey scale. The markers studied in this sensitivity analysis were: APD_{90} , RMP, time constants of the APD adaptation to changes in HR (τ_{fast} and τ_{slow}), S_{s1s2} , S_{dyn} , RP, CV and WL (calculated as the product of RP and CV). The maximum sensitivity for each marker is shown as a percentage in each of the black boxes, corresponding to the ionic property exerting the strongest influence on the marker. The sensitivity analysis included variations in ionic current conductances and gate time constants. However, gate time constants and some conductances, e.g. G_{Kr} and G_{Ks} , did not result in major alterations in the analyzed markers ($R_{m,p} < 0.2$) and therefore only significant results for sensitivity to ionic current conductances are shown in Tables 4.1 and 4.2.

Both SR and AF simulations show that G_{K1} is the ionic property exerting the strongest influence on most electrophysiological markers in human atria. In most cases, dependency of markers on ionic current properties was similar in SR and AF but to different extents, being absolute sensitivities smaller in AF than in SR.

As shown in Tables 4.1 and 4.2, the main modulator of steady-state APD_{90} and RMP is G_{K1} in both SR and AF conditions, in good agreement with the results shown in section 4.3.2 and in accordance with experimental studies showing the relevance of this current in atrial electrophysiology [148].

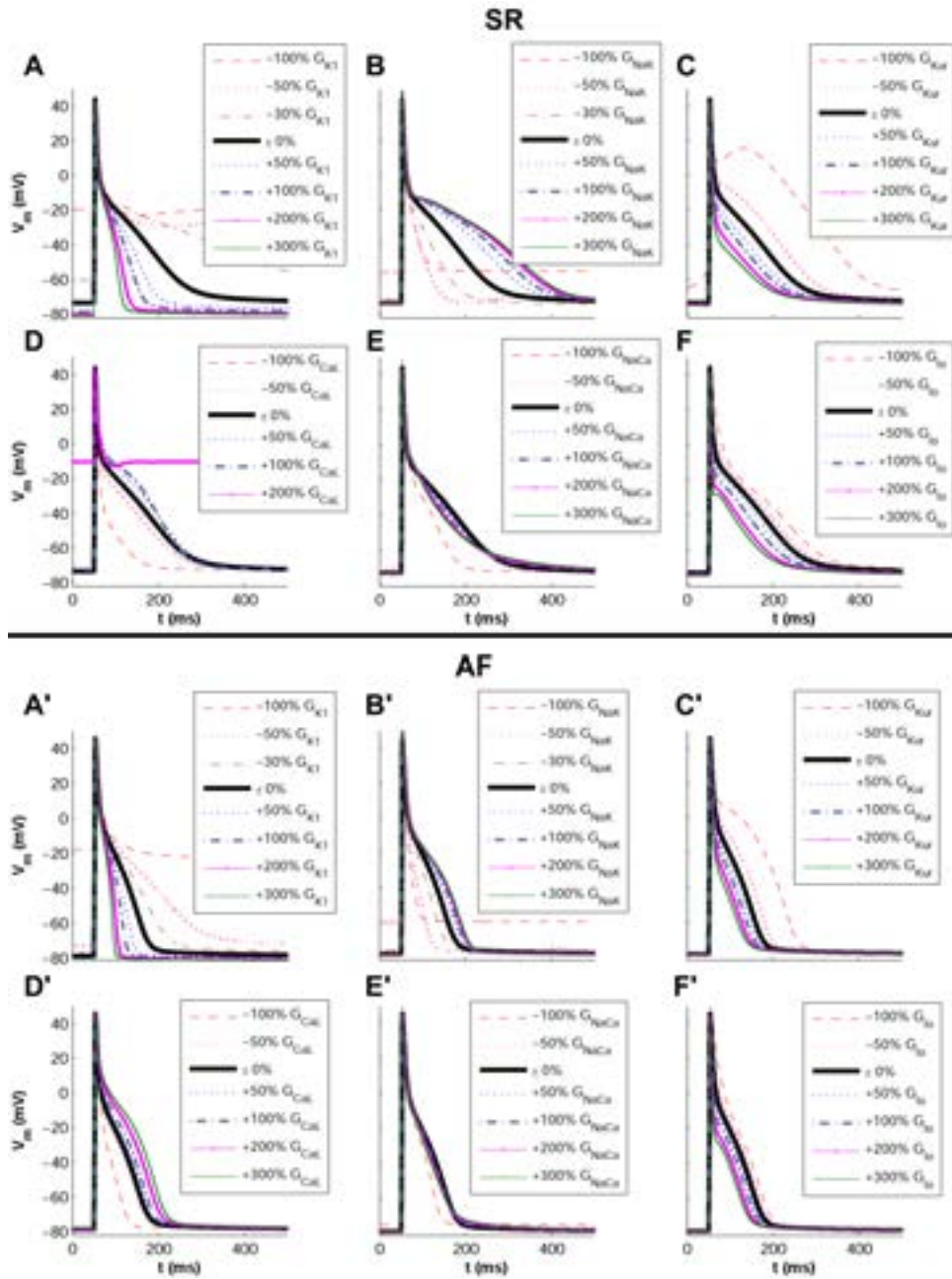


Figure 4.3: Steady-state human atrial AP in SR (top) and AF (bottom) for default ($\pm 0\%$) and following alterations in G_{K1} (panels A, A'), G_{NaK} (panels B, B'), G_{Kur} (panels C, C'), G_{CaL} (panels D, D'), G_{NaCa} (panels E, E') and G_{to} (panels F, F'), using the Maleckar model.

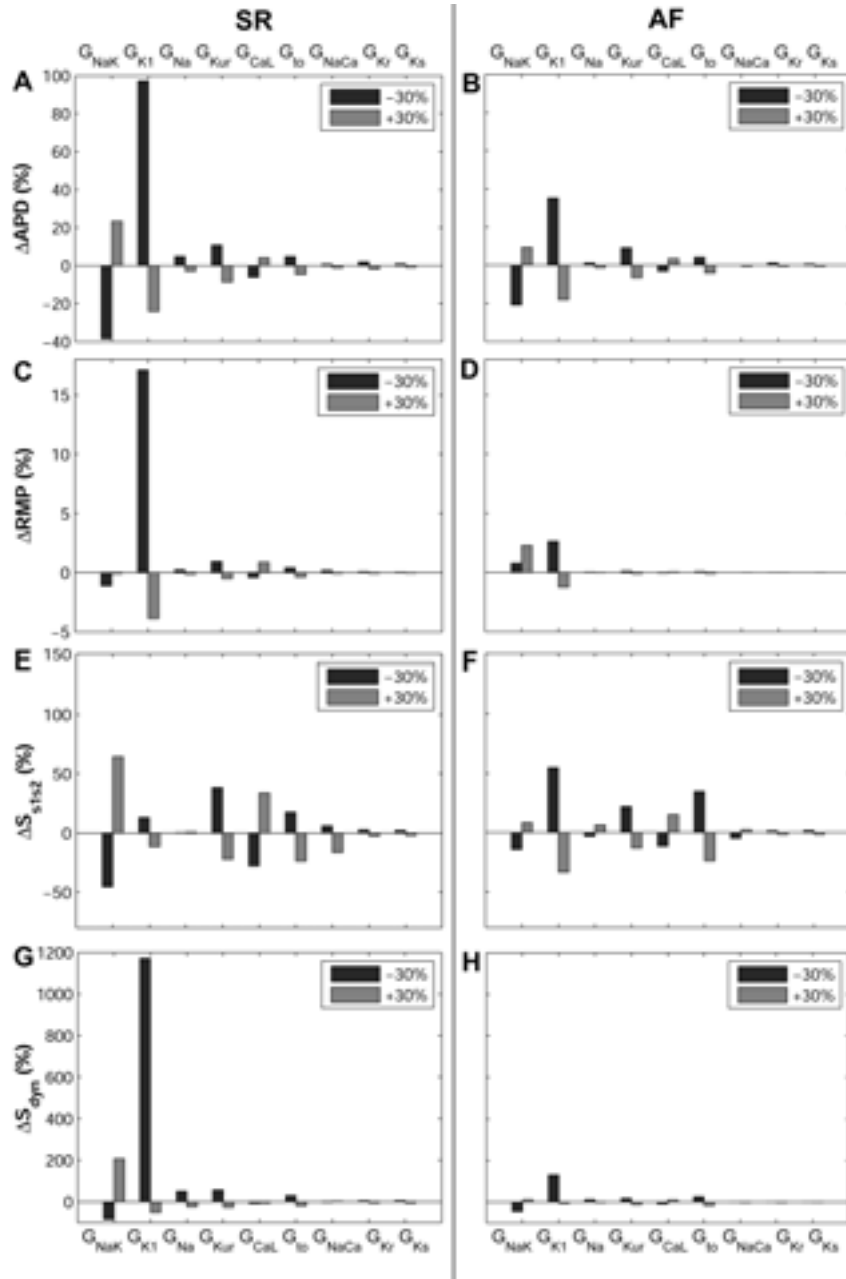


Figure 4.4: Percent changes in steady-state APD_{90} (ΔAPD_{90} , A-B), RMP (ΔRMP , C-D), S_{s1s2} (ΔS_{s1s2} , E-F) and S_{dyn} (ΔS_{dyn} , G-H) with respect to default conditions produced by $\pm 30\%$ alterations in ionic conductances for SR (left) and AF (right) using the Malekar model.

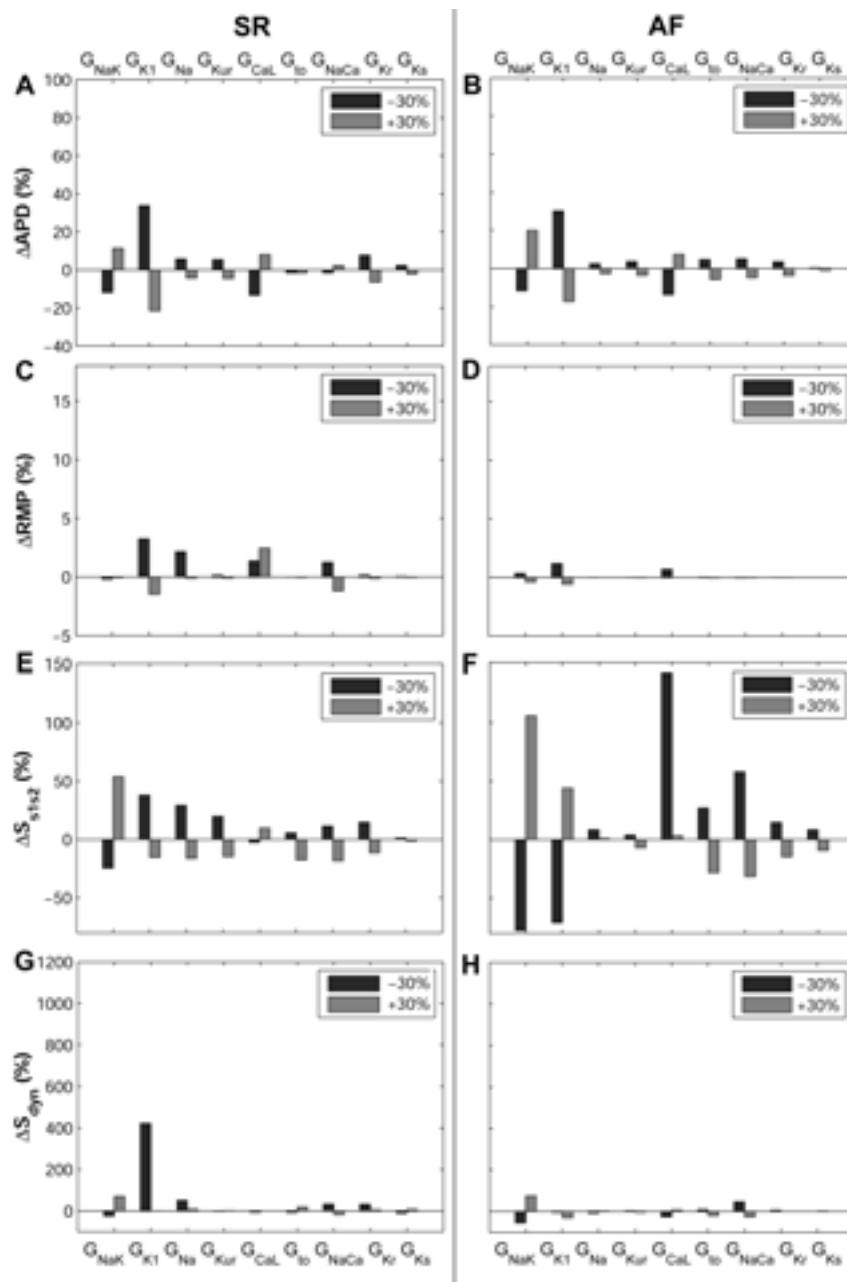
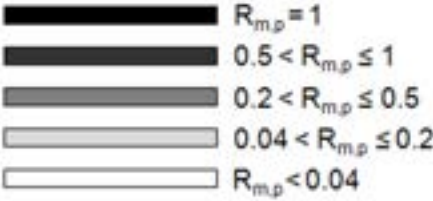


Figure 4.5: Percent changes in steady-state APD_{90} (ΔAPD_{90} , A-B), RMP (ΔRMP , C-D), S_{s1s2} (ΔS_{s1s2} , E-F) and S_{dyn} (ΔS_{dyn} , G-H) with respect to default conditions produced by $\pm 30\%$ alterations in ionic conductances for SR (left) and AF (right) using the Courtemanche model.

Table 4.1: Absolute and relative sensitivities in SR conditions obtained from cell and tissue simulations. The highest absolute sensitivities of each marker (listed in the first column) to changes in ionic conductances (listed in the first row) are shown as a % of change. Negative values are represented as "-". Relative sensitivities, $R_{m,p}$, are calculated for each marker and shown in a grey scale.

	G_{K1}	G_{NaK}	G_{Na}	G_{Kur}	G_{CaL}	G_{NaCa}	G_{to}
APD ₉₀	-141%		-	-		-	-
RMP	28%		-		-		
τ_{fast}			-	-	-1598%	-	-
τ_{slow}		-1005%			-		
S_{s1s2}	-			-92%		-	-
S_{dyn}	-1364%		-	-			-
RP	-74%	-	-	-			-
CV	-	-	71%				-
WL	-82%	-		-			-



$R_{m,p} = 1$
 $0.5 < R_{m,p} \leq 1$
 $0.2 < R_{m,p} \leq 0.5$
 $0.04 < R_{m,p} \leq 0.2$
 $R_{m,p} < 0.04$

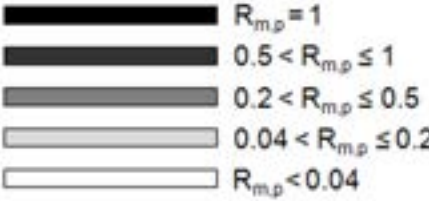
Other ionic mechanisms such as G_{NaK} were proven to be important for APD₉₀ and RMP as well, although their influence was not as strong as G_{K1} .

Regarding APD rate adaptation, we found that τ_{fast} was highly sensitive to G_{CaL} and G_{Kur} in SR with the Maleckar model (Table 4.1), in contrast with the results shown in chapter 3 with the Courtemanche model where G_{CaL} and G_{NaCa} were the main modulators of the fast phase of adaptation in SR conditions. However, the induced reduction in G_{CaL} and G_{Kur} in AF conditions resulted in G_{NaK} exerting the strongest influence on τ_{fast} (Table 4.2). Furthermore, G_{NaK} was the parameter playing the most important role in determining τ_{slow} , both in SR and AF (Tables 4.1 and 4.2), in good agreement with the results shown in chapter 3 with the Courtemanche model and with previous studies in human ventricular cells [80, 142].

Notable differences were found in the ionic mechanisms determining APDR slopes in SR and AF conditions. In SR, S_{s1s2} was similarly dependent on

Table 4.2: Absolute and relative sensitivities in AF conditions obtained from cell and tissue simulations. The highest absolute sensitivities of each marker (listed in the first column) to changes in ionic conductances (listed in the first row) are shown as a % of change. Negative values are represented as "-". Relative sensitivities, $R_{m,p}$, are calculated for each marker and shown in a grey scale.

	G_{K1}	G_{NaK}	G_{Na}	G_{Kur}	G_{CaL}	G_{NaCa}	G_{to}
APD ₉₀	-88%		.	.			.
RMP	6%						
T _{fast}		-154%
T _{slow}		-156%		.	.		.
S _{s1s2}	-92%			.			.
S _{dyn}	-151%	
RP	.	.	-61%	.			.
CV	.	.	72%				
WL	-56%	.		.			.



$R_{m,p} = 1$
 $0.5 < R_{m,p} \leq 1$
 $0.2 < R_{m,p} \leq 0.5$
 $0.04 < R_{m,p} \leq 0.2$
 $R_{m,p} < 0.04$

G_{Kur} , G_{K1} , G_{CaL} and G_{NaK} (Table 4.1), in agreement with previous studies showing important changes in S1S2 restitution curves with variations in G_{Kur} , G_{K1} , G_{CaL} and G_{to} . In AF, G_{K1} was the most important contributor to S_{s1s2} , with G_{NaK} playing a secondary role (Table 4.2). G_{K1} and, to a lesser extent G_{NaK} , were key in determining S_{dyn} in both SR and AF (Tables 4.1 and 4.2).

Interesting differences between SR and permanent AF were observed in the sensitivity of RP to changes in ionic current properties. In SR, RP was highly sensitive to G_{K1} and G_{NaK} , due to the dependence of APD₉₀ and RMP on those conductances (Table 4.1), in good agreement with previous human simulation studies [148]. Changes in G_{Na} , G_{CaL} and G_{Kur} also led to significant alterations in RP. In AF, however, G_{Na} was the ionic property with the strongest influence on RP followed by G_{K1} (Table 4.2).

As expected, due to the close relationship between G_{Na} and cellular excitability [56, 150], CV was mainly determined by G_{Na} in both SR and

AF with similar absolute sensitivities, whereas the influence of other ionic mechanisms on CV was insignificant (Tables 4.1 and 4.2).

Interestingly, WL was strongly affected by G_{K1} and, to a lesser extent, G_{NaK} in both SR and AF. The importance of G_{Na} in modulating WL was however reduced by the fact that it led to opposite-sign effects in RP and CV (Tables 4.1 and 4.2)[56, 150].

4.3.3 Temporal Adaptation of Human Atrial Electrophysiological Markers to Changes in Ionic Currents

Simulation results shown in the previous section highlight the importance of G_{NaK} and G_{K1} in modulating steady-state AP and restitution properties using two human atrial models, but the transient response of these properties is important to determine underlying causes of the steady-state values obtained, particularly in those cases presenting counterintuitive results such as G_{NaK} inhibition. An analysis of the temporal evolution of electrophysiological properties following ionic current alterations showed that atrial electrophysiological properties do not adapt instantaneously. Both the time required to complete the adaptation and the temporal evolution of the analyzed properties strongly depended on the specific ionic current being altered. Figure 4.6 illustrates the temporal evolution of human atrial AP properties (APD_{90} and RMP) following $\pm 30\%$ changes in ionic currents in SR (Figure 4.6A, 4.6C) and AF (Figure 4.6B, 4.6D) using the Maleckar model. The effects of ionic changes in modulating the temporal evolution of RP and CV were also investigated, as shown in Figure 4.6E-H. In these simulations, alterations in G_{NaK} , G_{K1} and G_{Na} were considered, since G_{NaK} and G_{K1} were identified as the main modulators of steady-state repolarization properties in our study and G_{Na} has been shown to have an important effect on atrial conductivity [151]. Alterations in ionic conductances other than G_{NaK} , G_{K1} and G_{Na} led to a fast adaptation response and small changes in the investigated properties and are therefore not shown.

As shown in Figure 4.6, RP and CV values could not be obtained following 5 min of I_{K1} blockade due to repolarization failure and subsequent propagation failure (panels E and G). This was caused by the gradual accumulation of electrotonic effects associated with the propagation of the triangular atrial AP. In this setting, the electrotonic current resulted in a net inward current opposing the outward potassium currents during the repolarization phase of the AP, which eventually resulted in repolarization failure. This was observed using the two models, although with a smaller degree of I_{K1} blockade in the Maleckar than in the Courtemanche model, due to the smaller contribution of I_{K1} to repolarization reserve in the Courtemanche model. RP and CV results computed with the Courtemanche model were qualitatively similar to those obtained with the Maleckar model, but the relative importance of G_{Na} in modulating RP in AF was slightly decreased

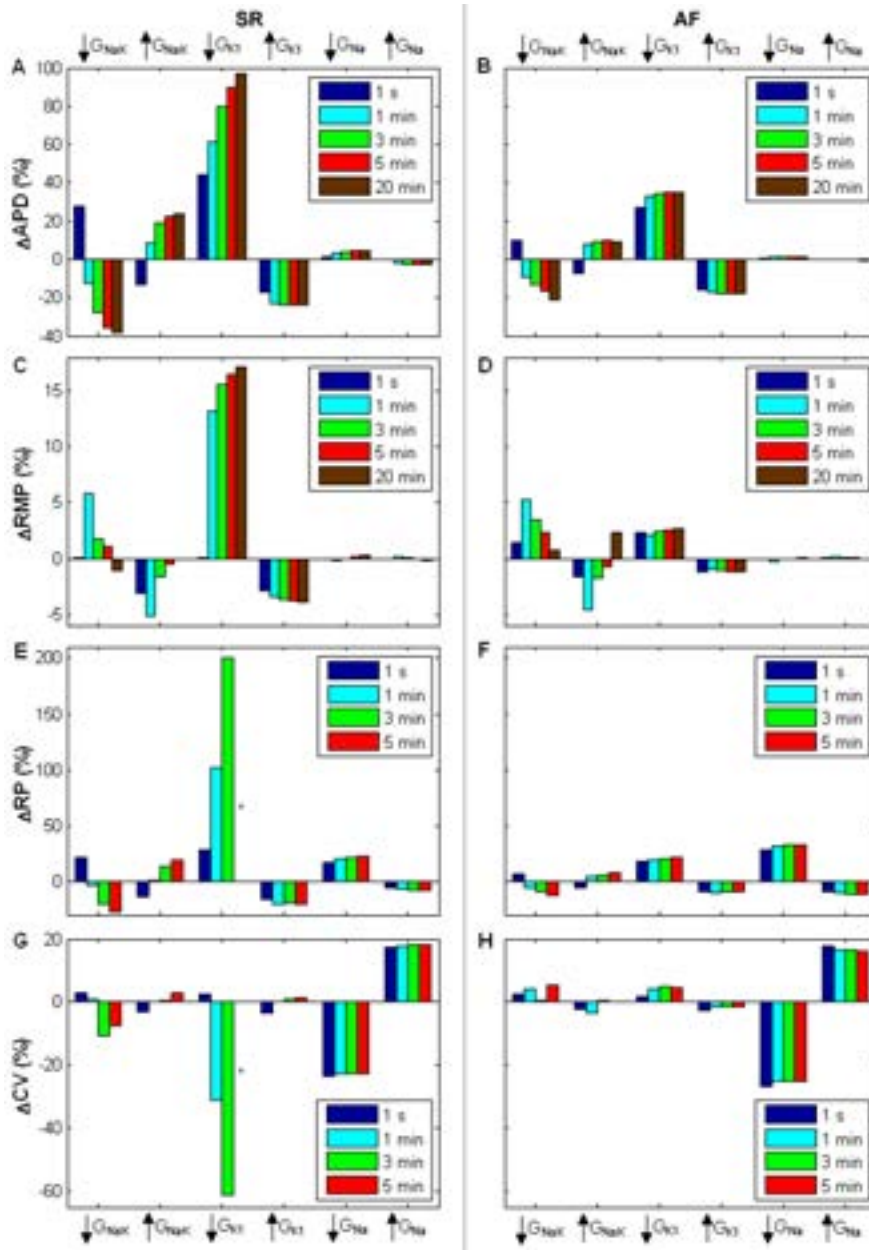


Figure 4.6: Temporal adaptation of percent changes in APD_{90} (ΔAPD_{90} , A-B) and RMP (ΔRMP , C-D), for single cell simulations, RP (ΔRP , E-F), for 2D tissue simulations, and CV (ΔCV , G-H), for 1D fiber simulations, with respect to default conditions during $\pm 30\%$ alterations in G_{NaK} , G_{K1} and G_{Na} in SR (left) and AF (right) using the Maleckar model. *Note: Following 5 min of G_{K1} 30% block repolarization fails.

(not shown).

Results in Figure 4.6 show that in most cases, alterations in ionic conductances resulted in monotonic changes in electrophysiological properties. Changes in G_{K1} and G_{Na} led to monophasic alterations in APD_{90} , RP, and CV. However, as shown in Figure 6, G_{NaK} block resulted in biphasic changes in APD_{90} and RP, with an initial prolongation followed by a progressive decrease. Increase in G_{NaK} led to an initial decrease in APD_{90} and RP followed by a progressive increase in those properties. The biphasic effect of altering G_{NaK} was also observed in RMP and CV (Figure 4.6). This transient behavior following G_{NaK} alterations also occurred for $CL=500$ ms and using the Courtemanche model (not shown). The APD_{90} and RP shortenings caused by a decrease in G_{NaK} can appear counterintuitive because inhibition of an outward current would be expected to prolong APD_{90} , as stated in [101] and as shown shortly after administration of ouabain [152]. However, in agreement with our results, strong blockade of NaK pump using strophanthidin has been shown to result in initial APD_{90} lengthening followed by a progressive shortening [16, 153, 154]. Figure 4.7 illustrates the ionic mechanisms involved in the biphasic AP changes induced by G_{NaK} inhibition. G_{NaK} block resulted in an initial APD_{90} lengthening caused by a decrease in the NaK pump outward current. However, sustained G_{NaK} block resulted in intracellular Na^+ (Figure 4.7B) and, to a lesser extent, diastolic and systolic Ca^{2+} accumulation (Figure 4.7C), which favored the outward component of the NaCa exchanger (Figure 4.7D), slightly prolonged the open state of the calcium-dependent inactivation gating variable of I_{CaL} (Figure 4.7E), and thus resulted in APD_{90} shortening (Figure 4.7A). Slight changes were therefore observed in I_{CaL} current (Figure 4.7E), whereas the amplitudes of the currents between sarcoplasmic reticulum (SRet) and intracellular space, such as the SRet calcium uptake current (I_{up} , Figure 4.7F) and the SRet calcium release current (I_{rel} , Figure 4.7G), were slightly increased, entailing the slight Ca^{2+} accumulation shown in Figure 4.7C (systolic intracellular Ca^{2+} increases $0.1 \mu M$, whereas diastolic Ca^{2+} increases $0.03 \mu M$).

4.3.4 Reentrant Activity in Human Atrial Tissue and Role of Ionic Currents in its Modulation

4.3.4.1 Ionic Modulation of DF and Stability of Reentrant Arrhythmias

The impact of the mechanisms unraveled in section 4.3.2.3 in the modulation of rotor dynamics in atrial tissue was investigated in this section. Simulations showed that after 10 seconds, DF increased from 3.52 Hz in SR to 7.2 Hz in AF, as shown in Figure 4.8, in agreement with previous clinical and theoretical studies [120, 155, 156].

Since G_{NaK} , G_{K1} and G_{Na} have been shown in this thesis to be the

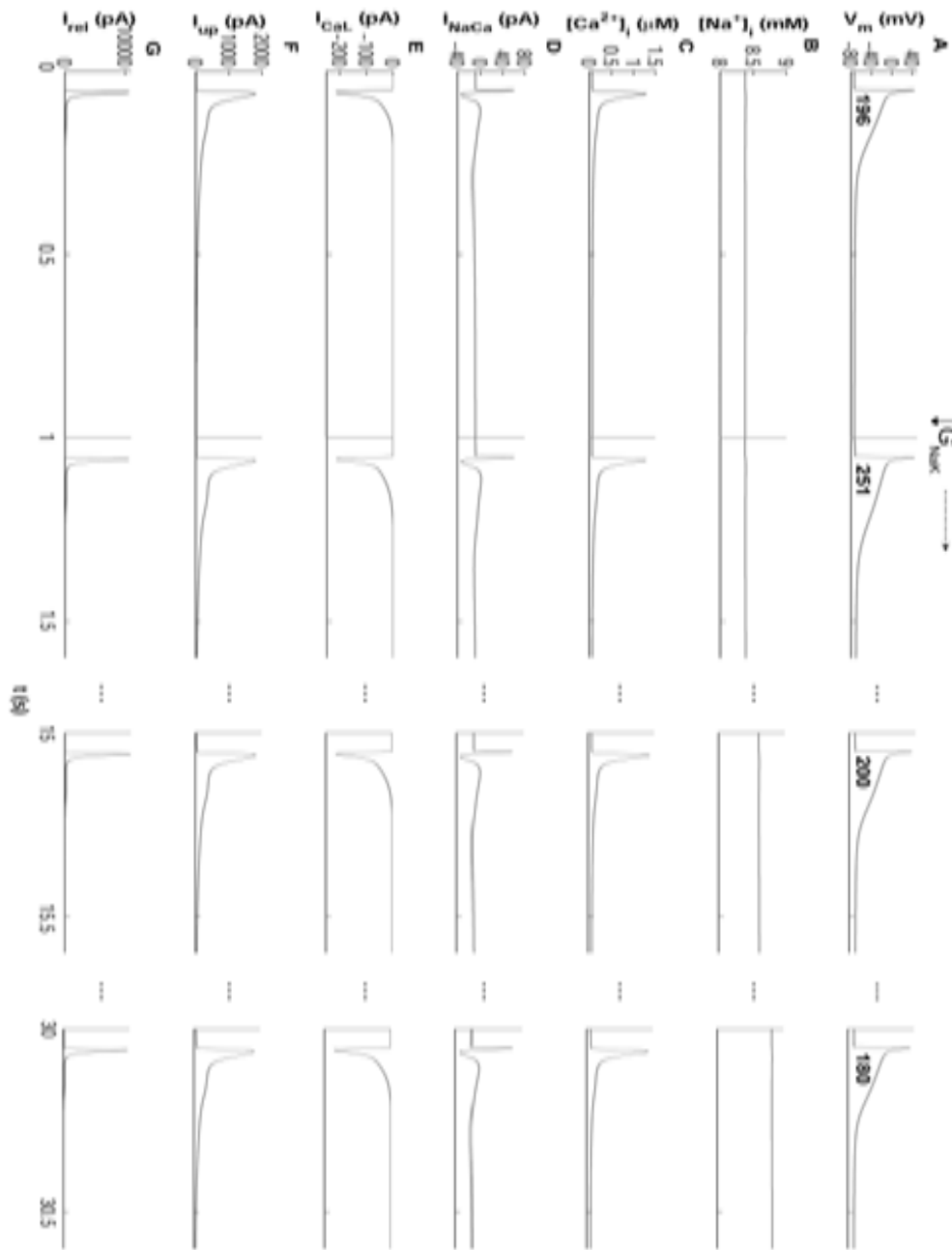


Figure 4.7: Time course of AP (A), $[Na^+]_i$ (B), $[Ca^{2+}]_i$ (C), I_{NaCa} (D), I_{CaL} (E), I_{up} (F) and I_{rel} (G) for default conditions (left), and following 15 s and 30 s after 30% G_{NaK} block using the Maleckar model. APD90 values are shown in bold for each AP.

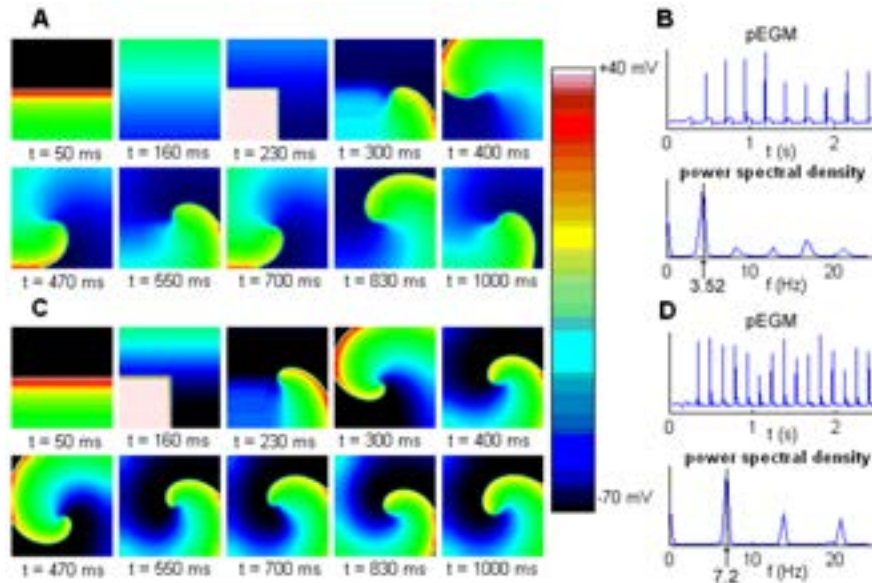


Figure 4.8: Reentrant activity in 2D $5 \times 5 \text{ cm}^2$ atrial tissue. A: Snapshots showing V_m distribution for different timings during the application of a S1S2 cross-stimulation protocol in SR. B: pEGM and power spectral density corresponding to the simulation shown in A. C: Snapshots showing V_m distribution for different timings during the application of an S1S2 cross-stimulation protocol in AF. D: pEGM and power spectral density corresponding to the simulation shown in C.

main ionic mechanisms involved in RP, CV and WL modulation, the effects of their alterations on reentrant dynamics were investigated. Figure 4.9 describes changes in DF values and rotor dynamics with respect to default conditions obtained after 10 s and 5 min of alterations in G_{NaK} , G_{K1} and G_{Na} in both SR (Figures 4.9A and C) and AF (Figures 4.9B and D), using the Maleckar model. Consistent with the results described in previous sections, simulations of rotor dynamics showed that: (i) G_{NaK} , G_{K1} and G_{Na} alterations were the interventions exerting the strongest influence on rotor dynamics; (ii) G_{NaK} , G_{K1} or G_{Na} inhibitions had larger effects on reentrant dynamics than their corresponding upregulations; (iii) alterations in the rest of ionic conductances entailed negligible effects on DF; (iv) the main difference found between control and AFER was an enhanced relevance of G_{Na} in AF and a decreased relevance of G_{K1} in AF.

Simulations showed that G_{NaK} , G_{K1} and G_{Na} block led to a decrease in DF values in both control and AFER immediately after the block. In the case of G_{K1} and G_{Na} block, the change in DF was monophasic, resulting in lower values following 5 min of block. The most significant changes occurred

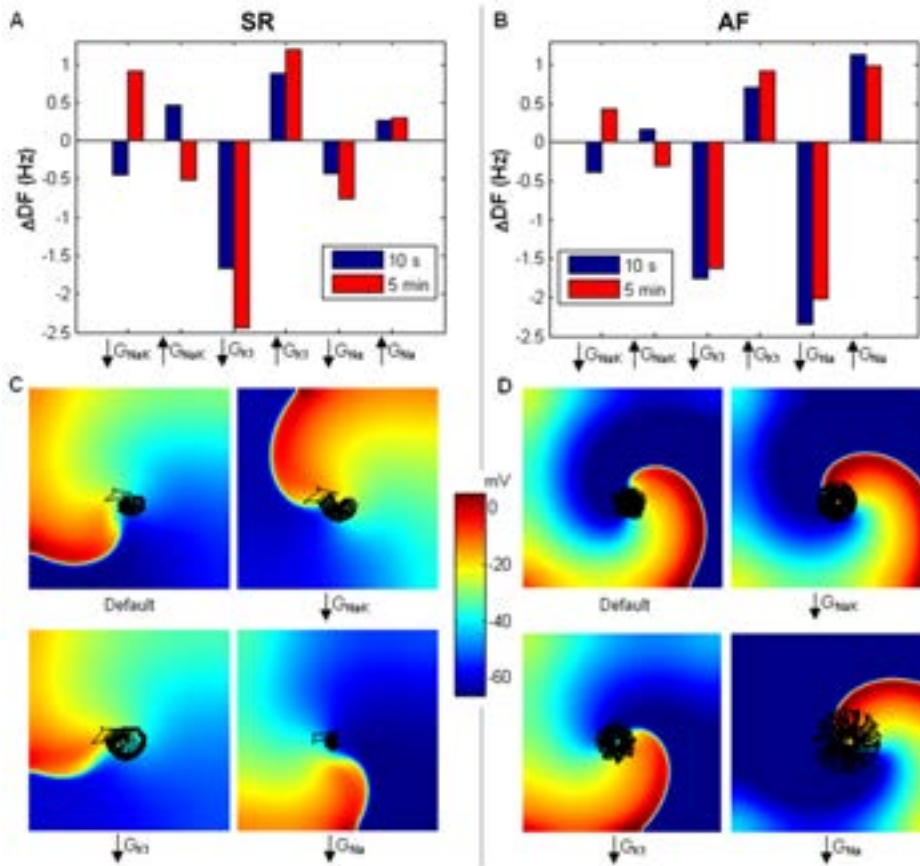


Figure 4.9: Percent changes in DF (ΔDF) with respect to default conditions produced by $\pm 30\%$ alterations in G_{NaK} , G_{K1} and G_{Na} in SR (A) and AF (B) using the Maleckar model. DF values are shown for reentry initiated at 10 s (blue bars) and 5 min (red bars) following changes in ionic parameters. Snapshots of reentry 10 s after the change in ionic parameters under default conditions and 30% block of G_{NaK} , G_{K1} and G_{Na} in SR (C) and AF (D). Black lines on snapshots represent the corresponding PS trajectories.

in two cases. Firstly, G_{K1} block in SR led to an immediate decrease in DF with respect to default conditions (Figure 4.9A). Secondly, G_{Na} block in AF resulted in a decrease in DF (Figure 4.9B). These effects were explained by the relative importance of G_{K1} and G_{Na} in modulating RP and CV in SR and AF, respectively, as highlighted in Figure 4.6E-H. As expected from the results shown in the previous section, alterations in G_{NaK} resulted in biphasic temporal changes in DF. A decrease in G_{NaK} initially decreased DF, but then led to an increase following 5 min block. An increase in G_{NaK} had the opposite effect (Figures 4.9A and B).

Figures 4.9C and D further illustrate alterations in reentrant dynamics following G_{NaK} , G_{K1} and G_{Na} inhibition. The surface area traced out by the PS over its trajectory under default SR conditions was 0.36 cm^2 . Figure 4.9C shows enlargement of the PS meandering in control after 30% block of G_{NaK} or G_{K1} , whereas 30% G_{Na} block led to a slightly smaller area of PS trajectory. In AF, the PS meandering surface was increased to 1.02 cm^2 , as shown in Figure 8D, in good agreement with previous studies [122]. The PS surface was only significantly altered when G_{Na} was blocked, leading to a three-fold increase in PS trajectory surface (3.01 cm^2), as compared to default AF conditions. This was consistent with the higher sensitivity of RP and CV to G_{Na} changes found in AF, in good agreement with previous studies [56].

4.3.4.2 Analysis of Vulnerability to Sustain Reentries in Human Atria

Tissue simulations were conducted to investigate how alterations in ionic current conductances modulate reentry susceptibility in atrial tissue under SR and AF. The cross stimulation protocol described in section 4.2.3 was used to initiate reentry in SR and AF. As shown in Figure 4.8, CI was much shorter, the wavefront was considerably narrower and the corresponding DF was 3.68 Hz higher in AF than in SR.

For each simulation, VW limits and W_{vw} , as well as DF, were calculated and results are shown in Figure 4.10 for SR (black segments) and AF (grey segments). 30% changes with respect to default values applied to ionic current conductances in each case are shown in the last row. For unaltered conditions (case marked **a** in Figure 4.10) in control, VW spanned CIs from 207 to 246 ms, thus $W_{vw}=39 \text{ ms}$, and DF was 3.52 Hz . In permanent AF, CIs in the VW were shorter, spanning from 137 to 185 ms, but with wider VW ($W_{vw}=48 \text{ ms}$), and higher DF of 7.2 Hz , consistent with human atrial simulation studies [120].

As shown in Figure 4.10, G_{NaK} , G_{K1} and G_{Na} were the ionic properties exerting the strongest influence on reentrant dynamics in both SR and AF (cases **b**, **c** and **d**), consistent with their key role in the modulation of tissue properties shown in previous section (Tables 4.1 and 4.2).

In all cases considered, once established, the reentrant circuit remained stable for the duration of the simulation. However, alterations in ionic currents conductances resulted in significant changes in VW limits, W_{vw} and DF. Reduction in channel conductances led to larger alterations than their overexpression, as shown in Figure 4.10 (i.e. in case marked **b**, 30% G_{K1} block in SR led to a 5 ms larger change in W_{vw} (Figure 4.10B) and a 0.12 Hz larger change in DF (Figure 4.10C) than its 30% overexpression). Also, the magnitude of resulting alterations was considerably smaller in AF, consistent with the smaller sensitivities reported in Tables 4.1 and 4.2.

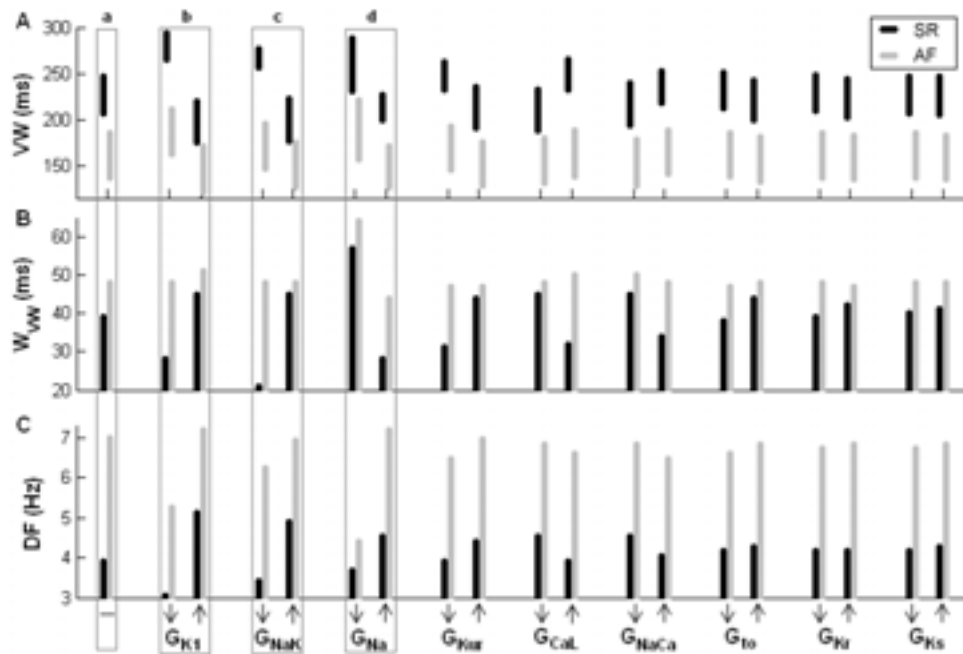


Figure 4.10: Changes in the characteristics of simulated reentry caused by changes in ionic current conductances for SR (black bars) and AF (grey bars). 30% increase/decrease of each ionic conductance is shown in the last row. Panels A, B and C show VW upper and lower limits, W_{vw} and DF, respectively, for each simulation. Specific cases **a**, **b**, **c** and **d** are referred in the text.

Single ionic changes that resulted in RP prolongation, i.e. inhibition of either G_{K1} , G_{NaK} or G_{Na} , also led to a shift of the VW towards longer CIs and smaller DF values, both in SR and AF conditions (see cases marked **b**, **c** and **d** in Figure 4.10). Inhibition of G_{K1} and G_{NaK} also led to narrow VWs, particularly in control (cases marked **b** and **c** in Figure 4.10). However, reduced values of G_{Na} , which resulted in proarrhythmic CV slowing, led to the widest VW, while increased G_{Na} led to VW narrowing (case marked **d** in Figure 4.10). Therefore, on top of blocking G_{K1} and G_{NaK} , there is a trade-off between decreasing and increasing G_{Na} depending on the objective to be achieved: low DF or narrow VW.

In order to obtain lower DF values and/or narrower VW, multi-channel variations of G_{K1} , G_{NaK} and G_{Na} were investigated. Figure 4.11 shows that simultaneous inhibition of G_{K1} and G_{NaK} , entailing a more significant RP lengthening than single ionic current conductance inhibitions, synergistically reduced W_{vw} and DF notably. The shift in VW towards longer CIs was maximal ($406 \text{ ms} < \text{CI} < 424 \text{ ms}$) and DF was minimal (1.59 Hz) for the

concomitant inhibition of the three conductances: G_{K1} , G_{NaK} and G_{Na} (case marked **e** in Figure 4.11). This can be explained by the fact that, as shown in Tables 4.1 and 4.2, alterations in G_{K1} , G_{NaK} and G_{Na} resulted in changes in RP of the same sign, and thus their simultaneous inhibition by 30% resulted in a large RP prolongation. Importantly, the concomitant overexpression of G_{Na} and inhibition of G_{K1} and G_{NaK} resulted in the narrowest VW (case marked **f** in Figure 4.11) spanning only 3 ms in control and 28 ms in AF, making the establishment of reentrant circuits unlikely. This can be explained by the fact that WL is almost doubled under these conditions, in both SR and AF, due to the concurrent increment in RP and CV (Tables 4.1 and 4.2).

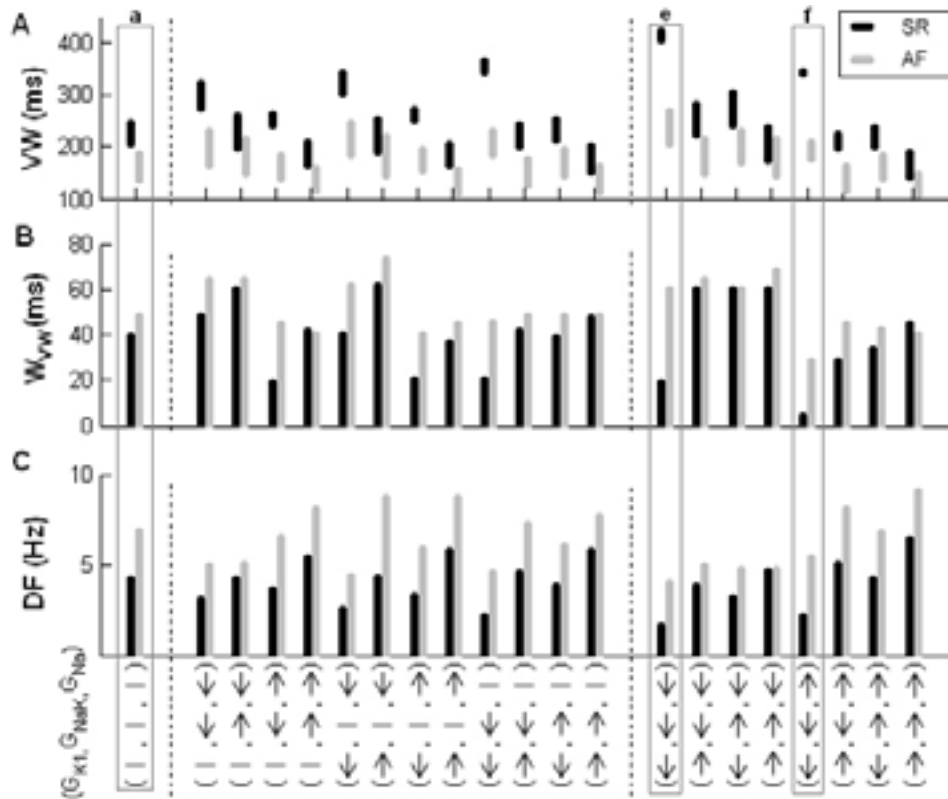


Figure 4.11: Changes in the characteristics of simulated reentry caused by simultaneous changes in G_{K1} , G_{NaK} and G_{Na} for SR (black bars) and AF (grey bars). 30% increase/decrease in G_{K1} , G_{NaK} and G_{Na} for each case is shown in the last row. Panels A, B and C show VW upper and lower limits, W_{vw} and DF, respectively, for each simulation. Specific cases **a** (same as in Figure 4.10), **e** and **f** are referred in the text.

Interestingly, a single rotor was initiated in most of the simulated cases

when the CI between stimuli was within the VW, whereas a double rotor was only generated under very specific conditions, such as the simultaneous inhibition of G_{Na} and overexpression of G_{K1} in AF with a CI=215 ms.

4.4 Discussion

In this chapter, a systematic investigation was conducted to identify the relative importance of ionic current conductances and kinetics in modulating refractoriness, CV and rotor dynamics in human atrial tissue in the presence and absence of AF. Throughout the present study, simulation results were compared to previous experimental and theoretical studies to reconstruct the complex mosaic of the ionic basis of AF-related mechanisms in human in a systematic framework. Simulations using two human atrial AP models were conducted to support the model independence of the main findings of the study. The simulation results obtained with the two models were overall qualitatively similar, but quantitative differences were observed, which could possibly be due to variability in human atrial electrophysiological measurements or differences in model construction. This analysis aids in the interpretation of existing controversies in our understanding of the ionic modulators of AF, and helps in the identification of novel aspects of human atrial electrophysiology. Importantly, our results identify G_{NaK} as a key modulator of human atrial steady-state and restitution properties as well as rotor dynamics, and confirm the importance of G_{K1} and G_{Na} in human atrial electrophysiology in both SR and AF. Other current properties including G_{Kur} and G_{CaL} play only a secondary role, which is in most cases negligible under the conditions investigated. Importantly, the ionic basis of human atrial dynamics were similar in SR and AF, but the sensitivity of electrophysiological properties to changes in ionic currents was in most cases smaller in AF than in SR. This could explain, at least in part, the lower efficacy of pharmacological treatment in patients with long-term versus short-term AF. Furthermore, our results revealed the great importance of G_{K1} in control and G_{Na} in AF in modulating rotor dynamics.

Role of I_{NaK}

Our simulation results highlight the importance of G_{NaK} as an essential determinant of human atrial electrophysiology, both in SR and AF. Alterations in G_{NaK} result in important changes in APD₉₀, APD restitution and RP, and therefore in DF. Our results also show biphasic adaptation of both APD₉₀, RP and DF after changes in G_{NaK} . These findings are supported by previous data showing that the pump current is a strong modulator of APD₉₀ and RMP in patients with and without chronic AF [149, 152]. The importance of the NaK pump as one of the key modulators of repolarization and rotor dynamics in human atria should be taken into consideration in the

evaluation and development of pharmacological treatments for AF. Previous investigations into AF-related mechanisms have, however, preferentially focused on sodium and potassium currents [157], systematically ignoring the effect of other currents and in particular the NaK pump [124]. Similarly, screening of drug compounds usually targets sodium, calcium and potassium channels. It is nevertheless important to note that some anti-AF drugs such as amiodarone interfere with NaK pump regulation [126]. Amiodarone is known to be more efficient in maintaining SR than some of their derivatives, such as dronedarone, which do not affect the activity of the pump [113, 126]. According to our results, the effects of amiodarone on NaK pump regulation could be important in explaining the anti-arrhythmic action of the drug. Furthermore, digitalis (i.e. I_{NaK} blocker) is also moderately successful in the treatment of AF patients with heart failure. The positive effects of digitalis in AF patients have been explained through the modulation of sodium and calcium concentrations [158]. Indeed, the NaK pump is essential to the maintenance of cell homeostasis but, as highlighted in our study, it is also a critical determinant of atrial refractoriness. Our results suggest that the antiarrhythmic properties of drugs such as amiodarone and digitalis used for AF treatment could at least in part be due to the modulation of important electrophysiological properties, such as APD restitution, by partial blocking of the NaK pump. The importance of G_{NaK} in modulating atrial electrophysiology is consistent in both human atrial models used in this study, and also in agreement with previous theoretical studies using human and rabbit ventricular AP models [80, 142, 159–161]. In all the models tested, G_{NaK} was consistently found to be one of the most important modulators of APD₉₀, restitution properties and rate adaptation dynamics. The importance of G_{NaK} therefore appears to be model-independent and consistent in atrial and ventricular models, even if the specific formulation of I_{NaK} in the models is different, as in the Maleckar and Courtemanche models. Experimental evidence also shows that the expression of some subunits of the NaK pump is 30-50% lower in human atria than in ventricles [158]. This could explain the higher sensitivity of atrial electrophysiology to a particular dose of drugs affecting G_{NaK} [102]. Experimental confirmation of the findings of the present study on the importance of G_{NaK} in AF-related dynamics could explain the outcome of current pharmacological therapies and guide the development of new avenues for a more effective treatment of patients with AF.

Role of I_{K1}

As in this study, previous investigations have highlighted the importance of I_{K1} in human atrial electrophysiology [120, 148] and therefore I_{K1} is considered a potential antiarrhythmic target. Furthermore, activation of inward rectifier potassium channels has been shown to increase DF in human atria [47], in good agreement with our results. Our simulations corroborate

G_{K1} as the most important modulator of electrophysiology and reentrant dynamics both in SR and AF atrial tissue. The antiarrhythmic effects of I_{K1} blockade are based on APD₉₀ and RP lengthening and therefore DF reduction.

Role of I_{Na}

The simulations performed in this chapter also confirm the strong influence of G_{Na} in the modulation of atrial rotor dynamics through alteration of CV and, to a minor extent, RP. G_{Na} alterations have a stronger effect following permanent AF-related remodeling than in SR. Sodium channel blockers such as flecainide, propafenone or pilsicainide are widely used for the treatment of short-term AF [56, 120, 123, 150]. A decrease in DF has been suggested as one of their mechanisms of action [151], which is in good agreement with our results (Figure 4.9). The identification of Class I compounds with different modes of action in atria and ventricles minimizing side effects, such as ranolazine, could be a promising path for AF treatment, in particular following permanent AF-related remodeling [123, 124].

Role of other ionic currents

In addition to G_{NaK} , G_{K1} and G_{Na} , conductances such as G_{Kur} , G_{CaL} and G_{to} also contribute to the regulation of atrial electrophysiology, particularly in control, before AF-related remodeling causes their reduction (Figure 4.1). Much attention has been paid to G_{Kur} because of its preferential expression in atrial tissue. Promising results have shown that drugs blocking I_{Kur} such as AVE0118 prolong atrial refractoriness with no effects on QT-interval in animal studies [162], but resulting in an increase in the peak intracellular calcium transient [16]. In agreement with these results, our simulations show that G_{Kur} modulates APD₉₀, and thus RP, S_{s1s2} and S_{dyn} . However, G_{Kur} effects are reduced in AF due to its lower conductance, and this could indicate potentially smaller efficacy of G_{Kur} block in the treatment of long-term AF (Figure 4.2). G_{CaL} is important in determining APD₉₀, S_{s1s2} and RP, which is consistent with previous studies showing its influence on PS tip meandering during reentry [120]. Our results could also explain the ability of verapamil, a calcium channel blocker, to attenuate the RP shortening caused by AF remodeling [163]. G_{to} , G_{Kr} and G_{Ks} have slight effects on atrial AP (Figures 4.3, 4.4, 4.5), and their alterations are delicate due to potential increase in ventricular arrhythmic risk. The I_{Kr} blockers sotalol and dofetilide are used for AF prevention due to their stronger effect on RP at slow rather than rapid heart rates [125, 157]. This is also reported in our simulations, which show larger increments in APD₉₀, and thus RP, when G_{to} , G_{Kr} and G_{Ks} are blocked in control than following AF.

Table 4.3 summarizes the ionic currents investigated in this simulation

Table 4.3: Ionic currents investigated in this study, drugs targeting them and modulation of atrial electrophysiological properties.

Ionic Current and Drug	References	Important Effects
I_{NaK}		
Amiodarone	[126, 127]	APD ₉₀ , S _{s1s2} , S _{dyn} ,
Strophantidin	[154]	RP, DF, VW
Digitalis	[158]	
Digoxin	[149]	
Ouabain	[152]	
I_{K1}		
Adenosine	[47]	APD ₉₀ , RMP, S _{s1s2} , S _{dyn} , RP, CV, DF, VW
I_{Na}		
Ranolazine	[123]	RP (AF), DF, VW
Flecainide	[123]	
Propafenone	[123]	
Lidocaine	[56]	
Pilsicainide	[151]	
Tetrodotoxin	[150]	
I_{to}, I_{Kur}		
AVE118	[162]	APD ₉₀ , S _{s1s2} , S _{dyn} , RP
I_{CaL}		
Verapamil	[163]	APD ₉₀ , S _{s1s2} , RP
I_{Kr}, I_{Ks}		
Sotalol	[157]	-
Dofetilide	[157]	

study, the experimental and clinical drug studies used for comparison with the results of this chapter, and the atrial electrophysiological properties found to be modulated by each of the investigated currents.

4.4.1 Limitations of the Study

This study focuses on unraveling the relative importance of ionic currents in modulating human atrial electrophysiology. The relevance of intracellular calcium dynamics was not investigated but it might be important, as shown in previous studies [16, 107].

Our study focused on the importance of ionic mechanisms in modulating electrophysiological properties related to rotor dynamics, and therefore other important aspects such as ectopic activity, structural changes during AF,

tissue anisotropy and heterogeneities caused by vagal stimulation were not investigated [56, 146, 147, 150]. Even though their effects on AF-related reentry could be important as shown in previous studies [56], they would have a confounding effect on the results interpretation and should be the focus of further investigations. Tissue simulations were restricted to 2D and thus a 3D atrial geometry was not considered. Previous studies, however, have shown that sodium blockers effects are qualitatively similar in 2D and 3D models [108, 124]. The role of atrial anatomy and heterogeneity in modulating pharmacological anti-AF interventions should be explored in further studies, building on insights provided by this study.

Finally, a few recent studies have focused on the comparison of different AP models aiming at targeting similar cell type and mammalian species, and have highlighted differences in dynamics because of differences in the model equations and parameters [107, 108, 142, 159, 161, 164]. The results of this study should be interpreted with caution since there could be different combinations of changes in the model parameters leading to similar results [165]. These limitations are common to other computational studies in cardiac electrophysiology. We have however conducted simulations using two different human atrial AP models varying model parameters to address some of these limitations.

Furthermore, specific conditions were used in this chapter to simulate SR and permanent AF, but these are likely to exhibit significant inter-subject variability, which is the focus of chapter 5 [119, 121, 122].

Chapter 5

Intercellular Variability in Human Atrial Action Potential in SR versus AF Patients

5.1 Introduction

An important challenge in understanding AF is the large intra- and inter-subject variability present in electrophysiological recordings obtained from human samples. Characterizing and understanding inter-subject variability in atrial cellular electrophysiology is important to determine not only the physiological range of AP properties, but also differences under disease conditions and in the response to treatment between patients. The causes of human atrial electrophysiological variability are largely unknown. However, recent studies highlight its temporally-dynamic nature and a variety of causes, pointing towards genetic differences (including sex [166]) but also factors such as age, circadian rhythms [167] and long-term drug effects [168].

In this chapter, inter-subject variability in human atrial AP morphology and duration of SR and AF patients is investigated using a combined experimental and computational population-based approach. Populations of over 2000 human atrial cell models are constructed and calibrated to mimic inter-subject variability in experimental data obtained from over 350 patients' atrial trabeculae. The models within the population share the same equations but include different combinations of sampled ionic current conductance values. The experimentally-calibrated human atrial AP model populations allow the quantitative characterization of the contribution of specific ionic currents to determining inter-subject variability in human atrial APD and morphology for SR and AF patients.

5.1.1 Objectives

The aims of this part of the thesis are:

1. Elucidate the main ionic determinants of inter-subject variability in human atrial cardiomyocytes from SR versus permanent AF patients through the generation of population of models mimicking this variability.
2. Investigate the synergistic effects of ionic variability on APD modulation measured at different stages of repolarization.
3. Analyze inter-subject variability in AP dependence on pacing rate.
4. Compare the ionic mechanisms underlying inter-subject variability obtained with different AP models.

5.2 Methods

5.2.1 Experimental Dataset

In order to validate the simulation results and properly calibrate the populations of models that were used in this part of the thesis, a set of experimental recordings and measurements performed at the Department of Pharmacology and Toxicology of the Dresden University of Technology (Germany) was used.

5.2.1.1 Patients Characteristics

All work with human samples conformed to the Declaration of Helsinki. The study was approved by the ethics committee of Dresden University of Technology (No. EK790799). Each patient gave written, informed consent. Right atrial appendages were obtained from 363 patients with SR (214 patients with paroxysmal, recent onset or non-signs of AF) and with permanent AF (149 patients with permanent AF for longer than 6 months at the time of tissue collection) receiving cardiac surgery because of coronary artery or valve disease. Preparations from patients with prescriptions of antiarrhythmic drugs were not included.

5.2.1.2 Experimental Measurements

Small pieces of human right atrial appendages were transported to the laboratory in a special Ca^{2+} -free transport medium at 20-25 °C, whose composition in mM was: 100.0 NaCl, 10.0 KCl, 1,2 KH₂PO₄, 5.0 MgSO₄, Taurin 50 mM, MOPS 5 mM, 30 mM BDM pH 7.0. Either free-running trabeculae or trabeculae together with attached atrial wall were dissected and

mounted on the bottom of a 5 ml organ bath perfused with 50 ml of recirculating, oxygenised Tyrode's solution at a flow rate of 7 ml/min at 36 ± 1 °C (composition in mM: 126.7 NaCl, 0.42 NaH₂PO₄, 22 NaHCO₃, 5.4 KCl, 1.8 CaCl₂, 1.5 MgCl₂, pH 7.4 when equilibrated with 5% CO₂ in O₂). Preparations were electrically stimulated at a basal rate of 1 Hz with square-wave stimuli of 1 ms duration and amplitude of 2 times diastolic threshold. Transmembrane potentials were recorded with glass microelectrodes filled with 2.5 M KCl. Tip resistances of the electrodes were 7-12 MΩ. Figure 5.1 shows three examples of AP recordings in SR and three in AF that reflect the large inter-subject variability that can be found in clinical practice. Both timing of the driving stimuli and pre-processing of the transmembrane potential responses were carried out with a computer-aided AP recording system. Each experiment was preceded by a 60 min equilibration period during which the preparations were allowed to stabilise. Numerical values of the main AP markers were required to remain constant, i.e. within a range of $\pm 5\%$ for at least 10 min [169, 170].

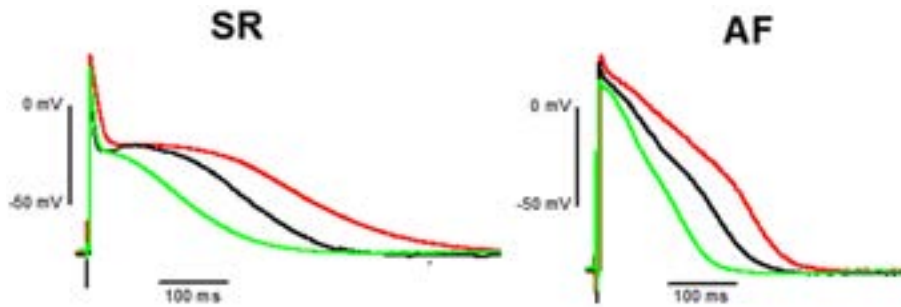


Figure 5.1: APs recorded in atrial preparations from SR (left) and AF (right) patients.

5.2.1.3 Analysis of AP Features

The following parameters were quantified to characterize inter-subject variability in human atrial electrophysiology: APD at 20, 50, and 90% repolarization (APD₂₀, APD₅₀ and APD₉₀, respectively), APA, RMP, plateau potential defined as the potential measured at 20% of the APD₉₀ time (V_{20}), and maximum upstroke velocity (dV/dt_{max}). Measured minimum, maximum and mean \pm standard deviation values for these features are presented in Table 5.1.

Table 5.1: Range of human atrial AP features in SR and AF patients

	SR			AF		
	Min. Value	Max. Value	Mean±SD	Min. Value	Max. Value	Mean±SD
APD ₉₀ (ms)	190	440	318±42	140	330	216±35***
APD ₅₀ (ms)	6	200	139±44	30	180	102±28***
APD ₂₀ (ms)	1	60	7±8	1	75	30±18***
APA (mV)	75	120	95±7	80	130	102±8***
RMP (mV)	-85	-65	-74±4	-85	-65	-77±4***
V ₂₀ (mV)	-35	10	-16±6	-30	20	-4±11***
dV/dt _{max} (V/s)	40	420	220±68	40	420	232±70*

(Mann-Whitney U test AF vs. SR: * $p < 0.05$; ** $p < 0.01$; *** $p < 0.001$)

5.2.2 Populations of Models of Human Atrial Electrophysiology

To account for inter-subject variability in atrial electrophysiology, three populations of sampled models of human atrial AP for SR and AF were generated, each one based on one of the original AP models (i.e. Maleckar, Courtemanche and Grandi models). All models in each population shared the same equations, as previously described [171–175], but the most important ionic current conductances in determining the human atrial AP (elucidated in chapter 4) were varied with respect to their original values. These were the conductances of I_{K1} , I_{CaL} , I_{to} , I_{Kur} and maximal NaK pump (I_{NaK}) and NaCa exchanger currents (I_{NaCa}), according to our previous sensitivity analysis study. Most other ionic current conductances and gating variable kinetics were shown to have significantly smaller or negligible effect on AP features.

Due to the high computational demand associated with the construction and calibration of the model populations, we first constructed coarse model populations with 2275 different ionic conductance combinations sampled over a $\pm 100\%$ variation range around their values in the original models, using the methodology described in the study of Marino *et al.* [176]. The aim of this step was to estimate median values and range of variation for the six key ionic conductances, required for simulated APs to be within experimental range. 2275 combinations were used to be consistent with the sampling methodology without losing sampling resolution [176].

The Maleckar, Courtemanche and Grandi default models were initially preconditioned by pacing at 1 Hz (using a 2-ms stimulus duration, twice diastolic threshold amplitude) until steady-state was reached. All APs within the populations were analyzed following a train of 90 periodic stimuli to quantify

APD₂₀, APD₅₀, APD₉₀, APA, RMP, V₂₀ and dV/dt_{max} . AP models were selected as in physiological range if all AP properties were in the experimental ranges described in Table 5.1 for SR and AF, respectively. Models with AP properties out of the experimental ranges described in Table 5.1 were discarded from the populations. Additionally, models presenting abnormalities such as DADs were also removed for subsequent analysis. Figure 5.2 shows median physiological values for each of the six ionic conductances from these initial populations calibrated with the human atrial recordings for SR and permanent AF patients. Note that, for all three model populations, most median values deviate from their original model value (represented as 0% in the figure) indicating that the original models are not representative of median behavior in our experimental recordings and that the calibration step was required. The deviation of the median value from the original one was often moderate for all ionic currents and all models, and within a $\pm 30\%$ range, with the exception of the NaCa exchanger in the Maleckar model which requires a significant up-regulation (+60%) for models to be within physiological range. In the three model populations, the ranges obtained for each of the conductances varied significantly between ionic currents, indicating differences in the sensitivity of the AP to variation in each of the currents. The ionic ranges in SR and AF often overlap, as shown in Figure 5.2, entailing similar APs in a significant percentage of models within the populations. Importantly, a comparison between SR and AF shows an overall increase in G_{K1} , G_{to} and G_{Kur} in AF, which is consistent with the ionic remodeling reported experimentally [119, 120, 122], and also highlights the importance of those conductances in the differences in AP between SR and chronic AF recordings.

Once the median value for each ionic conductance was estimated as described above, we refined the populations of sampled models by constructing newly generated populations of 2275 AP models with ionic currents sampled in the $\pm 30\%$ range around the estimated median physiological values. This maximized both the sampling resolution and number of accepted models in the six final AP model populations. The refined human atrial model populations were then experimentally-calibrated as previously described, to ensure that all models in the populations remained in range with their corresponding experimental ranges (SR or permanent AF) as described in Table 5.1.

The percentage of accepted models was 65.5% with the Maleckar model in SR and over 93% in the rest of cases, as shown in Table 5.2. The main cause for the differences in the number of models excluded from the population is that the Maleckar model is more prone to generate DADs at slow pacing than the Courtemanche and Grandi models under certain electrophysiological conditions, such as reduced I_{NaK} current [108].

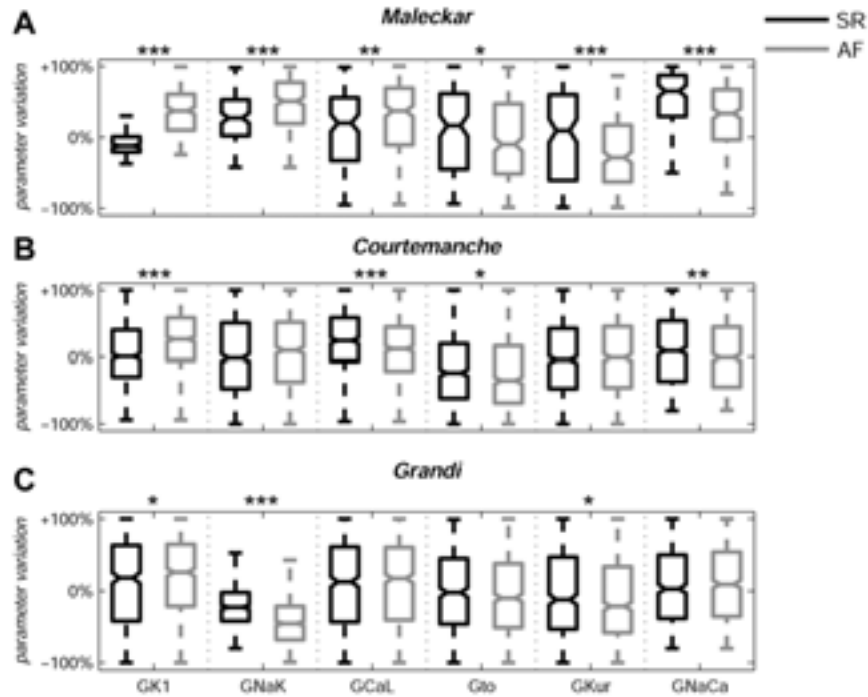


Figure 5.2: Variability of ionic conductances G_{K1} , G_{NaK} , G_{CaL} , G_{to} , G_{Kur} and G_{NaCa} in experimentally-calibrated populations of human atrial AP models, sampled within a $\pm 100\%$ range of their original values in the Maleckar (A), Courtemanche (B) and Grandi (C) human atrial AP models in SR (black) and AF (gray). Estimated median physiological values are shown as central horizontal lines within each boxplot. (Mann-Whitney U test: *p<0.05; **p<0.01; ***p<0.001).

5.2.3 Statistical Analysis

Regression methods were used for the quantification of the main determinants of inter-subject electrophysiological variability [171, 173, 174]. The dependence of APD_{20} , APD_{50} and APD_{90} on pairwise combinations of multiple ionic properties was analyzed using second-order multi-parametric regression on the accepted model populations. This was studied by calculating the coefficient of determination (R^2) of the computed regressions: the higher R^2 , the stronger the dependence of APD on the considered parameters. A third parameter was included in the analysis for those cases where $R^2 < 0.7$. Mechanisms of AP triangulation, calculated as the difference between APD_{90} and APD_{50} , were also analyzed by regression techniques.

The Mann-Whitney U test was used to determine statistical significance in the differences on ionic conductance distributions between populations.

Table 5.2: Number and percentages of accepted sampled models in the experimentally-calibrated Maleckar, Courtemanche and Grandi populations in SR and permanent AF out of a total of 2275 sampled models.

	SR	AF
<i>Maleckar</i>	1489 (65.5%)	2177 (95.7%)
<i>Courtemanche</i>	2275 (100%)	2271 (99.8%)
<i>Grandi</i>	2125 (93.4%)	2275 (100%)

5.3 Results

5.3.1 Ionic Determinants of Inter-subject Variability in APD

Figure 5.3 shows AP morphologies for human atrial cell models in SR and AF (left and right, respectively) obtained in simulations using the initial unrestricted population (with ionic currents sampled over a $\pm 100\%$ range of their original values, panel A), and with the experimentally-calibrated populations (panel B). Histograms illustrate the distribution of APD values obtained for the simulated populations (C) and the experimental recordings (D). Results in Figure 5.3 are shown for the Courtemanche model and similar coverage of the experimental range is provided for the Maleckar and Grandi models. Results show that the experimentally-calibrated populations of human atrial models were able to mimic the inter-subject variability in APD exhibited in the experimental recordings as quantified using the properties and values shown in Table 5.1.

Figure 5.4 shows the large variability existing in the time course of the ionic currents in the calibrated population with the Maleckar model, with representation of those corresponding to the maximum and minimum APD values measured at the different stages of repolarization. Most currents exhibited variability mainly in their peak value, as shown for I_{to} , I_{Kur} and I_{NaCa} . However, I_{K1} , I_{NaK} and I_{CaL} exhibited inter-subject variability also in their sustained current densities. Particularly, the rate of decay of I_{CaL} was found to be markedly slower for cellular models with longer APD values, and more so in permanent AF than in SR.

Figures 5.5 and 5.6 further illustrate the ionic mechanisms of inter-subject variability in human atrial AP shown in Figure 5.4. They provide quantitative results on variability from the regression analysis described in section 5.2.3 for human atrial APD_{90} , APD_{50} and APD_{20} with respect to their most important pairs of ionic modulators. Results are shown for the populations of sampled models constructed for the Maleckar (A-C), Courtemanche (D-F) and Grandi (G-I) models in SR (Figure 5.5) and AF (Figure

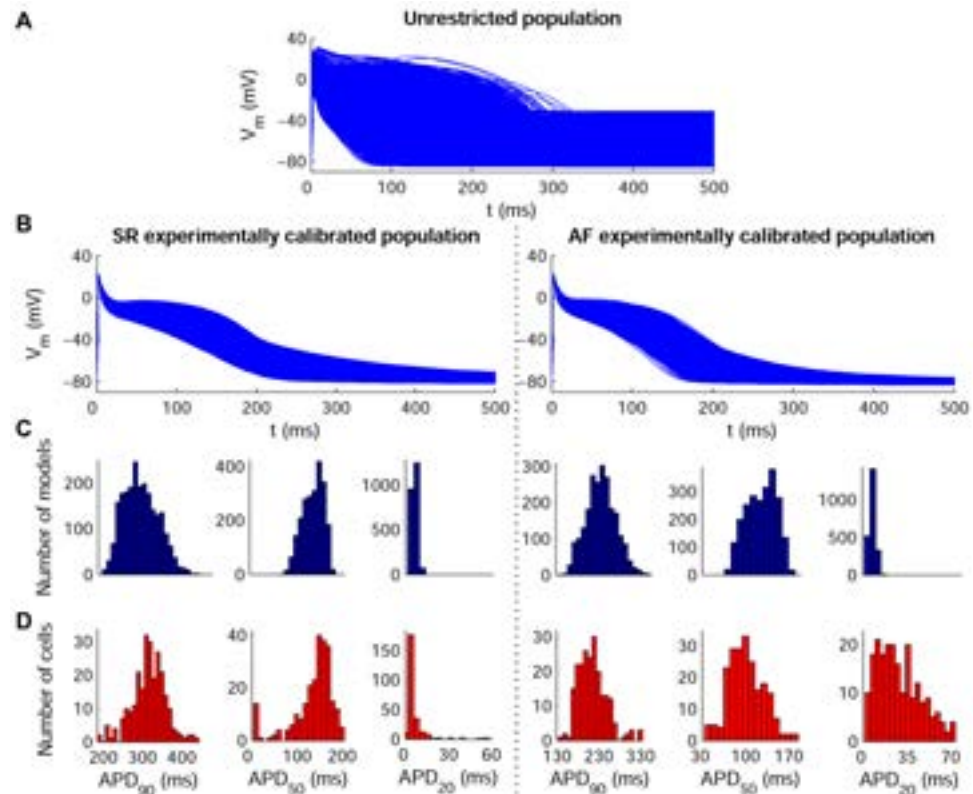


Figure 5.3: Experimentally-calibrated human AP model populations for SR (left) and AF (right) patients. Initial unrestricted $\pm 100\%$ sampled population (A), experimentally calibrated $\pm 30\%$ sampled populations (B) and histograms corresponding to APD₉₀, APD₅₀ and APD₂₀ distributions in both the calibrated model populations (C) and the experimental measurements (D) are shown based on the Courtemanche model. Histogram bar widths are 10 ms for both APD₉₀ and APD₅₀, and 4 ms for APD₂₀.

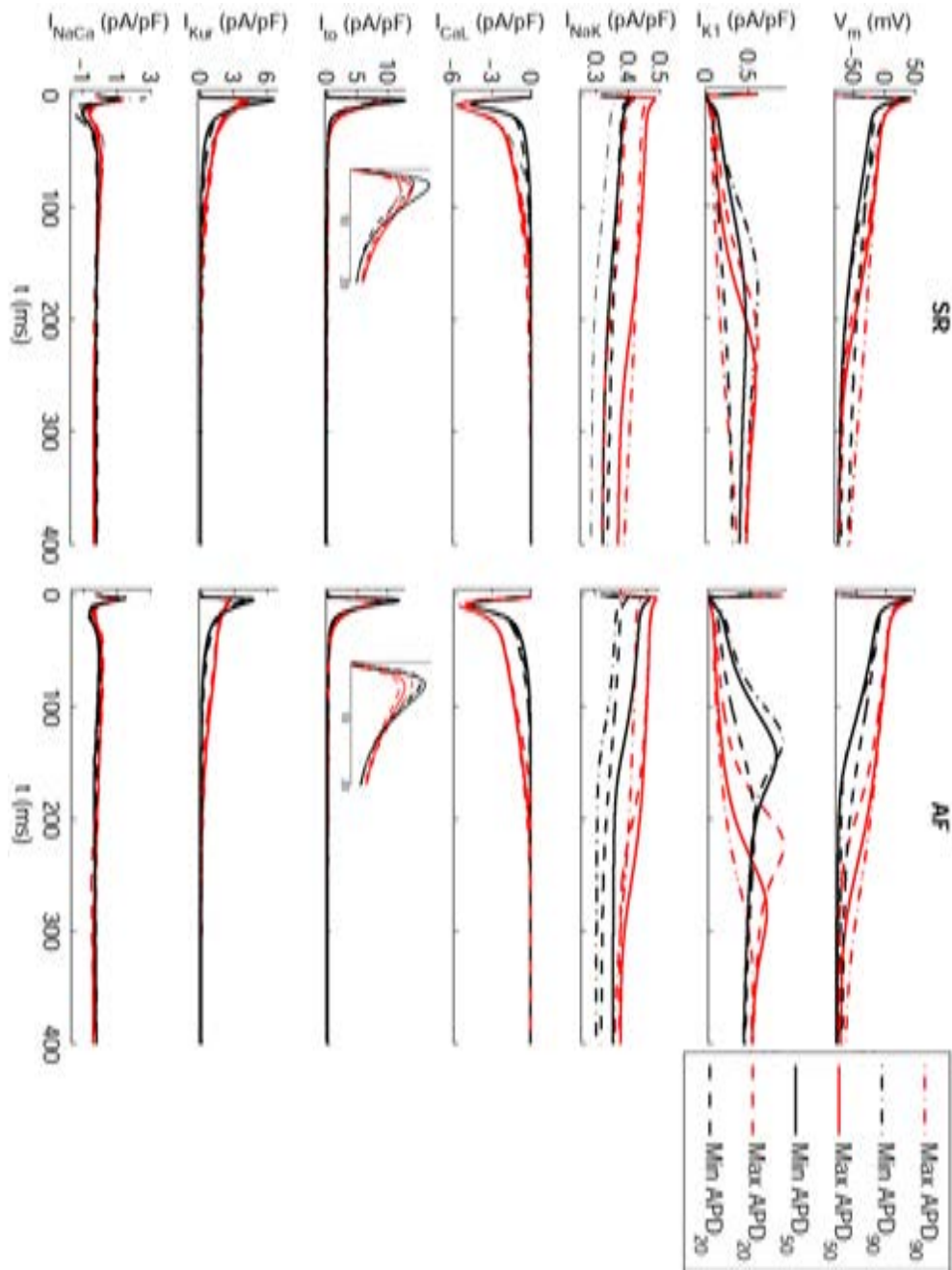


Figure 5.4: Transmembrane potential and ionic current traces in SR (left) and AF (right) with the Maleckar model corresponding to maximum APD_{90} (red dash-dotted lines), minimum APD_{90} (black dash-dotted lines), maximum APD_{50} (red thin solid lines), minimum APD_{50} (black thin solid lines), maximum APD_{20} (red dashed lines) and minimum APD_{20} (black dashed lines). Note: I_{to} panels are zoomed in.

5.6).

Simulations with the six model populations showed that variability in I_{K1} and importantly also in I_{NaK} entailed variability in APD_{90} in both SR (Figures 5.5A, 5.5D and 5.5G) and AF (Figures 5.6A, 5.6D and 5.6G). Results with the Courtemanche model population indicated an additional role of variability in I_{CaL} on variability in APD_{90} (Figure 4D; Figure 5.6D).

Regarding APD_{50} variability, our population-based analysis identified variability in I_{CaL} and I_{Kur} as key at the early stage of repolarization followed by a secondary role of variability in I_{K1} and I_{NaK} , particularly with the Grandi model population, in both SR and AF (Figures 5.5B, 5.5E and 5.5H; Figures 5.6B, 5.6E and 5.6H).

Finally, variability in APD_{20} strongly depended on variability in I_{to} and I_{Kur} in both SR (Figures 5.5C and 5.5F) and AF (Figures 5.6C, 5.6F and 5.6I), as shown in all 6 model populations. These effects were concealed by changes in I_{K1} and I_{NaK} in the Grandi model population in both SR and AF conditions (Figures 5.5I and 5.6I). Variability in I_{CaL} is relevant as well for modulation of APD_{20} variability in the Courtemanche model population (Figure 5.5F).

Figure 5.7 summarizes the elucidated ionic mechanisms modulating APD variability in each repolarization stage with the model populations in SR (left panel) and permanent AF (right panel). Interestingly, sources of inter-subject variability were similar in SR and permanent AF, with variability in I_{K1} and I_{NaK} modulating variability in APD_{90} , I_{CaL} and I_{Kur} in APD_{50} , and I_{to} and I_{Kur} in APD_{20} . The main differences between SR and permanent AF in terms of ionic mechanisms were found in the Grandi sampled models population, suggesting a decreased relevance of variability in I_{K1} and I_{NaK} in modulating the early stages of atrial cell repolarization in permanent AF, and a reduced role of variability in I_{CaL} in regulating APD at all stages of repolarization in AF. Differences in the ionic mechanisms underlying variability between the electrophysiological models reflected differences in the models' structure.

5.3.2 Ionic Determinants of Inter-subject Variability in AP Morphology

Figure 5.8 shows the most significant inter-subject differences in AP triangulation within the populations obtained with the Maleckar (Figure 5.8A), Courtemanche (Figure 5.8B) and Grandi (Figure 5.8C) models. Our simulation results are in agreement with previous studies reporting large variability in AP morphology measured in human atrial cells, exhibiting very different degrees of AP triangulation [106, 177, 178]. The regression analysis revealed variability in I_{K1} and I_{NaK} as the only underlying mechanisms of AP triangulation in the Maleckar and Grandi model populations ($R^2 > 0.96$), whereas

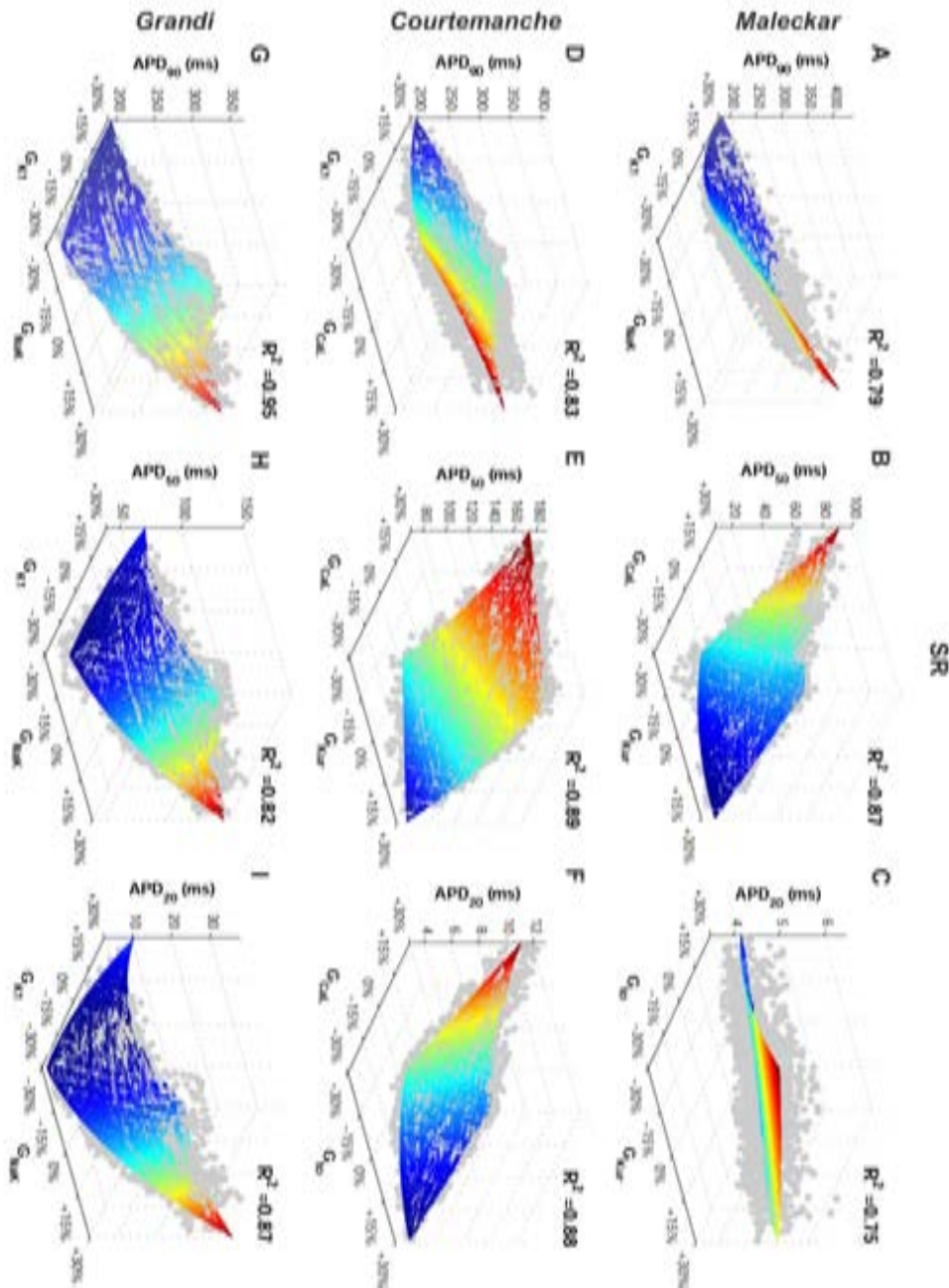


Figure 5.5: Ionic conductances determining inter-subject variability in the different stages of human atrial repolarization under SR conditions at 1 Hz pacing. Regression surfaces for APD_{90} , APD_{50} and APD_{20} are presented with respect to the two most significant ionic factors determining their variability, using populations of the Maleckar (A-C), Courtemanche (D-F), and Grandi (G-I) models of human atrial electrophysiology. Regression surfaces are color coded according to APD magnitudes, whereas each big dot denotes one simulated subject in the calibrated populations of sampled models.

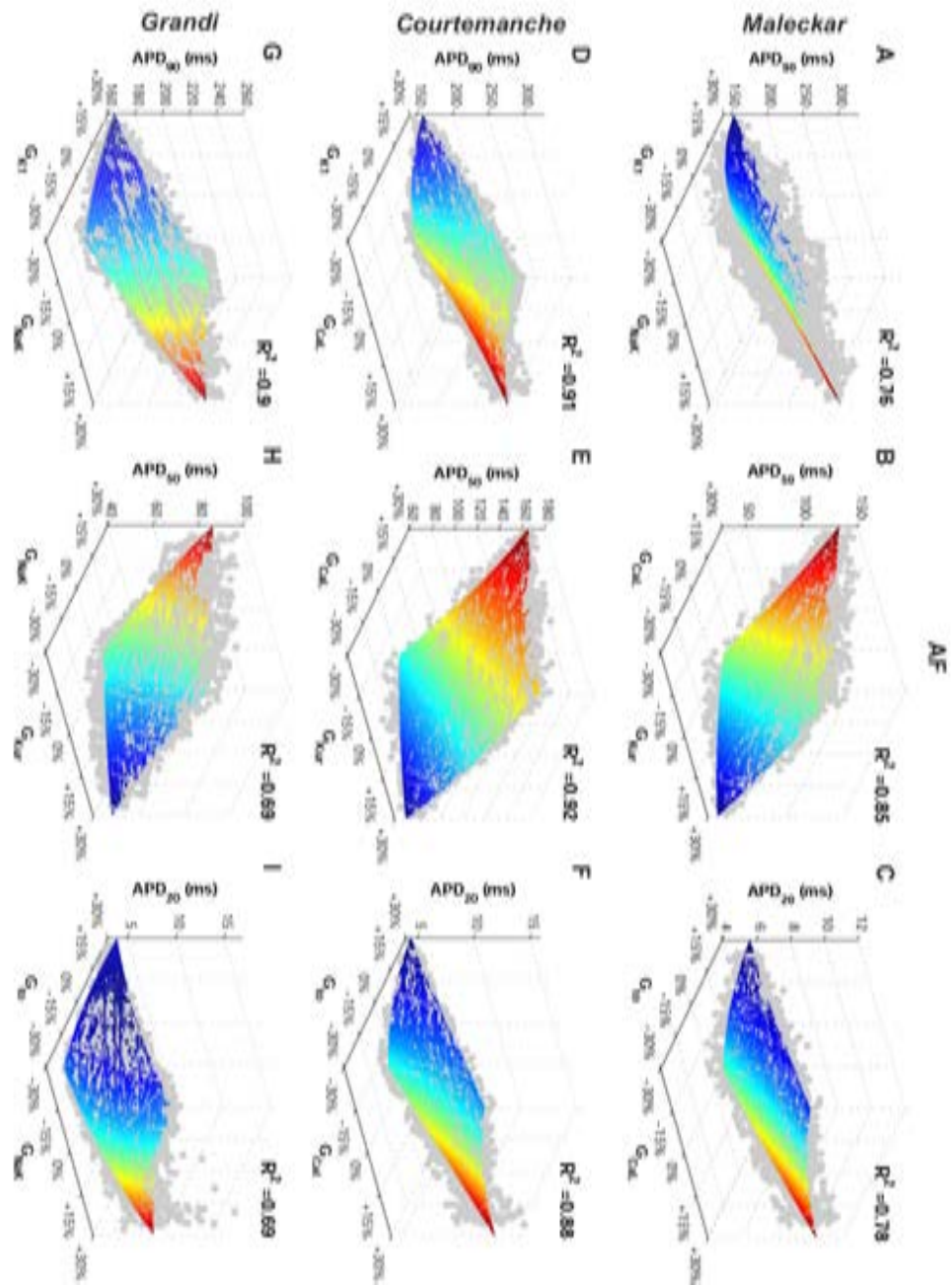


Figure 5.6: Ionic conductances determining inter-subject variability in the different stages of human atrial repolarization under AF conditions at 1 Hz pacing. Regression surfaces for APD₉₀, APD₅₀ and APD₂₀ are presented with respect to the two most significant ionic factors determining their variability, using populations of the Maleckar (A-C), Courtemanche (D-F), and Grandi (G-I) models of human atrial electrophysiology. Regression surfaces are color coded according to APD magnitudes, whereas each big dot denotes one simulated subject in the calibrated populations of sampled models.

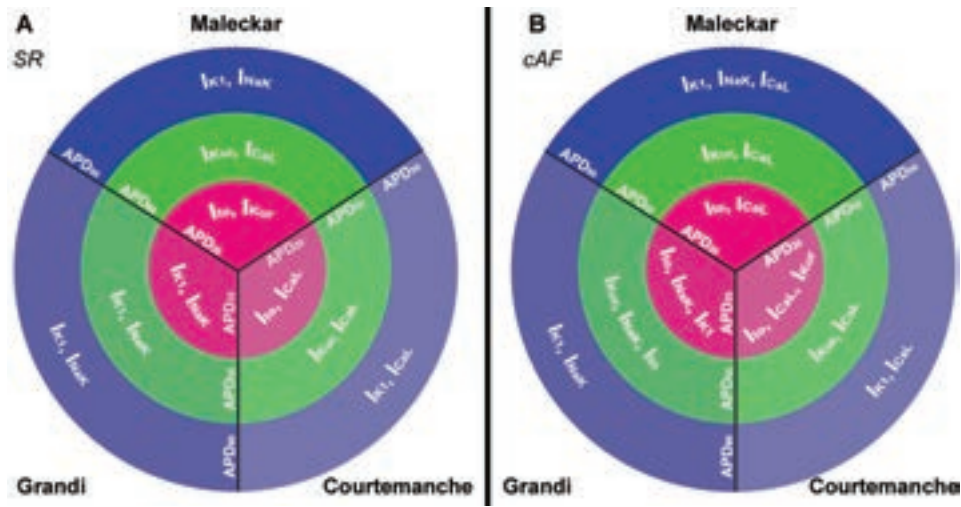


Figure 5.7: Main ionic determinants of inter-subject variability in human atrial APD₉₀ (blue), APD₅₀ (green) and APD₂₀ (pink) in SR (panel A) and permanent AF (panel B) with the Maleckar, Courtemanche and Grandi model populations.

the combination of changes in I_{K1} and I_{NaCa} led to the highest regression values with the Courtemanche model populations ($R^2=0.86$). Figure 5.8 (panels D, E and F) shows the combination of I_{K1} with either I_{NaK} and I_{NaCa} (depending on the model) leading to the different AP morphologies. The most triangular APs were generated for combinations of decreased I_{K1} and increased I_{NaK} (Maleckar and Grandi models) or I_{NaCa} (Courtemanche model) current amplitudes.

5.3.3 Ionic Determinants of Inter-subject Variability in AP Rate Dependence

Inter-subject variability in APD rate dependent properties of human atrial cardiomyocytes was also investigated by comparing the response of our populations of sampled human atrial models at CL=1000 and 400 ms. Overall, our results were qualitatively similar for both pacing rates and the role played by the ionic currents at the different stages of repolarization is similar at both pacing rates. Only an increased relevance of variability in I_{CaL} and I_{Kur} on the last repolarization stage could be found at fast pacing rates.

A particular feature of the Grandi population is its increased likelihood to generate AP alternans at fast pacing rates, in agreement with experimental studies [179–182]. AP alternans were characterized by generation of APs with low amplitude and slow upstrokes in 1 out of 2 APs in a significant percentage of the models within both SR and AF populations. Figure 5.9

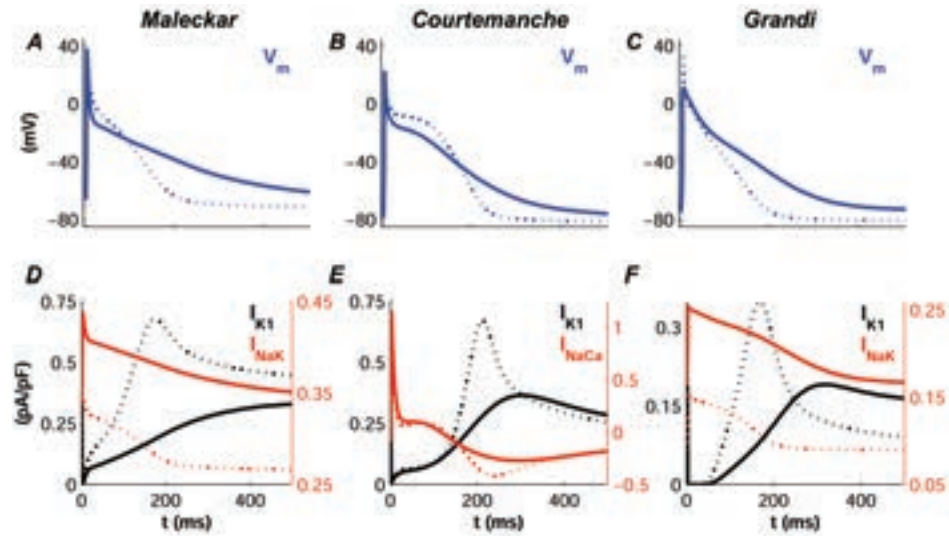


Figure 5.8: Intersubject variability in human atrial AP triangulation. The most and least triangular APs in each population are shown (solid and dotted lines, respectively), obtained with the Maleckar (A), Courtemanche (B) and Grandi (C) models in SR. Corresponding time course of ionic mechanisms of AP triangulation are shown: I_{K1} and I_{NaK} (D and F), I_{K1} and I_{NaCa} (E).

(panel A) shows clear alternating behavior in a large number of models in the Grandi SR model population for short CL. The alternating behavior occurred in models with low amplitude of I_{K1} and increased activity of I_{NaK} (Figure 5.9B). This is in good agreement with the important role played by both ionic currents in modulating APD at the different stages of repolarization (Figure 5.7). Furthermore, Figure 5.9 (panel B) shows that the effects of the rest of ionic currents in generating alternans were less statistically significant.

5.4 Discussion

The in silico investigations conducted in the present study provide a quantitative characterization of the ionic properties driving intersubject variability in the different stages of human atrial cell repolarization in SR and permanent AF patients. Populations of human atrial electrophysiology models were constructed and experimentally-calibrated to mimic the physiological AP range exhibited in a comprehensive set of electrophysiological recordings obtained from SR and AF patients [60]. The sampled populations were generated using three different human atrial AP models to test model in-

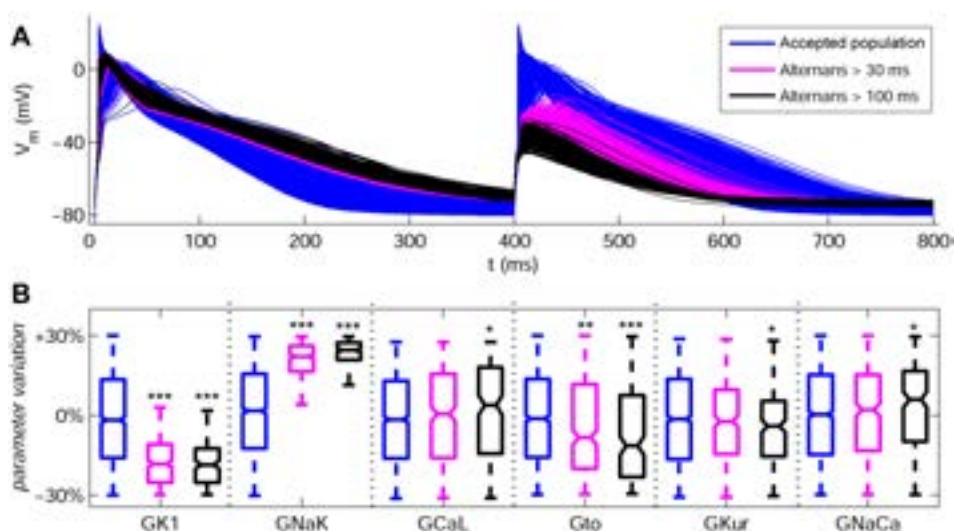


Figure 5.9: A: AP traces with the Grandi model population for $CL = 400$ ms in SR of the same accepted models as for $CL = 1000$ ms (blue), the models showing AP alternans ($|APD_{90,odd} - APD_{90,even}| > 30$ ms; magenta) and the models showing strong AP alternans ($|APD_{90,odd} - APD_{90,even}| > 100$ ms; black). B: Variability of ionic conductances G_{K1} , G_{NaK} , G_{CaL} , G_{to} , G_{Kur} and G_{NaCa} for the models in panel A. (Mann-Whitney U test alternans vs. accepted range: $*p < 0.05$; $**p < 0.01$; $***p < 0.001$).

dependence of the obtained results. The experimentally-calibrated human atrial cell model populations cover a wide range of ionic current magnitudes, AP duration and morphologies, consistent with human atrial recordings [19, 65, 183], and serve to elucidate ionic mechanisms underlying inter-subject variability in human atrial repolarization deviation and morphology in SR versus permanent AF patients. As such, they are expected to further promote the understanding of the causes and modulators of inter-subject variability in human atrial arrhythmia dynamics and the diversity of outcomes of antiarrhythmic therapies [60, 106].

Through our computational populations of models approach, we aim at and are able to identify and suggest what may be likely ranges and important players in explaining the variability in the human AP recordings [65, 183, 184]. An important methodological novelty is that it allows identifying how synergistic combinations of various ionic current densities determine inter-subject variability in the human atrial AP, which goes an important step beyond previously proposed sensitivity analysis methods [80, 142, 161]. In this thesis, we unraveled how complex non-linear combinations of simultaneous variations in multiple ionic conductances, as may be present in different individuals, lead to differences in atrial cellular re-

polarization in SR versus permanent AF patients. Our results offer the possibility to provide a deeper understanding on the penetration of different pharmacological therapies at the population level, which is critical in the interpretation of outcomes for anti-arrhythmic drug development and the lack of pharmacological response in some individuals.

The median electrophysiological values and ranges extracted from the unrestricted $\pm 100\%$ populations differed between SR and AF, as shown in Figure 5.2. Calibration of the Maleckar and Grandi populations with permanent AF recordings led to notably higher median values of G_{K1} in AF with respect to SR, reduction in G_{to} and reduction in G_{Kur} , which is in good agreement with the ionic remodeling observed in permanent AF patients in previous experimental studies [119, 120, 122]. The Courtemanche population, however, exhibited similar ionic ranges in SR and AF for G_{K1} , G_{to} and G_{Kur} . Insignificant differences were also observed in the G_{CaL} ranges between the SR and AF calibrated populations with the three models, which differs from experimental studies that reported a reduction of G_{CaL} in permanent AF patients [121].

The results obtained in this chapter of the thesis identify variability in I_{K1} as key in explaining inter-subject variability in APD_{90} , which supports the well-established importance of I_{K1} in human atrial electrophysiology [120, 148]. Alterations in I_{K1} may also modulate variations in APD_{50} and APD_{20} by modifying cellular excitability through the resting membrane potential. Importantly, our study highlights the importance of variability in I_{NaK} in inter-subject variability in APD_{90} , which further supports the results shown in chapter 4. The results therefore suggest the need for pharmacological assessment of potential drug effects on the NaK pump (as is the case of amiodarone, for example) due to its importance on atrial repolarization, in addition to effects on currently evaluated currents such as sodium, potassium and calcium channels [30, 113, 126, 127]. The results presented here also indicate that I_{K1} and I_{NaK} are the key determinants of variability in AP morphology in human atrial cardiomyocytes.

Our population-based results also highlight the importance of variability in I_{CaL} in determining inter-subject variability in APD_{50} , while its role in modulating variability in APD_{90} and APD_{20} is less significant. This may explain why some calcium channel blockers, such as verapamil, although significantly reducing the degree of electrical remodeling, only yield a minimal reduction in inducibility of AF, despite aiming at modifying tissue refractoriness in permanent AF patients [163].

Due to its atria specificity and negligible ventricular expression levels, I_{Kur} has been previously proposed as a potentially important ionic target for atrial antiarrhythmic therapies aiming at exclusively prolonging atrial refractoriness [29, 162, 170, 178, 185, 186]. The results of this study support its importance in modulating inter-subject variability in APD_{50} and

APD₂₀, with smaller importance in modulating APD₉₀. Another important modulator of variability in APD₂₀ is variability in I_{to} , which in contrast has only small effects on APD₉₀ and APD₅₀. This supports the potential of drugs such as AVE0118, which interfere with both I_{to} and I_{Kur} , and have been shown to modulate atrial repolarization with no apparent effects on ventricular repolarization [16, 162, 170, 186].

Finally, our results show a secondary role of I_{NaCa} in modulating APD inter-subject APD variability, as its effects are less prominent than those of the other currents. However, its influence on AP morphology cannot be neglected. Recent I_{NaCa} inhibitors have shown the potential to prevent arrhythmogenic events in ventricular myocardium by decreasing the amplitude of pharmacologically-induced early and delayed afterdepolarizations [33, 187], although their effects in atrial tissue still remain unexplored.

5.4.1 Limitations of the Study

The populations of human atrial models developed in this chapter were based on a large amount of experimental recordings obtained from trabeculae extracted from the right atrial appendage, which is available from biopsies. APs from other atrial locations may exhibit a different degree of variability. In this chapter, populations of sampled models were built to represent inter-subject variability in AP of human atrial cells, with additional effects being present in tissue preparations, such as inter-cellular coupling. These other effects of tissue coupling should be investigated in further studies, aiming at translating investigations of this study from cell to tissue model populations.

Furthermore, there are some other ionic currents not investigated in the present work whose effects on APD variability may not be negligible, such as the background chloride current (I_{bCL}). This ionic current was not included in the populations because it is only present in the Grandi model.

Chapter 6

Ionic Modulation of Atrial Fibrillation Dynamics in a Human Atrial 3D Model

6.1 Introduction

AF causes both structural changes, such as physical dilation, and electrical remodeling of ion channels in cardiac tissue involving short refractoriness and slow conduction favoring reentries [16, 119, 121, 122, 188]. These changes and the intrinsic electrophysiological and structural heterogeneities in the human atria favor the generation and stabilization of reentrant circuits that sustain the arrhythmia and entail chaotic activation patterns. This is associated with irregular HR and difficulty to distinguish P-waves on the ECG [40]. It is also well established that AF normally arises by rapid ectopic activity around the pulmonary veins (PV) generating stable reentrant circuits in LA combined with short duration wavelets that propagate through the whole atria to RA creating a chaotic activation that may then affect the ventricular rhythm [188]. Left-to-right atrial gradients are also an arrhythmic risk factor that may favor the stability of AF, as reported in previous studies [47, 189–192].

In combination with the analysis of the ECG, the understanding of the electrical behavior on the atrial surface by measuring EGM at different points to extract arrhythmia-related markers is key to properly apply anti-AF therapies (normally ablation combined with antiarrhythmic drugs). Disorganization in atrial activation is reflected on measurable indices in the EGM, such as heterogeneous DF, and reduced values of the morphological regularity index (RI), the spectral organization index (OI) and the morphological coupling between pairs of EGMs (CP), which will be further explained in section 6.2.4. Furthermore, disorganization can also be reflected in areas

of generation of complex fractionated atrial electrograms (CFAEs), usually associated with arrhythmia drivers and thus potentially suitable for surgical ablation [3, 193–195].

6.1.1 Objectives

The goals of this chapter are:

1. Investigate the effects of ionic changes on simulated arrhythmias using realistic 3D human atrial models.
2. Characterize fibrillatory behavior in a 3D human atrial model by analyzing a map of pseudo-EGM (pEGM) signals distributed throughout the whole atria in order to obtain arrhythmia-related markers.
3. Investigate the implications of inter-subject variability on arrhythmic behavior in 3D human atrial models.
4. Validate the results of AF simulations in 3D human atria with experimental data from both the literature and clinical EGM recordings from AF patients.

6.2 Methods

6.2.1 Cell and 3D Models of Human Atria

The Maleckar model was used to simulate cellular electrophysiology in a realistic 3D atrial model developed at the Karlsruhe Institute of Technology, as described in section 2.3 [65, 196]. In order to study the effect of altering specific ionic currents on AF dynamics, the simulations were performed in permanent AF conditions by altering ion channel conductances as described in section 4.2.1.1 according to previous studies [16, 119, 121, 122]: 70% I_{CaL} reduction; 50% I_{to} reduction; 50% I_{Kur} reduction; and 100% I_{K1} increment. Two different levels of [ACh], 1 nM (value used by default) and 5 nM, were included in the simulations through an I_{KAC_h} to investigate the effects of the parasympathetic activity [28].

As stated in section 2.3, the 3D model contains the main atrial structures: LA, RA, SAN, CT, PM, FO, BB, CTI, LAPG, RAPG, AVR and IAB. Furthermore, we included fiber orientation, conduction anisotropy and spatial heterogeneities in both ionic currents and CV in the 3D model, based on previous studies [65, 196, 197]. Simulated anisotropic ratio (transversal to longitudinal ratio of conductivity) and spatial heterogeneities are summarized in Table 6.1. In this thesis, we included differences between ionic currents in LA versus RA by simulating gradients in I_{Kr} (1.6 times greater

in LA than RA) and I_{KACH} (2 times greater in LA than RA) as shown in Table 6.1, according to previous studies [47].

Table 6.1: Human atrial tissue anisotropy and heterogeneities.

	Anis. ratio	CV (cm/s)	I_{to}^*	I_{CaL}^*	I_{Kr}^*	I_{KACH}^*
LA	1:2	59	1	1	$\sqrt{1.6}$	$\sqrt{2}$
RA	1:2	59	1	1	$1/\sqrt{1.6}$	$1/\sqrt{2}$
SAN	1:1	31	1	1	1	1
CT	1:10	116	1.35	1.6	0.9	1
PM	1:2	98	1.05	0.95	0.9	1
FO	1:2	59	1	1	1	1
RAPG	1:2	59	1	1	1	1
IAB	1:2	59	1	1	1	1
BB	1:2	98	1	1	1	1
CTI	1:1	44	1	1	1	1
LAPG	1:2	59	0.65	1.05	2.75	1
AVR	1:2	59	1.05	0.65	3	1

*Multiplicative factors with respect to default values in the AP model

Human atrial cells within the 3D model were stimulated using 2-ms duration and twice diastolic threshold current pulses. A preliminary conditioning of the 3D model was performed by applying a train of 40 periodic stimuli at the SAN cells at a CL of 500 ms. Then, 6 extra-stimuli were applied around the right pulmonary veins (RPVs) to generate reentries and fibrillatory behavior.

6.2.2 Simulated Ionic Current Alterations

In order to analyze the effects of ionic changes on fibrillatory dynamics, single blocks of the most relevant ionic currents modulating single cell and tissue markers were simulated, according to the results obtained in chapter 4 of the present thesis: 30% I_{K1} inhibition, 15% I_{Na} inhibition and 30% I_{NaK} inhibition. Notice stronger I_{Na} blocks led to propagation failure and therefore were not further analyzed.

6.2.3 Repolarization Variability within the 3D Model

In order to study how inter-subject variability in cellular repolarization affects AF properties and dynamics, a new population of human atrial cell models was generated by simultaneously modifying ionic current conductances (G_{K1} , G_{NaK} , G_{CaL} , G_{to} , G_{Kur} and G_{NaCa}) within a range in the same way as in the previous chapter, but using a default permanent AF-remodeled version of the Maleckar model: 50% I_{CaL} reduction; 70% I_{to} re-

duction; 50% I_{Kur} reduction; and 100% I_{K1} increment. This default model of permanent AF was constructed in order to increase the number of models within physiological range after the calibration process from 2177 (95.7% of the whole population, as shown in Table 5.1 in Chapter 5) to 2231 (98.1% of the whole population).

Out of the calibrated permanent AF population (Figure 6.1A), sub-populations were extracted according to their APD_{90} , APD_{50} and APD_{20} values, separating those models over the third quartile value (long APD) from those below the first quartile value (short APD), thus generating six sub-populations of models (Figure 6.1, panels B-D). The aim of the generation of these sub-populations was to obtain six virtual patients with different atrial cell repolarization properties.

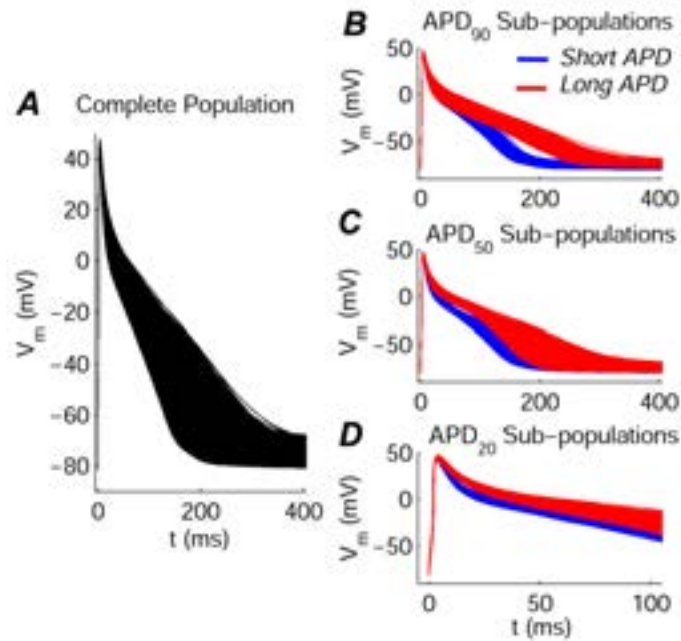


Figure 6.1: Population of simulated AF cell models (panel A). First (blue) and fourth (red) quartile sub-populations according to APD_{90} , APD_{50} and APD_{20} , respectively (panels B-D). Note zoomed in time axis in panel D.

In order to include the six sub-populations within six 3D human atrial models, each cell in a 3D atrial mesh was randomly assigned a model of the corresponding sub-population, maintaining the electrophysiological heterogeneities shown in Table 6.1.

6.2.4 EGM Processing and Arrhythmia-related Indices

In this thesis, we designed a map of 49 electrodes through both LA and RA located at a distance of about 2 mm from the tissue surface. This map was used to characterize the electrical activity in the atria by recording unipolar pEGM during the simulations after the last preconditioning stimulus was applied [138–140]. The time course of the intracellular calcium concentration was also measured at the atrial surface points closest to the locations of the 49 virtual electrodes (see Figure 6.2).

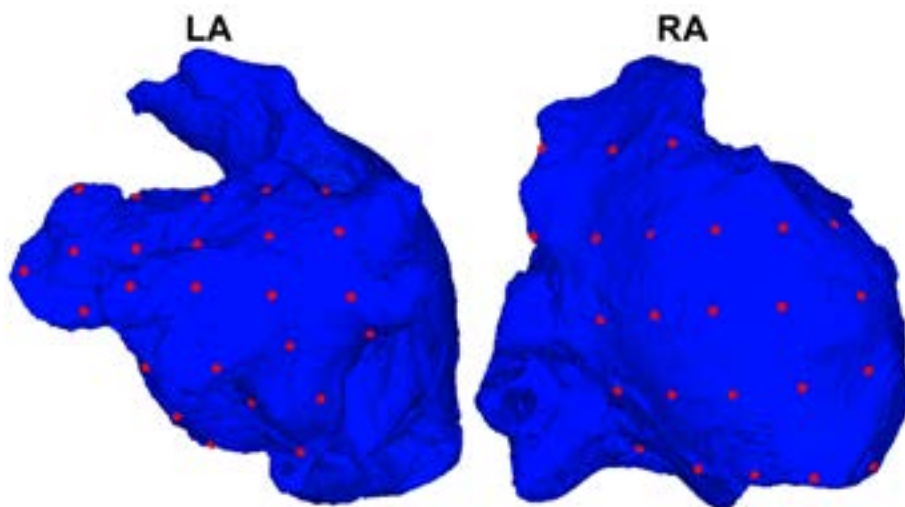


Figure 6.2: Position of the 49 virtual electrodes (red dots) in LA (left panel) and RA (right panel).

The preprocessing of pEGMs was as described in section 4.2.3: fourth-order Butterworth band-pass-filter ($f_{c1}=40$ Hz; $f_{c2}=250$ Hz), signal-rectifier and fourth-order Butterworth high-pass-filter ($f_c=20$ Hz) [141]. Then, in this thesis we analyzed the impact of ionic changes on fibrillatory activity by calculating some markers related to arrhythmic risk from pEGM signals:

- DF was obtained as the location of the maximum peak of the power spectral density of the preprocessed pEGM.
- OI was calculated as the ratio of the area under the power spectral density around the estimated $DF \pm 0.75$ Hz over the sum of the areas under $DF \pm 0.75$ Hz and the first three harmonic frequencies ($2DF \pm 0.75$ Hz, $3DF \pm 0.75$ Hz, $4DF \pm 0.75$ Hz) [198];
- RI and CP were calculated using morphological comparisons between local activation waves (LAWs, x_i) in every pEGM. The central points of these LAWs were obtained as those leading to gradient-peaks, and

their duration was set to 90 ms in order to avoid having more than one activation in the same LAW (see Figure 6.3). Two normalized LAWs (\hat{x}_i) were considered similar if the accumulated difference between them ($d(\hat{x}_i, \hat{x}_j)$) was lower than a certain threshold (ε), as shown in the following equations [199]:

$$RI_x = \frac{N_s}{N_{tot}} = \frac{\sum_{i=1}^N \sum_{j=1; j \neq i}^N \Theta(\varepsilon - d(\hat{x}_i, \hat{x}_j))}{N(N-1)}, \quad (6.1)$$

$$\rho_{xy} = \frac{N_{s_{xy}}}{N_{tot_{xy}}} = \frac{\sum_{i=1}^N \sum_{j=1; j \neq i}^N \Theta(\varepsilon - \max\{d(\hat{x}_i, \hat{x}_j), d(\hat{y}_i, \hat{y}_j)\})}{N(N-1)}, \quad (6.2)$$

$$CP_{xy} = \frac{2\rho_{xy}}{RI_x + RI_y}, \quad (6.3)$$

where N_s is the count of the number of pairs of activation waves with similar morphology; N_{tot} is the total number of comparisons performed; $\Theta(z)$ is the Heaviside function ($\Theta(z)=0$, if $z<0$; $\Theta(z)=1$, if $z>0$).

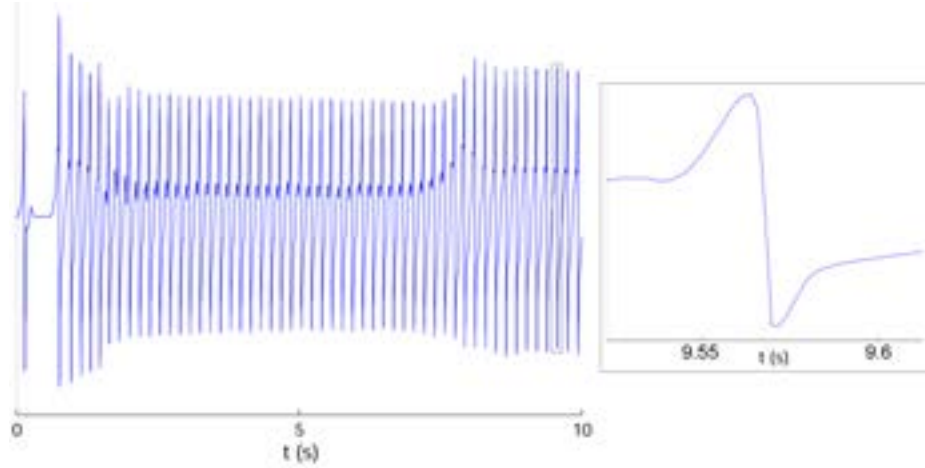


Figure 6.3: Pseudo-EGM signal measured at one of the 49 electrodes during a simulation of 10 s duration (left). Example of LAW obtained from the pEGM signal (right).

Regarding the analysis of calcium dynamics, both the average of the calcium transient duration (CaT) and the average of the maximum diastolic calcium concentration (CaT_{max}) were calculated.

6.2.5 Ann-Arbor Database

In order to validate our simulation results, we compared them with a set of intracardiac recordings provided by the Ann Arbor database [Ann Arbor Electrogram Libraries, Chicago, IL, USA]. Only recordings of patients with AF were analyzed in this study. Furthermore, out of all the registered signals (ECG leads and EGM at different points on cardiac surface), in this thesis we focused on the 20 unipolar EGM registered on either the HRA or the RAPG, since the rest of the signals in the database were registered in other parts of the cardiac surface different from that of the atria. The sampling rate used for signal acquisition was 1000 Hz.

The signal processing techniques described in section 6.2.4 were applied to calculate DF, OI and RI. CP was not calculated as only one EGM signal per patient was available.

6.3 Results

6.3.1 Parasympathetic Influence on Fibrillatory Dynamics

As shown in Figure 6.4, the level of [ACh] led to different propagation patterns through the atria. When [ACh] was set to 1 nM in the whole atria, the reentrant behavior was sustained by two main rotors located near the RPV and the RAPG, whereas when [ACh] was 5 nM, there was one main rotor at the RAPG and a few secondary rotors lasting for a few seconds (around the left pulmonary veins (LPV)) or being blocked by the main rotor (in the superior vena cava (SVC) or the mitral valve (MV)). DF distribution throughout the tissue was almost uniform due to the highly stable rotors when both [ACh] levels were simulated, but on average its value was slightly reduced for 5 nM (DF about 5.92 Hz) compared to 1 nM (DF about 6.15 Hz). The organization and regularity of the simulated arrhythmias were analyzed by calculating OI, RI and CP indices on the pEGM. OI distribution was also very homogeneous for both values of [ACh], taking higher values for [ACh]=1 nM. Regarding RI and CP, they were generally much lower when [ACh] was 5 nM due to the effects of temporary rotors on closely located pEGM (Figure 6.5).

6.3.2 Ionic Modulation of Reentrant Behavior in Human Atria

The effects of alterations in the ionic mechanisms unraveled in previous studies on AF dynamics were investigated to assess their relevance as potential targets of anti-AF drugs. As expected from our results shown in chapter 4 on cell and tissue properties, I_{K1} , I_{Na} and I_{NaK} modulate fibrillatory properties and rotor dynamics. It is important to remark that, once the re-entrant wavefronts were generated following the applied stimuli, the fibrillatory

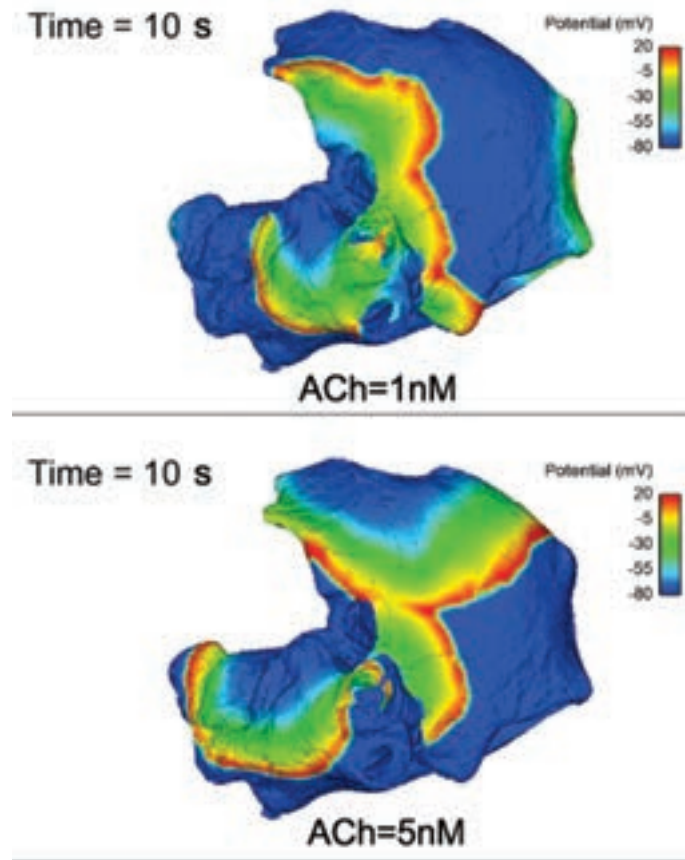


Figure 6.4: Dorsal view of the atria. V_m map after 10 seconds of simulation for AF when $[ACh]=1$ nM (top panel) and 5 nM (bottom panel).

behavior remained self-sustained for the duration of the simulation.

Figure 6.6 shows similar V_m map patterns following 10 seconds of simulation for AF (with the AF-remodeled version of the Maleckar model) and following 30% I_{K1} inhibition, 15% I_{Na} inhibition and 30% I_{NaK} inhibition over the AF-remodeled version of the Maleckar model. The centers of the main rotors were usually located near the RPV and the RAPG, and secondary rotors usually appeared close to the SVC and the MV.

Regarding DF results, its distribution was very homogeneous in all the simulations because the main rotors predominated over possible secondary rotors entailing certain periodicity of cell activation in all the atrial tissue. Inhibition of I_{Na} led to significantly smaller DF values (5.27 Hz in average), whereas I_{K1} and I_{NaK} inhibitions reduced DF slightly (5.66 Hz and 5.76 Hz, respectively, in average).

Figure 6.7 shows maps of the 49 OI and RI obtained from the pEGM and

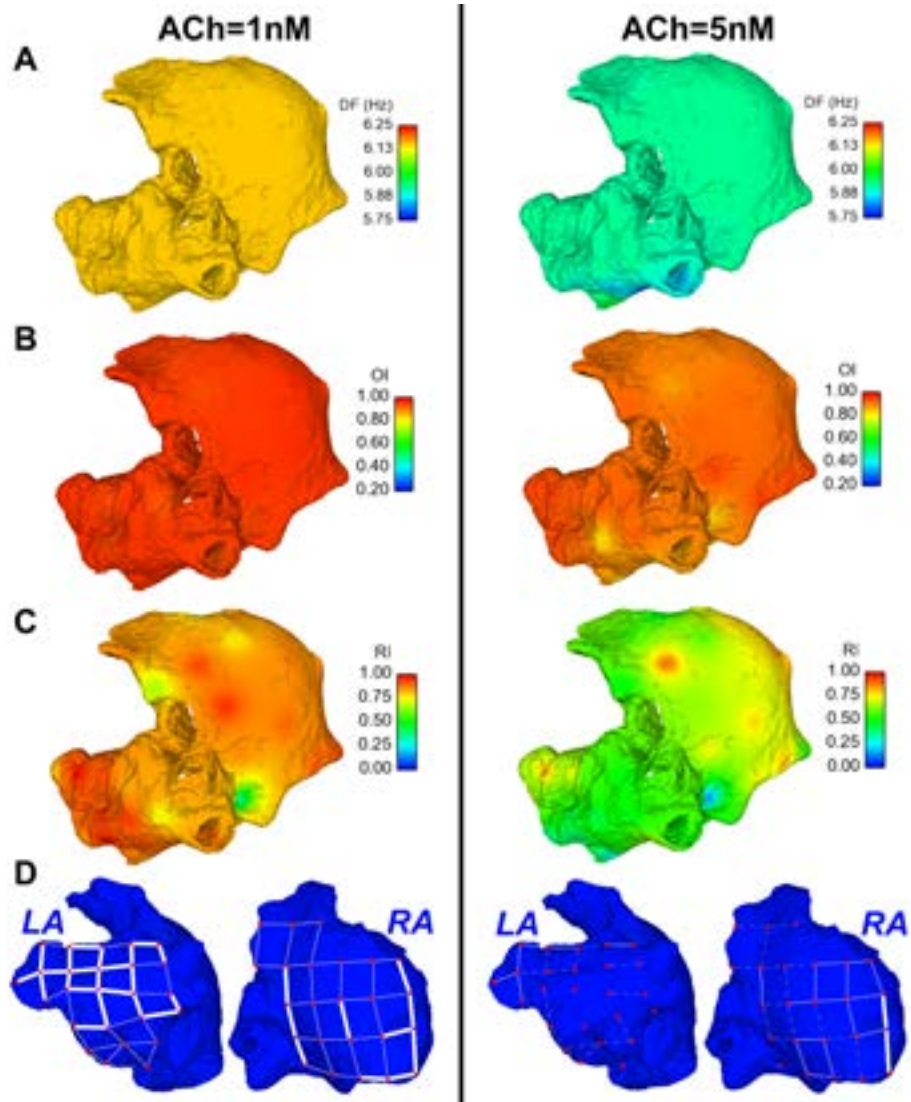


Figure 6.5: Dorsal view of the atria. Interpolated maps of DF (A), OI (B), RI (C) and CP (D) for $[ACh]=1\text{ nM}$ (left) and $[ACh]=5\text{ nM}$ (right).

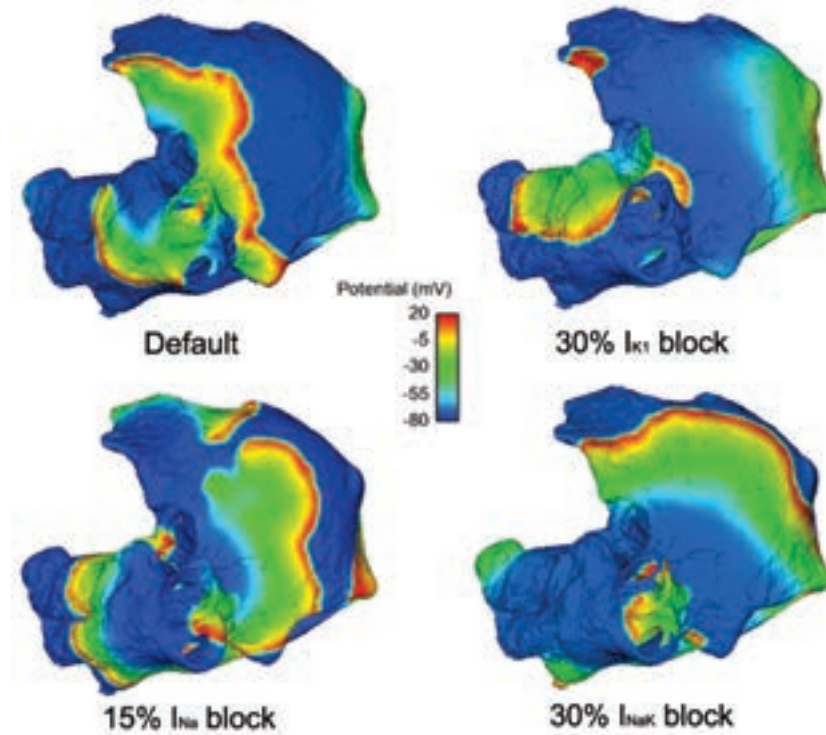


Figure 6.6: Dorsal view of the atria. V_m map after 10 seconds of simulation for AF, and following 30% I_{K1} inhibition, 15% I_{Na} inhibition and 30% I_{NaK} inhibition in AF, respectively.

their interpolation for all the cells in the model. Regarding OI distribution, it was almost uniform in all the simulated conditions, only being reduced near the SAN when I_{Na} was inhibited. Inhibition of I_{K1} led to a slight increase in RI around the RPV, but reduced organization in the LA. In contrast, inhibition of I_{Na} significantly increased organization in the LA, but reduced RI in the RA. Inhibition of I_{NaK} notably reduced RI in both atria.

6.3.3 Impact of Inter-subject Variability in Cell Repolarization on AF Dynamics

In this part of the thesis, the effects of inter-subject variability in cell repolarization on AF dynamics in 3D human atria were analyzed. AF dynamics and the extracted indices were compared between the simulations with the six sub-populations (with variability) and also with the 3D simulation using the AF-remodeled version of the Maleckar model that was used to generate the population of models (with no variability). The results obtained in the

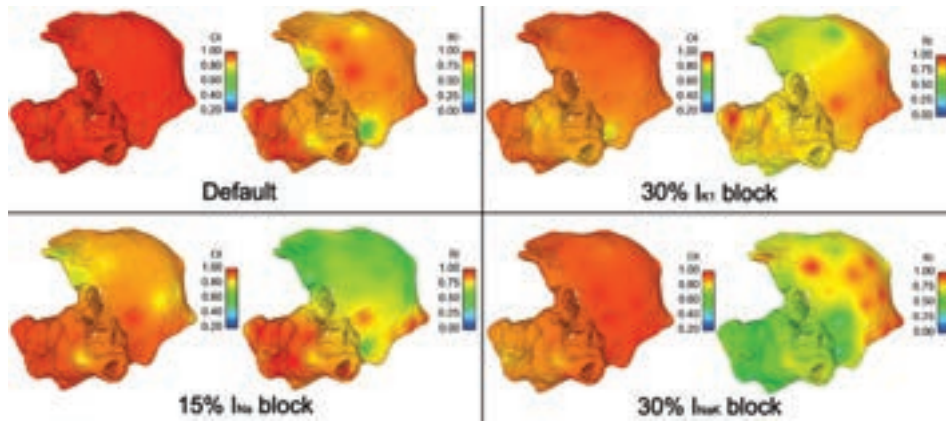


Figure 6.7: Dorsal view of the atria. Interpolated OI (left) and RI (right) map for default conditions (permanent AF), 30% I_{K1} inhibition, 15% I_{Na} inhibition and 30% I_{NaK} inhibition, respectively.

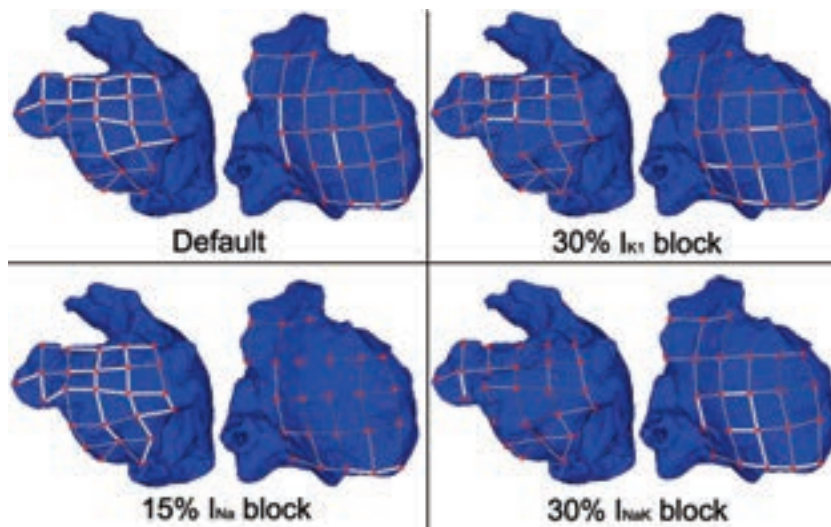


Figure 6.8: Coupling between pEGM in adjacent electrodes for LA (left) and RA (right) for default conditions (permanent AF), 30% I_{K1} inhibition, 15% I_{Na} inhibition and 30% I_{NaK} inhibition, respectively. Thick white lines represent $CP \geq 0.9$, thin solid lines represent $0.75 \leq CP < 0.9$ and soft gray lines represent $0.6 \leq CP < 0.75$. $CP < 0.6$ is represented by absence of lines.

simulation with no variability were used as a reference in the analysis of the results obtained with the other simulations including variability. The model with no variability could be seen as an "average permanent AF patient" in terms of cellular properties.

Fibrillatory behavior in the simulation with no variability was sustained by two main reentrant rotors located near the RPV and the RAPG. Figure 6.9 shows that the DF distribution throughout the tissue was almost uniform in each atrium due to the highly stable rotors, but DF was on average 0.69 Hz higher in the LA than in the RA (5.52 vs. 4.81 Hz). Regarding OI and RI, both markers exhibited higher values in the LA: OI was above 0.8 in both atria (except for a small area near the BB), whereas RI was more heterogenous taking high values near the RPV (0.75), but lower than 0.3 in areas around the BB and the RAPG. These areas with low RI were associated to either propagation block or collision between wavefronts. Regarding calcium dynamics, CaT was about 156 ms in the LA and 181 ms in the RA, while CaT_{max} was about 40 μM in all the tissue except for the RAPG where it was slightly above 50 μM .

Analogously to the 3D model with no variability, the six models representing cell repolarization variability could be seen as six different permanent AF patients with specific cellular properties. Comparing the two sub-populations with short and long APD_{90} , propagation was chaotic with some reentrant rotors coexisting for the short APD_{90} sub-population. Fibrillatory activity was sustained by one rotor in RA for the long APD_{90} sub-population. DF was higher for the short APD_{90} sub-population, particularly in the LA. OI was high for both sub-populations. Both RI and CP were very low in most of the tissue for the short APD_{90} sub-population, but notably higher for the long APD_{90} sub-population (Figures 6.10 and 6.11). Regarding calcium dynamics, the short APD_{90} sub-population showed much shorter CaT, but only slightly lower CaT_{max} with respect to the long APD_{90} sub-population (Figure 6.12). To sum up, the long APD_{90} sub-population was associated with more stable arrhythmias with slower activation frequency than those with the short APD_{90} sub-population.

Short and long APD_{50} simulations showed significant differences in both DF and OI calculated in the RA, due to inter-atrial propagation block occurring in one out of three wavefronts from the LA to the RA for the long APD_{50} simulation. However, RI and CP were similar between both scenarios (Figures 6.10 and 6.11). Calcium transients also showed notable differences between both simulations, being much longer and reaching higher concentration values for the long APD_{50} sub-population (Figure 6.12). To sum up, variability in APD_{50} did not entail important effects on the calculated indices, except for those derived from inter-atrial propagation block that occurred for some wavefronts with the long APD_{50} sub-population.

Finally, simulations with short and long APD_{20} sub-populations showed

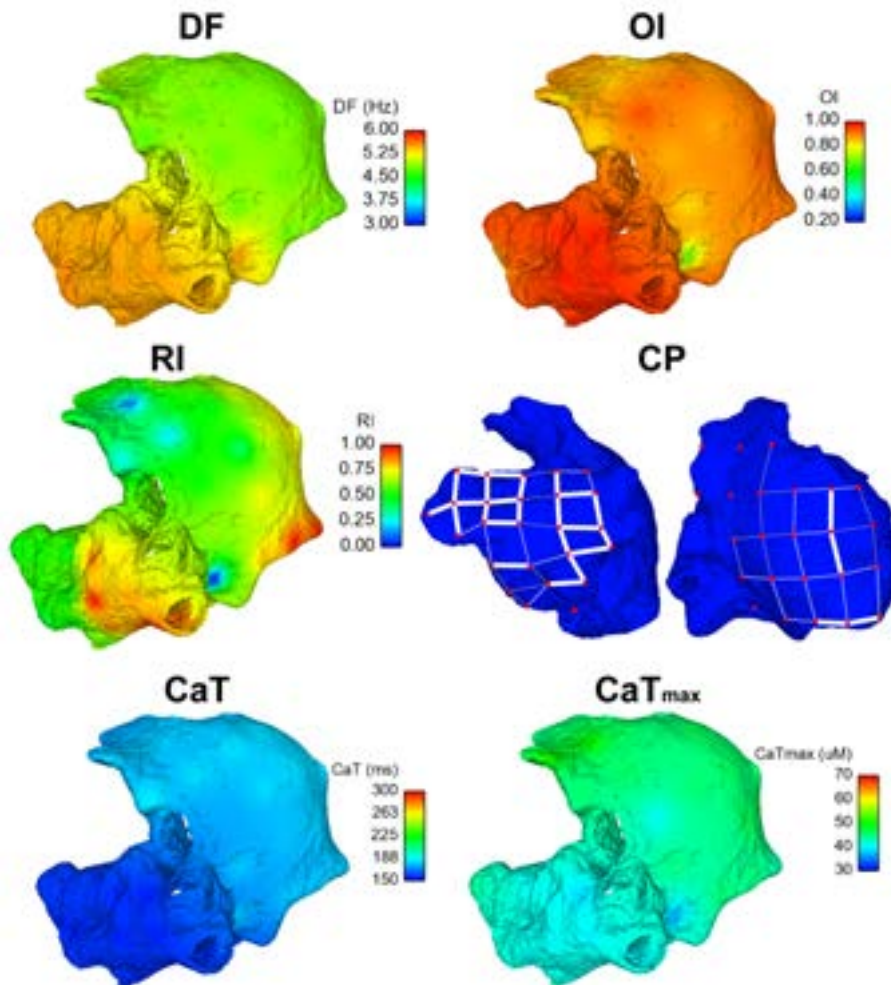


Figure 6.9: Dorsal view of the atria. Interpolated DF (top-left), OI (top-right), RI (middle-left), CP (middle-right; thick white lines represent $CP \geq 0.9$, thin solid lines represent $0.75 \leq CP < 0.9$ and soft gray lines represent $0.6 \leq CP < 0.75$. $CP < 0.6$ is represented by absence of lines), CaT (bottom-left) and CaT_{max} (bottom-right) for AF conditions with no variability.

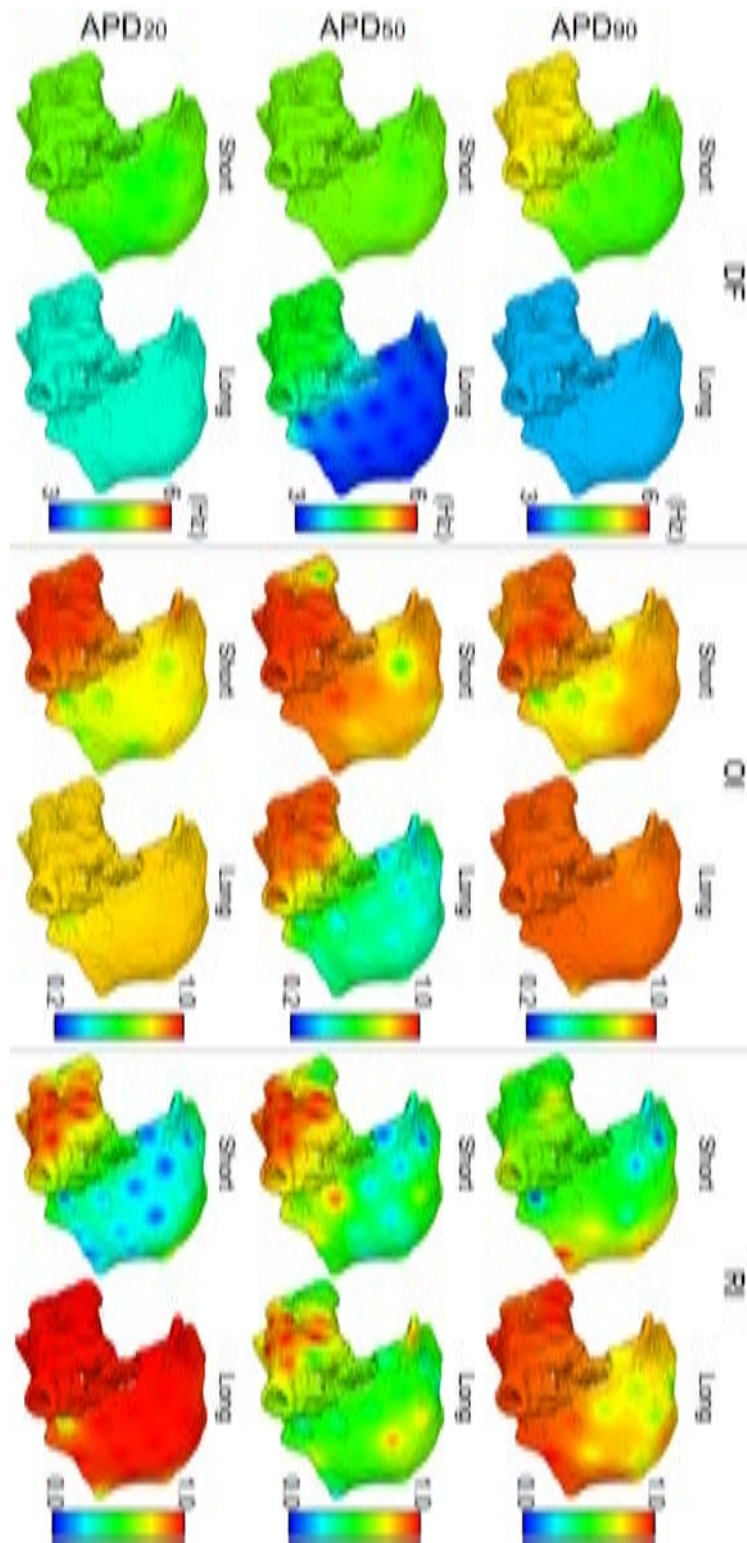


Figure 6.10: Dorsal view of the atria. Interpolated maps of DF, OI and RI for short and long APD₉₀, APD₅₀ and APD₂₀ sub-populations of models, respectively.

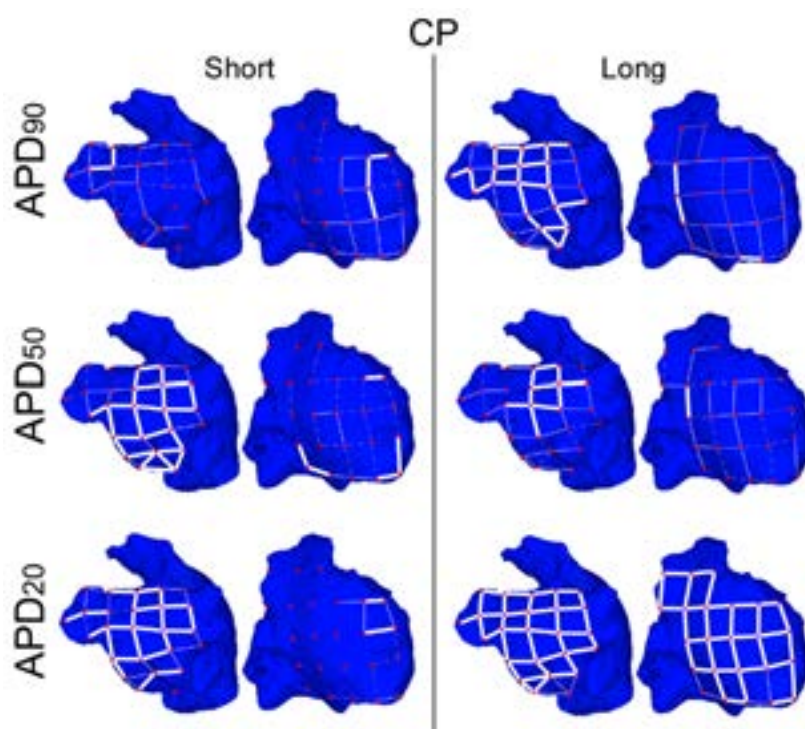


Figure 6.11: Dorsal view of the atria. CP between pEGM in adjacent electrodes for LA (left) and RA (right) for short and long APD₉₀, APD₅₀ and APD₂₀ sub-populations of models, respectively. Thick white lines represent $CP \geq 0.9$, thin solid lines represent $0.75 \leq CP < 0.9$ and soft gray lines represent $0.6 \leq CP < 0.75$. $CP < 0.6$ is represented by absence of lines.

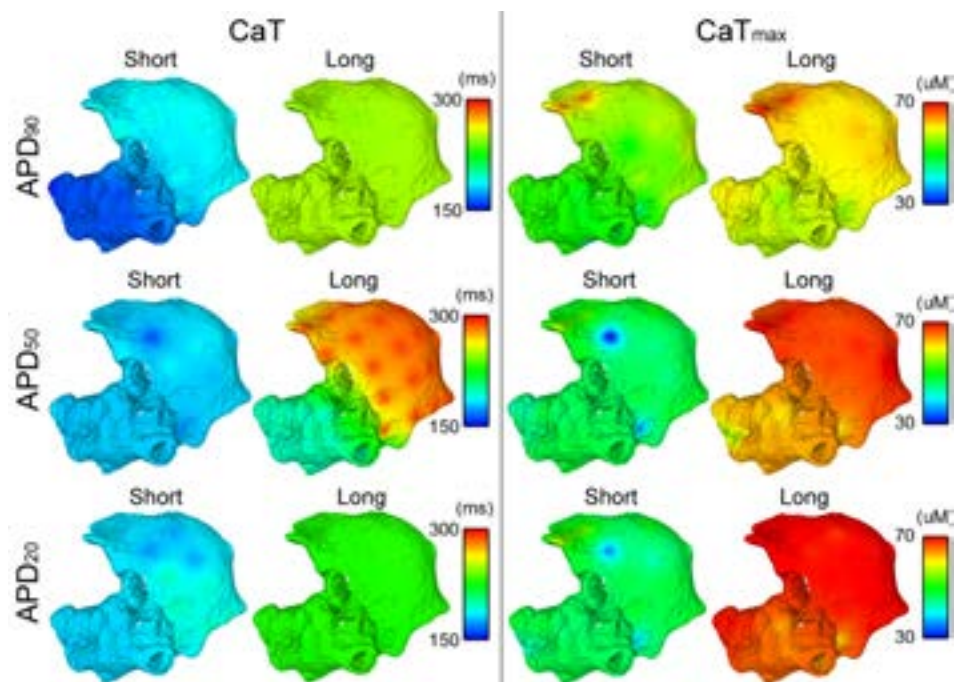


Figure 6.12: Dorsal view of the atria. Interpolated CaT and CaT_{max} for short and long APD_{90} , APD_{50} and APD_{20} sub-populations of models, respectively.

notable dissimilarities in the fibrillatory pattern. The simulation with short APD_{20} behaved similarly to that with short APD_{50} , but with a more chaotic propagation in the RA, as shown by the lower values of both OI and RI (Figures 6.10 and 6.11). Regarding the long APD_{20} , there was only one main rotor, with low DF, high OI, high RI and high CP in all the tissue (Figures 6.10 and 6.11), which stopped propagating after 6.3 seconds of simulation due to inter-atrial conduction block. Calcium transient was homogeneously distributed in both simulations, but significantly shorter and reaching lower maximum concentration values for short APD_{20} (Figure 6.12). To sum up, the long APD_{20} sub-population was associated with very regular and organized activation patterns as compared with those with the short APD_{20} sub-population.

6.3.4 Validation of Simulation Results with EGMs from AF Patients

Figure 6.13A shows 20 points corresponding to the values of the three markers (DF, OI and RI) calculated in each of the 20 EGM registered at the HRA in AF patients. Regarding DF, the values obtained were in a range between 3.84 and 6.56 Hz (Figure 6.13B), in good agreement with the range of DF obtained from all the simulations described in the previous sections of this chapter (see Figures 6.5, 6.9 and 6.10). Similarly, the ranges of OI (from 0.27 to 0.89) and RI (0.4 to 1), shown in Figure 6.13B, were practically the same as those obtained in the different simulations in this chapter (see Figures 6.5, 6.7, 6.9 and 6.10).

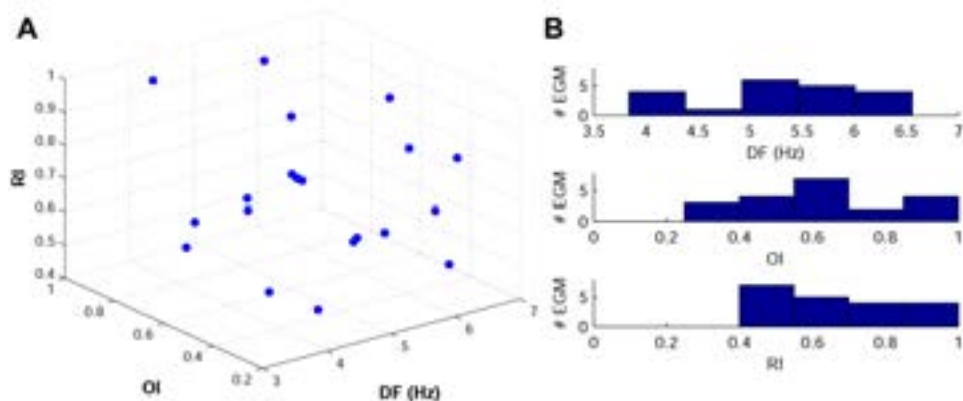


Figure 6.13: Scatter plot of DF, OI and RI calculated from the 20 EGM at the HRA in AF patients (A) and the corresponding histograms showing the number of EGMs for different intervals of DF, OI and RI (B).

6.4 Discussion

The results obtained in this chapter confirmed the importance of the parasympathetic system, through the inclusion of [ACh], on the modulation of AF dynamics. High levels of [ACh] significantly shortened both cellular APD and tissue RP, thus allowing several wavelets to propagate simultaneously as occurs in AF [28]. The simulations showed that high [ACh] levels promoted disorganization of arrhythmia despite not entailing very significant changes in DF.

Furthermore, in this study the relevance of certain ionic currents in modulating arrhythmic markers was confirmed (DF, OI, RI and CP). These markers can also be used in clinical practice with real EGMs in order to guide anti-arrhythmic therapies, such as ablation procedures. The main advantage of this technique was the capability of fully characterize the whole atria with only 49 electrodes. Regarding the ionic current alteration effects, changes in I_{Na} and, to a lesser extent, I_{K1} and I_{NaK} induced important effects on arrhythmogenesis in atrial tissue. Their inhibition led to an anti-arrhythmic decrease in DF, more prominent when the inhibited ionic current is I_{Na} than when I_{K1} or I_{NaK} were inhibited. Organization and regularity of fibrillatory waves were increased in the LA if an inhibition of I_{Na} was simulated, whereas reduction in either I_{K1} or I_{NaK} led to more disorganized electrical propagation in the LA. In contrast, inhibitions of I_{K1} or I_{NaK} maintained organization of the waves in the RA, whereas I_{Na} inhibition reduced RI and CP in this heart chamber.

Previous studies have remarked that smaller I_{K1} in human atria may lead to deceleration and decreased stability of rotors, as occurred in our study, but entails depolarized RMP associated with increased susceptibility to arrhythmias [125]. This is in agreement with our results showing highly organized arrhythmias with areas of low regularity when I_{K1} was inhibited.

I_{Na} inhibition effectively slows down CV, increases WL of reentrant circuits and reduces DF [120], in agreement with the results of the present study. However, the possible side effects on ventricular electrophysiology of sodium channel blockers highlight the necessity of finding more effective atrial selective therapies.

Regarding I_{NaK} , it is shown that alterations in the activity of the NaK pump in atrial tissue induced slight effects on fibrillatory dynamics and organization, despite its key role on cellular APD and rate adaptation, as shown in chapter 4.

In the study of the effects of inter-subject variability on AF-related markers, seven whole human atrial models with specific variability in cell repolarization dynamics were used: 1 corresponding the AF-remodeled version of the Maleckar model and 6 corresponding to the six-subpopulations extracted according to their APD. A more heterogeneous tissue has been associated in

previous studies with slower reentrant circuits, thus favoring the generation of secondary rotors and wavelets [51]. The simulations conducted in the present thesis showed notable differences in fibrillatory behavior between rapid and slow repolarization dynamics, with the results being highly dependent on the stage of atrial cell repolarization under investigation.

In this regard, differences in the final phase of repolarization (APD_{90}) led to significant changes in the fibrillatory pattern and therefore in the modulation of DF, RI and CaT, in good agreement with the effects of pharmacological interventions targeting ionic currents involved in this phase, such as I_{K1} , I_{NaK} , I_{Kr} or I_{Ks} (see section 1.3.3.1 of this thesis).

Differences in the middle repolarization phase (APD_{50}) highly influenced the propagation pattern, including inter-atrial conduction block when APD_{50} is long, leading to significant inter-atrial differences in DF, OI, and CaT. CaT_{max} was also strongly modulated by APD_{50} variability, as expected by the role of I_{CaL} in this repolarization phase.

Analysis of the initial phase of repolarization (APD_{20}) was similar to that of the middle phase, with the exception of the total propagation block of the reentrant circuit that occurred after 6.3 seconds of simulation when the APD_{20} was long. Differences in RI and CaT_{max} were explained by the role of ionic currents involved in this repolarization phase, particularly I_{to} , I_{Kur} and I_{CaL} .

6.4.1 Limitations of the Study

In this chapter of the thesis, reentrant behavior was generated using a particular stimulation protocol consisting of periodic stimuli applied at the SAN followed by 6 extra-stimuli near the RPV. However, AF in clinical practice may present multiple ectopic foci that trigger and sustain the arrhythmia, whereas their location may be variable as well.

Regarding the database used for experimental validation, only 20 EGMs of AF patients were recorded in either HRA or RAPG. An increase in both the number of recordings and the number of electrode locations in atrial surface would improve the accuracy of the validation of the simulations.

Another limitation of this study is the small number of virtual electrodes used (49) thus leading to visible interpolation artifacts. This number was the result of mapping both atria, LA and RA, with a precision of about 1 cm. Precision was high enough to properly characterize the arrhythmic behavior since the electrical propagation wavefronts were much coarser than the separation between adjacent electrodes.

As a final remark, the random assignment of a specific model within each sub-population to each cell in the 3D model could potentially lead to neighboring cells with very different electrophysiological properties. This effect was however reduced for two reasons: 1) variability in the AP within

each sub-population was relatively small (first and fourth quartiles of the subpopulations were chosen to represent the slight variability present within one subject); 2) the electrotonic coupling between cells strongly smoothed electrical gradients during propagation.

Chapter 7

Conclusions and Future Extensions

7.1 Conclusions

The results presented in this thesis improve the understanding of the mechanisms underlying properties related to human atrial arrhythmias through the use of cardiac computational modeling techniques. In this section the specific conclusions drawn through the chapters of this thesis are summarized.

7.1.1 Ionic Mechanisms Underlying Human Atrial Electrophysiology Markers in SR

Measurable markers in individual cardiomyocytes and cardiac tissue provide useful knowledge about the likelihood of arrhythmia generation. In this thesis, we unravel the ionic mechanisms underlying electrophysiological properties in human atria in order to improve the limited understanding of the intrinsic changes underlying AF and help in the design of new anti-arrhythmic therapies.

Among these properties, we start studying the ability of cardiac cells to adapt to changes in HR since its impairment has been related to higher arrhythmic risk. This property has been previously studied in ventricular cells and therefore its characterization understanding of the underlying mechanisms in atrial cells complements the knowledge of cellular rate adaptation in the whole heart. In this thesis, we calculate APD during the course of a pacing protocol simulating sudden and sustained changes in HR. We have confirmed that atrial APD adaptation takes several minutes to complete and consists of two different phases: an initial fast phase lasting for a few seconds (with an associated time constant τ_{fast} between 6 and 8 s, depending on the HR change (acceleration or deceleration)) followed by a slow phase lasting

for several minutes (time constant, τ_{slow} , between 4 and 7 minutes). Slight quantitative differences in the characterization of APD rate adaptation, i.e. different values of APD and time constants, are found between human atrial models.

The ionic mechanisms underlying both phases of APD rate adaptation are different. In the fast phase, the maximal activity of the $NaCa$ exchanger and the conductance of I_{CaL} are responsible for the abrupt alteration of the APD value during the first seconds following the HR acceleration or deceleration. Regarding the slow phase, intracellular sodium dynamics, $[Na^+]_i$, modulate slow accommodation of APD. The NaK pump plays an important role in $[Na^+]_i$ dynamics, and thus is key in the modulation of the slow APD adaptation. These mechanisms are different from those obtained in human ventricular cells regarding the fast phase of adaptation, where the activation kinetics of I_{CaL} and the inactivation kinetics of I_{Ks} were identified as the major determinants. However, the ionic mechanisms modulating the slow adaptation are consistent in cells from both cardiac cavities, being $[Na^+]_i$ and NaK pump the most relevant players in both cases.

Regarding the relationship between APD adaptation and arrhythmogenesis, protracted APD adaptation to changes in HR has been associated with higher arrhythmic risk in the ventricle and have been investigated here in the human atrium. Conditions entailing longer time constants for both the fast phase and the slow phase of adaptation are related to higher likelihood of generating atrial arrhythmias, as shown by the markers studied in this thesis: calcium current reactivation, AP triangulation and slopes of APDR curves.

To extend the analysis of the ionic mechanisms underlying arrhythmia-related properties, we also quantify the relative importance of ionic current conductances and kinetics in modulating AP (APD and RMP) and APD restitution curves in single human atrial cell, and refractoriness (RP), CV and rotor dynamics (WL, PS and VW) in human atrial tissue. The analysis performed in this thesis uncovers G_{NaK} as a key modulator of refractoriness and rotor dynamics in human atria and confirms G_{K1} and G_{Na} as important determinants of AF-related electrophysiological properties. Simultaneous changes in these three ionic properties are also studied in this thesis to assess their effects on the dynamics and vulnerability of human atrial tissue to reentrant arrhythmias. We evaluate vulnerability to reentries by calculating the range of CIs between consecutive stimuli leading to stable rotors. This vulnerability is found to be minimized by simultaneous reduction in both G_{K1} and G_{NaK} and increase in G_{Na} , while the lowest reentrant frequency is obtained when G_{K1} , G_{NaK} and G_{Na} are simultaneously reduced.

Furthermore, in this thesis we analyze the temporal adaptation that occurs following the application of an ionic change, since in most cases the steady-state is not reached instantaneously. Changes in G_{NaK} entail bipha-

sis adaptation of the electrophysiological markers studied, while adaptation is monophasic when changes in the rest of the ionic properties are simulated. The relevance of G_{NaK} in modulating atrial electrophysiology is anticipated to have important implications for the interpretation of the efficacy of anti-AF drugs that interfere with G_{NaK} , such as amiodarone and digitalis.

7.1.2 Ionic Mechanisms Underlying Human Atrial Electrophysiology Markers in AF Conditions

In order to study the effects of the changes associated with AF on the ionic mechanisms underlying atrial electrophysiology, AF-remodeled versions of the models are used in this thesis. Simulation results are compared to those obtained in SR.

Overall, similar results regarding the ionic mechanisms underlying atrial electrophysiological markers are obtained in AF conditions with respect to SR, but with smaller effects of ionic current changes on atrial electrophysiology in AF. This may explain the reported lower efficacy of pharmacological interventions targeting ionic currents in the treatment of long-term versus short-term AF patients. Regarding the ionic mechanisms underlying electrophysiological properties, the most significant changes in AF with respect to SR are: enhanced relevance of G_{K1} in modulating APD restitution, increased importance of G_{Na} in modulating tissue refractoriness and reduced relative importance of G_{CaL} .

The in-depth characterization of the ionic basis of atrial electrophysiology and AF-related mechanisms provided in this thesis could guide the identification of more effective therapies against AF.

7.1.3 Ionic Mechanisms Underlying Inter-subject Variability in Human Atrial AP

In the first parts of this thesis, cardiac computational models with no variability are used to ascertain the ionic mechanisms underlying electrophysiological properties related to arrhythmic risk. However, inter-subject variability present in nature is often responsible for both the different likelihood of arrhythmia generation and the different response to anti-arrhythmic agents between patients. Variability in APD at different repolarization stages (APD₉₀, APD₅₀ and APD₂₀) and variability in AP morphology (calculated as the difference between APD₉₀ and APD₅₀) are particularly notable in both SR and AF patients: APD₉₀ ranges from about 190 ms to 440 ms in SR and from about 140 to 330 in AF, APD₅₀ ranges from about 6 ms to 200 ms in SR and from about 30 ms to 180 ms in AF and APD₂₀ ranges from about 1 ms to 60 ms in SR and from about 140 ms to 330 ms in AF. The ionic determinants of this variability in SR and AF patients are investigated in the present thesis. To do so, we design a computational model population-based

approach developed based on a large range of human atrial electrophysiological recordings: 469 AP recordings corresponding to 363 patients with SR (214 patients with paroxysmal, recent onset or non-signs of AF) and with AF (149 patients with permanent AF for longer than 6 months at the time of tissue collection). We use three atrial AP models as a reference to generate populations of models in SR and AF conditions by simulating 2275 combinations of the six ionic conductances previously unraveled in this thesis as exerting the strongest effects on atrial properties: G_{K1} , G_{NaK} , G_{CaL} , G_{to} , G_{Kur} and G_{NaCa} .

Analysis of model populations reveals that the main ionic mechanisms modulating inter-subject variability in the different stages of repolarization of the AP are similar in SR and AF. In both populations of models, G_{CaL} , G_{to} and G_{Kur} are key in modulating inter-subject differences in APD_{20} and APD_{50} , whereas G_{K1} and G_{NaK} determine patient-specific values of APD_{90} , in good agreement with their key role in APD modulation ascertained in previous parts of this thesis. The unraveled ionic mechanisms underlying variability in AP morphology are G_{K1} , G_{NaK} and G_{NaCa} .

Simulation results of this part of the thesis are slightly dependent on the computational model taken as reference to generate the populations. Different relevance in the role of G_{CaL} in modulating variability in APD_{90} and of both G_{K1} and G_{NaK} in modulating variability in APD_{20} was observed.

The populations of human atrial cell models are used to provide information on the ionic mechanisms of variability, which may underlie AP measurements. Elucidating ionic mechanisms underlying inter-subject variability in atrial electrophysiological properties may be crucial in the understanding of inter-subject differences in human atrial dynamics and the response to anti-AF pharmacological therapies.

7.1.4 Ionic Mechanisms Underlying AF Dynamics in 3D Virtual Human Atria

The use of realistic 3D atrial models is very useful to analyze arrhythmic dynamics from a macroscopic point of view close to what occurs in real hearts. Since a whole atria is a combination of thousands of cells and tissues with specific properties, the simulation results obtained in previous parts of this thesis are useful to guide simulations in 3D virtual human atria.

In the last part of this thesis, the role of ionic currents in modulating AF dynamics in realistic 3D atrial models is determined. We simulate arrhythmic behavior by applying rapid pacing near PV. Then, the distribution of DF, organization and morphological regularity of the arrhythmia are calculated through signal processing of pEGM signals recorded at different points of atrial surface.

Since the main mechanisms modulating atrial cell and tissue properties

are G_{K1} , G_{NaK} and G_{Na} , as previously described in the thesis, changes in these ionic properties are investigated in realistic 3D atrial models. Simulations confirm the potential interest of developing atrial selective anti-AF drugs aiming at inhibiting either G_{K1} or G_{Na} or G_{NaK} . Inhibition of any of these ionic current conductances reduces DF, in good agreement with the results shown in previous parts of the thesis, whereas the regularity and organization of the electrical propagation increase in the LA when G_{Na} is reduced, but not when either G_{K1} or G_{NaK} are inhibited. Effects of ionic changes on the electrical activity in the RA are negligible.

Furthermore, since the activity of the parasympathetic system has been suggested to play a role in modulating AF dynamics via the modulation of APD and tissue refractoriness, this is evaluated in this thesis through the simulation of different levels of [ACh]. Simulations show that high [ACh] levels promote more disorganized activation patterns, whereas their effect on DF is not significant.

As previously stated, inter-subject variability plays a key role in both arrhythmogenesis and response to anti-arrhythmic drugs between different patients. Furthermore, the analysis of inter-subject variability in 3D virtual human atria contributes to improve our understanding of concurrent mechanisms promoting and maintaining AF. In this part of the thesis, we simulate six realistic human atria with different cell repolarization dynamics. In order to do this, populations of models in AF are generated to represent inter-subject variability in AF patients, and then six sub-populations of models are extracted out of the whole population according to their values of APD₂₀, APD₅₀ or APD₉₀. Those models in the first quartile are classified as associated with short repolarization, and those models in the fourth quartile are classified as associated with long repolarization. Simulations show that patients with long atrial APD present slow but very regular fibrillatory patterns, whereas short APDs may entail high frequency reentrant rotors and higher organization. Furthermore, fibrillatory dynamics and electrical propagation depend on the specific repolarization characteristics of each subject: short APD₂₀, long APD₂₀, short APD₅₀, long APD₅₀, short APD₉₀ and long APD₉₀.

7.2 Future Extensions

Some of the possible future research lines identified during the development of this thesis are:

1. *New 3D atrial models and fibrosis.* In this thesis we have used one 3D atrial model as a basis for our investigations, but it would be worthwhile exploring if significant differences are found when using refined 3D meshes or distinct anatomical structures. Furthermore, it

would be of interest to include the effects of fibrosis in the 3D models, whose generation is closely related to AF structural remodeling, so as to more realistically investigate atrial tissue characteristics under AF conditions.

2. *Whole heart model.* One of the most challenging tasks in the development of human heart models is the generation of a unique 3D model including the four cavities and the Purkinje system. Most studies use models from ionic to 3D levels for either the atria, as done in this thesis, or the ventricles or the Purkinje system, but not all of them together. This would provide a global view of the behavior of the human heart under physiological or pathophysiological conditions.
3. *Electromechanic effects.* In this thesis, we have only focused on electrophysiological aspects of atrial activity. The effects of heart movements during its contraction-relaxation course could be investigated through the use of more complex human atrial models with the ability of being deformable in order to simulate more realistic cardiac behavior.
4. *Torso model.* In this thesis, electrical signals measured on the atrial surface of a 3D atrial model are analyzed, representing EGM signals. The use of a torso model would provide the possibility of computing simulated signals on the body surface, which could then be compared with ECG recordings of AF patients.
5. *Patient-specific models.* In this thesis, inter-subject variability has been proven to be relevant in the study of arrhythmogenesis, with different patients showing different proneness to suffer an arrhythmia. Therefore, a promising future line could be to investigate and generate electrophysiological models adapted to each specific patient aiming at improving the treatments and therapies to apply.
6. *Populations of models to study dependence on gender.* We have studied and compared populations of models in SR and AF, but other aspects such as gender could be included in the populations to specifically investigate their contribution to arrhythmogenesis. As regards gender, experimental studies have proven the existence of differences in the mRNA between atrial cells in male vs. female patients. The analysis of the differences between male and female in the ionic mechanisms underlying atrial electrophysiology and their relation to arrhythmic risk could be a matter of future investigations, particularly considering that the incidence of AF is significantly higher in men than in women.

Glossary

1D	One-dimensional
2D	Two-dimensional
3D	Three-dimensional
ACh	Acetylcholine
[ACh]	Acetylcholine concentration
AF	Atrial fibrillation
AP	Action potential
APA	AP amplitude
APD	AP duration
APD ₂₀	APD at 20% repolarization
APD ₅₀	APD at 50% repolarization
APD ₉₀	APD at 90% repolarization
APDR	APD restitution
ATP	Adenosine triphosphate
AVR	Atrioventricular ring
[Ca ²⁺] _i	Intracellular calcium concentration
[Ca ²⁺] _o	Extracellular calcium concentration
[Ca ²⁺] _{rel}	Calcium concentration in release compartment
[Ca ²⁺] _{up}	Calcium concentration in uptake compartment
CaT	Calcium transient
CaT _{max}	Maximum concentration during CaT
CBC	Carbamylcholine
CFAE	Complex fractionated atrial EGM
CI	Coupling interval
CL	Cycle length
C _m	Membrane capacitance
[Cm _{dn}] _{max}	Total calmodulin concentration in myoplasm
C _{m,p}	Parameter value for sensitivity analysis
CP	Coupling index between pairs of EGMs
CT	Cresta terminalis
CTI	Cavotricuspid isthmus
CV	Conduction velocity
<i>d</i>	Activation gating variable of <i>I_{CaL}</i>

D	Diffusion coefficient
DAD	Delayed afterdepolarization
DF	Dominant frequency
dV/dt_{max}	Maximum AP upstroke velocity
$d(\hat{x}_i, \hat{x}_j)$	Accumulated difference between \hat{x}_i and \hat{x}_j
EAD	Early afterdepolarization
E_{Ca}	Equilibrium potential for calcium ions
ECG	Electrocardiogram
EGM	Electrogram
E_K	Equilibrium potential for potassium ions
E_{Na}	Equilibrium potential for sodium ions
f	Inactivation gating variable of I_{CaL}
F	Faraday constant
f_c	Cutoff frequency
f_{Ca}	Calcium-dependent inactivation gating variable of I_{CaL}
FO	Fossa ovalis
f_v	V_m -dependent variable of I_{NaK}
g_{bCa}	Constant conductance associated with $I_{b,Ca}$
g_{bNa}	Constant conductance associated with $I_{b,Na}$
g_{CaL}	Constant conductance associated with I_{CaL}
G_{CaL}	Maximal conductance associated with I_{CaL}
g_{K1}	Constant conductance associated with I_{K1}
G_{K1}	Maximal conductance associated with I_{K1}
G_{KACH}	Maximal conductance associated with I_{KACH}
g_{Kr}	Constant conductance associated with I_{Kr}
G_{Kr}	Maximal conductance associated with I_{Kr}
g_{Ks}	Constant conductance associated with I_{Ks}
G_{Ks}	Maximal conductance associated with I_{Ks}
g_{Kur}	Constant conductance associated with I_{Kur}
G_{Kur}	Maximal conductance associated with I_{Kur}
g_{Na}	Constant conductance associated with I_{Na}
G_{Na}	Maximal conductance associated with I_{Na}
G_{NaK}	Maximal conductance associated with I_{NaK}
G_{NaCa}	Maximal conductance associated with I_{NaCa}
g_{to}	Constant conductance associated with I_{to}
G_{to}	Maximal conductance associated with I_{to}
h	Inactivation gating variable of I_{Na}
hERG	I_{Kr} -associated channels
HR	Heart rate
HRA	High right atrium
IAB	Inter-atrial bridges
$I_{b,Na}$	Background sodium leak current
$I_{b,Ca}$	Background calcium leak current
I_{Ca}	Total calcium current

I_{CaL}	L-type calcium current
$I_{CaL,peak}$	Peak value of I_{CaL}
I_{CaT}	T-type calcium current
I_{ion}	Total transmembrane ionic current
I_K	Total potassium current (Hodgkin & Huxley model)
I_{K1}	Inward rectifier potassium current
I_{KACh}	ACh-activated potassium current
I_{Kr}	Rapid delayed rectifier potassium current
I_{Ks}	Slow delayed rectifier potassium current
I_{Kur}	Ultrarapid delayed rectifier potassium current
I_l	Total current of other ions (Hodgkin & Huxley model)
$I_{Na,t}$	Total sodium current (Hodgkin & Huxley model)
I_{Na}	Fast sodium current
I_{NaL}	Late sodium current
I_{pCa}	Calcium pump current
$I_{pCa,max}$	Constant associated with I_{pCa}
I_{rel}	Calcium release current from JSR
I_{se}	Stimuli applied to extracellular space
I_{si}	Stimuli applied to extracellular space
I_{st}	Stimulation current
I_{to}	Transient outward potassium current
I_{tr}	Transfer calcium current from NSR to JSR
I_{up}	Uptake calcium current by NSR
$I_{up,leak}$	Calcium leak current by NSR
j	Inactivation gating variable of I_{Na}
JSR	Junctional sarcoplasmic reticulum (release compartment)
KIT	Karlsruhe Institute of Technology
$[K^+]_i$	Intracellular potassium concentration
$[K^+]_o$	Extracellular potassium concentration
$K_{m,Ca}$	Half-affinity constant for calcium
$K_{m,cmdn}$	Calcium half-saturation constant for calmodulin
$K_{m,K}$	Half-affinity constant for potassium
$K_{m,Na}$	Half-affinity constant for sodium
$K_{m,trpn}$	Calcium half-saturation constant for troponin
K_{NaCa}	I_{NaCa} scaling factor
k_{sat}	Saturation factor for I_{NaCa}
LA	Left atrium
LAPG	Left atrial appendage
LAW	Local activation wave
LPV	Left PV
m	Activation gating variable of I_{Na}
$max_p\{S_{m,p}\}$	Maximum absolute sensitivity
MRI	Magnetic resonance imaging
MV	Mitral valve

N	Number of activation waves
N_s	Number of pairs of similar activation waves
N_{tot}	Total Number of pairs of activatin waves
$[Na^+]_i$	Intracellular sodium concentration
$[Na^+]_o$	Extracellular sodium concentration
NaCa	Sodium/calcium
NaK	Sodium/potassium
NCX	Sodium/calcium exchanger
NSR	Network sarcoplasmic reticulum (uptake compartment)
o_a	Activation gating variable of I_{to}
ODE	Ordinary differential equation
o_i	Inactivation gating variable of I_{to}
OI	Organization index
PDE	Partial differential equation
pEGM	Pseudo-EGM
PM	Pectinate muscles
p_{NaK}	Maximum NaK pump permeability
PS	Phase singularities
PV	Pulmonary vein
R	Gas constant
R^2	Coefficient of determination
RA	Right atrium
RAPG	Right atrial appendage
RI	Regularity index
R_K	Resistor of potassium (Hodgkin & Huxley model)
R_l	Resistor of the rest of ions (Hodgkin & Huxley model)
RMP	Resting membrane potential
$R_{m,p}$	Relative sensitivity
R_{Na}	Resistor of sodium (Hodgkin & Huxley model)
RP	Refractory period
RPV	Right PV
SAN	Sinoatrial node
S_{dyn}	Dynamic APDR curve slope
$S_{m,p}$	Absolute sensitivity
SR	Sinus rhythm
SRet	Sarcoplasmic reticulum
S_{s1s2}	S1-S2 APDR curve slope
SVC	Superior vena cava
t	Time
T	Temperature
t_{90}	Time to reach 90% of adaptation
$[Trpn]_{max}$	Total troponin concentration in myoplasm
u_a	Activation gating variable of I_{Kur}
u_i	Inactivation gating variable of I_{Kur}

V_{20}	V_m at 20% of APD ₉₀ time
V_i	Intracellular volume
V_m	Transmembrane potential
V_{rel}	Volume of the release compartment
V_{up}	Volume of the uptake compartment
VW	Vulnerability window
WL	Wavelength
W_{vw}	VW width
\hat{x}_i	Normalized LAW
x_r	Activation gating variable of I_{Kr}
x_s	Activation gating variable of I_{Ks}
χ	Surface to volume ratio
δ	AP triangulation
ϵ	Threshold value
ϕ_e	Extracellular potential
γ	V_m -dependent parameter for I_{NaCa}
γ_K	Hill coefficient for potassium
γ_{Na}	Hill coefficient for sodium
ρ	Calcium current reactivation index
$\rho_{x,y}$	Unnormalized coupling between pairs of EGMs
σ	Monodomain conductivity tensor
σ_e	Extracellular conductivity tensor
σ_i	Intracellular conductivity tensor
τ_{fast}	Fast phase of adaptation time-constant
τ_{slow}	Slow phase of adaptation time-constant
$\theta(z)$	Heaviside function

Publications Derived from the Thesis

Publications in Journal Articles

- C. Sánchez, A. Corrias, A. Bueno-Orovio, P. Laguna, M. Davies, J. Swinton, I. Jacobson, E. Pueyo and B. Rodríguez. The Na⁺/K⁺ Pump is an Important Modulator of Atrial Refractoriness and Rotor Dynamics in Human Atria. *Am J Physiol Heart Circ Physiol*, vol. 302, pp. H1146-H1159, 2012.
- A. Bueno-Orovio, C. Sánchez, E. Pueyo and B. Rodríguez. Na/K Pump Regulation of Cardiac Repolarization: Insights from a Systems Biology Approach. *Pflügers Arch Eur J Physiol*, vol. 466, pp. 183-193, 2014.
- C. Sánchez, A. Bueno-Orovio, E. Wettwer, S. Loose, J. Simon, U. Ravens, E. Pueyo and B. Rodríguez. Inter-subject Variability in Human Atrial Action Potential in Sinus Rhythm versus Chronic Atrial Fibrillation. *PLoS ONE*, 2014, (submitted).
- C. Sánchez, A. Bueno-Orovio, M. W. Krueger, G. Seemann, O. Dössel, E. Pueyo and B. Rodríguez. Ionic Modulation of Atrial Fibrillation Dynamics in Heterogeneous Human 3D Virtual Atria with Repolarization Variability. (in preparation).

Publications in Conference Proceedings

- C. Sánchez, E. Pueyo, P. Laguna and B. Rodríguez. Cardiac Memory in Human Atria and Relation to Arrhythmogenesis. *Computers in Cardiology*, Park City (Utah, USA), September 2009, vol. 36, pp. 81-84.
- C. Sánchez, A. Corrias, P. Laguna, M. Davies, J. Swinton, I. Jacobson, E. Pueyo and B. Rodríguez. Sensitivity of Atrial Fibrillation Related

Biomarkers to Changes in Ionic Current Properties. *Heart Rhythm Society Scientific Sessions*, Denver (Colorado, USA), May 2010, vol. 7, n° 5, pp. S227.

- C. Sánchez, A. Corrias, P. Laguna, M. Davies, J. Swinton, I. Jacobson, E. Pueyo and B. Rodríguez. Potential Pharmacological Therapies for Atrial Fibrillation. A Computational Study. *Computing in Cardiology*, Belfast (Northern Ireland, United Kingdom), September 2010, vol. 37, pp. 413-416.
- C. Sánchez, B. Rodríguez and E. Pueyo. Ionic Modulators of Electrophysiology and Re-entry Properties in Human Atria. *Computing in Cardiology*, Hangzhou (China), September 2011, vol. 38, pp. 77-80.
- C. Sánchez, M. W. Krueger, G. Seemann, O. Dössel, E. Pueyo and B. Rodríguez. Ionic Modulation of Atrial Fibrillation Dynamics in a Human 3D Atrial Model. *Computing in Cardiology*, Krakow (Poland), September 2012, vol. 39, pp. 137-140.
- C. Sánchez, A. Bueno-Orovio, E. Pueyo and B. Rodríguez. Cell Repolarization Variability Modulates Atrial Fibrillation Dynamics in 3D Virtual Human Atria. *Computing in Cardiology*, Zaragoza (Spain), September 2013, vol. 40, pp. 911-914.

Bibliography

- [1] “Inebase,” tech. rep., Instituto Nacional de Estadística, Feb. 2012.
- [2] P. G. Morton, *Critical Care Nursing: A Holistic Approach*. Lippincott Williams&Wilki, 2005.
- [3] K. Nademanee, J. McKenzie, E. Kosar, M. Schwab, B. Sunsanee-witayakul, T. Vasavakul, C. Khunnawat, and T. Ngarmukos, “A new approach for catheter ablation of atrial fibrillation: mapping of the electrophysiologic substrate,” *Journal of the American College of Cardiology*, vol. 43, pp. 2044–2053, June 2004.
- [4] L. Hove-Madsen, A. Llach, A. Bayes-Genis, S. Roura, E. Rodriguez Font, A. Aris, and J. Cinca, “Atrial fibrillation is associated with increased spontaneous calcium release from the sarcoplasmic reticulum in human atrial myocytes,” *Circulation*, vol. 110, pp. 1358–1363, Sept. 2004.
- [5] L. Hove-Madsen, C. Prat-Vidal, A. Llach, F. Ciruela, V. Casado, C. Lluis, A. Bayes-Genis, J. Cinca, and R. Franco, “Adenosine A2A receptors are expressed in human atrial myocytes and modulate spontaneous sarcoplasmic reticulum calcium release,” *Cardiovasc Res*, vol. 72, pp. 292–302, Nov. 2006.
- [6] L. Hove-Madsen and L. Tort, “L-type Ca^{2+} current and excitation-contraction coupling in single atrial myocytes from rainbow trout,” *American Journal of Physiology - Regulatory, Integrative and Comparative Physiology*, vol. 275, pp. R2061–R2069, Dec. 1998.
- [7] C. E. Molina, H. Gesser, A. Llach, L. Tort, and L. Hove-Madsen, “Modulation of membrane potential by an acetylcholine-activated potassium current in trout atrial myocytes,” *Am. J. Physiol. Regul. Integr. Comp. Physiol.*, vol. 292, pp. R388–395, Jan. 2007.
- [8] D. Werry, J. Eldstrom, Z. Wang, and D. Fedida, “Single-channel basis for the slow activation of the repolarizing cardiac potassium current, I_{Kr} ,” *PNAS*, vol. 110, pp. E996–E1005, Mar. 2013.

- [9] X. Grosmaître, A. Vassalli, P. Mombaerts, G. M. Shepherd, and M. Ma, “Odorant responses of olfactory sensory neurons expressing the odorant receptor MOR23: a patch clamp analysis in gene-targeted mice,” *PNAS*, vol. 103, pp. 1970–1975, Feb. 2006.
- [10] R. Fischmeister, R. K. A. Jr, and R. L. DeHaan, “Some limitations of the cell-attached patch clamp technique: a two-electrode analysis,” *Pflugers Arch.*, vol. 406, pp. 73–82, Jan. 1986.
- [11] A. L. Hodgkin and A. F. Huxley, “A quantitative description of membrane current and its application to conduction and excitation in nerve,” *J. Physiol. (Lond.)*, vol. 117, pp. 500–544, Aug. 1952.
- [12] L. Sörnmo and P. Laguna, *Bioelectrical signal processing in cardiac and neurological applications*. Elsevier Academic Press, June 2005.
- [13] A. Nygren, C. Fiset, L. Firek, J. W. Clark, D. S. Lindblad, R. B. Clark, and W. R. Giles, “Mathematical model of an adult human atrial cell: the role of K^+ currents in repolarization,” *Circ. Res.*, vol. 82, pp. 63–81, Jan. 1998.
- [14] Z. Wang, B. Fermini, and S. Nattel, “Delayed rectifier outward current and repolarization in human atrial myocytes,” *Circ. Res.*, vol. 73, pp. 276–285, Aug. 1993.
- [15] M. Courtemanche, R. J. Ramirez, and S. Nattel, “Ionic mechanisms underlying human atrial action potential properties: insights from a mathematical model,” *Am. J. Physiol.*, vol. 275, pp. H301–321, July 1998.
- [16] E. Grandi, S. V. Pandit, N. Voigt, A. J. Workman, D. Dobrev, J. Jalife, and D. M. Bers, “Human atrial action potential and Ca^{2+} model: sinus rhythm and chronic atrial fibrillation,” *Circ. Res.*, vol. 109, pp. 1055–1066, Oct. 2011.
- [17] J. T. Koivumäki, T. Korhonen, and P. Tavi, “Impact of sarcoplasmic reticulum calcium release on calcium dynamics and action potential morphology in human atrial myocytes: a computational study,” *PLoS Comput. Biol.*, vol. 7, no. 1, p. e1001067, 2011.
- [18] M. M. Maleckar, J. L. Greenstein, W. R. Giles, and N. A. Trayanova, “ K^+ current changes account for the rate dependence of the action potential in the human atrial myocyte,” *Am. J. Physiol. Heart Circ. Physiol.*, vol. 297, pp. H1398–1410, Oct. 2009.
- [19] J. Feng, G. R. Li, B. Fermini, and S. Nattel, “Properties of sodium and potassium currents of cultured adult human atrial myocytes,” *Am. J. Physiol.*, vol. 270, pp. H1676–1686, May 1996.

- [20] C. H. Luo and Y. Rudy, "A dynamic model of the cardiac ventricular action potential. i. simulations of ionic currents and concentration changes," *Circ. Res.*, vol. 74, pp. 1071–1096, June 1994.
- [21] S. Sossalla, B. Kallmeyer, S. Wagner, M. Mazur, U. Maurer, K. Toischer, J. D. Schmitto, R. Seipelt, F. A. Schöndube, G. Hasenfuss, L. Belardinelli, and L. S. Maier, "Altered $na(+)$ currents in atrial fibrillation effects of ranolazine on arrhythmias and contractility in human atrial myocardium," *J. Am. Coll. Cardiol.*, vol. 55, pp. 2330–2342, May 2010.
- [22] T. J. Kamp and J. W. Hell, "Regulation of cardiac l-type calcium channels by protein kinase a and protein kinase c," *Circulation Research*, vol. 87, pp. 1095–1102, Dec. 2000.
- [23] H. Irisawa, H. F. Brown, and W. Giles, "Cardiac pacemaking in the sinoatrial node," *Physiol. Rev.*, vol. 73, pp. 197–227, Jan. 1993.
- [24] H. Karaki, H. Ozaki, M. Hori, M. Mitsui-Saito, K.-I. Amano, K.-I. Harada, S. Miyamoto, H. Nakazawa, K.-J. Won, and K. Sato, "Calcium movements, distribution, and functions in smooth muscle," *Pharmacol Rev*, vol. 49, pp. 157–230, June 1997.
- [25] S. Koumi, C. L. Backer, and C. E. Arentzen, "Characterization of inwardly rectifying $k+$ channel in human cardiac myocytes. alterations in channel behavior in myocytes isolated from patients with idiopathic dilated cardiomyopathy," *Circulation*, vol. 92, pp. 164–174, July 1995.
- [26] Z. Wang, B. Fermini, and S. Nattel, "Rapid and slow components of delayed rectifier current in human atrial myocytes," *Cardiovasc. Res.*, vol. 28, pp. 1540–1546, Oct. 1994.
- [27] S. S. Demir, J. W. Clark, and W. R. Giles, "Parasympathetic modulation of sinoatrial node pacemaker activity in rabbit heart: a unifying model," *American Journal of Physiology - Heart and Circulatory Physiology*, vol. 276, pp. H2221–H2244, June 1999.
- [28] J. Kneller, R. Zou, E. J. Vigmond, Z. Wang, L. J. Leon, and S. Nattel, "Cholinergic atrial fibrillation in a computer model of a two-dimensional sheet of canine atrial cells with realistic ionic properties," *Circ. Res.*, vol. 90, pp. E73–87, May 2002.
- [29] G. J. Amos, E. Wettwer, F. Metzger, Q. Li, H. M. Himmel, and U. Ravens, "Differences between outward currents of human atrial and subepicardial ventricular myocytes," *J Physiol*, vol. 491, pp. 31–50, Feb. 1996.

- [30] A. Bueno-Orovio, C. Sánchez, E. Pueyo, and B. Rodriguez, “Na/K pump regulation of cardiac repolarization: insights from a systems biology approach,” *Pflugers Arch.*, vol. 466, pp. 183–193, Feb. 2014.
- [31] D. C. Gadsby, “Ion channels versus ion pumps: the principal difference, in principle,” *Nat. Rev. Mol. Cell Biol.*, vol. 10, pp. 344–352, May 2009.
- [32] D. M. Bers, “Calcium fluxes involved in control of cardiac myocyte contraction,” *Circ. Res.*, vol. 87, pp. 275–281, Aug. 2000.
- [33] N. Jost, N. Nagy, C. Corici, Z. Kohajda, A. Horvath, K. Acsai, P. Biliczki, J. Levijoki, P. Pollesello, T. Koskelainen, L. Otsomaa, A. Toth, J. G. Papp, A. Varro, and L. Virag, “ORM-10103, a novel specific inhibitor of the Na^+ / Ca^{2+} exchanger, decreases early and delayed afterdepolarizations in the canine heart,” *Br. J. Pharmacol.*, vol. 170, pp. 768–778, Oct. 2013.
- [34] T. J. Hund, J. P. Kucera, N. F. Otani, and Y. Rudy, “Ionic charge conservation and long-term steady state in the Luo-Rudy dynamic cell model,” *Biophys. J.*, vol. 81, pp. 3324–3331, Dec. 2001.
- [35] R. L. Rasmusson, J. W. Clark, W. R. Giles, K. Robinson, R. B. Clark, E. F. Shibata, and D. L. Campbell, “A mathematical model of electrophysiological activity in a bullfrog atrial cell,” *Am. J. Physiol.*, vol. 259, pp. H370–389, Aug. 1990.
- [36] L. Gr, F. J, W. Z, and N. S, “Transmembrane chloride currents in human atrial myocytes,” *Am J Physiol*, vol. 270, pp. C500–7, Feb. 1996.
- [37] L. Yue, J. Feng, G. R. Li, and S. Nattel, “Transient outward and delayed rectifier currents in canine atrium: properties and role of isolation methods,” *Am. J. Physiol.*, vol. 270, pp. H2157–2168, June 1996.
- [38] A. C. Zygmunt and W. R. Gibbons, “Properties of the calcium-activated chloride current in heart,” *J. Gen. Physiol.*, vol. 99, pp. 391–414, Mar. 1992.
- [39] T. O. of Health Economics, “Estimating the direct costs of atrial fibrillation to the NHS in the constituent countries of the UK and at SHA level in England, 2008,” Nov. 2009.
- [40] V. Fuster, L. E. Rydén, D. S. Cannom, H. J. Crijns, A. B. Curtis, K. A. Ellenbogen, J. L. Halperin, G. N. Kay, J.-Y. Le Huezey, J. E. Lowe, S. B. Olsson, E. N. Prystowsky, J. L. Tamargo, and L. S. Wann, “2011 ACCF/AHA/HRS focused updates incorporated into the ACC/AHA/ESC 2006 guidelines for the management of patients with

- atrial fibrillation: a report of the american college of cardiology Foundation/American heart association task force on practice guidelines developed in partnership with the european society of cardiology and in collaboration with the european heart rhythm association and the heart rhythm society,” *J. Am. Coll. Cardiol.*, vol. 57, pp. e101–198, Mar. 2011.
- [41] S. Lévy, “Classification system of atrial fibrillation,” *Curr. Opin. Cardiol.*, vol. 15, pp. 54–57, Jan. 2000.
- [42] S. Lévy, A. J. Camm, S. Saksena, E. Aliot, G. Breithardt, H. J. G. M. Crijns, D. W. Davies, G. N. Kay, E. N. Prystowsky, R. Sutton, A. L. Waldo, D. G. Wyse, Working Group on Arrhythmias of European Society of Cardiology, Working Group of Cardiac Pacing of European Society of Cardiology, and North American Society of Pacing and Electrophysiology, “International consensus on nomenclature and classification of atrial fibrillation: A collaborative project of the working group on arrhythmias and the working group of cardiac pacing of the european society of cardiology and the north american society of pacing and electrophysiology,” *J. Cardiovasc. Electrophysiol.*, vol. 14, pp. 443–445, Apr. 2003.
- [43] V. Markides and R. J. Schilling, “Atrial fibrillation: classification, pathophysiology, mechanisms and drug treatment,” *Heart*, vol. 89, pp. 939–943, Aug. 2003.
- [44] M. Haïssaguerre, P. Jaïs, D. C. Shah, A. Takahashi, M. Hocini, G. Quiniou, S. Garrigue, A. Le Mouroux, P. Le Métayer, and J. Clémenty, “Spontaneous initiation of atrial fibrillation by ectopic beats originating in the pulmonary veins,” *N. Engl. J. Med.*, vol. 339, pp. 659–666, Sept. 1998.
- [45] J. Jalife, “Rotors and spiral waves in atrial fibrillation,” *J. Cardiovasc. Electrophysiol.*, vol. 14, pp. 776–780, July 2003.
- [46] J. Kalifa, J. Jalife, A. V. Zaitsev, S. Bagwe, M. Warren, J. Moreno, O. Berenfeld, and S. Nattel, “Intra-atrial pressure increases rate and organization of waves emanating from the superior pulmonary veins during atrial fibrillation,” *Circulation*, vol. 108, pp. 668–671, Aug. 2003.
- [47] F. Atonza, J. Almendral, J. Moreno, R. Vaidyanathan, A. Talkachou, J. Kalifa, A. Arenal, J. P. Villacastín, E. G. Torrecilla, A. Sánchez, R. Ploutz-Snyder, J. Jalife, and O. Berenfeld, “Activation of inward rectifier potassium channels accelerates atrial fibrillation in humans: evidence for a reentrant mechanism,” *Circulation*, vol. 114, pp. 2434–2442, Dec. 2006.

- [48] G. Moe, "On the multiple wavelet hypothesis of atrial fibrillation," *Arch Int Pharmacodyn Ther*, vol. 140, pp. 183–188, 1962.
- [49] S. Lee, J. Sahadevan, C. M. Khrestian, D. M. Durand, and A. L. Waldo, "High density mapping of atrial fibrillation during vagal nerve stimulation in the canine heart: Restudying the moe hypothesis," *Journal of Cardiovascular Electrophysiology*, vol. 24, no. 3, p. 328â335, 2013.
- [50] F. D. Murgatroyd and A. J. Camm, "Atrial arrhythmias," *Lancet*, vol. 341, pp. 1317–1322, May 1993.
- [51] M. C. Wijffels, C. J. Kirchhof, R. Dorland, and M. A. Allesie, "Atrial fibrillation begets atrial fibrillation. a study in awake chronically instrumented goats," *Circulation*, vol. 92, pp. 1954–1968, Oct. 1995.
- [52] B. Burstein and S. Nattel, "Atrial fibrosis: mechanisms and clinical relevance in atrial fibrillation," *J. Am. Coll. Cardiol.*, vol. 51, pp. 802–809, Feb. 2008.
- [53] M. R. Rosen, "Classification of antiarrhythmic drugs," *Card Electrophysiol Rev*, vol. 4, pp. 181–185, Sept. 2000.
- [54] E. M. Vaughan Williams, "A classification of antiarrhythmic actions reassessed after a decade of new drugs," *J Clin Pharmacol*, vol. 24, pp. 129–147, Apr. 1984.
- [55] R. E. Klabunde, "Sodium-channel blockers (class i antiarrhythmics)," <http://www.cvpharmacology.com/antiarrhy/sodium-blockers.htm>," 2011.
- [56] P. Comtois, M. Sakabe, E. J. Vigmond, M. Munoz, A. Texier, A. Shiroshita-Takeshita, and S. Nattel, "Mechanisms of atrial fibrillation termination by rapidly unbinding na+ channel blockers: insights from mathematical models and experimental correlates," *Am. J. Physiol. Heart Circ. Physiol.*, vol. 295, pp. H1489–1504, Oct. 2008.
- [57] C. M. Tracy, A. E. Epstein, D. Darbar, J. P. DiMarco, S. B. Dunbar, N. M. Estes III, T. B. Ferguson Jr, S. C. Hammill, P. E. Karasik, M. S. Link, J. E. Marine, M. H. Schoenfeld, A. J. Shanker, M. J. Silka, L. W. Stevenson, W. G. Stevenson, and P. D. Varosy, "2012 ACCF/AHA/HRS focused update incorporated into the ACCF/AHA/HRS 2008 guidelines for device-based therapy of cardiac rhythm abnormalities: A report of the american college of cardiology Foundation/American heart association task force on practice guidelines and the heart rhythm society," *Journal of the American College of Cardiology*, vol. 61, pp. e6–e75, Jan. 2013.

- [58] A. Ames and W. G. Stevenson, "Cardiology patient page. catheter ablation of atrial fibrillation," *Circulation*, vol. 113, pp. e666–668, Apr. 2006.
- [59] E. Grandi, F. S. Pasqualini, and D. M. Bers, "A novel computational model of the human ventricular action potential and ca transient," *J. Mol. Cell. Cardiol.*, vol. 48, pp. 112–121, Jan. 2010.
- [60] M. Wilhelms, H. Hettmann, M. M. Maleckar, J. T. Koivumäki, O. Dössel, and G. Seemann, "Benchmarking electrophysiological models of human atrial myocytes," *Front Physiol*, vol. 3, p. 487, 2012.
- [61] M. Potse, *Integrated Electrocardiographic Mapping: Combined Analysis of Multichannel Endocardial and Body Surface ECG Data*. PhD thesis, Universiteit van Amsterdam [Host], 2001.
- [62] J. Pitt-Francis, M. O. Bernabeu, J. Cooper, A. Garny, L. Momtahan, J. Osborne, P. Pathmanathan, B. Rodriguez, J. P. Whiteley, and D. J. Gavaghan, "Chaste: using agile programming techniques to develop computational biology software," *Philos Trans A Math Phys Eng Sci*, vol. 366, pp. 3111–3136, Sept. 2008.
- [63] J. P. Keener and J. Sneyd, *Mathematical Physiology*. Springer, Jan. 1998.
- [64] J. P. Whiteley, "An efficient numerical technique for the solution of the monodomain and bidomain equations," *IEEE Trans Biomed Eng*, vol. 53, pp. 2139–2147, Nov. 2006.
- [65] G. Seemann, C. Höper, F. B. Sachse, O. Dössel, A. V. Holden, and H. Zhang, "Heterogeneous three-dimensional anatomical and electrophysiological model of human atria," *Philos Trans A Math Phys Eng Sci*, vol. 364, pp. 1465–1481, June 2006.
- [66] L. Dang, N. Virag, Z. Ihara, V. Jacquemet, J. M. Vesin, J. Schlaepfer, P. Ruchat, and L. Kappenberger, "Evaluation of ablation patterns using a biophysical model of atrial fibrillation," *Ann Biomed Eng*, vol. 33, pp. 465–474, Apr. 2005.
- [67] C. Tobon, C. A. Ruiz-Villa, E. Heidenreich, L. Romero, F. Hornero, and J. Saiz, "A three-dimensional human atrial model with fiber orientation. electrograms and arrhythmic activation patterns relationship," *PLoS ONE*, vol. 8, no. 2, p. e50883, 2013.
- [68] "COR web, <http://cor.physiol.ox.ac.uk/>."
- [69] "Cellml web, <http://www.cellml.org/>."

- [70] “Chaste web, <http://www.cs.ox.ac.uk/chaste/>.”
- [71] G. R. Mirams, C. J. Arthurs, M. O. Bernabeu, R. Bordas, J. Cooper, A. Corrias, Y. Davit, S.-J. Dunn, A. G. Fletcher, D. G. Harvey, M. E. Marsh, J. M. Osborne, P. Pathmanathan, J. Pitt-Francis, J. Southern, N. Zemezmi, and D. J. Gavaghan, “Chaste: an open source c++ library for computational physiology and biology,” *PLoS Comput. Biol.*, vol. 9, no. 3, p. e1002970, 2013. PMID: 23516352.
- [72] D. Abramson, M. O. Bernabeu, B. Bethwaite, K. Burrage, A. Corrias, C. Enticott, S. Garic, D. Gavaghan, T. Peachey, J. Pitt-Francis, E. Pueyo, B. Rodriguez, A. Sher, and J. Tan, “High-throughput cardiac science on the grid,” *Philos Trans A Math Phys Eng Sci*, vol. 368, pp. 3907–3923, Aug. 2010.
- [73] E. A. Heidenreich, J. M. Ferrero, M. Doblaré, and J. F. Rodríguez, “Adaptive macro finite elements for the numerical solution of monodomain equations in cardiac electrophysiology,” *Ann Biomed Eng*, vol. 38, pp. 2331–2345, July 2010.
- [74] D. Thain, T. Tannenbaum, and M. Livny, “Distributed computing in practice: The condor experience: Research articles,” *Concurr. Comput. : Pract. Exper.*, vol. 17, p. 323â356, Feb. 2005.
- [75] “EnSight gold, <http://www.ceisoftware.com/ensight-gold/>.”
- [76] E. Pueyo, P. Smetana, P. Caminal, A. B. de Luna, M. Malik, and P. Laguna, “Characterization of QT interval adaptation to RR interval changes and its use as a risk-stratifier of arrhythmic mortality in amiodarone-treated survivors of acute myocardial infarction,” *IEEE Trans Biomed Eng*, vol. 51, pp. 1511–1520, Sept. 2004.
- [77] A. Shvilkin, J. Danilo, P. J. Wang, D. Burkhoff, E. P. Anyukhovskiy, E. A. Sosunov, M. Hara, and M. R. Rosen, “Evolution and resolution of long-term cardiac memory,” *Circulation*, vol. 97, pp. 1810–1817, May 1998.
- [78] A. Grom, T. S. Faber, M. Brunner, C. Bode, and M. Zehender, “Delayed adaptation of ventricular repolarization after sudden changes in heart rate due to conversion of atrial fibrillation. a potential risk factor for proarrhythmia?,” *Europace*, vol. 7, pp. 113–121, Mar. 2005.
- [79] M. R. Franz, C. D. Swerdlow, L. B. Liem, and J. Schaefer, “Cycle length dependence of human action potential duration in vivo. effects of single extrastimuli, sudden sustained rate acceleration and deceleration, and different steady-state frequencies,” *J. Clin. Invest.*, vol. 82, pp. 972–979, Sept. 1988.

- [80] E. Pueyo, Z. Husti, T. Hornyik, I. Baczko, P. Laguna, A. Varro, and B. Rodriguez, "Mechanisms of ventricular rate adaptation as a predictor of arrhythmic risk," *Am. J. Physiol. Heart Circ. Physiol.*, vol. 298, pp. H1577–1587, May 2010.
- [81] M. Hara, A. Shvilkin, M. R. Rosen, J. Danilo, P, and P. A. Boyden, "Steady-state and nonsteady-state action potentials in fibrillating canine atrium: abnormal rate adaptation and its possible mechanisms," *Cardiovasc. Res.*, vol. 42, pp. 455–469, May 1999.
- [82] K. Hoshiyama, M. Hara, K. Yasui, H. Mitamura, F. Ohsuzu, I. Kodama, and S. Ogawa, "Altered action potential dynamics in electrically remodeled canine atria: evidence for altered intracellular Ca^{2+} handling," *Circ. J.*, vol. 70, pp. 1488–1496, Nov. 2006.
- [83] P.-C. Zhang, A. Llach, X. Y. Sheng, L. Hove-Madsen, and G. F. Tibbits, "Calcium handling in zebrafish ventricular myocytes," *Am. J. Physiol. Regul. Integr. Comp. Physiol.*, vol. 300, pp. R56–66, Jan. 2011.
- [84] M. R. Franz, "The electrical restitution curve revisited: steep or flat slope—which is better?," *J. Cardiovasc. Electrophysiol.*, vol. 14, pp. S140–147, Oct. 2003. PMID: 14760916.
- [85] B.-S. Kim, Y.-H. Kim, G.-S. Hwang, H.-N. Pak, S. C. Lee, W. J. Shim, D. J. Oh, and Y. M. Ro, "Action potential duration restitution kinetics in human atrial fibrillation," *J. Am. Coll. Cardiol.*, vol. 39, pp. 1329–1336, Apr. 2002. PMID: 11955851.
- [86] S. M. Narayan, D. Kazi, D. E. Krummen, and W.-J. Rappel, "Repolarization and activation restitution near human pulmonary veins and atrial fibrillation initiation: a mechanism for the initiation of atrial fibrillation by premature beats," *J. Am. Coll. Cardiol.*, vol. 52, pp. 1222–1230, Oct. 2008. PMID: 18926325.
- [87] L. H. Frame and M. B. Simson, "Oscillations of conduction, action potential duration, and refractoriness. a mechanism for spontaneous termination of reentrant tachycardias," *Circulation*, vol. 78, pp. 1277–1287, Nov. 1988. PMID: 3180384.
- [88] P. C. Viswanathan and Y. Rudy, "Pause induced early afterdepolarizations in the long QT syndrome: a simulation study," *Cardiovasc. Res.*, vol. 42, pp. 530–542, May 1999.
- [89] L. M. Hondeghem, L. Carlsson, and G. Duker, "Instability and triangulation of the action potential predict serious proarrhythmia, but action potential duration prolongation is antiarrhythmic," *Circulation*, vol. 103, pp. 2004–2013, Apr. 2001.

- [90] H. Gelband, H. L. Bush, M. R. Rosen, R. J. Myerburg, and B. F. Hoffman, "Electrophysiologic properties of isolated preparations of human atrial myocardium," *Circ. Res.*, vol. 30, pp. 293–300, Mar. 1972.
- [91] K. H. W. J. ten Tusscher and A. V. Panfilov, "Alternans and spiral breakup in a human ventricular tissue model," *Am. J. Physiol. Heart Circ. Physiol.*, vol. 291, pp. H1088–1100, Sept. 2006.
- [92] E. Carmeliet, "Intracellular $ca(2+)$ concentration and rate adaptation of the cardiac action potential," *Cell Calcium*, vol. 35, pp. 557–573, June 2004.
- [93] T. Watano, Y. Harada, K. Harada, and N. Nishimura, "Effect of Na^+/Ca^{2+} exchange inhibitor, KB-R7943 on ouabain-induced arrhythmias in guinea-pigs," *Br. J. Pharmacol.*, vol. 127, pp. 1846–1850, Aug. 1999. PMID: 10482915 PMCID: PMC1566184.
- [94] S. Miyamoto, B.-M. Zhu, K. Kamiya, Y. Nagasawa, and K. Hashimoto, "KB-R7943, a Na^+/Ca^{2+} exchange inhibitor, does not suppress ischemia/reperfusion arrhythmias nor digitalis arrhythmias in dogs," *Jpn. J. Pharmacol.*, vol. 90, pp. 229–235, Nov. 2002.
- [95] C. Pott, X. Ren, D. X. Tran, M.-J. Yang, S. Henderson, M. C. Jordan, K. P. Roos, A. Garfinkel, K. D. Philipson, and J. I. Goldhaber, "Mechanism of shortened action potential duration in na^+-ca^{2+} exchanger knockout mice," *Am. J. Physiol., Cell Physiol.*, vol. 292, pp. C968–973, Feb. 2007.
- [96] G. Klein, F. Schröder, D. Vogler, A. Schaefer, A. Haverich, B. Schieffer, T. Korte, and H. Drexler, "Increased open probability of single cardiac l-type calcium channels in patients with chronic atrial fibrillation. role of phosphatase 2A," *Cardiovasc. Res.*, vol. 59, pp. 37–45, July 2003.
- [97] R. F. Bosch, X. Zeng, J. B. Grammer, K. Popovic, C. Mewis, and V. Kühnkamp, "Ionic mechanisms of electrical remodeling in human atrial fibrillation," *Cardiovasc. Res.*, vol. 44, pp. 121–131, Oct. 1999.
- [98] R. Laszlo, C. Eick, N. Rueb, S. Weretka, H.-J. Weig, J. Schrieck, and R. F. Bosch, "Inhibition of the renin-angiotensin system: effects on tachycardia-induced early electrical remodelling in rabbit atrium," *J Renin Angiotensin Aldosterone Syst*, vol. 9, pp. 125–132, Sept. 2008.
- [99] L. Yue, J. Feng, R. Gaspo, G. R. Li, Z. Wang, and S. Nattel, "Ionic remodeling underlying action potential changes in a canine model of atrial fibrillation," *Circ. Res.*, vol. 81, pp. 512–525, Oct. 1997.

- [100] G. R. Li and S. Nattel, "Properties of human atrial I_{Ca} at physiological temperatures and relevance to action potential," *Am. J. Physiol.*, vol. 272, pp. H227–235, Jan. 1997.
- [101] E. Carmeliet, "Action potential duration, rate of stimulation, and intracellular sodium," *J. Cardiovasc. Electrophysiol.*, vol. 17 Suppl 1, pp. S2–S7, May 2006.
- [102] J. Wang, R. H. Schwinger, K. Frank, J. Müller-Ehmsen, P. Martin-Vasallo, T. A. Pressley, A. Xiang, E. Erdmann, and A. A. McDonough, "Regional expression of sodium pump subunits isoforms and na⁺-ca⁺⁺ exchanger in the human heart," *J. Clin. Invest.*, vol. 98, pp. 1650–1658, Oct. 1996.
- [103] D. M. Bers, W. H. Barry, and S. Despa, "Intracellular na⁺ regulation in cardiac myocytes," *Cardiovasc. Res.*, vol. 57, pp. 897–912, Mar. 2003.
- [104] M. R. Boyett and D. Fedida, "Changes in the electrical activity of dog cardiac purkinje fibres at high heart rates," *J. Physiol. (Lond.)*, vol. 350, pp. 361–391, May 1984.
- [105] A. J. Drake, M. I. Noble, V. Schouten, A. Seed, H. E. Ter Keurs, and B. Wohlfart, "Is action potential duration of the intact dog heart related to contractility or stimulus rate?," *J. Physiol. (Lond.)*, vol. 331, pp. 499–510, Oct. 1982.
- [106] A. Nygren, L. J. Leon, and W. R. Giles, "Simulations of the human atrial action potential," *Phil. Trans. R. Soc. Lond. A*, vol. 359, pp. 1111–1125, June 2001.
- [107] E. M. Cherry and S. J. Evans, "Properties of two human atrial cell models in tissue: restitution, memory, propagation, and reentry," *J. Theor. Biol.*, vol. 254, pp. 674–690, Oct. 2008.
- [108] E. M. Cherry, H. M. Hastings, and S. J. Evans, "Dynamics of human atrial cell models: restitution, memory, and intracellular calcium dynamics in single cells," *Prog. Biophys. Mol. Biol.*, vol. 98, pp. 24–37, Sept. 2008.
- [109] B. Trenor, L. Romero, J. Ferrero, Jose Maria, J. Saiz, G. Molto, and J. M. Alonso, "Vulnerability to reentry in a regionally ischemic tissue: a simulation study," *Ann Biomed Eng*, vol. 35, pp. 1756–1770, Oct. 2007.
- [110] J. Andrade, P. Khairy, D. Dobrev, and S. Nattel, "The clinical profile and pathophysiology of atrial fibrillation relationships among clin-

- ical features, epidemiology, and mechanisms,” *Circulation Research*, vol. 114, pp. 1453–1468, Apr. 2014.
- [111] P. Jais and D. L. Packer, “Ablation vs. drug use for atrial fibrillation,” *European Heart Journal Supplements*, vol. 9, pp. G26–G34, Sept. 2007.
- [112] P. A. Schweizer, R. Becker, H. A. Katus, and D. Thomas, “Dronedaronone: current evidence for its safety and efficacy in the management of atrial fibrillation,” *Drug Des Devel Ther*, vol. 5, pp. 27–39, 2011.
- [113] J. P. Piccini, V. Hasselblad, E. D. Peterson, J. B. Washam, R. M. Califf, and D. F. Kong, “Comparative efficacy of dronedarone and amiodarone for the maintenance of sinus rhythm in patients with atrial fibrillation,” *J. Am. Coll. Cardiol.*, vol. 54, pp. 1089–1095, Sept. 2009.
- [114] C. M. Ambrosi, C. M. Ripplinger, I. R. Efimov, and V. V. Fedorov, “Termination of sustained atrial flutter and fibrillation using low-voltage multiple-shock therapy,” *Heart Rhythm*, vol. 8, pp. 101–108, Jan. 2011.
- [115] F. H. Fenton, S. Luther, E. M. Cherry, N. F. Otani, V. Krinsky, A. Pumir, E. Bodenschatz, and J. Gilmour, Robert F, “Termination of atrial fibrillation using pulsed low-energy far-field stimulation,” *Circulation*, vol. 120, pp. 467–476, Aug. 2009.
- [116] S. Luther, F. H. Fenton, B. G. Kornreich, A. Squires, P. Bittihn, D. Hornung, M. Zabel, J. Flanders, A. Gladuli, L. Campoy, E. M. Cherry, G. Luther, G. Hasenfuss, V. I. Krinsky, A. Pumir, J. Gilmour, Robert F, and E. Bodenschatz, “Low-energy control of electrical turbulence in the heart,” *Nature*, vol. 475, pp. 235–239, July 2011.
- [117] S. M. Schumacher and J. R. Martens, “Ion channel trafficking: a new therapeutic horizon for atrial fibrillation,” *Heart Rhythm*, vol. 7, pp. 1309–1315, Sept. 2010.
- [118] B. Rodriguez, K. Burrage, D. Gavaghan, V. Grau, P. Kohl, and D. Noble, “The systems biology approach to drug development: application to toxicity assessment of cardiac drugs,” *Clin. Pharmacol. Ther.*, vol. 88, pp. 130–134, July 2010.
- [119] M. Courtemanche, R. J. Ramirez, and S. Nattel, “Ionic targets for drug therapy and atrial fibrillation-induced electrical remodeling: insights from a mathematical model,” *Cardiovasc. Res.*, vol. 42, pp. 477–489, May 1999.

- [120] S. V. Pandit, O. Berenfeld, J. M. B. Anumonwo, R. M. Zaritski, J. Kneller, S. Nattel, and J. Jalife, "Ionic determinants of functional reentry in a 2-d model of human atrial cells during simulated chronic atrial fibrillation," *Biophys. J.*, vol. 88, pp. 3806–3821, June 2005.
- [121] D. R. Van Wagoner, A. L. Pond, M. Lamorgese, S. S. Rossie, P. M. McCarthy, and J. M. Nerbonne, "Atrial l-type ca^{2+} currents and human atrial fibrillation," *Circ. Res.*, vol. 85, pp. 428–436, Sept. 1999.
- [122] D. R. Van Wagoner, A. L. Pond, P. M. McCarthy, J. S. Trimmer, and J. M. Nerbonne, "Outward k^{+} current densities and $kv1.5$ expression are reduced in chronic human atrial fibrillation," *Circ. Res.*, vol. 80, pp. 772–781, June 1997.
- [123] A. Burashnikov, J. M. Di Diego, A. C. Zygmunt, L. Belardinelli, and C. Antzelevitch, "Atrium-selective sodium channel block as a strategy for suppression of atrial fibrillation: differences in sodium channel inactivation between atria and ventricles and the role of ranolazine," *Circulation*, vol. 116, pp. 1449–1457, Sept. 2007.
- [124] S. Nattel and B. N. Singh, "Evolution, mechanisms, and classification of antiarrhythmic drugs: focus on class III actions," *Am. J. Cardiol.*, vol. 84, pp. 11R–19R, Nov. 1999. PMID: 10568655.
- [125] J. R. Ehrlich and S. Nattel, "Novel approaches for pharmacological management of atrial fibrillation," *Drugs*, vol. 69, no. 7, pp. 757–774, 2009.
- [126] F. Forini, G. Nicolini, S. Balzan, G. M. Ratto, B. Murzi, V. Vanini, and G. Iervasi, "Amiodarone inhibits the 3,5,3'-triiodothyronine-dependent increase of sodium/potassium adenosine triphosphatase activity and concentration in human atrial myocardial tissue," *Thyroid*, vol. 14, pp. 493–499, July 2004.
- [127] D. F. Gray, A. S. Mihailidou, P. S. Hansen, K. A. Buhagiar, N. L. Bewick, H. H. Rasmussen, and D. W. Whalley, "Amiodarone inhibits the na^{+} - k^{+} pump in rabbit cardiac myocytes after acute and chronic treatment," *J. Pharmacol. Exp. Ther.*, vol. 284, pp. 75–82, Jan. 1998.
- [128] S. Nattel, D. Li, and L. Yue, "Basic mechanisms of atrial fibrillation—very new insights into very old ideas," *Annu. Rev. Physiol.*, vol. 62, pp. 51–77, 2000.
- [129] F. Xie, Z. Qu, A. Garfinkel, and J. N. Weiss, "Electrical refractory period restitution and spiral wave reentry in simulated cardiac tissue," *Am. J. Physiol. Heart Circ. Physiol.*, vol. 283, pp. H448–460, July 2002.

- [130] B. Rodriguez, B. Tice, R. Blake, D. Gavaghan, and N. Trayanova, "Vulnerability to electric shocks in the regionally-ischemic ventricles," *Conf Proc IEEE Eng Med Biol Soc*, vol. 1, pp. 2280–2283, 2006.
- [131] E. M. Cherry and F. H. Fenton, "Effects of boundaries and geometry on the spatial distribution of action potential duration in cardiac tissue," *J. Theor. Biol.*, vol. 285, pp. 164–176, Sept. 2011.
- [132] F. Fenton and A. Karma, "Vortex dynamics in three-dimensional continuous myocardium with fiber rotation: Filament instability and fibrillation," *Chaos*, vol. 8, pp. 20–47, Mar. 1998.
- [133] J. P. Keener, "An eikonal-curvature equation for action potential propagation in myocardium," *J Math Biol*, vol. 29, no. 7, pp. 629–651, 1991.
- [134] D. W. Frazier, P. D. Wolf, J. M. Wharton, A. S. Tang, W. M. Smith, and R. E. Ideker, "Stimulus-induced critical point. mechanism for electrical initiation of reentry in normal canine myocardium," *J. Clin. Invest.*, vol. 83, pp. 1039–1052, Mar. 1989.
- [135] A. T. Winfree, "Various ways to make phase singularities by electric shock," *J. Cardiovasc. Electrophysiol.*, vol. 11, pp. 286–289, Mar. 2000.
- [136] Z. J. Engelman, M. L. Trew, and B. H. Smaill, "Structural heterogeneity alone is a sufficient substrate for dynamic instability and altered restitution," *Circ Arrhythm Electrophysiol*, vol. 3, pp. 195–203, Apr. 2010.
- [137] L. Hou, M. Deo, P. Furspan, S. V. Pandit, S. Mironov, D. S. Auerbach, Q. Gong, Z. Zhou, O. Berenfeld, and J. Jalife, "A major role for HERG in determining frequency of reentry in neonatal rat ventricular myocyte monolayer," *Circ. Res.*, vol. 107, pp. 1503–1511, Dec. 2010.
- [138] A. Baher, Z. Qu, A. Hayatdavoudi, S. T. Lamp, M.-J. Yang, F. Xie, S. Turner, A. Garfinkel, and J. N. Weiss, "Short-term cardiac memory and mother rotor fibrillation," *Am. J. Physiol. Heart Circ. Physiol.*, vol. 292, pp. H180–189, Jan. 2007.
- [139] K. Gima and Y. Rudy, "Ionic current basis of electrocardiographic waveforms: a model study," *Circ. Res.*, vol. 90, pp. 889–896, May 2002.
- [140] R. Plonsey and Y. Rudy, "Electrocardiogram sources in a 2-dimensional anisotropic activation model," *Med Biol Eng Comput*, vol. 18, pp. 87–94, Jan. 1980.

- [141] G. W. Botteron and J. M. Smith, "A technique for measurement of the extent of spatial organization of atrial activation during atrial fibrillation in the intact human heart," *IEEE Trans Biomed Eng*, vol. 42, pp. 579–586, June 1995.
- [142] L. Romero, E. Pueyo, M. Fink, and B. Rodriguez, "Impact of ionic current variability on human ventricular cellular electrophysiology," *Am. J. Physiol. Heart Circ. Physiol.*, vol. 297, pp. H1436–1445, Oct. 2009.
- [143] M. Boutjdir, J. Y. Le Heuzey, T. Lavergne, S. Chauvaud, L. Guize, A. Carpentier, and P. Peronneau, "Inhomogeneity of cellular refractoriness in human atrium: factor of arrhythmia?," *Pacing Clin Electrophysiol*, vol. 9, pp. 1095–1100, Nov. 1986.
- [144] A. J. Workman, K. A. Kane, and A. C. Rankin, "Cellular bases for human atrial fibrillation," *Heart Rhythm*, vol. 5, pp. S1–6, June 2008.
- [145] A. J. Workman, K. A. Kane, and A. C. Rankin, "The contribution of ionic currents to changes in refractoriness of human atrial myocytes associated with chronic atrial fibrillation," *Cardiovasc. Res.*, vol. 52, pp. 226–235, Nov. 2001.
- [146] K. Miyamoto, T. Tsuchiya, S. Narita, T. Yamaguchi, Y. Nagamoto, S.-i. Ando, K. Hayashida, Y. Tanioka, and N. Takahashi, "Bipolar electrogram amplitudes in the left atrium are related to local conduction velocity in patients with atrial fibrillation," *Europace*, vol. 11, pp. 1597–1605, Dec. 2009.
- [147] D. Dobrev, E. Graf, E. Wettwer, H. M. Himmel, O. Hála, C. Doerfel, T. Christ, S. Schüler, and U. Ravens, "Molecular basis of downregulation of g-protein-coupled inward rectifying k(+) current (i(K,ACh) in chronic human atrial fibrillation: decrease in GIRK4 mRNA correlates with reduced i(K,ACh) and muscarinic receptor-mediated shortening of action potentials," *Circulation*, vol. 104, pp. 2551–2557, Nov. 2001.
- [148] S. Kharche, C. J. Garratt, M. R. Boyett, S. Inada, A. V. Holden, J. C. Hancox, and H. Zhang, "Atrial proarrhythmia due to increased inward rectifier current (i(k1)) arising from KCNJ2 mutation—a simulation study," *Prog. Biophys. Mol. Biol.*, vol. 98, pp. 186–197, Nov. 2008. PMID: 19041665.
- [149] H. H. Rasmussen, G. T. Okita, R. S. Hartz, and R. E. ten Eick, "Inhibition of electrogenic na(+)-pumping in isolated atrial tissue from patients treated with digoxin," *J. Pharmacol. Exp. Ther.*, vol. 252, pp. 60–64, Jan. 1990.

- [150] J. Kneller, J. Kalifa, R. Zou, A. V. Zaitsev, M. Warren, O. Berenfeld, E. J. Vigmond, L. J. Leon, S. Nattel, and J. Jalife, "Mechanisms of atrial fibrillation termination by pure sodium channel blockade in an ionically-realistic mathematical model," *Circ. Res.*, vol. 96, pp. e35–47, Mar. 2005.
- [151] D. Horiuchi, A. Iwasa, K. Sasaki, S. Owada, M. Kimura, S. Sasaki, and K. Okumura, "Effect of pilsicainide on dominant frequency in the right and left atria and pulmonary veins during atrial fibrillation: association with its atrial fibrillation terminating effect," *Eur. J. Pharmacol.*, vol. 608, pp. 54–61, Apr. 2009.
- [152] A. J. Workman, K. A. Kane, and A. C. Rankin, "Characterisation of the na, k pump current in atrial cells from patients with and without chronic atrial fibrillation," *Cardiovasc. Res.*, vol. 59, pp. 593–602, Sept. 2003.
- [153] G. M. Faber and Y. Rudy, "Action potential and contractility changes in [na(+)](i) overloaded cardiac myocytes: a simulation study," *Biophys. J.*, vol. 78, pp. 2392–2404, May 2000.
- [154] A. J. Levi, "The effect of strophanthidin on action potential, calcium current and contraction in isolated guinea-pig ventricular myocytes," *J. Physiol. (Lond.)*, vol. 443, pp. 1–23, Nov. 1991.
- [155] A. Harada, K. Sasaki, T. Fukushima, M. Ikeshita, T. Asano, S. Yamauchi, S. Tanaka, and T. Shoji, "Atrial activation during chronic atrial fibrillation in patients with isolated mitral valve disease," *Ann. Thorac. Surg.*, vol. 61, pp. 104–111; discussion 111–112, Jan. 1996.
- [156] S. Nattel, "New ideas about atrial fibrillation 50 years on," *Nature*, vol. 415, pp. 219–226, Jan. 2002.
- [157] K. Derakhchan, C. Villemaire, M. Talajic, and S. Nattel, "The class III antiarrhythmic drugs dofetilide and sotalol prevent AF induction by atrial premature complexes at doses that fail to terminate AF," *Cardiovasc. Res.*, vol. 50, pp. 75–84, Apr. 2001.
- [158] A. A. McDonough, J. B. Velotta, R. H. G. Schwinger, K. D. Philipson, and R. A. Farley, "The cardiac sodium pump: structure and function," *Basic Res. Cardiol.*, vol. 97 Suppl 1, pp. I19–24, 2002.
- [159] J. Carro, J. F. Rodríguez, P. Laguna, and E. Pueyo, "A human ventricular cell model for investigation of cardiac arrhythmias under hyperkalaemic conditions," *Philos Trans A Math Phys Eng Sci*, vol. 369, pp. 4205–4232, Nov. 2011.

- [160] A. Corrias, W. Giles, and B. Rodriguez, "Ionic mechanisms of electrophysiological properties and repolarization abnormalities in rabbit purkinje fibers," *Am. J. Physiol. Heart Circ. Physiol.*, vol. 300, pp. H1806–1813, May 2011.
- [161] L. Romero, B. Carbonell, B. Trenor, B. Rodríguez, J. Saiz, and J. M. Ferrero, "Systematic characterization of the ionic basis of rabbit cellular electrophysiology using two ventricular models," *Prog. Biophys. Mol. Biol.*, vol. 107, pp. 60–73, Oct. 2011.
- [162] Y. Blaauw, H. Gögelein, R. G. Tieleman, A. van Hunnik, U. Schotten, and M. A. Allessie, "'Early" class III drugs for the treatment of atrial fibrillation: efficacy and atrial selectivity of AVE0118 in remodeled atria of the goat," *Circulation*, vol. 110, pp. 1717–1724, Sept. 2004.
- [163] R. G. Tieleman, C. De Langen, I. C. Van Gelder, P. J. de Kam, J. Grandjean, K. J. Bel, M. C. Wijffels, M. A. Allessie, and H. J. Crijns, "Verapamil reduces tachycardia-induced electrical remodeling of the atria," *Circulation*, vol. 95, pp. 1945–1953, Apr. 1997.
- [164] A. Bueno-Orovio, E. M. Cherry, and F. H. Fenton, "Minimal model for human ventricular action potentials in tissue," *J. Theor. Biol.*, vol. 253, pp. 544–560, Aug. 2008.
- [165] Z. Syed, E. Vigmond, and L. Leon, "Automated modeling of cardiac electrical activity," in *Proceedings of the 25th Annual International Conference of the IEEE Engineering in Medicine and Biology Society, 2003*, vol. 1, pp. 55–58 Vol.1, Sept. 2003.
- [166] C. M. Ambrosi, K. A. Yamada, J. M. Nerbonne, and I. R. Efimov, "Gender differences in electrophysiological gene expression in failing and non-failing human hearts," *PLoS ONE*, vol. 8, no. 1, p. e54635, 2013. PMID: 23355885 PMCID: PMC3552854.
- [167] D. Jeyaraj, S. M. Haldar, X. Wan, M. D. McCauley, J. A. Ripperger, K. Hu, Y. Lu, B. L. Eapen, N. Sharma, E. Ficker, M. J. Cutler, J. Gulick, A. Sanbe, J. Robbins, S. Demolombe, R. V. Kondratov, S. A. Shea, U. Albrecht, X. H. T. Wehrens, D. S. Rosenbaum, and M. K. Jain, "Circadian rhythms govern cardiac repolarization and arrhythmogenesis," *Nature*, vol. 483, pp. 96–99, Mar. 2012. PMID: 22367544 PMCID: PMC3297978.
- [168] L. Xiao, J. Xiao, X. Luo, H. Lin, Z. Wang, and S. Nattel, "Feedback remodeling of cardiac potassium current expression: a novel potential mechanism for control of repolarization reserve," *Circulation*, vol. 118, pp. 983–992, Sept. 2008. PMID: 18711016.

- [169] E. Wettwer, T. Christ, S. Endig, N. Rozmaritsa, K. Matschke, J. J. Lynch, M. Pourrier, J. K. Gibson, D. Fedida, M. Knaut, and U. Ravens, "The new antiarrhythmic drug vernakalant: ex vivo study of human atrial tissue from sinus rhythm and chronic atrial fibrillation," *Cardiovasc. Res.*, vol. 98, pp. 145–154, Apr. 2013.
- [170] E. Wettwer, O. Hála, T. Christ, J. F. Heubach, D. Dobrev, M. Knaut, A. Varró, and U. Ravens, "Role of IK_{ur} in controlling action potential shape and contractility in the human atrium: influence of chronic atrial fibrillation," *Circulation*, vol. 110, pp. 2299–2306, Oct. 2004.
- [171] O. J. Britton, A. Bueno-Orovio, K. Van Ammel, H. R. Lu, R. Towart, D. J. Gallacher, and B. Rodriguez, "Experimentally calibrated population of models predicts and explains intersubject variability in cardiac cellular electrophysiology," *Proc. Natl. Acad. Sci. U.S.A.*, vol. 110, pp. E2098–2105, June 2013.
- [172] E. Pueyo, A. Corrias, L. Virág, N. Jost, T. Szél, A. Varró, N. Szentandrassy, P. P. Nánási, K. Burrage, and B. Rodríguez, "A multiscale investigation of repolarization variability and its role in cardiac arrhythmogenesis," *Biophys. J.*, vol. 101, pp. 2892–2902, Dec. 2011.
- [173] A. X. Sarkar, D. J. Christini, and E. A. Sobie, "Exploiting mathematical models to illuminate electrophysiological variability between individuals," *J. Physiol. (Lond.)*, vol. 590, pp. 2555–2567, June 2012.
- [174] E. A. Sobie and A. X. Sarkar, "Regression methods for parameter sensitivity analysis: applications to cardiac arrhythmia mechanisms," *Conf Proc IEEE Eng Med Biol Soc*, vol. 2011, pp. 4657–4660, 2011.
- [175] J. Walmsley, J. F. Rodriguez, G. R. Mirams, K. Burrage, I. R. Efimov, and B. Rodriguez, "mRNA expression levels in failing human hearts predict cellular electrophysiological remodeling: a population-based simulation study," *PLoS ONE*, vol. 8, no. 2, p. e56359, 2013.
- [176] S. Marino, I. B. Hogue, C. J. Ray, and D. E. Kirschner, "A methodology for performing global uncertainty and sensitivity analysis in systems biology," *J. Theor. Biol.*, vol. 254, pp. 178–196, Sept. 2008.
- [177] Z. Syed, E. Vigmond, S. Nattel, and L. J. Leon, "Atrial cell action potential parameter fitting using genetic algorithms," *Med Biol Eng Comput*, vol. 43, pp. 561–571, Sept. 2005.
- [178] Z. Wang, B. Fermini, and S. Nattel, "Sustained depolarization-induced outward current in human atrial myocytes. evidence for a novel delayed rectifier k⁺ current similar to kv1.5 cloned channel currents," *Circ. Res.*, vol. 73, pp. 1061–1076, Dec. 1993.

- [179] M. E. Díaz, S. C. O'Neill, and D. A. Eisner, "Sarcoplasmic reticulum calcium content fluctuation is the key to cardiac alternans," *Circ. Res.*, vol. 94, pp. 650–656, Mar. 2004.
- [180] M. R. Franz, S. M. Jamal, and S. M. Narayan, "The role of action potential alternans in the initiation of atrial fibrillation in humans: a review and future directions," *Europace*, vol. 14 Suppl 5, pp. v58–v64, Nov. 2012.
- [181] M. L. Koller, M. L. Riccio, and J. Gilmour, R F, "Dynamic restitution of action potential duration during electrical alternans and ventricular fibrillation," *Am. J. Physiol.*, vol. 275, pp. H1635–1642, Nov. 1998.
- [182] E. J. Pruvot, R. P. Katra, D. S. Rosenbaum, and K. R. Laurita, "Role of calcium cycling versus restitution in the mechanism of repolarization alternans," *Circ. Res.*, vol. 94, pp. 1083–1090, Apr. 2004.
- [183] M. W. Krueger, G. Seemann, K. Rhode, D. U. J. Keller, C. Schilling, A. Arujuna, J. Gill, M. D. O'Neill, R. Razavi, and O. Dössel, "Personalization of atrial anatomy and electrophysiology as a basis for clinical modeling of radio-frequency ablation of atrial fibrillation," *IEEE Trans Med Imaging*, vol. 32, pp. 73–84, Jan. 2013.
- [184] J. Feng, L. Yue, Z. Wang, and S. Nattel, "Ionic mechanisms of regional action potential heterogeneity in the canine right atrium," *Circ. Res.*, vol. 83, pp. 541–551, Sept. 1998.
- [185] L. Firek and W. R. Giles, "Outward currents underlying repolarization in human atrial myocytes," *Cardiovasc. Res.*, vol. 30, pp. 31–38, July 1995.
- [186] U. Ravens, C. Poulet, E. Wettwer, and M. Knaut, "Atrial selectivity of antiarrhythmic drugs," *J. Physiol. (Lond.)*, June 2013.
- [187] P. Milberg, C. Pott, G. Frommeyer, M. Fink, M. Ruhe, T. Matsuda, A. Baba, R. Klocke, T. H. Quang, S. Nikol, J. Stypmann, N. Osada, F. U. Müller, G. Breithardt, D. Noble, and L. Eckardt, "Acute inhibition of the Na^{+}/Ca^{2+} exchanger reduces proarrhythmia in an experimental model of chronic heart failure," *Heart Rhythm*, vol. 9, pp. 570–578, Apr. 2012.
- [188] S. Nattel, B. Burstein, and D. Dobrev, "Atrial remodeling and atrial fibrillation mechanisms and implications," *Circ Arrhythm Electrophysiol*, vol. 1, pp. 62–73, Apr. 2008.
- [189] F. Atienza, J. Almendral, J. Jalife, S. Zlochiver, R. Ploutz-Snyder, E. G. Torrecilla, A. Arenal, J. Kalifa, F. Fernández-Avilés, and

- O. Berenfeld, “Real-time dominant frequency mapping and ablation of dominant frequency sites in atrial fibrillation with left-to-right frequency gradients predicts long-term maintenance of sinus rhythm,” *Heart Rhythm*, vol. 6, pp. 33–40, Jan. 2009.
- [190] M. Mansour, R. Mandapati, O. Berenfeld, J. Chen, F. H. Samie, and J. Jalife, “Left-to-right gradient of atrial frequencies during acute atrial fibrillation in the isolated sheep heart,” *Circulation*, vol. 103, pp. 2631–2636, May 2001.
- [191] F. Sarmast, A. Kolli, A. Zaitsev, K. Parisian, A. S. Dhamoon, P. K. Guha, M. Warren, J. M. B. Anumonwo, S. M. Taffet, O. Berenfeld, and J. Jalife, “Cholinergic atrial fibrillation: I(K,ACh) gradients determine unequal left/right atrial frequencies and rotor dynamics,” *Cardiovasc. Res.*, vol. 59, pp. 863–873, Oct. 2003.
- [192] N. Voigt, A. Trausch, M. Knaut, K. Matschke, A. Varró, D. R. Van Wagoner, S. Nattel, U. Ravens, and D. Dobrev, “Left-to-right atrial inward rectifier potassium current gradients in patients with paroxysmal versus chronic atrial fibrillation,” *Circ Arrhythm Electrophysiol*, vol. 3, pp. 472–480, Oct. 2010.
- [193] O. Berenfeld and J. Jalife, “Complex fractionated atrial electrograms: is this the beast to tame in atrial fibrillation?,” *Circ Arrhythm Electrophysiol*, vol. 4, pp. 426–428, Aug. 2011.
- [194] K. Nademanee and N. Oketani, “The role of complex fractionated atrial electrograms in atrial fibrillation ablation moving to the beat of a different drum,” *J. Am. Coll. Cardiol.*, vol. 53, pp. 790–791, Mar. 2009.
- [195] S. M. Narayan, M. Wright, N. Derval, A. Jadidi, A. Forclaz, I. Nault, S. Miyazaki, F. Sacher, P. Bordachar, J. Clémenty, P. Jaïs, M. Haïssaguerre, and M. Hocini, “Classifying fractionated electrograms in human atrial fibrillation using monophasic action potentials and activation mapping: evidence for localized drivers, rate acceleration, and nonlocal signal etiologies,” *Heart Rhythm*, vol. 8, pp. 244–253, Feb. 2011.
- [196] M. W. Krueger, V. Schmidt, C. Tobón, F. M. Weber, C. Lorenz, D. U. J. Keller, H. Barschdorf, M. Burdumy, P. Neher, G. Plank, K. Rhode, G. Seemann, D. Sanchez-Quintana, J. Saiz, R. Razavi, and O. Dössel, “Modeling atrial fiber orientation in patient-specific geometries: A semi-automatic rule-based approach,” in *Functional Imaging and Modeling of the Heart* (D. N. Metaxas and L. Axel, eds.), no. 6666 in Lecture Notes in Computer Science, pp. 223–232, Springer Berlin Heidelberg, Jan. 2011.

-
- [197] C. Tobon Zuluaga, *Modelización y evaluación de factores que favorecen las arritmias auriculares y su tratamiento mediante técnicas quirúrgicas. Estudio de simulación*. PhD thesis, June 2010.
- [198] t. Everett, T H, L. C. Kok, R. H. Vaughn, J. R. Moorman, and D. E. Haines, “Frequency domain algorithm for quantifying atrial fibrillation organization to increase defibrillation efficacy,” *IEEE Trans Biomed Eng*, vol. 48, pp. 969–978, Sept. 2001.
- [199] L. Faes and F. Ravelli, “A morphology-based approach to the evaluation of atrial fibrillation organization,” *IEEE Eng Med Biol Mag*, vol. 26, pp. 59–67, Aug. 2007.

